



**University of
Nottingham**

UK | CHINA | MALAYSIA

Structural and Fluidic Investigation of Piezoelectric Synthetic Jet Actuators for Performance Enhancements

Baris Gungordu

Thesis submitted to the University of Nottingham
for the degree of Doctor of Philosophy

November 2021

To my parents and family

Abstract

Synthetic jet actuators are zero-net-mass-flux actuators with a wide range of applications including aerodynamic flow control, jet vectoring and mixing enhancement. They present advantages thanks to their compact size and ease of installation, compared to other active flow control devices. A piezoelectric driven synthetic jet actuator is a structural, fluidic and acoustic device that may in principle afford improvements in engineering applications, such as providing aerodynamic drag reduction over an aircraft wing or vertical tail, although further research is required before potential implementation.

This thesis aims to bring a new perspective to the structural mechanics modelling of piezoelectric actuators, as well as modelling of synthetic jet actuators by both analytical and multiphysics methods. The findings presented here may contribute to improved performance metrics of synthetic jet actuators, such as exit jet velocity and power conversion efficiency which was supported by an extensive experimental study.

In this thesis, three structural mechanics models were derived for the modal analysis of the unimorph piezoelectric actuator, in order to obtain an accurate model for both natural frequency and displacement. These models use transfer matrix method together with the extensional-flexural deflection of plates, and are derived from first principles of classical vibration theory. The models were then validated with both in-house and previously published experimental data. The mean estimation accuracy of the first mode of oscillation (i.e., natural frequency) is under 1.5% for the set of validation cases. Furthermore, mechanical damping identification is studied for frequency response functions, accurate estimations of displacement ($\pm 10\%$) for which were obtained when compared with the experimental data.

A fluidic-acoustic analytical model from the literature was extended by implementing the structural model obtained for the piezoelectric actuator. The main limitation of the existing analytical model was the lack of estimation of the natural frequency and peak diaphragm displacement, which were fixed by the implementation. The new structural-fluidic-acoustic model presented here obtained peak jet velocity estimations within $\pm 10\%$ on the three validation cases of in-house experimental data.

Also, within the study, a finite element method based multiphysics model was developed which enabled the accurate modelling of different synthetic jet actuator configurations. Existing CFD models in the literature do not fully model the behaviour of the piezoelectric diaphragm or the Helmholtz resonance, which limits the study to a forcing frequency envelope less than the Helmholtz resonance. The multiphysics model developed here covers the entire actuation frequency including Helmholtz and mechanical diaphragm reso-

nance. It was used for computations of diaphragm deflection profile and exit jet velocity for both opposite and adjacent orifice-diaphragm configuration synthetic jet actuator. The jet velocity estimations fit the experimental data by $\pm 10\%$ on the three validation cases of in-house experimental data.

In order to achieve increased transverse displacement, bimorph polycrystalline piezoelectric diaphragms, which consist of two piezoceramic layers, were tested. Despite the enhanced transverse diaphragm displacement and jet velocity compared to a similar overall thickness unimorph, bimorph's current consumption is substantially higher than their counterparts, in turn reducing the power conversion efficiency. With a bimorph piezoelectric driven synthetic jet actuator a peak jet velocity of 92 ms^{-1} is obtained with a electric-to-fluidic power conversion efficiency of 6.4%, at a peak supply voltage of 40 V.

The electromechanical coupling ratio of polycrystalline piezoceramics are inherently low and the effect of using more advanced piezoceramic such as single crystal was also investigated. It was identified that single crystal piezoceramic promotes three times more transverse diaphragm displacement and two times more jet velocity, compared to the polycrystalline piezoelectric actuator for the same input diaphragm voltage. Consequently, employing single crystal piezoceramic enhanced electric-to-fluidic power conversion efficiency. A peak exit jet velocity of 99.5 ms^{-1} was obtained at 40 V of peak supply voltage which can be classified as a low voltage supply compared to the studies in the literature which obtained similar exit jet velocity. Also, the power conversion efficiency of 70% was achieved corresponding to the Helmholtz resonance dominated actuation region.

Different cavity-orifice arrangements, namely, opposite and adjacent configurations are studied in which showed that the peak jet velocity drops by approximately 10% when adjacent configuration is used instead of the similar size opposite configuration synthetic jet actuator, at the same supply voltage.

A single modal frequency response synthetic jet actuator was developed and it is identified that 46% of electric-to-fluidic power conversion is attained with an exit jet velocity of 62 ms^{-1} which is significantly higher in power conversion efficiency compared with the bimodal frequency response synthetic jet actuator.

Acknowledgements

First and foremost, I would like to thank my supervisor Assistant Professor Mark Jabbal. Mark, thanks for the opportunity to be a member of your team. I am grateful for all of the support and helpful discussions about synthetic jet actuators and also for guiding me patiently during the thesis write-up. Special thanks also go to Professor Atanas Popov. Atanas, thanks for taking initiative on the project and leading me through the developments of the structural mechanics' analysis of the piezoelectric actuators. Also, your meticulous care in the thesis write-up helped a lot towards the accomplishment.

I would like to thank Professor Yuying Yan for providing the hot wire anemometer equipment and Associate Professor David Branson for providing me with working space at the robotics lab. FLUTE group provided financial support for my project and I am grateful to Associate Professor Buddhika Hewakandamby as the head of the group.

Adeel and Peter thank you so much for being very supportive colleagues at all times, it was a pleasure to be in the same team with you. Kerem and Dimitris, it was great to meet you and our time at the office was great. Perhaps more importantly, thanks for the friendship we developed for life, which made these PhD years much more enjoyable. I want to express my gratitude to Dr Alican Guran for always being a supportive friend and available to rectify issues at all times for a long time. Dr Gizem Morris, you have been always inspirational and supportive since we met and I am also grateful to have you available whenever is needed. Also, I want to say thanks to Dr Diva Ulucay who supported me patiently throughout my PhD process.

Last but not least, the biggest thank you goes to my mother and father. Without your support, this would not have been possible. Thank you from my heart for your endless love. Buse, you were always there for unconditional love and support throughout my education and the pain to lose you cannot be described with words. This thesis is dedicated to you and I know this will make you proud where ever you are now. You will be remembered. Rest in peace.

List of Abbreviations

BS Bessel Functions

CFD Computational Fluid Dynamics

CPT Classical Plate Theory

FEM Finite Element Methods

FRF Frequency Response Function

IATA International Air Transport Association

LEM Lumped Element Modelling

ME Matrix Exponential

PMN-PT Lead magnesium niobite-lead titanite

PZT Lead zirconate titanate

SJ Synthetic Jet

SJA Synthetic Jet Actuator

TMM Transfer Matrix Method

TPT Thin Plate Theory

Nomenclature

A_o	Area of orifice	m^2
$A(r)$	Transfer matrix constituted by the selected state variables	[-]
c	Speed of sound	ms^{-1}
C_μ	Momentum Coefficient	[-]
C_I	Inertia Coefficient	[-]
C_d	Orifice discharge coefficient	[-]
d_{31}	Transverse piezoelectric coefficient	pm/V
d_o	Orifice diameter	m
D_A	Acoustic piezoelectric coefficient	m^3/V
D_c	Cavity diameter	m
D_s	Flexural rigidity of Substrate Layer	$Pa.m^3$
D_{pzt}	Flexural rigidity of Piezoelectric Layer	$Pa.m^3$
D_{bs}	Plate Integrated Bending Stiffness	$Pa.m^3$
D_{pzt}	Diameter of the piezoceramic plate	m
D_s	Diameter of the substrate plate	m
E_p	Young's Modulus of Piezoelectric Layer	Pa
f	Actuation frequency	$1/s$ (Hz)

f_c	Nyquist criterion of sampling	Hz
f_h	Helmholtz (cavity acoustic) resonance frequency	Hz
f_m	First-mode of oscillation/fundamental frequency	Hz
f_s	Frequency of sampling	Hz
F_{ext}	Force exerted by the moving wall	N
H	Cavity Height	m
$H(\omega)$	Magnitude of frequency response at the given frequency	m
$H(\omega_n)$	Magnitude of frequency response at the resonance frequency	m
$H(\omega_0)$	Magnitude of frequency response at the quasi-static frequency	m
I	Current	A
I_p	Peak Current	A
k	Non-dimensional Wave Parameter, $\frac{\rho h \omega^2}{D}$	[-]
k_p	Electro-mechanical coupling ratio of a piezoceramic	[-]
K	Fluidic loss term	[-]
l_{eff}	Effective orifice neck length	m
l_o	Orifice neck length	m
L	Stroke length	m
m_t	Total Mass of diaphragm and air in the cavity	kg
$M_r(r)$	Bending moment	Nm
p_i	Pressure in the cavity	Pa
P_f	Fluidic power	W

P_e	Electric power	W
$Q_r(r)$	Shear force	N
r	Radius on a circular plate	m
Re	Reynolds number	[-]
S	Stokes number	[-]
St	Strouhal number	[-]
t	Thickness of a plate	m
t_{pzt}	Thickness of Piezoceramic Layer	m
t_s	Thickness of Substrate Layer	m
T	Period of cycle, (1/f)	s
U	Orifice exit flow velocity	ms^{-1}
U_p	Peak orifice exit jet velocity	ms^{-1}
U_0	Time-averaged exit jet velocity during blowing cycle	ms^{-1}
U_∞	Free-stream velocity	ms^{-1}
V_{AC}	Diaphragm supply voltage	V
V_0	Cavity Volume	m^3
V_p	Peak supply voltage	V
$w(r)$	Transverse displacement of the diaphragm	m
$W(r)$	Transverse displacement vector of the diaphragm	m
x_w	Moving wall displacement	m
\dot{x}_w	Moving wall velocity	ms^{-1}

z_d	Neutral Plane Position	m
-------	------------------------	---

Greek symbols

β	Magnification factor	[-]
---------	----------------------	-----

β_r	Ratio of orifice diameter to cavity diameter	[-]
-----------	--	-----

ΔV_0	Displaced Cavity Volume	m^3
--------------	-------------------------	--------------

Δl_e	Correction factor for the effective orifice length	[-]
--------------	--	-----

ν_p	Poisson's Ratio of Piezoceramic Layer	[-]
---------	---------------------------------------	-----

ν_s	Poisson's Ratio of Substrate Layer	[-]
---------	------------------------------------	-----

ω	Angular frequency of vibration/actuation, $2\pi f$	rad/s
----------	--	-------

ω_n	Angular frequency of natural frequency of the actuator, $2\pi f_m$	rad/s
------------	--	-------

$\Phi(r)$	Radial Derivative of the $W(r)$, $\frac{dW(r)}{dr}$	[-]
-----------	--	-----

η	Electric-to-fluidic power conversion efficiency	[-]
--------	---	-----

ρ	Density of material or air depending on the context	kg/m^3
--------	---	------------------------

θ	Radial direction on a circular plate	radian
----------	--------------------------------------	--------

ϕ	Phase difference angle	$^\circ$
--------	------------------------	----------

ζ	Material damping ratio of the piezoelectric diaphragm	[-]
---------	---	-----

ζ_{mf}	Material damping ratio obtained by magnification factor method	[-]
--------------	--	-----

ζ_{hp}	Material damping ratio obtained by half-power method	[-]
--------------	--	-----

Contents

Abstract	i
Acknowledgements	iii
List of Abbreviations	iv
Nomenclature	v
1 Introduction	1
1.1 Motivation	1
1.2 Approach to Research	4
1.3 Aim and Objectives	7
1.4 Research Methodology	8
1.5 Organisation of the Thesis	12
1.6 Publication and Conferences	13
2 Literature Review and Background Theory	14
2.1 Motivation and Overview	14
2.2 Flow Control	14
2.3 Actuators	15
2.3.1 Flow Control With SJA	20
2.4 Piezoelectricity	20
2.5 Composite Piezoelectric Actuator	23
2.6 Synthetic Jet Actuator	27
2.6.1 Geometry and Operation	28
2.6.2 Frequency Response of the Actuator	29
2.6.3 Parameters and Fundamental Relationships	33
2.6.4 Jet Formation Criterion	35

2.6.5	Power Conversion Efficiency	38
2.7	Experimental Studies and Performance of SJA To-Date	40
2.8	Modelling Studies	41
2.9	Identified Research Gaps from the Literature Review	47
2.9.1	Modelling of the Free and Forced Vibrations of Piezo- electric Actuator	47
2.9.2	Analytical Modelling of SJA	48
2.9.3	CFD Modelling of SJA	49
2.9.4	Jet velocity and Power Efficiency Enhancement of SJA	50
3	Experimental Methods and Apparatus	51
3.1	Experimental Validation Strategy	51
3.1.1	Proposed Experimental Investigation	52
3.1.2	Nature of Periodic Data and Requirements	53
3.2	Piezoelectric Actuator	54
3.3	Clamping and Cavity-Orifice Arrangement Manufacturing	57
3.4	Piezoelectric Actuator Displacement Measurements	62
3.5	Power Measurements	64
3.6	Jet Velocity Measurements	65
3.7	In-cavity Pressure Measurements	69
3.8	Temperature Measurements	72
3.9	Discussion	73
3.10	Summary	74
4	Theoretical Development and Experimental Validation of Nat- ural Frequency and Mode Shape	77
4.1	Introduction	77
4.2	Theory 1: Approach with CPT and TMM	81
4.2.1	Theory Derivation of CPT with TMM	83
4.2.2	Results and Experimental Validation	89
4.3	Theory 2: Approach with Matrix Exponentials and TMM	91
4.3.1	Formulation and Derivation of the Model	92

4.3.2	Computational Model	95
4.3.3	Experimental Validation and Comparison with the CPT Model	96
4.4	Theory 3: Composite Plate Theory with Steps	97
4.4.1	Theoretical model and computational procedure	97
4.4.2	Derivation of the governing system of six first-order ODEs	103
4.4.3	Transfer matrix formulation	107
4.4.4	Natural frequencies and mode shapes calculation	111
4.4.5	Experimental Validation and Comparison with Previous Theory	112
4.5	Clamping Effect on Natural Frequency: A Special Consideration	113
4.6	Theoretical and Practical Insight	118
4.7	Discussion	120
4.8	Summary	123
5	Experimental Validation and Numerical Verification of Dy- namic Response Modelling	126
5.1	Introduction	126
5.2	Formulation of the governing equations	128
5.3	Experimental frequency sweep	132
5.4	Identification of Mechanical Damping	134
5.5	Dynamic response model validation against experimental data .	137
5.5.1	Experimental validation of the voltage sweep	138
5.6	FEM of the Composite Piezoelectric Diaphragm	140
5.6.1	Geometry and Equations	141
5.6.2	Boundary Conditions and Mesh	142
5.6.3	Verification cases	143
5.7	Discussion	145
5.8	Summary	147
6	Extension and Experimental Validation of Physical Models for Synthetic Jet Actuators	149

6.1	Introduction	149
6.2	Analytical Modelling	153
6.2.1	Review of the piston-based fluidic-acoustic model	153
6.2.2	Improvement requirements of the piston-based analytical model	157
6.2.3	Diaphragm-based Analytical Model	159
6.3	Validation of the Diaphragm-based Analytical Model	161
6.3.1	Validation Case 1	162
6.3.2	Validation of Isothermal Operation Assumption	166
6.3.3	Validation Case 2	167
6.3.4	Validation Case 3	172
6.4	Multiphysics Modelling	175
6.4.1	Mathematical Model - Pressure Acoustics with Viscosity	175
6.4.2	Geometry, Meshing and Time Domain Study	177
6.5	Validation of the Multiphysics Model	179
6.5.1	Validation Case 1	179
6.5.2	Validation Case 2	182
6.5.3	Time-domain Response and Phase Relationships	184
6.5.4	Velocity Contours	187
6.5.5	Vorticity Contours	188
6.5.6	Validation Case 3	192
6.5.7	Time-domain Response and Phase Relationships	194
6.5.8	Velocity Contours	196
6.5.9	Vorticity Contours	198
6.6	Discussion	202
6.6.1	Discussion of SJA - Analytical Model	202
6.6.2	Discussion of SJA - Multiphysics Model	205
6.7	Summary	208
7	Investigation of achieving high jet velocity and power conversion efficiency	211

7.1	Introduction	211
7.2	Comparison Between Polycrystal and Single Crystal Disc	217
7.2.1	Design of Experiments	217
7.2.2	Opposite Orifice-Diaphragm Configuration	218
7.2.3	Diaphragm Displacement	218
7.2.4	Jet Velocity	220
7.2.5	Current Draw	222
7.2.6	Electric-to-Fluidic Power Conversion Efficiency	224
7.2.7	Adjacent Orifice-Diaphragm Configuration	228
7.2.8	Jet Velocity	229
7.2.9	Current Draw	230
7.2.10	Electric-to-Fluidic Power Conversion Efficiency	233
7.3	Comparison Between Unimorph and Bimorph Disc	235
7.3.1	Design of Experiments	235
7.3.2	Opposite Orifice-Diaphragm Configuration	236
7.3.3	Diaphragm Displacement	236
7.3.4	Jet Velocity	239
7.3.5	Current Drawn	241
7.3.6	Electric-to-Fluidic Power Efficiency	241
7.3.7	Adjacent Orifice-Diaphragm Configuration	245
7.3.8	Jet Velocity	245
7.3.9	Current Drawn	247
7.3.10	Electric-to-Fluidic Power Conversion Efficiency	247
7.4	Single Modal Frequency Response SJA	251
7.4.1	Jet Velocity	252
7.4.2	Current Consumption and Power Efficiency	252
7.5	Discussion	257
7.5.1	Implications of the research	257
7.5.2	Implications for industry	261
7.6	Summary	265

8 Conclusions	270
8.1 Review of aim and objectives	270
8.2 Summary and Contributions	274
8.3 Recommendations for Future Work	276
Bibliography	278

List of Tables

2.1	Comparison of Helmholtz resonance equations	31
2.2	Comparison of diaphragm mechanical resonance equations	33
2.3	Selected Experimental Study	41
2.4	Selected Studies of LEM	43
2.5	Selected Studies of Analytical Model of SJA	44
2.6	Selected Studies of CFD Model of SJA	47
3.1	Piezoelectric diaphragm groups and piezoelectric properties	56
3.2	PSV-300 Laser Board Acquisition Specifications	63
3.3	Accuracy of the equipment used in the experimental campaign	74
4.1	Test cases for the theory validation	90
4.2	Material Properties of the Piezoelectric Actuator	91
4.3	Theoretical versus experimental results for the diaphragm's natural frequency	91
4.4	Theoretical versus experimental results for the diaphragm's natural frequency	96
4.5	Theoretical versus experimental results for the diaphragm's natural frequency	96
4.6	Theoretical versus experimental results for the diaphragm's natural frequency	113
4.7	Material Properties of the Piezoelectric Actuator	114
4.8	Test cases for the theory validation	114
4.9	Test case results with Gomes's experiments	115

4.10	Theoretical versus FEM results for the diaphragm's natural frequency	116
4.11	Test cases for the theory validation	117
4.12	Theoretical versus experimental results for the diaphragm's natural frequency - Simply Supported	117
4.13	A brief comparison of models	120
4.14	Summary of Validation Cases Studied in the Chapter 4	124
5.1	Test cases for the theory validation	132
5.2	Material Properties of the Piezoelectric Actuator	132
5.3	Results for the experimental centre displacement	133
5.4	Damping identification of the experimental FRF cases	136
5.5	Peak centre displacement by FEM and experiments at the resonant frequency	145
5.6	Summary of Validation Cases Studied in the Chapter 5	148
6.1	Comparison of effective orifice length equations	155
6.2	Validation Case 1 - Diaphragm and actuator size, model parameters and computed resonance frequency	163
6.3	Validation Case 1 - Comparison of model and experiment results at resonant frequency	165
6.4	Validation Case 2 - Diaphragm and actuator size, and model parameters	168
6.5	Validation Case 2 - Comparison of model and experiment results at resonant frequency	170
6.6	Validation Case 3 - Diaphragm and actuator size, and model parameters	172
6.7	Validation Case 3 - Comparison of model and experiment results at resonant frequency	174
6.8	Simulation mesh convergence test	179
6.9	Validation Case 1 - Diaphragm and actuator size	180

6.10	Validation Case 1 - Comparison of model and experiment results at resonant frequency	180
6.11	Validation Case 2 - Diaphragm and actuator size	182
6.12	Validation Case 2 - Comparison of model and experiment results at resonant frequency	183
6.13	Key non-dimensional flow parameters at the mechanical reso- nance frequency	184
6.14	Validation Case 3 - Diaphragm and actuator size	192
6.15	Validation Case 3 - Comparison of model and experiment results at resonant frequency	194
6.16	Key non-dimensional flow parameters at the mechanical reso- nance frequency	194
6.17	$(f_1x f_2)$ vs $(f_hx f_m)$	203
6.18	Summary of SJA Modelling Validation Cases for diaphragm- based analytical model and multiphysics model	208
7.1	Fluidic and electric power definitions in the literature	214
7.2	A comparison of the experimental studies with key actuator di- mensions, voltage supplied and achieved jet velocity and power conversion efficiency	214
7.3	Polycrystalline and single crystal actuator dimensions and prop- erties	217
7.4	Cavity-orifice arrangement size and operational parameters . . .	218
7.5	Comparison of peak power conversion efficiency values	226
7.6	Cavity-orifice arrangement size and operational parameters . . .	229
7.7	Comparison of peak power conversion efficiency values	235
7.8	Polycrystalline unimorph and bimorph configuration actuator dimensions and properties	236
7.9	Cavity-orifice arrangement dimensions and operational param- eters	236

7.10 Comparison of peak power conversion efficiency values 243

7.11 Dimensions of cavity-orifice arrangement and operational pa-
rameters 245

7.12 Comparison of peak power conversion efficiency values 249

7.13 Piezoelectric diaphragm and cavity-orifice dimensions 252

7.14 Comparison of peak power conversion efficiency values 257

7.15 Comparison of the selected experimental research with present
work 260

List of Figures

1.1	Schematic of a synthetic jet actuator	4
1.2	Synthetic Jet Actuator Orifice-Diaphragm Configurations (a) Opposite (b) Adjacent	6
1.3	SJA Types Performance Comparison [17]	7
1.4	A block diagram of the result chapters	11
2.1	Classification of flow control actuators	16
2.2	Types of Synthetic Jet Actuators (a) Piezoelectric Driven (PZT) [27] (b) Electro-active Polymer (EAP) [28] (c) Ferromagnetic Shape Memory Alloy (FSMA) [29] (d) Plasma SJA (PSJA) [30]	19
2.3	Illustration of the piezoelectric material polarisation [39]	21
2.4	Illustration of the circular composite piezoelectric actuator	23
2.5	First four mode shapes of clamped unimorph piezoelectric ac- tuator [64]	27
2.6	Synthetic Jet Illustration (a) Initial Suction Stroke where air is sucked in the cavity (b) Vortex ring production during ejection stroke (c) Vortex ring propagation out of the orifice even though the diaphragm is in suction stroke	28
2.7	Geometry of a typical actuator	29
2.8	Typical Jet Velocity Output of SJA	30
2.9	Formation Criterion Proposed by Zhou et al. [78]	37
3.2	Illustration of frequency aliasing [65]	53

3.3	(a) Schematic of unimorph piezoelectric actuator (b) Schematic of bimorph piezoelectric actuator (c) Unimorph piezoelectric actuator (upper and lower surfaces) (d) Bimorph piezoelectric actuator (upper and lower surfaces) (soldered)	55
3.4	2-D Illustration of the clamping mechanism	57
3.5	3-D design of diaphragm container, piezoelectric actuator and clamping plate (a) view from outer side (b) view from inner side	59
3.6	View of clamped piezoelectric actuator on the test bed (a) front side (b) back side	60
3.7	3-D assembly drawing of the cavity-orifice arrangement and piezoelectric diaphragm (a) view from outer side (b) view from inner side	61
3.8	Laser Operation Setup	63
3.9	A Sample Data for Voltage and Current	65
3.10	Illustration of hot-wire probe positioning and setup	66
3.11	HWA Calibration Curve Fit with 4 th and 5 th Order Polynomials	68
3.12	A Sample Velocity Signal	69
3.13	Illustration of pressure transducer and hot-wire probe positioning and setup	70
3.14	Meggitt 8507C-5 Pressure Transducer and Model 136 DC Amplifier [116]	71
3.15	Meggitt 8507C-5 Pressure Transducer Detailed Drawing [116] . .	71
3.16	A Sample In-Cavity Pressure Data	72
3.17	A Sample Data for Thermocouples Demonstrating the Operation	73
4.1	Simplified model of a piezoelectric disc actuator with a substrate layer and single active upper layer	79
4.2	Natural Frequency determination with TMM	90
4.3	Configuration for the clamped stepped circular plate - with axisymmetric step	90

4.4	Convention for a coordinate frame and signs of internal forces in the circular plate model. (a) Plate coordinate frame. (b) Plate vertical cross-section. Note: the coordinate system $Ar\theta$ does not coincide with the plate mid-plane, in general. (c) Positive sign conventions for internal plate forces and moments.	98
4.5	Configuration for the clamped stepped circular plate - with asymmetric step	114
4.6	FEM model of a piezoelectric disc actuator for Case 1	115
4.7	Effect of varying (a) Brass diameter (b) Piezoceramic diameter (c) Brass Thickness (d) Piezoceramic thickness on Natural Frequency	119
4.8	FEM Study on the variation of bonding layer thickness (a) $t_{bonding} = 0 \mu\text{m}$ (b) $t_{bonding} = 3 \mu\text{m}$ (c) $t_{bonding} = 5 \mu\text{m}$ (d) $t_{bonding} = 10 \mu\text{m}$	122
5.1	Radial displacement profile at resonant frequency	131
5.2	Experimental Frequency Sweep of Selected Test Cases	133
5.3	FRF illustration of the critical frequency parameters used in damping identification	135
5.4	Dynamic Response modelling with two damping models (a) Case 1 (b) Case 2 (c) Case 3	139
5.5	Piezoelectric actuator centre displacement versus the driving voltages	140
5.6	2-D axisymmetric geometry of the piezoelectric actuator	141
5.7	First-mode of oscillation with FEM analysis	142
5.8	Frequency response function of FEM and experiment (a) Case 1 (b) Case 2 (c) Case 3	144
6.1	Block diagram of the piston-based analytical model	157
6.2	Wall deflection (piston-based analytical model) to diaphragm deflection (diaphragm-based analytical model)	159

6.3	Block diagram of the diaphragm-based analytical model	160
6.4	Deflection of the diaphragm from the structural model	160
6.5	A Sample Signal and Peaks	162
6.6	Validation Case 1 - Diaphragm displacement comparison of the model and experiment	163
6.7	Validation Case 1 - Cavity pressure comparison of the model and experiment	164
6.8	Validation Case 1 - Mean jet velocity comparison of the model and experiment	165
6.9	Temperature measurements of the in-cavity and orifice exit at the resonance frequency	166
6.10	Validation Case 2 - Diaphragm displacement comparison of the model and experiment	169
6.11	Validation Case 2 - Mean peak jet velocity comparison of the model and experiment	169
6.12	Validation Case 2 - Stiff Diaphragm with $f_m = 10kHz$	171
6.13	Validation Case 3 - Diaphragm displacement comparison of the model and experiment	173
6.14	Validation Case 3 - Peak Jet Velocity Comparison of the model and experiment	174
6.15	Geometry, meshing and boundary conditions for opposite diaphragm- orifice configuration	178
6.16	Geometry, meshing and boundary conditions for adjacent diaphragm- orifice configuration	178
6.17	Case 1 - Diaphragm displacement comparison of the model and experiment	181
6.18	Case 1 - Mean peak jet velocity comparison of the model and experiment	181
6.19	Case 2 - Diaphragm displacement comparison of the model and experiment	183

6.20 Case 2 - Mean peak jet velocity comparison of the model and experiment	184
6.21 Normalised time-domain response of key variables	185
6.22 Diaphragm locations where flow visualizations are presented . . .	186
6.23 Case 2 - Phase angle relationships	187
6.24 Numerical solutions for the validation Case 2 - Velocity Contours	189
6.26 Case 3 - Diaphragm displacement comparison of the model and experiment	193
6.27 Case 3 - Mean peak jet velocity comparison of the model and experiment	193
6.28 Normalised time-domain response of key variables	195
6.29 Case 3 - Phase angle relationships	196
6.30 Diaphragm locations where flow visualizations are presented . . .	197
7.1 Opposite and Adjacent Orifice-Diaphragm Configuration SJA Array	212
7.2 Opposite Configuration SJA - Centre peak diaphragm displacements of SJA (a) PZT-5A diaphragm driven SJA (b) PMN-PT diaphragm driven SJA	219
7.3 Mean Peak Exit Jet Velocity (a) PZT-5A diaphragm driven SJA (b) PMN-PT diaphragm driven SJA	221
7.4 Opposite Configuration SJA - Mean Peak Current Draw of SJA (a) PZT-5A diaphragm driven SJA (b) PMN-PT diaphragm driven SJA	223
7.5 Power factor ($\cos \phi$) of PZT-5A and PMN-PT diaphragms	224
7.6 Opposite Configuration SJA - Power Conversion Efficiency (a) PZT-5A diaphragm driven SJA (b) PMN-PT diaphragm driven SJA	227

7.7	Adjacent Configuration SJA - Mean Peak Exit Jet Velocity (a) PZT-5A diaphragm driven SJA (b) PMN-PT diaphragm driven SJA	231
7.8	Adjacent Configuration SJA - Mean Peak Current Draw (a) PZT-5A diaphragm driven SJA (b) PMN-PT diaphragm driven SJA	232
7.9	Adjacent Configuration SJA - Power Conversion Efficiency (a) PZT-5A diaphragm driven SJA (b) PMN-PT diaphragm driven SJA	234
7.10	Opposite Configuration SJA - Centre Peak Diaphragm Dis- placement (a) Unimorph diaphragm driven SJA (b) Bimorph diaphragm driven SJA	238
7.11	Opposite Configuration SJA - Mean Peak Exit Jet Velocity (a) Unimorph diaphragm driven SJA (b) Bimorph diaphragm driven SJA	240
7.12	Opposite Configuration SJA - Mean Peak Current Draw (a) Unimorph diaphragm driven SJA (b) Bimorph diaphragm driven SJA	242
7.13	Opposite Configuration SJA - Power Conversion Efficiency of (a) Unimorph Driven SJA (b) Bimorph Driven SJA	244
7.14	Adjacent Configuration SJA - Mean Peak Exit Jet Velocity (a) Unimorph diaphragm driven SJA (b) Bimorph diaphragm driven SJA	246
7.15	Adjacent Configuration SJA - Mean Peak Current Draw by (a) Unimorph diaphragm driven SJA (b) Bimorph diaphragm driven SJA	248
7.16	Adjacent Configuration SJA - Power Conversion Efficiency (a) Unimorph diaphragm driven SJA (b) Bimorph diaphragm driven SJA	250

7.17	Mean Peak Exit Jet Velocity of the Single Modal SJA (a) PZT-5A and PMN-PT Driven SJA - 20 V_p (b) PZT-5A and PMN-PT Driven SJA - 40 V_p	253
7.18	Mean Peak Current Draw of the Single Modal SJA (a) PZT-5A and PMN-PT Driven SJA - 20 V_p (b) PZT-5A and PMN-PT Driven SJA - 40 V_p	255
7.19	Power Conversion Efficiency of (a) Single Modal Response SJA - 20 V_p (b) Single Modal Response SJA - 40 V_p	256
7.20	C_μ and power consumption requirement calculations for the conditions provided by Mooney et al. [31] (a) Peak jet velocity (U_p) versus the momentum coefficient C_μ (b) Number of actuators versus the power consumption	264
7.21	C_μ/P_e calculations for the conditions provided by Mooney et al. [31]	265

Chapter 1

Introduction

1.1 Motivation

According to the International Air Transport Association (IATA), the total number of passengers for commercial flights was 4.5 billion in 2019, a number projected to increase to approximately 7.2 billion by 2035 [1]. Currently, air transport accounts for 2.5% of the total global man-made carbon emissions [2]. By 2050, the aim is to reduce emissions back to the levels in 2005 despite the rapid growth expected in commercial flights [3]. Flight Path 2050 project of European Union propose a protocol which aims 75% CO₂ reduction per passenger per kilometre and 90% NO_x emissions to be cut compared to aircraft manufactured in 2000 as of 2050 [4]. In addition, in October 2021, IATA approved a resolution for the global air transport industry to achieve net-zero carbon emissions by 2050 which is also parallel with the Paris Agreement goals regarding global warming [5]. Therefore, in order to comply with the protocols, the emissions should be reduced to obtain a more efficient flight. The targets are only achievable if the necessary improvements on flight operations are made.

It is known that 1% of drag reduction leads to a 0.2% reduction in the operating costs for a civil transport aircraft [6]. Furthermore, this means less space for fuel, hence a lighter aeroplane. A potential 1% reduction in fuel (power)

consumption would have a significant impact on aeronautics industry and society. The potential economic impact of that reduction would be around 1.32 billion GBP for the current fuel consumption around the World.

Another issue regarding commercial flight industry is noise emission, which creates a discomfort for people living near airports. In addition, aircraft noise has been linked to serious diseases, causing it to be a major public health issue. To illustrate, people living near London Heathrow are reported to have a 15% higher stroke and heart disease rate compared to people from other areas of London [7]. With flow control, noise emissions are likely to be reduced as the thrust requirement would be minimized, especially in the landing configuration.

Flow control has great potential to help towards achieving aforementioned emission levels (i.e., CO, CO₂, NO_x), as well as drag and noise reductions by controlling flow separation to reduce aerodynamic drag. The benefits will especially be evident at take-off and landing flight configurations, in which the flow separation contributes significantly to the overall aerodynamic drag. Also, an effective flow control system can be used to obtain a smaller vertical tail which is oversized to ensure symmetric thrust in case of an engine failure [8], and also, to control flow separation at the engine/wing junction [9]. Flow control mechanisms are separated into two types: namely passive and active methods. Passive flow control is achieved by changing/adding a structure on the aeroplane (i.e., vane-type vortex generators). Active methods involve the addition of energy/power via an actuator or a similar system.

On the other hand, aerodynamic flow control can also be implemented to ground vehicles and wind turbine blades, which would enhance power efficiency by reducing their pressure drag. Flow control could also help to increase efficiency for electric cars to extend their range similar to the application made by Renault to control flow separation and wake size [10]. For ground vehicles, a 12% reduction in fuel consumption in the US alone would save up to 3.3 billion gallons of diesel per year and prevent 28 million tons of CO₂ emissions

[11]. As for wind turbines, a 10% reduction of the drag on the blades would increase the energy produced by roughly 4%, and they may also benefit from an active flow control system to reduce pressure drag [12].

Due to its compact size and no requirement for piping, a synthetic jet actuator (SJA) is a high-potential flow control mechanism for a full-scale aeroplane implementation. A SJA, which is also known as zero-net-mass-flux jet, is driven by a structural or acoustic pressure amplification mechanism, such as a piezoelectric actuator, piston or loudspeaker.

Figure 1.1 presents a schematic of a SJA. The actuation mechanism oscillates periodically to input momentum to the still air in the cavity (air sealed) which then discharges through an orifice turning the flow into an unsteady jet. The diaphragm motion has two cycles, namely, ingestion and expulsion. When the diaphragm moves away from the orifice opening (i.e., ingestion cycle), the net volume of the cavity increases which causes a pressure drop. Thereby, the fluid outside of the orifice exit plane is sucked inside the cavity. On contrary, during the expulsion stage, the diaphragm moves towards the orifice which causes the fluid in the cavity to discharge to the outer medium through the orifice neck, inducing a boundary layer along the inner side of the orifice neck. The boundary layer separates at the cavity-orifice neck junction due to the sharp geometric contraction, which is followed by roll-up of the separated shear layer. The rolled-up shear layers close their selves to form vortex rings which give rise to an unsteady train of vortices forming the synthetic jet as the diaphragm oscillates. Once the jet formation criterion is met, the vortical structure moves further downstream during the backward motion with its self-induced velocity and is therefore unaffected by the suction of the diaphragm. Owing to the unsteady nature of the jet, the jet velocity vector has negative and positive cycles for suction and expulsion, respectively. The time-average of the exit jet velocity is zero, but the momentum flux is not. The jet ejected by a SJA can be used to control flow separation or thrust vectoring [13].

For a passive or active flow control mechanism, the first arising question should

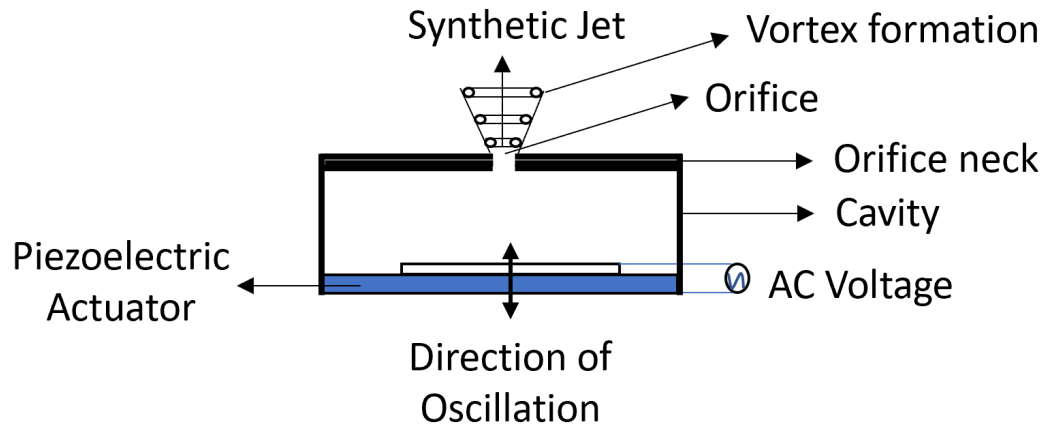


Figure 1.1: Schematic of a synthetic jet actuator

be that of the effectiveness (for flow control), followed by the power conversion efficiency of the actuator for a given application. The current issues of SJA are the low jet velocity (compared to the cruise condition U_∞ of a modern passenger aircraft) and power conversion efficiency, which should be further studied. For example, Plasma SJA can reach jet velocities exceeding 300 ms^{-1} with an electro-mechanical efficiency of 0.1-1%, which can be considered as a high jet velocity but low power conversion efficiency (voltage supply O(kV) is required) [14]. To achieve effective flow control, the peak jet velocity of the actuator should be $3 \times U_\infty$ and for a vertical tail the local flow velocity (U_∞) is around 70 ms^{-1} [15]. Therefore, an acceptable SJA jet velocity is around 200 ms^{-1} to grant flow control effectiveness for a vertical tail. Nevertheless, power consumption should also be monitored to make sure that it does not exceed the limits of power supply system.

1.2 Approach to Research

The motivation of this study is to develop stand alone, highly accurate and efficient modelling tools as well as to achieve state-of-the-art performance metrics of the SJA development towards full-scale implementation. The goal is to improve theoretical knowledge and extend the existing approaches for modelling SJA towards getting enhanced performance characteristics for a potential flow

control application in terms of exit jet velocity and efficiency of the actuator. Ultimately, the motivation is to investigate whether the synthetic jet actuator technology would have the potential for a full-scale flow control application in aeronautics, at least within laboratory conditions. However, the other SJA attributes such as noise and ability to operate in real-life conditions (i.e., rain, snow, dust etc.) are not evaluated within this project.

Ideally, the actuator should have sufficiently large exit jet velocity to grant flow control in the presence of a cross-flow. It should also have an acceptable electrical power consumption so that the beneficial work done; such as, against reducing the aerodynamic drag of a body, is not dissipated to the actuators power consumption. However, both performance indicators are relative to a specific implementation case and should be evaluated for the purpose of engineering application.

Assuming the performance criteria for a potential flow control application are met, another open question is how to identify the different actuator and design configurations. The SJA configuration analysis is one of the motivations of this study. The classical and well-known configuration of the SJA has the arrangement which piezoceramic diaphragm is parallel to the orifice (e.g. Figure 1.1). In recent years, another configuration where the diaphragm is adjacent to the orifice has also been studied. Figure 1.2 presents the opposite and adjacent orifice-diaphragm SJA configurations. For a flow control application, SJAs would be used in an array such that actuators are connected in series. The adjacent configuration has the advantage of having closer consecutive orifices which is important to grant effective flow control. It is evident that, both configurations have their advantages and disadvantages which should be further studied.

One should primarily understand the physics and behaviour of the piezoelectric diaphragm, which is a pure study of structural mechanics. This approach would include testing and modelling of the diaphragms of various sizes (i.e., diameter and thickness) under similar clamping conditions to those in the

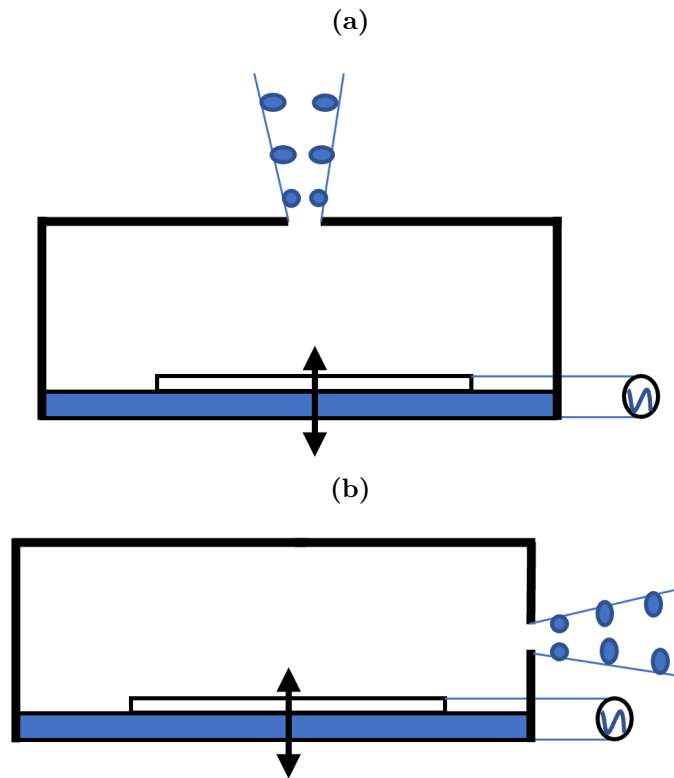


Figure 1.2: *Synthetic Jet Actuator Orifice-Diaphragm Configurations (a) Opposite (b) Adjacent*

synthetic jet actuator case. The piezoelectric diaphragm's precise modelling should estimate natural frequency, also known as the first-mode of oscillation, and displacement profile.

Therefore, in essence, a synthetic jet actuator can be considered as a fluid-structure interaction problem leaving out one other important phenomenon; Helmholtz resonance thus the acoustics side of the problem. The cavity acoustic resonance is caused by the presence of air sealed cavity and orifice neck, giving rise of a critical acoustical phenomenon called Helmholtz resonance.

Thus, the understanding of the following is required.

- I. Structural mechanics for the piezoelectrical diaphragm
- II. Fluid dynamics, which governs the jet formation
- III. Acoustics, which plays an important role with the Helmholtz resonance
- IV. Electric power, to understand the power consumption and conversion efficiency

The rationale behind the actuator selection is based on the pros and cons of

potential actuator candidates. Electrical power consumed by an actuator is an important figure-of-merit which can be investigated for the actuator selection [16]. For an industrial application, the mass and volume of the actuator candidate should be as low as possible to avoid fitting problems. In addition, the actuators should promote acceptable power specific mass and power.

Figure 1.3 demonstrates the power specific mass and power specific volume of four synthetic jet actuator types, which are piezoelectrical driven (PZT), electro-active polymer (EAP), ferro shape memory alloy (FSMA), plasma synthetic jet actuator (PSJA). The power specific mass and volume calculations do not include the cabling, power supply equipments and purely take the ratio of the output power to the mass and size of the actuator into account.

As per Figure 1.3, piezoelectrical driven SJA promotes the highest power specific mass and power specific volume [17]. Therefore, within this thesis, only piezoelectrical driven synthetic jet actuators are studied.

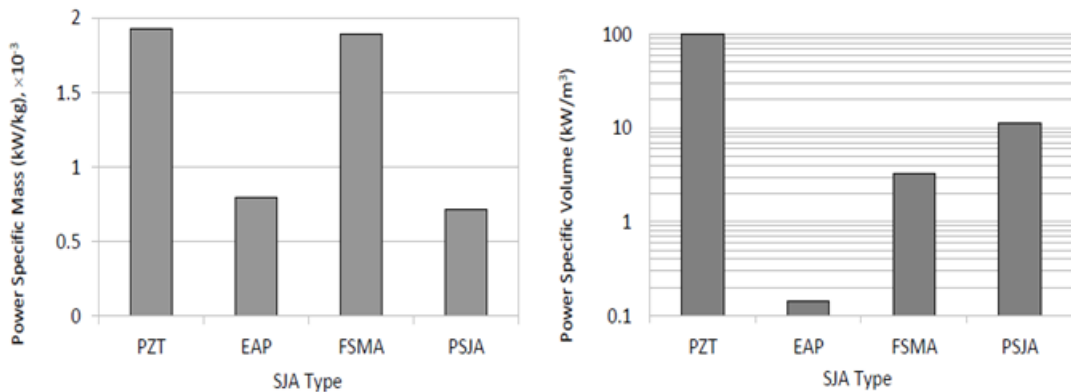


Figure 1.3: *SJA Types Performance Comparison [17]*

1.3 Aim and Objectives

The aim of the research is to model the structural, fluidic and acoustic characteristics of synthetic jet actuators in quiescent (i.e., no cross-flow) conditions towards increasing the state-of-the-art performance criteria, namely peak exit jet velocity and power conversion efficiency.

To achieve the above aim, the objectives of this work are as follows:

- **Objective 1:** To develop accurate and efficient structural mechanics model of the circular unimorph piezoelectric actuator to estimate natural frequencies of mechanical diaphragm.
- **Objective 2:** To extend the structural mechanics model to compute displacement of the piezoelectric diaphragm under potential difference and to verify results with a finite element method analysis.
- **Objective 3:** To extend analytical and finite element method based structural mechanics models to account for the fluidic and acoustic characteristics of the synthetic jet actuators. Essentially, the objective is to achieve a more realistic coupling between structural, fluidic and acoustic domains to compute diaphragm displacement, in-cavity pressure and exit jet velocity.
- **Objective 4:** To conduct an investigation using experiment and extended analytical model to investigate and maximise the performance criteria (exit jet velocity and electric-to-fluidic power conversion efficiency) by use of different SJA configurations (i.e., opposite and adjacent orifice-diaphragm configuration SJA) and different piezoelectric actuators (i.e., unimorph with advanced type piezoceramics, bimorph configuration piezoelectric actuator).

1.4 Research Methodology

The work conducted throughout this research can be classified into two primary parts: modelling and experimentation. Both primary parts are then sub-classified further into two secondary parts: piezoelectric diaphragm and synthetic jet actuator. Thus, the analytical models covering the modal response of the piezoelectric actuator are combined with experiments for response validation purposes. Similarly, the mathematical models (both analytical and multiphysics) of SJA are studied and experimentally validated.

A unique feature of the present study compared to most of the existing work is the richness of having multiple modelling and variety of experimental tools. Novel models of piezoelectric diaphragm and synthetic jet actuator, which do not rely on significant assumptions, are harmonised with in-house experimental work. For example, the natural frequency and peak displacement of the diaphragm is not assumed to be known for the piezoelectric diaphragm and SJA models. In addition, for the synthetic jet actuator models, the actuation frequency envelope involves the cavity acoustic and diaphragm mechanical resonance. Therefore, the study is not limited to low actuation frequency only. Some of the well established studies only validate their models through previously published experimental work [18, 19] as these disciplines are very different from each other. Besides, in the studies which experiment and modelling works are combined not all details of the experiments are revealed, such as not covering diaphragm displacement, power consumption or electric-to-fluidic power conversion efficiency [20]. Therefore, this study aims to present a broader research context of SJA to address aforementioned points.

The research work presented within this thesis consists of an iterative modal analysis of unimorph piezoelectric actuator to obtain a sufficiently accurate estimation of the natural frequency regardless of the diaphragm composition (i.e., thickness or diameter). The natural frequency estimation is combined with a dynamic frequency response function of piezoelectric actuator under potential difference, which also takes into account the transverse piezoelectric coefficient. Analytical and computational models of synthetic jet actuator and experimental work concentrate on different size piezoelectric diaphragm and orifice-diaphragm configurations to test and demonstrate the capabilities of models. Furthermore, to understand the effect and advance the current state-of-the-art power conversion efficiency and exit jet velocity, unimorph single-crystal piezoceramic and bimorph piezoceramic diaphragms are experimentally tested.

Figure 1.4 presents in-detail the flow of the results chapters 4-7 and the research

methodology to reflect the rationale behind the structure of chapters. With the arrows, links between the chapters are also shown. The result chapters meet the objectives defined in Section 1.3 (i.e., Objective 1 - Chapter 4).

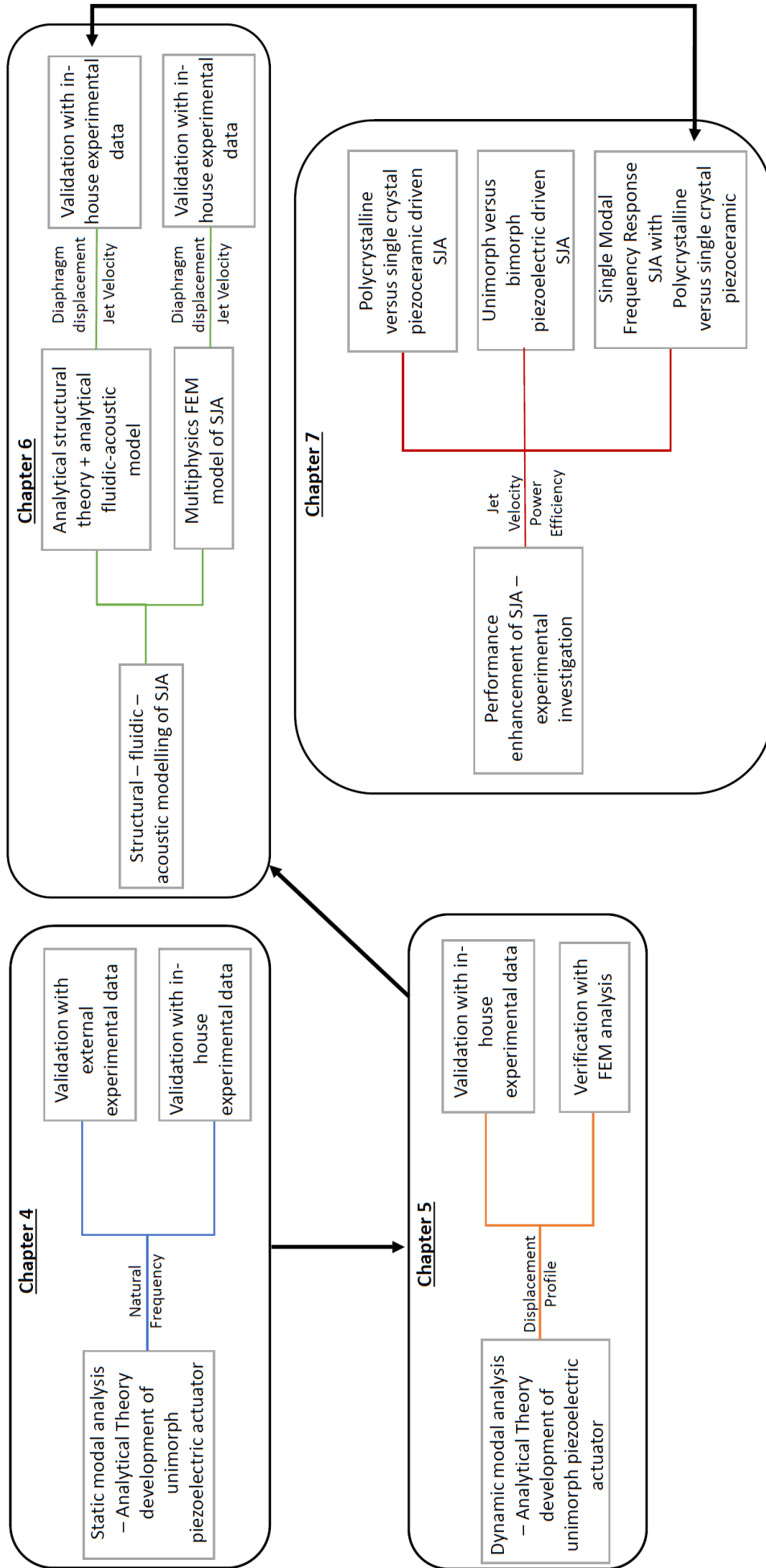


Figure 1.4: A block diagram of the result chapters

1.5 Organisation of the Thesis

This thesis consists of 8 chapters including the present chapter;

- **Chapter 2** presents a comprehensive literature review of piezoelectric actuator and SJA related studies and investigates modelling and experimental studies. The research gaps are also identified and listed.
- **Chapter 3** introduces and discusses the experimental equipment and methods used throughout the thesis.
- **Chapter 4** concentrates on the accurate and effective computation of the natural frequency of the circular unimorph piezoelectric actuator which comprises two layers; active and passive. The chapter consists of the analytical theory development from less accurate to the most advanced theories. The study concentrates on the static analysis of the piezoelectric actuator. Accuracy of the theory is both validated using previously published experimental data and in-house cases.
- **Chapter 5** is devoted to the extension of the natural frequency analysis to frequency response functions in dynamic condition when a potential difference is applied to the active layer of the unimorph piezoelectric actuator. The chapter involves the investigation of different material damping models and theory is validated on in-house experimental data and verified using a finite element model (FEM) analysis.
- **Chapter 6** is focused on the modelling of circular unimorph piezoelectric actuator driven SJA. The chapter utilises the developed analytical frequency response function (FRF) and FEM model and extends them by means of using analytical and computational methods, respectively. An analytical fluidic-acoustic model from the existing literature is taken and integrated to the FRF model of the piezoelectric actuator. In addition, a FEM model of the SJA is created which couples the structural,

acoustic and fluidic features of the resonator. Each model is validated on three different in-house experimental data.

- **Chapter 7** mainly concentrates on experimental studies. It also involves some elements from the SJA models developed in Chapter 6. The study elaborates on the exit jet velocity, power consumption and electric-to-fluidic power conversion efficiency of SJA driven by various piezoceramic or piezoelectric actuator configurations. Different SJA configurations are studied including opposite and adjacent orifice-diaphragms.
- **Chapter 8** presents conclusions of the key results of the research conducted and highlights the novelty in the present study, as well as suggestions for the future work.

1.6 Publication and Conferences

Conference Proceedings and Presentations

- Gungordu B., Jabbal M., Popov A.A. (2021), Modelling of Synthetic Jet Actuators, 2021 AIAA SciTech Forum, USA, 11-15 & 19-21 January 2021.
- Gungordu B., Jabbal M., Popov A.A. (2020), Development of High Authority Synthetic Jet Actuator For Aerospace Applications, 1st Aerospace European Conference, France, 25-28 February 2020.
- Gungordu B., Jabbal M., Popov A.A. (2019), Frequency Response Optimisation of Piezoelectrical Driven Synthetic Jet Actuators, 10th Airbus DipaRT Conference, UK, 27-28 November 2019.
- Gungordu B., Jabbal M., Popov A.A. (2019), Experimental and Computational Analysis of Single Crystal Piezoelectrical Driven Synthetic Jet Actuator, 8th European Conference for Aeronautics and Space Sciences (EUCASS), Spain, 1-4 July 2019.

Chapter 2

Literature Review and Background Theory

2.1 Motivation and Overview

This chapter presents an overview of the fundamental concepts, well established and published work on the piezoelectric actuator, synthetic jet and performance criterion. The pioneering research which both contributes towards the physical principles, modelling and performance enhancement regarding the actuator is studied. The specific focus of this chapter is on the piezoelectric actuator and synthetic jets in quiescent conditions parallel to the upcoming chapters of this thesis. Identified gaps in the literature is listed at the end of each section.

2.2 Flow Control

The specific aim of this project is to advance state-of-the-art performance metrics of SJA in which aerodynamic applications can benefit such as the flow control over an aerofoil, or bluff body such as an Ahmed model (i.e., idealised model for a truck trailer) or the wind turbine blades. For an aerofoil means of flow control could be separation delay especially at high angle angle of attack

and for the bluff body modification of the pressure field in the wake of the body. There are alternative ways of providing with flow control with passive (i.e., no energy input) and active methods (i.e., with energy input). The most recent and effective passive flow control devices are the winglets, added to the end of the wings reducing the vortex size and increasing the effective wing area. The winglets implementation have helped achieving 5% savings in burned fuel and 5% CO₂ emissions [21]. The advantage of active flow control systems is to have the ability to turn them on and off to provide proportional (i.e., feedback) control. The disadvantage of the active flow control systems are the reduced reliability and safety and increased system costs due to installation and added mass. Hybrid systems which combines both passive and active technologies are also studied by using vortex-generator and synthetic jet actuator on a flat plate by Van Buren et. al [22] without a significant outcome. Due to the complexity of the flow control problem, it is extremely challenging to move a laboratory prototype to a real-world engineering application. Nevertheless, alternative technology for flow control should be studied to develop further progress until the technology becomes more mature and, eventually, used for a practical application. The most popular type of flow control devices are the actuators which are in the form of vibrating flaps, time-periodic diaphragm, oscillators and morphing surfaces.

2.3 Actuators

The flow control actuators are studied and reviewed by Cattafesta and Sheplak in 2011 [23]. For an actuator the design issues are listed as quasi-static response, dynamic response, other factors (e.g. electrical power requirement, efficiency, size, weight, cost, noise) and trade-offs (e.g. gain versus bandwidth, displacement versus force) [23].

Figure 2.1 presents the type of flow control actuators and is reprinted from the study of Cattafesta and Sheplak [23]. The advantages of disadvantages of the

flow control actuators can be found in the same study.

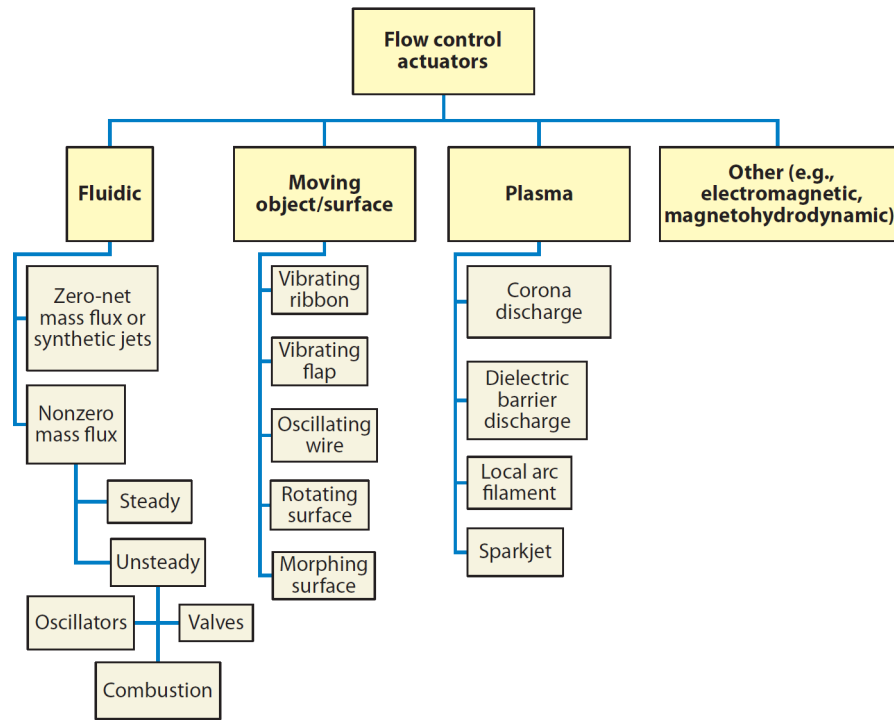


Figure 2.1: Classification of flow control actuators [23]

Suction and oscillatory blowing actuators are currently a trending method for flow control which stands out with their ability to input large momentum to the external surface of the actuator. The idea behind the suction and oscillatory blowing actuators is to suck the low energy flow (i.e. separated) and energise the flow with periodic blowing. Suction takes place in the upstream of the surface using slots which is followed by blowing in the downstream. However, they need pressurized air source to operate and they are difficult to fit (i.e., due to their size) most of the potential applications such as an aerofoil [24, 25]. The piezoelectrical diaphragm driven synthetic jet actuators, also know as zero-net mass flux actuator, have the advantage of high efficiency and jet velocity when compared to its counterpart actuators. Synthetic jet does not require external fluid source and no piping, have adjustable size and is suitable for feedback control. The jet velocity is limited to moderate subsonic speeds (see Section 2.7 for highest performance SJA's reported to date). Also, they, at least in theory, produce the maximum jet velocity at the resonant actuation

frequency. Thus, they are likely to experience structural fatigue after a time of oscillation. However, in a recent study of 2020, Lipowski et al. have shown the data for piezoelectrical diaphragm driven SJA for 600 hours in which both jet velocity and current consumption is recorded [26]. The jet is reported to have an average exit velocity of 41 ms^{-1} and the current consumption was constant over the time. This is an encouraging result regarding the robustness and reliability of SJA.

Different types of flow control actuators are listed and compared in terms of their performance.

- Piezoceramic diaphragm (PZT) [27]: electro-mechanical-fluidic transduction.
- Electro-active polymer (EAP) [28]: electro-mechanical-fluidic transduction.
- Ferromagnetic shape memory alloy (FSMA) [29]: electro-magneto-mechanical-fluidic transduction.
- Plasma synthetic jet actuator (PSJA) [30]: electro-magneto-hydrodynamic transduction.

PZT-driven (PZT) and electro-active polymer (EAP) have common cavity-orifice geometry with different actuation mechanism. PZT driven SJAs utilise a piezoelectric actuator (which usually consist of composite piezoceramic and a metal substrate) in which the electro-active polymer uses thin and stretched elastomeric dielectric membrane. The transverse displacement of the electro-active polymer is low compared to the piezoelectric actuator therefore it promotes a lower output jet velocity [28]. Ferromagnetic shape memory alloy (FSMA) consists of a ferromagnetic material and super-elastic grade shape memory alloy. The ferromagnetic material produces a magnetic force by the electromagnet due to the magnetic field gradient and the memory alloy sustains large stress and induce reversible strain. To create synthetic jet it needs

a large electric field (so a sufficient transverse displacement) which is a detrimental for the power conversion efficiency [29]. Plasma synthetic jet actuator (PSJA) have many types in which dielectric barrier discharges (DBDs) is investigated herein. Fundamental working principle of PSJA is to create kinetic energy inside the boundary layer of an external flow. DBD Plasma SJAs consists of an asymmetric arrangement of two electrodes in which one of them is exposed to the atmosphere and the other embedded on the surface where it is applied. Two electrodes are separated by dielectric material. Under high supply voltage, DBD plasma is created in the inter-facial gap and then creates a synthetic jet [30]. It has three working cycles which are energy deposition, jet discharge and refill (as shown in Figure 2.2d). Heating is an important problem for DBD PSJAs which reduces the power conversion efficiency.

Figure 2.2 presents the geometries of different synthetic jet actuators types. Figure 1.3 (presented in Chapter 1.2) compares actuator power densities of the different SJAs [17]. Power specific mass and power specific volume are evaluated from the fluidic power delivered by the actuator against the mass and volume of the actuator unit. PZT and FSMA SJAs have comparable power specific masses. However, PZT has a significantly higher power specific volume relative to the other actuators: PZT $\sim O(100)$, PSJA $O(10)$, FSMA $\sim O(1)$ and EAP $\sim O(0.1)$. From Figure 1.3, the leap in power density required to meet volume installation requirements is relatively small for PZT-based SJA, thereby making it the most viable SJA for implementation. The calculations only considers the performance criteria of the actuators and do not include the mass/volume of power supply units, container, cabling etc. An important note here, about the plasma synthetic jet actuators, which can reach up to jet velocity of 300 ms^{-1} but power consumption is extremely high due to operating at voltages of $\sim O(kV)$ [14].

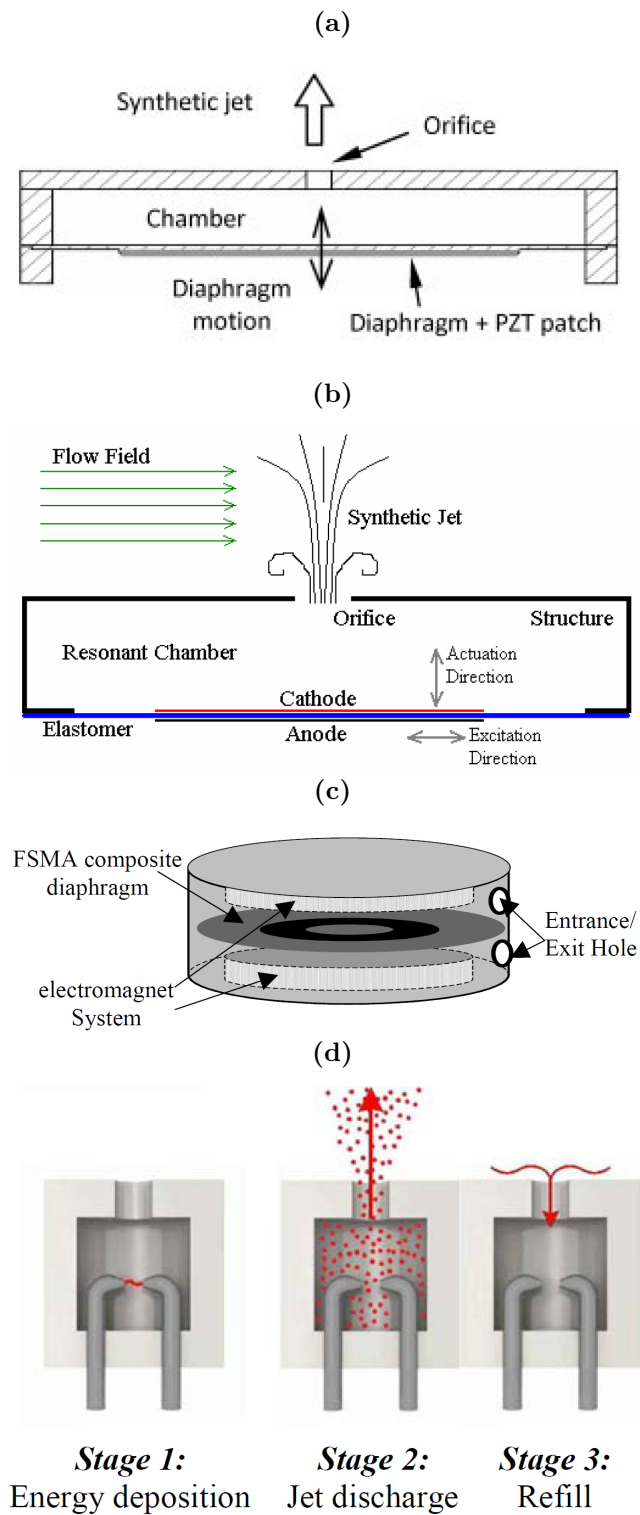


Figure 2.2: Types of Synthetic Jet Actuators (a) Piezoelectric Driven (PZT) [27] (b) Electro-active Polymer (EAP) [28] (c) Ferromagnetic Shape Memory Alloy (FSMA) [29] (d) Plasma SJA (PSJA) [30]

2.3.1 Flow Control With SJA

Synthetic jet actuators (SJA) are widely employed in different engineering applications for flow control. The main principle behind using an actuator to control flow is to energise boundary layer forming on the aerodynamic surface to delay separation which would consequently reduce the pressure drag [13]. The flow separation control using fluidic actuators may be applied in different real-life applications such as in aerospace (i.e., vertical tail [31], wing-pylon junction [9]), road vehicles (i.e., wake of square-backs [32]) or wind turbines (i.e., wake of the turbine blade [12]). SJA can also be used to enhance fluid mixing [33] and to cool electronics [34].

2.4 Piezoelectricity

”Piezoelectricity is a property of certain dielectric materials to physically deform in the presence of an electric field, or conversely, to produce an electrical charge when mechanically deformed” [35]. A number of different materials exhibit the physical property described including natural quartz crystals, polycrystalline and single-crystals.

Piezoelectric materials were discovered by Curie brothers in 1880 and related history of the discovery is explained in detail of the study of Katzir [36]. Piezoelectric materials under the material classification falls under ceramics, as they are neither metallic nor non-organic. Thus, they are also known as piezoceramic. Manufacturing of the piezoceramic and polarisation process are not the focus of the current research, thus details regarding to that are not included to this section.

The piezoelectricity can have two potential applications [37]:

- 1) Direct piezoelectric effect, voltage generation by applying mechanical stress to the piezoceramic. A typical application is the energy harvesters [38].
- 2) Inverse piezoelectric effect, strain generation by voltage load to the piezo-

ceramic. A typical application is piezo injectors.

In the current study, inverse piezoelectric effect is the focus of the research. Then important physical properties of the piezoelectric materials under voltage load can be described such as stress and strain relationships, coercive electric field and piezoelectric coefficients.

Figure 2.3 shows the typical axis used for the notation of the piezoceramic physical properties and it is reprinted from Datta's study [39]. The horizontal axis (shown with x) is the principal axis which the displacement is described using it as a reference. On the left hand side, the z-polarized piezoceramic exhibits the dominant displacement in the vertical (z) axis, it is also known as $\langle 001 \rangle$ polarisation. The crystal polarisation directions (i.e., 123) are aligned with XYZ axes of material coordinate system. On the right hand side figure, an x-poled piezo is shown in which the first principal axis (i.e., 1) is aligned with the z-axis of the material coordinate system.

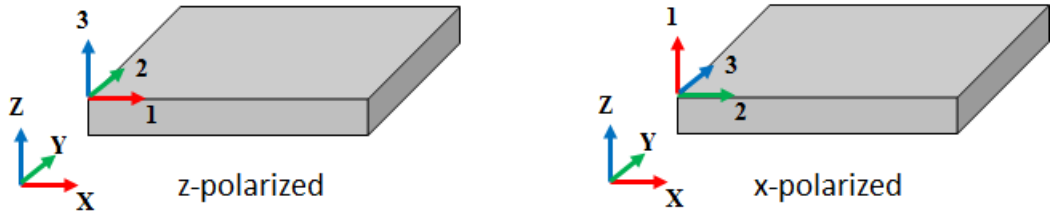


Figure 2.3: *Illustration of the piezoelectric material polarisation [39]*

Piezoelectric coupling factor (k_{31} , k_{33} , k) indicates the overall strength of the electromechanical effects. The piezoelectric coupling factor is always less than one due to the inability of lossless conversion; all of the electrical energy into to the mechanical energy and vice versa for inverse piezoelectric effect. k^2 is the ratio between the converted (mechanical) and supplied energy (electrical) and is a measure of the transduction efficiency of the material. The formula of the piezoelectric coupling factor (k^2) is [40]:

$$k^2 = \frac{\text{mechanical energy}}{\text{electrical energy}} \quad (2.1)$$

The piezoelectric charge constant, d , is the polarization generated per unit of

mechanical stress (T) applied to a piezoelectric material or, alternatively, is the mechanical strain (S) experienced by a piezoelectric material per unit of electric field applied. The piezoelectric charge coefficient is usually expressed as d_{xy} . For example d_{31} is the generation of polarisation in the electrodes normal to the transverse (3) direction with the stress being mechanically applied in the lateral direction (1). Similarly, d_{33} means that the polarisation generated in the transverse direction like the applied stress (T) [40]. The d is a matrix of size 3×6 .

Dielectric displacement (D_i) can be related to d_{ij} and T_j by the following equation [35]:

$$D_i = d_{ij}T_j \quad (2.2)$$

The piezoelectric voltage constant, g factor, is the ratio of the electric field generated to the unit mechanical stress applied. It is expressed with the following equation [35]:

$$E_i = -g_{ij}T_j \quad (2.3)$$

The piezoelectric strain coefficient (S) can be expressed by the following equation using electric field (E):

$$S = d_{ij}E \quad (2.4)$$

Other important parameter is the coercive electric field (E_c), which is a measure of maximum voltage could be applied to the piezoceramic without experiencing depolarisation or going under plastic deformation. It is usually about 6-10 *kV/cm* of the piezoceramic thickness [35].

The best known piezoceramics are Lead zirconate titanate (PZT), barium titanate ($BaTiO_3$), lead titanate ($PbTiO_3$), lithium niobate ($LiNbO_3$), lithium titanate ($LiTaO_3$). Among all, the most investigated is the PZT which repre-

sents a large family of lead zirconate titanate piezoceramics including PZT-4, PZT-5A, PZT-5H, PZT-5J, PZT-5X etc. The mechanical quality, coupling factor and piezoelectric charge coefficient of the PZT piezoceramic slightly vary. The most available piezoceramic in the market is PZT-5A. A detailed review including manufacturing and mechanical properties of the PZT based piezoceramics can be found in the book chapter of Kimura [41].

A special type of piezoceramic is the, $Pb(Mg_{1/3}Nb_{2/3})O_3-PbTiO_3$, high-performance single crystal which are also known as PMN-PT. They exhibit around 5 times more electromechanical coupling than the PZT family. PMN-PT has been identified as the next generation norm piezoceramic with higher electromechanical capabilities [42]. The current problems of the PMN-PT is the manufacturing costs and the lower coercive electric field (E_c) compared to the PZT family ($\sim 2.5kV/cm$).

2.5 Composite Piezoelectric Actuator

In this section, the review of literature concentrates on the models which are used to obtain modal parameters, such as the natural frequency and displacement profile, of the circular plates with piezoceramic elements of the composite piezoelectric actuator. Figure 2.4 illustrates side-view of the circular piezoelectric actuator which consist of metal substrate (passive layer) and a piezoceramic patch (active layer).

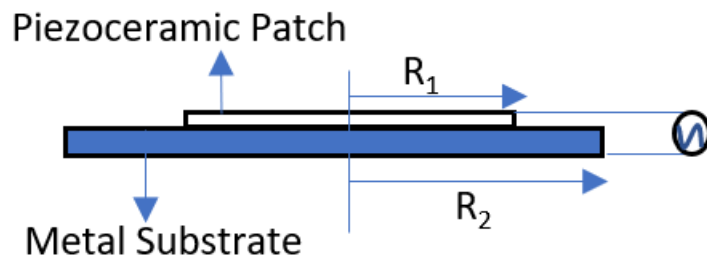


Figure 2.4: Illustration of the circular composite piezoelectric actuator

Piezoelectric actuators have a wide range of applications including fan cooling [43], vibration control [44], energy harvesting [45], and aerodynamic flow control [46].

Piezoelectric actuator consist of plate layers of substrate material and piezoelectric element. The most commonly used piezoelectric actuator configuration is unimorph where a substrate plate is bonded to a single layer of piezoelectric plate by using conductive adhesive layer. As per the illustration in Figure 2.4, the presence of the piezoceramic patch introduces a step change in thickness. With this structural configuration, the piezoelectric actuator can be classified as a multi-plate electromechanical structural device which can be investigated using modal analysis.

Accurate modal analysis of the actuator is important to identify the resonant frequency, mode shapes and mechanical damping [47]. The modal analysis is required to design the piezoelectric actuator/sensor such as to decide the frequency of operation and identifying efficacy for the application. There has been a large interest in piezoelectric actuator's free and forced vibrations to estimate the natural frequency and displacement.

The theory development of the homogenous plates is accepted to start with Kirchoff's theory which calculate deformations and stresses for thin plates. Kirchoff theory is extended by Stavsky and Lowevey [48] for the axisymmetric vibrations of composite non-piezoelectric circular plates. They have proven that coupled extensional-flexural inertia terms plays an important role on the natural frequency of plates as well as the classical extensional and rotatory inertia terms. Using Bessel functions and a dynamics matrix of 3×3 they obtained natural frequency estimations and compared with experiment results. They only considered clamped boundary conditions without clear justification using experimental vibration data.

Adelman and Stavsky [49] studied the dynamic response of a composite piezoelectric circular plate. Their physical model is a continuation of Stavsky and Lowevey [48] but extended for piezoelectricity and dynamic response under

voltage load. They employed a dynamics matrix of size 4×4 with state vectors of radial and circumferential normal resultant force and moments. Their test case had the equal size of piezoceramic and metal substrate. Therefore, an application of the asymmetric step change is not demonstrated.

Sato and Shimiuzu [50] studied circular plates with asymmetric thickness step using transfer matrix method and a 4×4 transfer matrix. They used used fourth order transfer deflection equation and derived state variables using Bessel functions comparing results with previously published data and stated they obtained acceptable match. They did not reveal the size and material properties of the test case and natural frequency.

Li and Chen [51] studied a 3-layer model with the active plate (i.e., piezoceramic), passive layer (i.e., substrate metal) and adhesive bonding layer in between active and passive layers. They established assumed linear strain in both layers due to the stiffness (i.e., Young's modulus) is comparable in both layers. Also, established a formula for the neutral axis which is then used by [52] as well. They compared their experimental result for a single piezoelectric actuator under voltage load obtaining an accurate match. They commented on the effect of bonding layer and they found that, for the plates which are thinner than $200 \mu\text{m}$, it is important to model bonding layer as well.

Prasad et. al [53] studied a two-port lumped-element model to model the deflection profile of a clamped unimorph piezoelectric actuator. By using the equilibrium equations of the axisymmetric plate which was also presented by [48], they obtained an accurate natural frequency estimation for their test case with a percentage difference of 2.6% between their experiment and the model. However, their model is a static model and only validated through experimental data of actuation frequency 100 Hz.

Deshpande and Saggere [54] studied an analytical model of the circular multi-layered diaphragm-type piezoelectric actuators using composite thin plate theory in which subjected to voltage and pressure loading. They considered coupled extensional-flexural deformations of the plate and obtained a good match

with finite element analysis ($\pm 0.5\%$). The relevance and significance of the neutral plane is not mentioned and they used half of the brass thickness as the reference plane.

Papila et al. studied the unimorph and bimorph piezoelectric actuators under pressure load using the equilibrium equations of circular plates formulated using Bessel functions [55]. The modal analysis formulation was an extension of Prasad's study [53] to include a pressure forcing instead of voltage load. Papila et al. conducted parameter sensitivity analysis and concluded that without a frequency bandwidth limitation, bimorph actuator provides a larger volume displacement compared to the unimorph actuator.

Gomes [56] studied thin plate theory and derived a state matrix of 6×6 with Bessel functions to estimate the natural frequency of five selected cases. Gomes obtained a mean of 24% difference on five test cases compared with the experimental data, attributed the difference to be conducted by effects of clamping conditions and the damping. Then, by applying adjustments more accurate estimations are obtained. Their model is extended to study the dynamic cases with a continuation study [57] to investigate the frequency sweep of centre deflection of five test cases.

Hu et al. [58] studied the non-linear deflection of the circular piezoelectric actuator under voltage and pressure loads. They used energy methods (i.e., Hamiltonian) with Rayleigh-Ritz method. They concluded that in case of high voltage or pressure load the linearity disappears and a non-linear model is required. In their second study, Hu et al. [52], studied the piezoelectric actuator for gas compression in micro-pumps developing an analytical model using Kirchoff thin plate theory. They identified a 6% difference between their experiments and analytical model on a single test cases. In another study, Hu et al. [59], have had an analytical model (based on Hamiltonian approach and Rayleigh-Ritz method), finite element method and experimental data in the same study. They identified 10% difference between the analytical model and the experiments over a set of three piezoelectric discs with the same diameter

and different thickness.

Jeyalingam [60] numerically studied the clamped unimorph piezoelectric actuators and identified the first four mode shapes. Figure 2.5 presents the 3-D mode shape visualisations. It is also identified that the highest net transverse displacement is associated with the first-mode of oscillation, similar to the observation of Gomes [57].

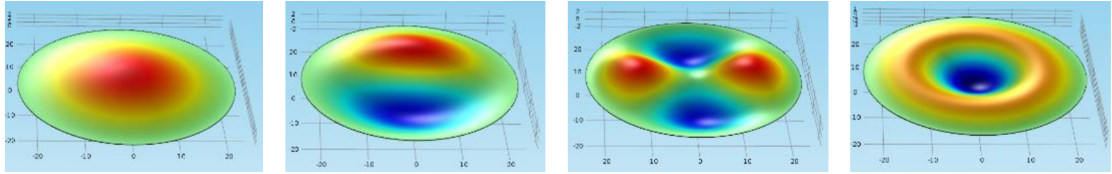


Figure 2.5: *First four mode shapes of clamped unimorph piezoelectric actuator [64]*

2.6 Synthetic Jet Actuator

This section covers fundamental aspects of the synthetic jet actuator, governing equations and flow physics behind the operation. The analysis demonstrated in this section is also used in the different parts of the results chapters.

The synthetic jet concept is first proposed by Lighthill by mentioning a method of fluid stream generation through an opening by viscous effects [61]. The synthetic jet is a fluid-stream which discharges through the orifice and mainly composed by vortices which then turns to be a terrain of vortex in case of successful formation. Synthetic jet is a periodic flow with consecutive ejection and expulsion of the fluid out of the orifice opening (i.e., usually circular or rectangular slot) which have a zero net mass-flux but non-zero time-averaged momentum [62]. It is important to note that the jet slug should be sufficiently away from the orifice in order not to be sucked back into the cavity [63].

Figure 2.6 presents an illustration for the suction and ejection strokes of a typical SJA and taken from the study of Gil and Strzelczyk [64]. The numbers in Figure 2.6 stands as follows: ① - cavity, ② - diaphragm, ③ - orifice, ④ - ingested fluid and ⑤ - vortex ring. The motion of the diaphragm (as shown

with red arrows in Figure 2.6) accelerates the initially still air in the cavity which then starts discharging through the orifice opening. Fluid velocity and pressure gradient in the cavity depends on the amplitude of the oscillation and, as they grow, the boundary layer separates from the inner cavity walls and edge of the orifice neck and eventually separated fluid rolls up to close itself producing a vortex ring. For the successful formation, the vortex rings should be sufficiently away from the orifice exit plane, thus cannot be sucked back by the negative pressure gradient caused by the diaphragm in suction stroke.

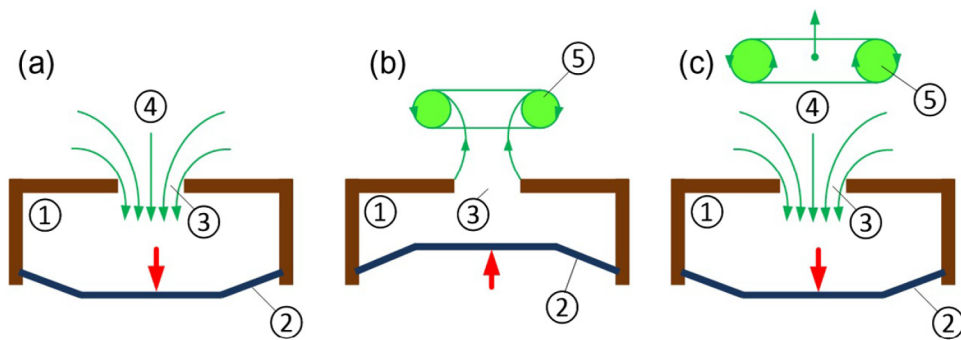


Figure 2.6: Synthetic Jet Illustration (a) Initial Suction Stroke where air is sucked in the cavity (b) Vortex ring production during ejection stroke (c) Vortex ring propagation out of the orifice even though the diaphragm is in suction stroke

For clarity this section is divided into subsections which are geometry and operation, frequency response of the actuator, governing non-dimensional parameters and fundamental relationships, jet formation criterion and power conversion efficiency.

2.6.1 Geometry and Operation

Figure 2.7, presents a typical actuator geometry with diaphragm, cavity and enclosed orifice opening. The cavity diameter (D_c), orifice diameter (d_o), cavity height (H) and orifice neck height (h) is shown on the figure. The formation of the synthetic jet is also illustrated. The diaphragm for a piezoelectric diaphragm driven actuator should be supplied with AC voltage to provide an amplitude (i.e., voltage) and oscillation frequency.

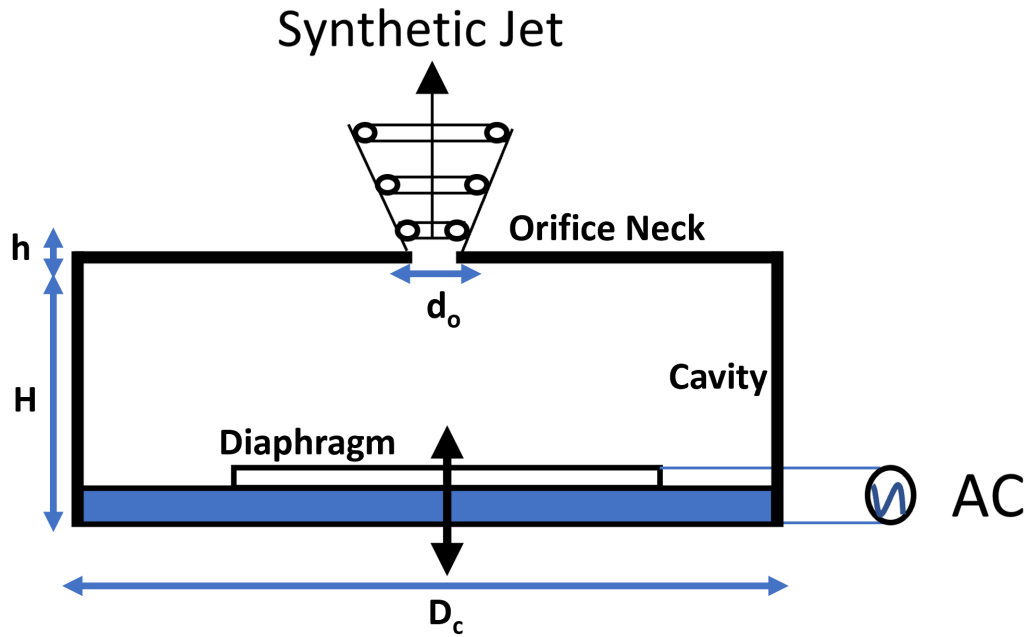


Figure 2.7: Geometry of a typical actuator

2.6.2 Frequency Response of the Actuator

The frequency response of the actuator are usually associated with a double peak response originating from Helmholtz resonance and mechanical (i.e., natural frequency) diaphragm resonance. The geometry of the actuator is essentially a Helmholtz resonator which gives a rise to a Helmholtz resonance. SJA is a Helmholtz resonator due to its design (i.e., being composed of a closed chamber opened to the exterior via an orifice neck) and the fluid inside the cavity acts like a spring in which the orifice neck acts like a mass. The resulting system is a spring-mass oscillator which would have a natural frequency which occurs when reactance goes to zero. The frequency of the Helmholtz resonance highly depends on the actuator geometry, assuming constant fluid density, as shown with Equation 2.5 below. The maximum jet velocity is expected to be located at the diaphragm mechanical resonance. Figure 2.8 shows a bi-modal frequency response with Helmholtz and mechanical diaphragm resonances. Typically, the Helmholtz (i.e. cavity acoustic) resonance promotes smaller output jet velocity than the mechanical diaphragm resonance.

Helmholtz frequency (f_H) for inviscid, incompressible flow is as:

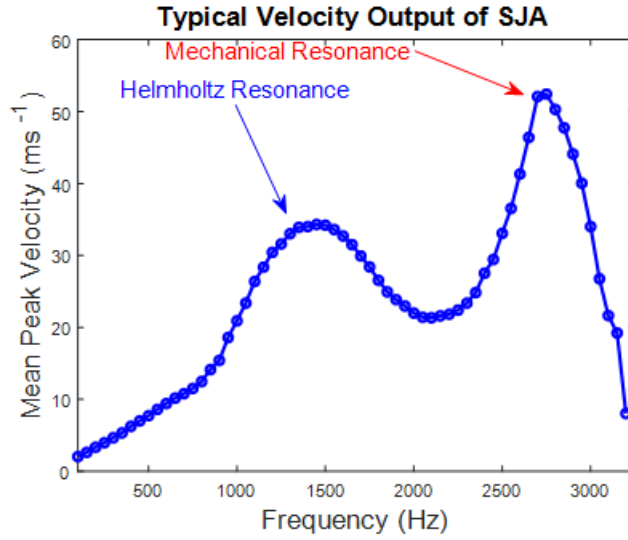


Figure 2.8: Typical Jet Velocity Output of SJA

$$f_H = \frac{a}{2\pi} \sqrt{\frac{A_o}{Vh}} \quad (2.5)$$

Where a is the speed of sound, A_o is the area of the orifice outlet plane, V is the volume of the chamber and h is the depth of the orifice. Equation 2.5 is a conservative equation and compressibility and heat losses are not included [65] resulting in overestimation of the Helmholtz frequency for the orifice design where compressibility and heat losses are dominant.

For a cylindrical cavity with circular orifice, the equation becomes:

$$f_H = \frac{a}{2\pi} \sqrt{\frac{(d_o/2)^2}{(D_c/2)^2 Hh}} \quad (2.6)$$

Equation 2.6 is an important design (i.e., sizing) equation provides fundamental insight into role of geometry. It can be observed that, Helmholtz frequency is inversely proportional to the cavity height with an inverse square fitting. Formula given in Eq. 2.6 overestimates the Helmholtz frequency by nearly 20% which is consistent in various studies including [66], [67] and [68]. However, it is not clear whether the overestimation is due to the formula used to calculate the Helmholtz resonance or its due to the relative positioning of the Helmholtz (i.e., acoustic cavity) resonance with respect to the mechanical resonance of

the diaphragm.

Orifice neck length for a round orifice should account for the end correction.

Gomes [66] used effective orifice length (l_{eff}):

$$l_{eff} = h + 0.85d_0 \quad (2.7)$$

An alternative definition of l_{eff} is proposed by de Luca et al. [69] by proposing the constant next to the orifice diameter as 0.62.

$$l_{eff} = h + 0.62d_0 \quad (2.8)$$

Lv et al. used the following equation for the Helmholtz resonance frequency which takes into account the air density and compressibility [70].

$$f_H = \frac{1}{2\pi} \sqrt{\left(\frac{4\rho h}{3\pi(d_o/2)^2} + \frac{8\rho}{3\pi^2(d_o/2)}\right) \frac{V_c}{\rho a^2}}^{-1} \quad (2.9)$$

Table 2.1 shows the different calculations of Helmholtz resonance (f_H) for the fixed geometry of an actuator size $d_o = 1.2$ mm, $D_c = 25$ mm, $h = 2.5$ mm, $H = 0.67$ mm.

Table 2.1: Comparison of Helmholtz resonance equations

Models of Helmholtz resonance estimation	f_H (Hz)
Eq. 2.6	2025
Eq. 2.6 with l_{eff} by Eq.2.7	1706
Eq. 2.6 with l_{eff} by Eq.2.8	1774
Eq. 2.9	1633

To clarify which one of these four equations provide the most accurate estimation of the Helmholtz resonance frequency further analysis is needed.

The structural mechanics side of the piezoelectric actuator is usually not the expertise of fluid dynamics researcher, a comprehensive understanding of the modal parameters (i.e., natural frequency, displacement, structural damping) of the piezoelectric actuator cannot be studied. Therefore, some simplified

models with a single equation are used to have a rough estimation of the natural frequency. The presented models below only consider substrate (i.e., passive) layer of the composite piezoelectric diaphragm and does not consider the piezoceramic patch (i.e., uniform thickness). The natural frequency of the composite piezoelectric diaphragm is a function of its dimensions (i.e., diameter and thickness of metal shim and piezoceramic), material properties and clamping conditions. Therefore, the simplistic models which estimate the natural frequency of the piezoelectric diaphragm is not expected to be accurate. First of the so-called simplistic equation for the piezoelectric diaphragm natural frequency (f_m) is presented by Lv. et al [70]:

$$f_m = \frac{1}{2\pi} \left[\left(\frac{m}{6\pi r_c^4} \right) \left(\frac{\pi r_c^6 (1 - \nu^2)}{16Et^3} \right) \right]^{-0.5} \quad (2.10)$$

Where r_c is the diaphragm radius, E is the elastic modulus, ν is the Poisson ratio, t is the total thickness of the diaphragm, and m is the diaphragm mass. Rathnasingham [71] and De Luca and Girfoglio [69] used the following equation for the natural frequency of the diaphragm (i.e., first mode of oscillation):

$$f_m = \frac{10.2}{\pi\sqrt{3}} \frac{t_b}{D^2} \sqrt{\frac{E}{\rho(1 - \nu^2)}} \quad (2.11)$$

Where D is the diaphragm diameter, E is the elastic modulus, ν is the Poisson ratio, t_b is the thickness of the substrate layer.

Another equation is presented by the well-known book of Blevins on natural frequency and mode shapes of uniform thickness plates [72]. The equation involves an empirical term; mechanical damping (ζ). The equation is also used in the study of Jabbal and Kykotis [73].

$$f_m = \frac{10.22t_D}{2\pi(D/2)^2} \sqrt{\frac{E(1 - 2\zeta)}{12\rho(1 - \nu^2)}} \quad (2.12)$$

Where the constant 10.22 is for a clamped edge circular plate, D is the diaphragm diameter, E is the elastic modulus, ν is the Poisson ratio, t_D is the

total diaphragm thickness, ζ is the structural damping. In the study of Jabbal and Kykotis, it is used as 4.98 which is for a simply supported plate [73].

To compare the equations and understand the validity of these simplistic models, results produced by the presented equations are compared with an experimentally investigated case in Chapter 4. A diaphragm is considered with an outer diameter of 27 mm, brass thickness of 0.22 mm, total thickness of 0.45 mm, Young's modulus (E) of 110 GPa, density of 8500 kg/m³ and Poisson ratio of 0.34. Mechanical damping is taken as 0.03.

Table 2.2 shows the estimations of presented simplistic models for the natural frequency of composite piezoelectric actuator and the experimental measurement. The difference between the models are significant and none of them are close to the measured natural frequency. Thus, with the simplistic models, natural frequency estimation of the composite piezoelectric diaphragm cannot be conducted accurately. The free and forced vibrations of the composite piezoelectric patch and substrate material (with change in thickness) should be studied in more detail, with completely physical models, for SJA applications.

Table 2.2: Comparison of diaphragm mechanical resonance equations

Natural Frequency	f_m (Hz)
Eq. 2.10	4079
Eq. 2.11	2172
Eq. 2.12	4316

2.6.3 Parameters and Fundamental Relationships

The flow originated by the motion of the piezoelectric diaphragm that results in an unsteady jet can be characterised by non-dimensional numbers.

For on-bench operation of the actuator, i.e., quiescent conditions, the key geometrical dimensions are the orifice diameter (d_o), orifice length (h), cavity diameter (D_c) and cavity height (H). The parameters regarding the physical mechanism involves are the density (ρ) and kinematic viscosity (ν) of the air. The operational parameters are the frequency (f) and the voltage (V). The

diaphragm displacement is related to the applied voltage, thus, voltage term can be changed by the Δ , diaphragm oscillation amplitude.

Zhong et. al have identified 5 non-dimensional Buckingham-pi groups (non-dimensional equations which govern the physics of a dynamic system) based on the parameters listed [74].

$$\pi_1 = \frac{fd_o^2}{\nu}, \pi_2 = \frac{\Delta}{d_o}, \pi_3 = \frac{D_c}{d_o}, \pi_4 = \frac{H}{d_o}, \pi_5 = \frac{h}{d_o} \quad (2.13)$$

As can be seen by the non-dimensional π groups, the most important geometric parameter is the orifice diameter. Therefore, it is the most important parameter used for the scaling in the governing parameters.

Stokes number (S) is a ratio of orifice diameter to the unsteady boundary layer thickness along the orifice neck [75]. The frequency can be expressed in angular form, $\omega = 2\pi f$.

$$S = \sqrt{\frac{\omega d_o^2}{\nu}} \quad (2.14)$$

The stroke length of the synthetic jet represents the length of a fluid column pushed out during the expulsion cycle of the operation.

$$L_0 = \bar{U}_0 T \quad (2.15)$$

Period of a cycle (T) is $1/f$ and \bar{U}_0 is the time-average blowing velocity over the entire cycle [74],

$$\bar{U}_0 = \frac{1}{T} \int_0^{T/2} u_o(t) dt \quad (2.16)$$

Where $u_o(t)$ is the instantaneous space-averaged jet velocity at the orifice exit. The stroke length can be non-dimensionalised by dividing it by the orifice diameter.

$$L = \frac{L_0}{d_o} \quad (2.17)$$

The Reynolds number can be expressed in terms of the stroke length:

$$Re_L = \frac{\bar{U}_0 L_0}{\nu} \quad (2.18)$$

\bar{U} is the spatial and time-averaged exit jet velocity and related to the slug velocity with $\bar{U} = 2\bar{U}_0$ [76]. The scale of the exit jet velocity can be written in terms of non-dimensional Strouhal number (St) or a ratio of squared Stokes number (S^2) and Reynolds number (Re).

$$St = \frac{S^2}{Re} \quad (2.19)$$

Now that the important parameters and governing equations are identified. Thus, the jet formation criterion can be introduced.

2.6.4 Jet Formation Criterion

There have been various studies and descriptions regarding the jet formation criterion. These studies can be grouped with respect to the non-dimensional actuation frequency, Stokes number. As per the description in Eq. 2.14, Stokes number is the ratio of the unsteady forces to the viscous forces.

In this study, Stokes number (S) is in the range of $4 \leq S \leq 50$.

Stokes Regime I: Low - $0.2 \leq S \leq 7.2$

Timchenko et al. [77] computationally studied jet formation criterion and searched for a more complex jet formation criterion for axisymmetric jets with Reynolds numbers in the range of $6.5 < Re < 35$ and a Stokes number range of $0.2 \leq S \leq 7.2$.

Reynolds number is defined as $Re = \bar{U}d_o/\mu$ in [77] with the spatial and time-averaged velocity definition of:

$$\bar{U} = \frac{2}{T} \frac{4}{\pi d_o^2} \int_{-d_o/2}^{d_o/2} \int_{T/2}^0 u(r, t) 2\pi r dr dt \quad (2.20)$$

For the low Stokes number region (between $0.2 \leq S \leq 7.2$), the formation criterion is reported as a function of Strouhal number ($St = \frac{S^2}{Re}$):

$$S = 7.5St^{\frac{1}{2.24}} \quad (2.21)$$

For the higher Stokes number region (between $1.8 \leq S \leq 7.2$), the formation criterion is as a function of Strouhal number ($St = \frac{S^2}{Re}$):

$$S = 5.4St^{\frac{1}{1.65}} \quad (2.22)$$

Nevertheless, the work is based on micro synthetic jets (with the largest orifice diameter of 0.2 mm) and specified Stokes numbers of study relatively low.

Stokes Regime II: Intermediate - $6 \leq S \leq 36$

Holman et al. [76] studied a jet formation formulation for the synthetic jet actuators based on the induced velocity arising from the vortices. Study investigated two-dimensional and axisymmetric orifice to evaluate a formation criterion based on the governing parameters.

$$\frac{1}{St} = \frac{Re}{S^2} > K \quad (2.23)$$

K is found to be 0.16 for axisymmetric jets and 1 for two-dimensional jets respectively. This threshold (K) is valid for relatively thick orifice plates, $h/w > 2$ where h is the thickness of orifice neck and w is the width of two-dimensional orifice. This definition is valid between $6 \leq S \leq 36$.

With the re-arrangement of fundamental equations and using the assumption of the slug model $\bar{U} = 2U_0$, the Holman's criterion of K can be translated into a non-dimensional stroke-length:

$$\frac{Re\bar{U}}{S^2} = \frac{\bar{U}d_o}{\frac{\omega d_o^2}{\nu}} = \frac{\bar{U}d_o}{\omega d_o^2} > K \quad (2.24)$$

For axisymmetric jets, Holman identified that the formation criterion (K)

should be 0.16. Then, the spatially and time-averaged velocity can be expressed as:

$$\bar{U} > K\omega d_o = 0.16(2\pi)fd_o \quad (2.25)$$

The non-dimensional stroke length (L) is:

$$L = \frac{L_0}{d_o} = \frac{\bar{U}T}{d_o} \quad (2.26)$$

Combining Equations 2.25 and 2.26:

$$L = \frac{0.16(\pi)fd_oT}{d_o} = 0.16(2\pi) = 1.0053 \quad (2.27)$$

Thus, the non-dimensional stroke length should be larger than 1 for jet formation. Zhou et. al [78], studied the formation criterion of the synthetic jets and concentrated on the intermediate Stokes number ($2 \leq S \leq 26$). They classified flow regions as no jet formation, jet formation without vortex roll-up and jet formation with vortex roll-up as shown in the Figure 2.9, which is reprinted from [78].

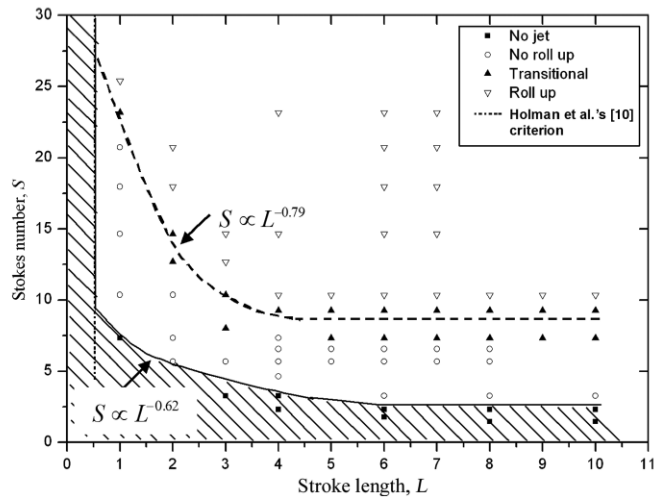


Figure 2.9: Formation Criterion Proposed by Zhou et al. [78]

Stokes Regime III: High - $S \leq 300$

Travnicek et. al studied the formation criterion experimentally using loud-

speaker in the Stokes number range of $S = 73-292$ [79]. They separated the Stokes number envelope into two; S smaller than 160 and S larger than 160. For S smaller than 160, $(L/d_o) = 0.5$ as established by [76]. For S larger than 160 they reported a reduction of the non-dimensional Stroke length, $(L/d_o) = 0.25$ parallel to [80]. An equation regarding the criterion Reynolds number for throughout the Stokes number range is established [79]:

$$S = \frac{Re^{1.42}}{2.42} \quad (2.28)$$

2.6.5 Power Conversion Efficiency

The definition of power efficiency is quite important for the evaluation of performance of the SJA. In this study, the electric-to-fluidic power efficiency is adopted throughout the thesis, like studies including [27, 81, 82].

The electric-to-fluidic power efficiency (η) is the ratio of the fluidic power (P_f) to the electric power (P_e):

$$\eta = \frac{P_f}{P_e} \quad (2.29)$$

P_f is the time derivative of the fluidic-energy.

$$P_f = \frac{1}{2}\dot{m}U_0^2 = \frac{1}{2}\rho A_o U_0^3 \quad (2.30)$$

Where \dot{m} is the fluid mass flow rate ($\rho A_o U_0$), A_o is the orifice area and U_0 is the time average of the velocity signal over the blowing cycle and can be expressed as a function of peak jet velocity (U_p), assuming sinusoidal input:

$$U_0 = \frac{1}{T} \int_0^{T/2} u(t) dt = \frac{U_p}{\pi} \quad (2.31)$$

Some alternative definitions of the fluidic power exists such as in the study of Kordik [83] such as Eq. 2.32.

$$\dot{E}_f = P_f = \frac{1}{3}\rho\pi^2 A_o U_0^3 \quad (2.32)$$

Nevertheless, to keep the analysis consistent with the majority of previous studies Eq. 2.30 is used.

The electrical power is given by the following statement:

$$P_e = \frac{1}{T} \int_0^T V(t)I(t)dt \quad (2.33)$$

Due to the capacitive nature of the piezoceramic patch, there is a phase difference between voltage and current signals. In this analysis, the interest is true power (i.e., actual power) with the phase difference (ϕ_{vt}). The phase difference between the voltage and current is a property of the piezoceramic and it cannot be controlled.

$$\phi_{vt} = 2\pi ft \quad (2.34)$$

Then the true power is [84]:

$$P_e = V_p I_p \cos(\phi_{vt}) \quad (2.35)$$

The advantage of this type of efficiency calculation is the independence from external factors. Also, the experimental procedure is straightforward. With a different perspective Seifert introduced an alternative definition called overall figure of merit (OFM) using the weight of the actuator (W_a), peak jet velocity (U_p), power consumption (P) and the thrust generated (F_a) by the actuator [85].

$$OFM = \frac{F_a^2 U_p}{W_a P} \quad (2.36)$$

The figure of merit introduced by Eq. 2.36 increases the experimental difficulty and requires an additional apparatus such as a digital force/mass balance which

can sample data at the same frequency as the hot-wire anemometry. Also, the thrust will be a function of the inertia (mass) of the actuator case. The measured force would not be the same for a 300 gram steel case and a 3D printed 30 gram weighing actuator even with the same piezoelectric actuator.

2.7 Experimental Studies and Performance of SJA To-Date

In this section, the notable experimental studies with the highest output jet velocity and electric-to-fluidic power efficiency are listed.

The most complete experimental study is by Van Buren et al. [81] due to inclusion of output jet velocity, voltage and current, in-cavity pressure and temperature measurements. Studies of Gomes and Crowther [27, 66] has also a large experimental scope including the measurements of jet velocity, in-cavity pressure and voltage & current. In addition the study used an adjacent orifice-diaphragm configuration SJA without size optimisation.

Jabbal and Kykkotis [86] studied an adjacent orifice-diaphragm configuration SJA which used two round orifices which is actuated through a common piezoelectric actuator. They obtained a peak jet velocity of 38 ms^{-1} with $50 V_p$ and electric-to-fluidic power conversion efficiency (η) of 15%. They reported the peak efficiency drops by 50% at $100 V_p$.

Weigel et al. [9] also studied an adjacent orifice-diaphragm configuration and obtained a peak jet velocity of 100 ms^{-1} with $100 V_p$ and a relatively low power conversion efficiency of 3%.

Table 2.3 present selected cases of SJA which are actuated by piezoelectric diaphragm which contributes towards the understanding of the current state-of-the-art in terms of exit jet velocity and power conversion efficiency. Table 2.3 have the dates of publication in chronological order, orifice diameter (d_o), cavity diameter (D_c), peak supply voltage (V_p), peak jet velocity (U_p) and electric-

to-fluidic power conversion efficiency (η). The power conversion efficiency is not reported directly in all studies and where possible calculated/approximated by the given data. The reported power conversion efficiency of the studies reported are based on their own definitions and are not consistent. The orifice type may differ in the table and circular orifices are represented by their diameter only. The slot orifices are shown as a multiplication of their width and length (e.g. 1x4).

By considering the performance metrics given in Table 2.3, it can be deduced that the power conversion efficiency levels are low especially at higher jet velocities (i.e., $+50 \text{ ms}^{-1}$). The size optimisation of adjacent orifice-diaphragm configuration SJA is an important topic (due to its advantage of being able to grant effective flow control when used as an array) which is not covered in detail to-date. Also, using different diaphragm configurations/materials such as bimorph piezoelectric actuator or single crystal piezoceramic patch was not investigated.

Table 2.3: Selected Experimental Study

Study	Year	$d_o(mm)$	$D_c(mm)$	$V_p(V)$	$U_p(ms^{-1})$	$\eta(\%)$
Gomes & Crowther [66]	2006	1.2	25	125	130	7
Crowther & Gomes [27]	2008	1.2	25	50	70	14
Li et al.[87]	2011	1x4	30	80	35	25
Jabbal and Kykkotis[86]	2014	1	27	50	38	15
Feero et al. [68]	2015	2	30.8	100	50	45
Girfoglio et al.[88]	2015	5	80	35	25	65
Van Buren et al.[81]	2016	1x12	80	150	120	3.5
Van Buren et al.[81]	2016	1x12	80	150	211	N/A
Smyk et al.[89]	2020	10	52.5	N/A	12	9
Weigel et al.[9]	2020	2.5	35	100	100	3

2.8 Modelling Studies

This section investigates some of the modelling efforts published to-date. The studies listed are the most interesting or relevant to the work presented in

Chapter 6.

Synthetic Jet (SJ) modelling studies can be divided into three categories: Lumped-element method, analytical (i.e., equation based) and CFD-type. The actuation mechanism such as loudspeaker, piston and piezoelectric disc studied in different studies.

Even though LEM is not a specifically studied within this study, it is beneficial to describe the rationale behind it and the important outcomes.

LEM assumes that the characteristic length scale is much larger than the largest geometric dimension and therefore may become invalid at very high actuation frequencies [90]. The first LEM study for SJ presented by McCormick [91] using a loudspeaker driven actuator for a boundary layer separation control application. They idealised the actuator by using resistive and capacitive elements and springs. Nevertheless, they did not focus on the frequency response of the actuator. The LEM approach improved by Gallas et al. [20] where they focused on the quiescent condition (on bench) actuator for a piezoelectric diaphragm driven SJ. They studied two configurations for a single-modal and bi-modal frequency response of the jet velocity at a constant supply voltage. While they achieved an acceptable response for the single-modal response actuator they could not locate the resonant frequency and jet velocity magnitude successfully for the bi-modal response. In the follow up study they used a multi-objective optimisation algorithm and improved results drastically [92] by optimising of damping coefficient of diaphragm, d_a term.

Tang and Zhong [93] studied LEM model of SJA further, in which minor losses at the orifice is studied and linked to the jet velocity. The study identified a good match in the frequency sweep in the incompressible region compared with the other models. The study identified a good agreement at the Helmholtz resonance velocity but was not able to capture the right phase (i.e., temporal exit jet velocity) compared to the numerical simulation.

Persoons [94] studied lumped element model and brought an integrated perspective for loudspeaker, electromagnetic and piezoelectric diaphragm actu-

ated synthetic jets. The proposed model requires only two empirical terms of nozzle fluid damping and inertia. Even though an acceptable response for the jet velocity is obtained, experimental validation is stated as a must for different size actuators and configurations.

Table 2.4 presents a summary of the LEM studies. The parameters compared are the orifice diameter (or size in case of 2-D shape) (d_o), cavity diameter (D_c), pressure loss term (K), highest jet velocity and, if reported, accuracy with respect to the highest experimental jet velocity (% Diff.).

Table 2.4: Selected Studies of LEM

Study	Year	$d_o(mm)$	$D_c(mm)$	K	$U_p (ms^{-1})$	% Diff. (%)
Gallas et. al [20]	2003	1.65	23.5	1	29	140
Gallas et. al [20]	2003	0.84	37	1	63	5
Tang and Zhong [93]	2009	0.5	20	2	2.1	10
Persoons [94]	2012	5	75	1.14	N/A	N/A

The second type of models will be referred to as equation based models. Sharma introduced an equation based fluidic-acoustic analytical model to study a Helmholtz resonator actuated by a moving wall (i.e., piston) [18]. In the study the mechanical diaphragm resonance frequency and the displacement profile was assumed to be known. The model was validated against Gallas's experimental cases and obtained promising results. Girfoglio et al. also studied Sharma's model based on a mechanical diaphragm equation of the substrate plate only and a dynamic fitting parameter [69]. Tang and Zhong studied two models namely the static incompressible (SC) and dynamic incompressible (DI) models. In the SC model, the fluid in the cavity is considered as compressible, modelling the fluid motion in the cavity and orifice separately. Orifice is modelled using the continuity equation and a simplified form of Navier-Stokes equations (for fully-developed pipe flow). The cavity's fluid motion is modelled using the mass conservation equation in integral form. DI model uses a simplified form of jet velocity estimation which was previously published in [95]. The investigation was performed in the low frequency range and a pa-

parameter sensitivity analysis was performed to compare the analytical and CFD models. Even though, the models demonstrated some accurate agreement, the diaphragm displacement was assumed and only very low frequency forcing (up to 200 Hz) was studied. As experimental data was not presented, the CFD result is used in the table (Table 2.5) to compare the accuracy of the peak jet velocity.

Table 2.5 presents a summary of the analytical models using the same comparison elements used in Table 2.4.

Table 2.5: Selected Studies of Analytical Model of SJA

Study	Year	$d_o(mm)$	$D_c(mm)$	K	$U_p (ms^{-1})$	% Diff. (%)
Sharma [18]	2007	1.65	23.5	0.78	29	N/A
Sharma [18]	2007	0.84	37	0.78	63	N/A
De Luca et al. [69]	2014	2	35	1.46	16.2	1.2
Tang and Zhong [96]	2007	1	45	N/A	1.5	10

The third approach to modelling is based on CFD models using commercial software packages to study Navier-Stokes equations on a meshed geometry. The commercial software packages have been developed and have become more commonly available in the last decade or so.

Kral et al. conducted a numerical study using both incompressible laminar and turbulent models to study synthetic jets [97]. The turbulent model uses Spalart-Almagaras (S-A) one-equation model for the turbulence closure. They applied a boundary condition at the orifice exit for suction and blowing. By using a laminar flow model the development of vortex pairs was captured.

Rizzetta et al. studied compressible and unsteady Navier-Stokes equation for both inside the cavity and to external flow field [98]. Their actuator had a slot orifice and was studied a single frequency with a boundary condition replicating the piezoelectric diaphragm motion. They compared 2-D and 3-D simulations and stated that only the 3-D simulations can resolve the span-wise instabilities which leads to the breakup of the coherent vortex structures.

Mallinson et al. studied incompressible and unsteady Navier-Stokes equations

with $k-\epsilon$ turbulence model [99]. Their model and validation used a micro actuator (i.e., having an orifice diameter of $d_o = 0.2$ mm). They captured the primary and secondary vortex rings formed at the orifice exit and their advection. They concluded that the micro-scale synthetic jets have a similar flow behaviour for the cavity and actuator.

Rusovici and Lesieutre used the ANSYS commercial solver to study polycrystalline and single crystal (PMN-PT) piezoceramic patches of equal dimensions [100]. Even though, the study did not reveal a full frequency sweep of the actuator or the working model, they suggested that the single-crystal piezoceramic would be the next generation norm of piezoelectric actuators with higher coupling ratio, jet velocity and electric-to-fluidic efficiency compared to the polycrystalline piezoceramic.

Tang and Zhong also studied SJ using numerical methods [101]. They did not model the diaphragm motion and adopted a boundary condition having a sinusoidal waveform. Two different diaphragm displacement settings were employed with laminar and turbulent flow. They did not study the full frequency response and instead studied a single frequency capturing the traverse velocity profile at the orifice. The conclusion of the study was the best turbulence model choice would be RNG, $k-\epsilon$, and $k-\omega$.

Rusovici and Lesieutre [100] numerically studied the effect of using single crystal piezoceramic to actuate an SJA. Their analysis was purely fluidic and they identified that due to its enhanced electromechanical coupling using single crystal piezoceramic patch instead of polycrystalline would increase the transverse displacement and the exit jet velocity. Nevertheless, analysis was not revealed full details of the simulation and did not have an experimental validation.

Jain et al. employed an inlet velocity boundary condition for a bi-morph diaphragm at a fixed actuation frequency [102]. They studied cylindrical, parabolic and conical cavity shapes for an axisymmetric orifice. The approximations of the boundary condition is reported to miscompute the orifice jet velocity top hat profile.

Alimohammadi et al. studied adjacent synthetic jets actuated with two diaphragms at a single actuation frequency [103]. Their model is validated against PIV data but the actuation frequency was kept low at 57 Hz where the Helmholtz resonance was reported to be 485 Hz. Therefore, the frequency of actuation is not contaminated by the jet velocity rise due to Helmholtz resonance. The study concentrated on the flow visualisation validation for different phase angles between the diaphragms and a reasonable match was obtained for the transverse velocity.

Ziade et al. numerically studied the experiments previously done by Feero [68] regarding the effect of the cavity shape on the jet velocity [19]. They studied a low frequency ($0.71 f_H$) similar to previous studies and confirmed the experimental results previously conducted by [68]. Vortex formation was identified both in the cavity and outside of the orifice.

Quayoum and Malik utilized COMSOL Multiphysics to study an incompressible synthetic jet actuated by a piezoelectric actuator which was properly modelled on an 2-D axisymmetric geometry [104]. Navier-Stokes equations with $k - \epsilon$ turbulence model was solved in the time-domain and the results compared to the experimental work of Mane et al [105]. An acceptable match was achieved at very low actuation frequencies (10-32 Hz).

Table 2.6 shows key results from selected CFD studies which included experimental validation. The table considers the year of publication, size of orifice (or slot), cavity diameter, actuation frequency, turbulent model and % difference with the experimental data at peak exit jet velocity. From the selected studies, the following can be observed, i) there is still gap for improvement to reduce the difference between experimental and computational jet velocity results ii) In most cases very low actuation frequency is studied which does not have much of significance in practise iii) behaviour of the diaphragm is often not modelled accurate and replicated with a sinusoidal boundary condition iv) there is no such computational model which can both obtain jet velocity response corresponding to Helmholtz and diaphragm mechanical resonance.

Table 2.6: Selected Studies of CFD Model of SJA

Study	Year	$d_o(mm)$	$D_c(mm)$	$f(Hz)$	Model	%Diff.
[97]	1997	0.5 x 75	N/A	1000	Spalart-Allmagaras	10
[101]	2005	5	45	50	Laminar	13
[102]	2011	3	45	200-1100	Laminar	28
[103]	2016	1.65 x 9.6	75	57	DM Turbulent	3
[19]	2018	2	30.8	199	Laminar	16.5
[104]	2019	3	40	20	$\kappa - \epsilon$	15

2.9 Identified Research Gaps from the Literature Review

The research gaps identified are categorised into subtopics such as piezoelectric actuator modelling, analytical modelling (i.e., equation based) of SJA, and jet velocity and power conversion efficiency enhancement. The identified research gaps are linked to the objectives of the research, presented in Section 1.3.

2.9.1 Modelling of the Free and Forced Vibrations of Piezoelectric Actuator

By the review made in Section 2.5, it is identified that studies concentrating on the free and forced vibrations of the composite piezoelectric actuators had the following issues:

- Analytical models develop does not fully justify the effect of coupling extensional-flexural vibrations on the natural frequency estimations.
- The determination and role of the neutral plane/axis is not justified.
- Effect of bonding layer thickness is not studied in detail and usually overlooked.
- Dynamic response (i.e., under voltage load) of the piezoelectric actuators not widely studied and not validated against experimental data.

By addressing the points listed, the following should be developed and experimentally validated over a range of different size piezoelectric actuator. The size range should cover the most commonly used actuators which is with 15 mm to 35 mm of outer diameter.

- Physical and accurate model (i.e., nonlinear) of the piezoelectric unimorph actuator which takes into account the full composition (i.e., thickness/diaphragm of the substrate and piezoceramic) for the preliminary design of the synthetic jet actuator using the thin plate equations. The model should be able to compute the natural frequency of the piezoelectric diaphragm within $\pm 3\%$ compared to the experimental data.
- Frequency response functions to study the transverse deflection of the diaphragm under voltage load.
- Accurate identification of the mechanical damping ratio for circular piezoelectric actuator.

Development of the theory and analysis of free and forced vibrations of the piezoelectric actuator as per the listed points above are aligned with the Objectives 1 and 2 (given in Section 1.3).

2.9.2 Analytical Modelling of SJA

The analytical models to-date have had various limitations and employed major assumptions for justification. The problem originates by not being able to predict the natural frequency of the piezoelectric actuator and its response (displacement) under voltage load. Therefore, these should be addressed to obtain an accurate and reliable analytical model which may work as a quick SJA design tool. The following should be developed and experimentally validated over a range of relevant actuator cases.

- A structural mechanics model which can estimate the modal parameters of the piezoelectric actuators which is integrated to a fluidic-acoustic

model.

- The structural-fluidic-acoustic model should take voltage supply as an input.

Development of a diaphragm-based model which also utilise fluidic-acoustic equations of SJA by considering the issues listed are aligned with the Objective 3 (given in Section 1.3).

2.9.3 CFD Modelling of SJA

The CFD modelling review indicates that there is still a gap in the literature to cover the full spectrum of actuation frequency with a focus on the piezoelectric actuator's mechanical resonance. Most of the studies used a boundary condition to replicate the motion of the diaphragm. On the other hand, it is identified that the studies usually focused on the low frequency at around the Helmholtz resonance or even lower. There can be a list of potential reasons for this:

- 1) Modelling the piezoelectric diaphragm, which consists of a passive layer of substrate with an active layer of piezoceramic patch, increases simulation complexity.
- 2) The simulation software package may not allow the proper modelling of the piezoelectric diaphragm's structural mechanics.
- 3) The computational time increases massively for a converged time-dependent solution in case whole frequency envelope is computed.
- 4) The non-linearity at high-frequency increases, which then turbulence (i.e., highly unsteady) and compressibility effects should be considered.

The following should be developed and experimentally validated over a range of actuator cases.

- A structural-fluidic-acoustic model to provide with accurate estimations of the jet velocity corresponding to the mechanical and Helmholtz resonance frequency.

- The emphasis of the model should be on the realistic structural mechanics modelling of the piezoelectric actuator.

Development of a diaphragm-based FEM model which fully couples structural-fluidic-acoustic domains as per the listed points above are aligned with the Objective 3 (given in Section 1.3).

2.9.4 Jet velocity and Power Efficiency Enhancement of SJA

As per the review of the state-of-the-art SJA performance review in Section 2.7, the effect of changing orifice-diaphragm (i.e., from opposite orifice-diaphragm configuration to adjacent) on exit jet velocity/power conversion efficiency is not well documented in the literature. The cavity-orifice size optimisation was concentrated on the opposite orifice-diaphragm configuration SJA. Also, the effect of utilizing single crystal piezoceramics or bimorph configuration piezoelectric actuator on jet velocity and power conversion efficiency is not experimentally studied. The following should be experimentally studied to provide novel knowledge.

- Effect of employing identical polycrystalline and single crystal piezoelectric actuators on common cavity-orifice arrangement geometry to assess jet velocity and power efficiency.
- Effect of utilizing unimorph and bimorph piezoelectric actuator on common cavity-orifice arrangement geometry to assess jet velocity and power efficiency.
- Understanding the effect of different the SJA configuration which is more viable for a potential flow control application (i.e., adjacent orifice-diaphragm arrangement) on jet velocity and power conversion efficiency.

Running an extensive experimental investigation to study the listed points above are aligned with the Objective 4 (given in Section 1.3).

Chapter 3

Experimental Methods and Apparatus

3.1 Experimental Validation Strategy

An investigation is carried out to obtain experimental data regarding various piezoelectric actuators and synthetic jets performance. The experimental campaign involved tests of different types/dimension piezoelectric diaphragm and validating mathematical models developed within this study. This chapter concentrates on the experimental methods, apparatus and their setup. Where applicable, the rationale behind the experimental methods are explained and compared to studies in the literature.

Test campaign is divided into two: i) investigation regarding the piezoceramic diaphragm natural frequency ii) dynamic response on their own and performance measurements of the piezoelectric driven synthetic jet actuator. The former mainly aims to validate the analytical structural models of composite piezoelectric diaphragm, presented in Chapter 4 and Chapter 5. The latter investigation endeavours to validate both analytical and computational models presented in Chapter 6 and improve the field's current knowledge regarding performance metrics of SJA (Chapter 7).

3.1.1 Proposed Experimental Investigation

The test campaign consists of two main categories:

I. Executing frequency sweep tests (varying the frequency which piezoelectric diaphragm oscillates) under excitation voltage (potential difference) to locate the mechanical resonance frequency (i.e., first mode of oscillation, shown in Chapter 2.5, Figure 2.5) of the piezoceramic diaphragm on its own on a similar clamp to the synthetic jet actuator configuration. This set of experiments aims to identify the resonant frequency and peak displacement and determine the effect of clamping on both. An illustration of piezoelectric actuator is shown in Figure 3.1a.

II. Testing and recording various performance indicators of the synthetic jet actuator design of different configurations in which the performance indicators include output jet velocity and the current consumption. This part of the tests involve measurement of temporal cavity pressure and temperature behaviour both inside the cavity and outside of the orifice. This set of experiments aims to obtain the exit jet velocity of the actuator and collate data to calculate fluidic-to-electric power conversion efficiency of SJA. An illustration of synthetic jet actuator is shown in Figure 3.1b.

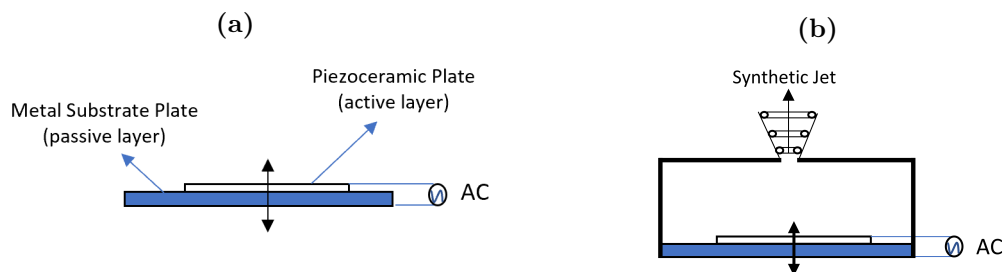


Figure 3.1: Illustration of (a) Piezoelectric Actuator (b) Synthetic Jet Actuator

3.1.2 Nature of Periodic Data and Requirements

Sampling periodic data is a challenging experimental task. The tests should be designed in such a way to keep experimental uncertainty and error as low as possible.

In the present study, the synthetic jet actuator is operated with periodic sinusoidal excitation under AC voltage to the piezoelectric diaphragm. Therefore, oscillation of the piezoelectric diaphragm (unsteady), fluid motion in the cavity and the jet formed outside the orifice are all sinusoidal periodic data.

Mathematically, sinusoidal periodic data can be described with Equation 3.1, assuming an initial phase angle with respect to the time origin in radians.

$$x(t) = X \sin(2\pi f_0 t + \theta) \quad (3.1)$$

Thus, the time history of the synthetic jet's periodic data essentially looks like a sine wave. The unsteady and sinusoidal nature of waveform may lead to a further problem: signal temporal aliasing. Signal temporal aliasing happens when the acquisition frequency is less than the frequency of true signal. The difference between the real and aliased signal is shown in Figure 3.2 [65]. Signal aliasing might cause a misleading and inaccurate collection of data.

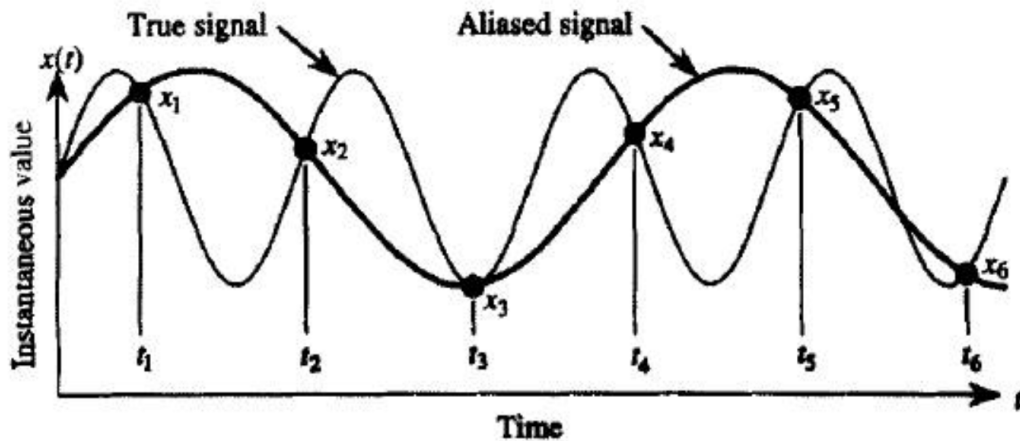


Figure 3.2: Illustration of frequency aliasing [65]

In order to avoid signal aliasing, the Nyquist sampling theorem should be taken into account. The Nyquist theory states that the sampling frequency (f_s) should be at least twice the highest frequency contained in the signal (f_c) [106]. Nyquist criterion is shown by Equation 3.2.

$$f_s \geq 2f_c \quad (3.2)$$

Sampling with a higher rate than the Nyquist criterion (i.e., oversampling) reduces the quantization error and noise, resulting in a continuous random signal converted to discrete data. Oversampling for long periods might challenge computer systems capacity and increase the acquisition time of the data. Ultimately, the sampling frequency selection is a combination of the equipment's frequency resolution and the highest frequency in the signal.

For the mean quantities, such as the mean of peaks of a signal, sufficiently long acquisition time is also essential. For a periodic flow, the acquisition time should also allow for the flow settling time, especially in continuous operation, when a frequency is changed to another without a rest time. Finally, to ensure that the data is consistent and reliable, the experiments should be repeated possibly on different days to ensure ambient temperature have no effect on the results.

3.2 Piezoelectric Actuator

This section covers an overview of the piezoelectric actuators used in the thesis. A piezoelectric diaphragm consists of two main elements: piezoceramic and substrate material. The elements are bonded together using silver loaded epoxy for adhesion to ensure current transfer. The substrate material is also referred to as the passive layer and the piezoceramic as the active layer. The manufacturing of the piezoceramic actuators is not included within this part/study as it is not the research focus within this thesis.

The piezoelectric elements used within this study can be classified into two groups based on the type of piezoceramic: polycrystalline (here, lead zirconate-titanate, PZT-5A) and single crystal (here, lead magnesium niobate-lead titanate, PMN-PT). The polycrystalline piezoceramic group are available as unimorph and bimorph. Unimorph piezoelectric actuator have a single active and passive layer, as shown in Figure 3.3c. Figure 3.3d shows a bimorph diaphragm with a single passive layer of substratum in between two active layers of piezoceramic. All piezoelectric actuators used in this study are purchased manufactured and ready to use.

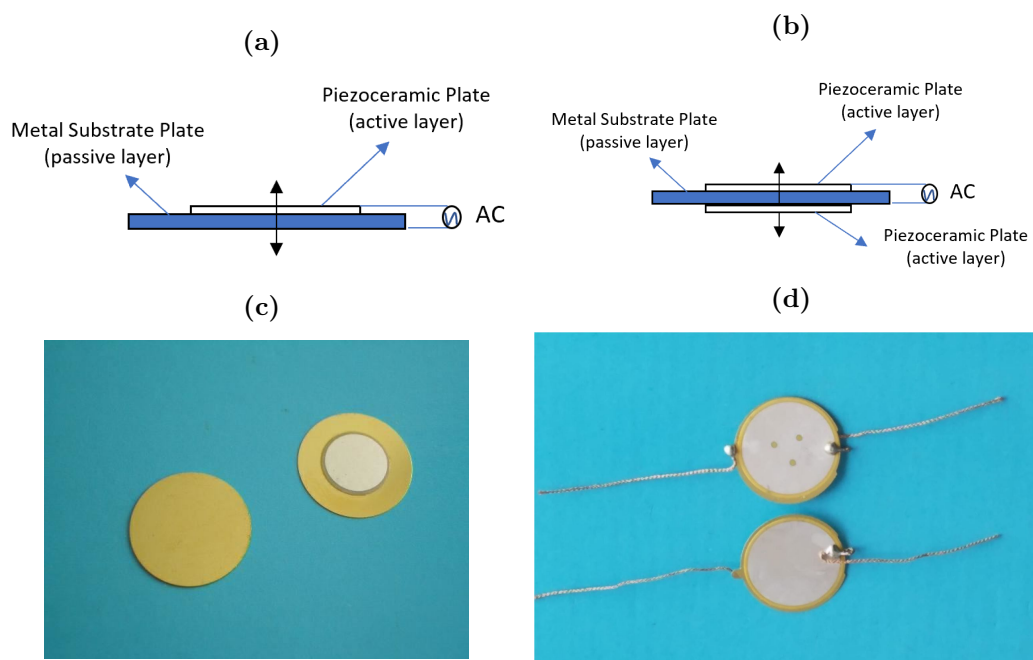


Figure 3.3: (a) Schematic of unimorph piezoelectric actuator (b) Schematic of bimorph piezoelectric actuator (c) Unimorph piezoelectric actuator (upper and lower surfaces) (d) Bimorph piezoelectric actuator (upper and lower surfaces) (soldered)

As substrate metal, brass shim is employed which is a common practice in this research due to its high durability, low unit cost and ease of manufacturing (cutting into the geometric shape for the requirement).

Unimorph polycrystalline discs are supplied by OBO company (diameter range 15 mm to 50 mm) [107], bimorph diaphragm of a single size from American Piezo Company [108] and single crystal piezoceramic of a single size from TRS Ceramics [109].

Although the unit cost of a piezoelectric diaphragm is under \$1, often their minimum purchase order quantity is more than 1000, which increases the cost for off-the-shelf products. The piezoceramic diaphragm can be customized, for specific diameter and thickness compositions. However, the unit price would be +\$100 and +\$350, respectively for polycrystalline and single crystal piezoceramic unimorph.

Table 3.1 presents the key physical properties of the piezoceramic discs [107–109]. All piezoceramic discs used within this study are polarised in $\langle 001 \rangle$, vertical polling to get maximum deflection in the standard vertical axis in the Cartesian system. The measurements are made 24 hours after polarization. Standard measurement tolerance of d_{31} value is reported as $\pm\%20$.

Table 3.1: Piezoelectric diaphragm groups and piezoelectric properties

Type	Unimorph Polycrystalline	Unimorph Single Crystal	Bimorph Polycrystalline
Diameter (mm)	11.3 - 25	19.8	24.6
Thickness (mm)	0.17 - 0.58	0.23	0.13 ¹
E_c (kV/cm)	12.0	2.0	19.7
$-d_{31}$ (pC/N)	180	560	175
k_p	0.72	0.93	0.63
$\tan(\delta)$ (%)	2.0	0.6	2.0

The coercive electric field (E_c) is important to know before conducting an experimental design as it plays an important role in the maximum supply voltage applicable before piezoceramic fracture. The transverse charge coefficient (d_{31}), is a measure of deflection under voltage load in the vertical axis. The electromechanical coupling factor (k_p) defines the ratio of the converted mechanical energy to input electrical energy and it is an important figure-of-merit of the piezoceramic selection. Dielectric loss (also known as the loss tangent), $\tan(\delta)$, accounts for the internal viscoelastic loss caused by the phase lag between charge displacement and electric field [35].

The dielectric loss results in an electrical resistance which is a function of the capacitance (C_d) and the driving frequency of the actuator ($\omega = 2\pi f$). The

¹0.13 mm x 2 for the bimorph has two active layers

power dissipation due to the dielectric losses are expressed by Equation 3.3 where V_p is the peak driving voltage of the piezoelectric actuator [17].

$$P \approx \frac{1}{4} \tan(\delta) C_d \omega V_p^2 \quad (3.3)$$

Assuming identical conditions, polycrystalline piezoceramic would have 3.3 times more electrical power converted to heat as dissipation, compared to the single crystal piezoceramic.

3.3 Clamping and Cavity-Orifice Arrangement Manufacturing

The so-called clamping plates are used for the piezoelectric actuator experiments. Clamping plates which are used in Chapter 4 and Chapter 5 are designed in the CAD environment and manufactured using a Prusa i3 MK3 printer (nozzle size = 0.4 mm) using poly-lactic acid (PLA) material. The print is conducted with an infill rate of 100% to ensure toughness of the product when clamped. For a given piezoelectric actuator, there are two clamping plates which comprises of an upper part with an extended lip and a lower part acting as a container; with a groove to fit the actuator [54, 58]. Figure 3.4 presents a 2-D axisymmetric side view of the diaphragm clamping arrangement.

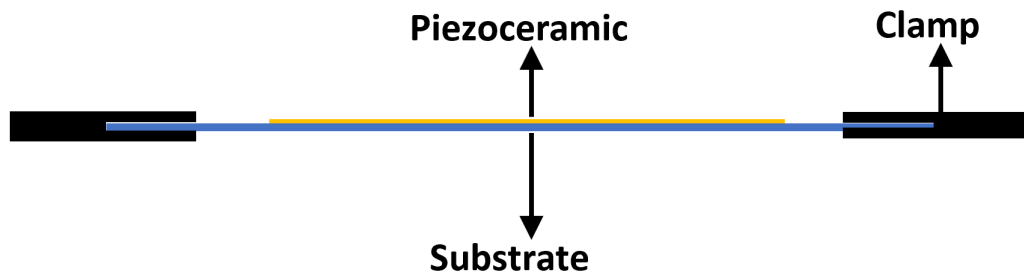


Figure 3.4: 2-D Illustration of the clamping mechanism

Both plates have 8 holes for M3 screws and other 8 holes for M4 screws to connect the plates to the test bed. The edge-to-edge distance between the

actuator (i.e., diaphragm) and the screw hole is 3.5 mm for all clamping plates. Figure 3.5 shows the 3-dimensional assembly drawings of bottom and top plates with screw holes in CAD environment. Figure 3.5a presents the view from the outer side of the clamping arrangement and shows the diaphragm container (groom), shim (substrate) and so-called clamping plate with the O-ring like lip for clamping. Figure 3.5b presents the view from the inner side of the clamping arrangement and shows the diaphragm container (groom), piezoelectric element (active layer) and so-called clamping plate with screws.

Figure 3.6 shows a clamped piezoelectric actuator on the steel test bed. Figure 3.6a presents a clamped piezoelectric actuator with solders. The figure is annotated and displays the diaphragm container, piezoelectric actuator, soldered wires, clamping screws and test bed connection screws with the clamps. Figure 3.6b presents the back view of the clamping setup with the annotations of: clamping plate, piezoelectric actuator (only the shim is visible), steel test bed, clamping screws and the connection screws between the clamping and the test bed.

The cavity-orifice arrangement (for synthetic jet actuator) are printed with Stereolithography (SLA) Printer (Formlabs Form 2) for better precision and smooth surface finish. Grey hard pro resin material is used. The size precision of the product is 0.05 mm. The manufactured prints are washed and cured and polished when necessary.

Figure 3.7 presents an exploded view of the cavity-orifice arrangement and the piezoelectric diaphragm. Figure 3.7a presents the view from the outer side with respect to the cavity and presents the orifice hole, shim (substrate) and the clamping plate. Figure 3.7b presents the view from the inner side of the cavity and shows the shim, cavity depth with the orifice, piezoelectric element and outer side of the clamping plate.

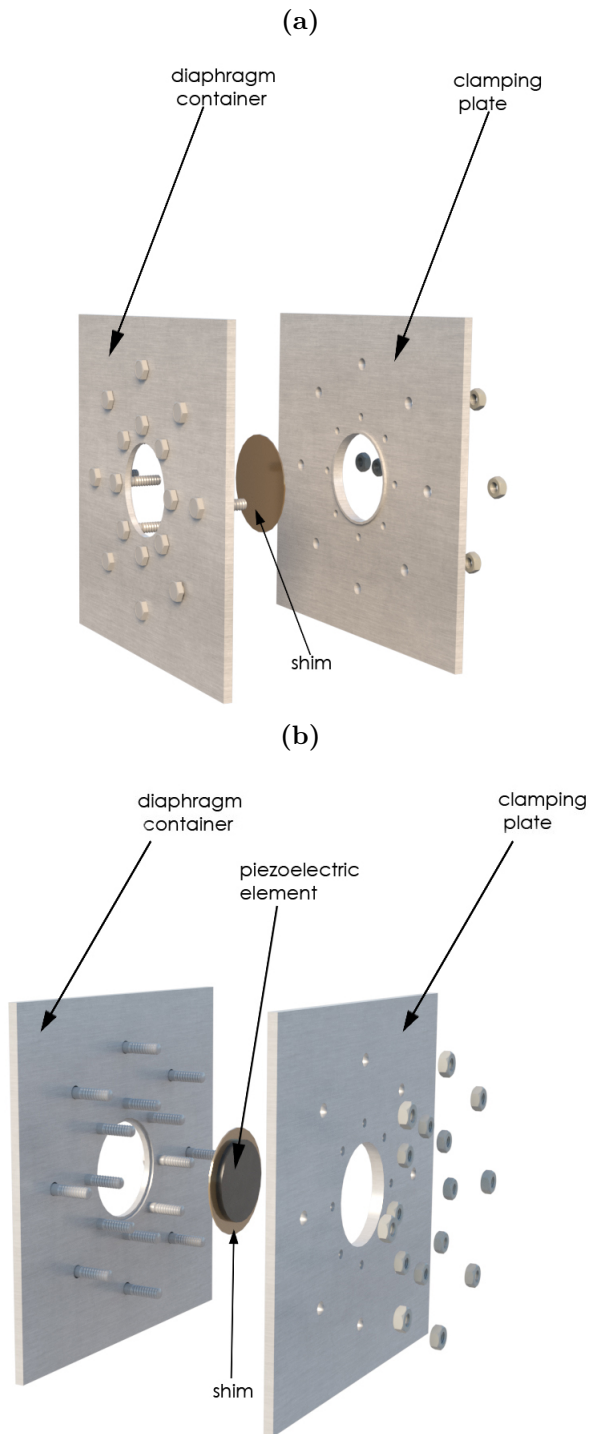


Figure 3.5: 3-D design of diaphragm container, piezoelectric actuator and clamping plate (a) view from outer side (b) view from inner side

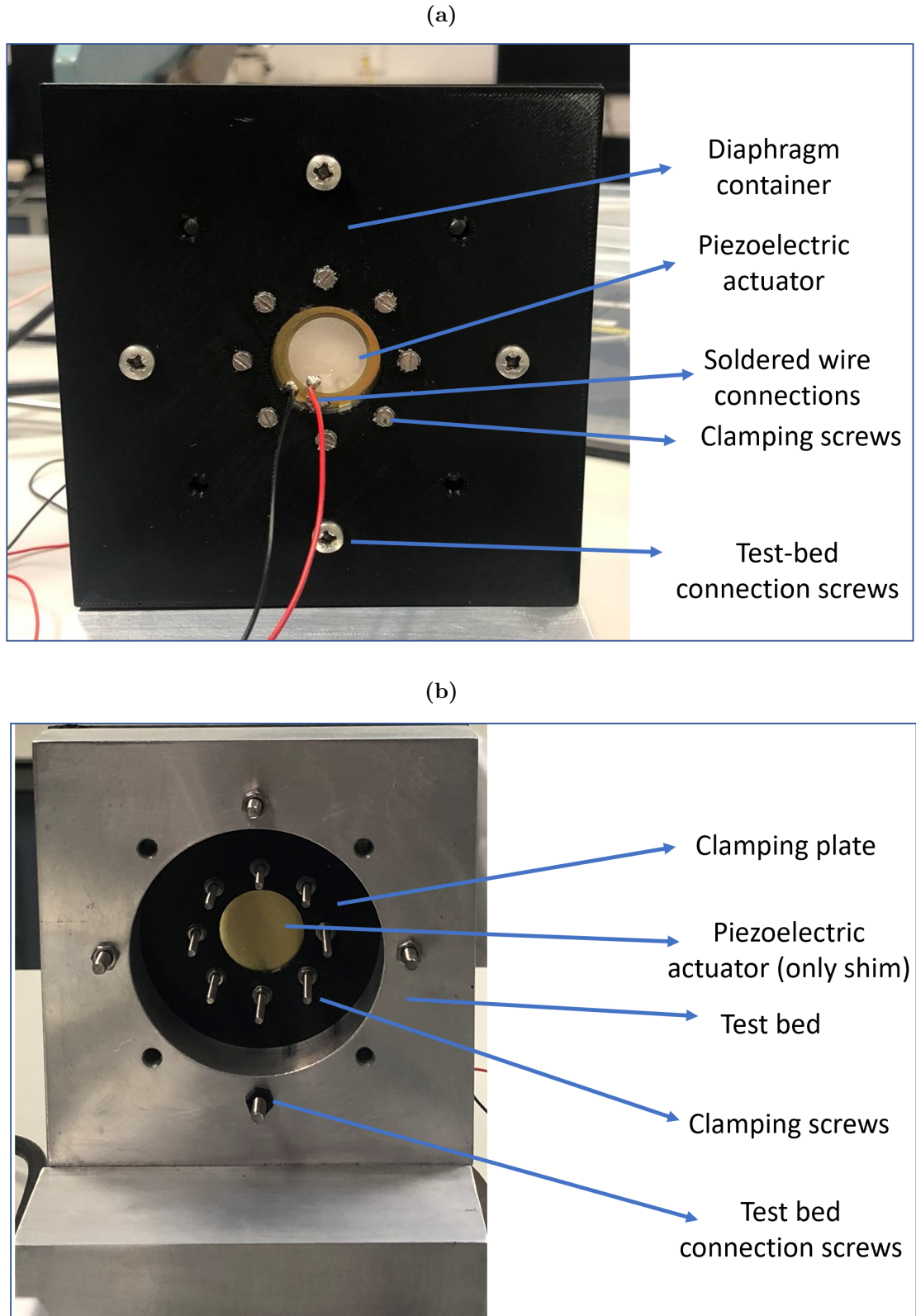


Figure 3.6: View of clamped piezoelectric actuator on the test bed (a) front side (b) back side

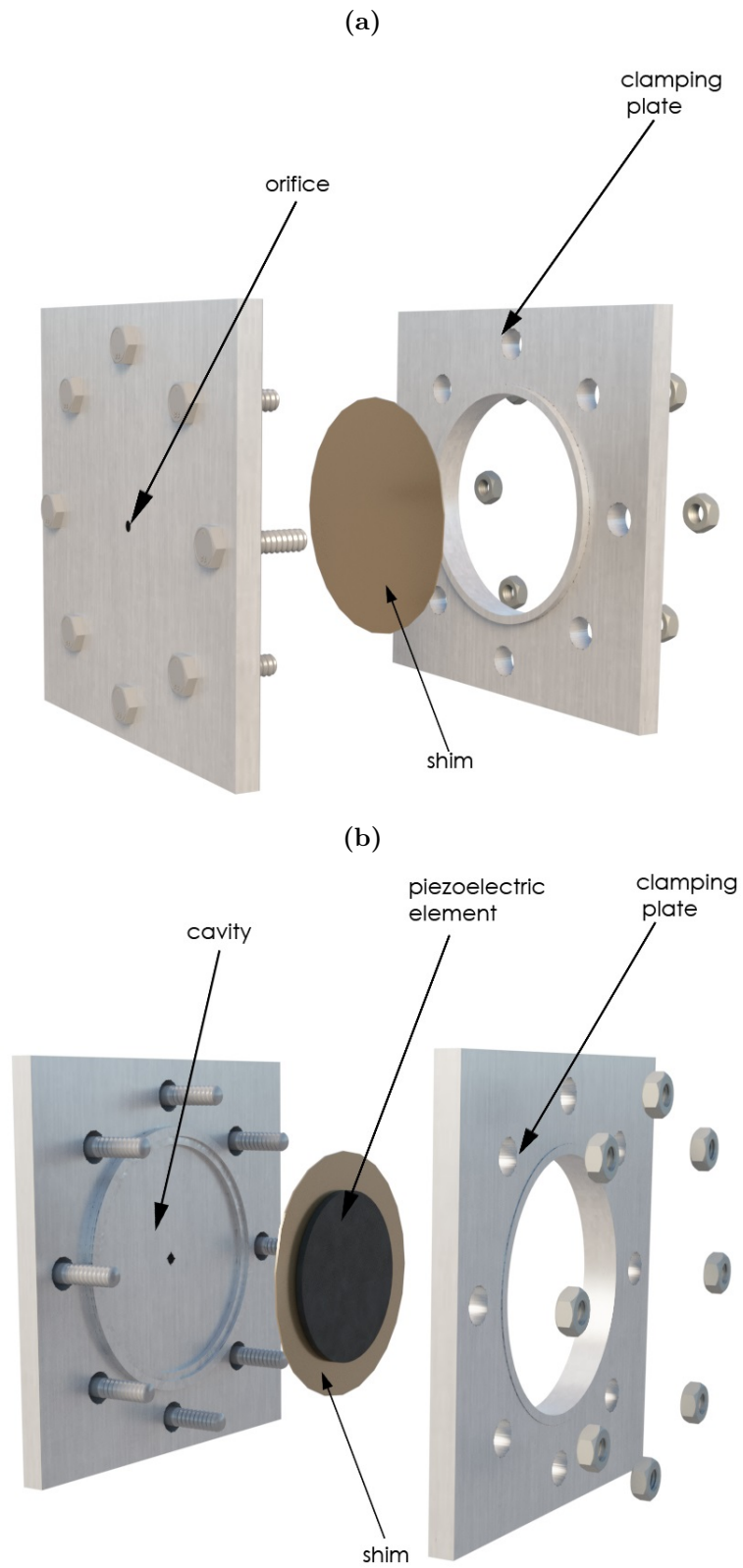


Figure 3.7: 3-D assembly drawing of the cavity-orifice arrangement and piezoelectric diaphragm (a) view from outer side (b) view from inner side

3.4 Piezoelectric Actuator Displacement Measurements

Displacement of the piezoelectric actuator is measured by Laser Doppler vibrometer (LDV). LDV is a non-contact method which is employed to measure the displacement of the piezoelectric diaphragm when voltage is applied. The diaphragm centre displacement is an essential measure of the performance for the diaphragm and the actuator. Therefore, laser vibrometer scanning utilised to measure the clamped diaphragm's displacement under AC voltage. Additionally, the measurements have been taken while the piezoelectric diaphragm is clamped together with the cavity and orifice plate.

The laser scanning head used within the experimental campaign is a Polytec Scanning Vibrometer, PSV 300 (Polytec GMBH, Germany). The scanning head is connected to its workstation and controller. The laser type is helium neon with class II which is eye-safe when the laser beam source is not stared at. The helium-neon laser in the scanning head requires a 30-minutes of heating time to reach a thermal equilibrium with the surroundings as per its operation manual. Figure 3.8 presents the connections of signal generator (SR785), piezo power amplifier (PZD 350), laser controller, workstation and laser scanning head.

The vast majority of the laser measurements investigation concentrates on identifying the resonant frequency and peak displacement at the centre of the diaphragm. The centre position of the circular diaphragm is targeted as it is one of the key piezoelectric performance indicators and linked to the exit jet velocity in many modelling studies [93, 110]. The position of the laser beam is aligned using the data acquisition software integrated to the laser scanning head. The available software does not allow to take multiple measurements simultaneously. Frequency response functions results in clear modes indicating

there is no contamination by secondary modes on the first mode, also checked using finite element analysis.

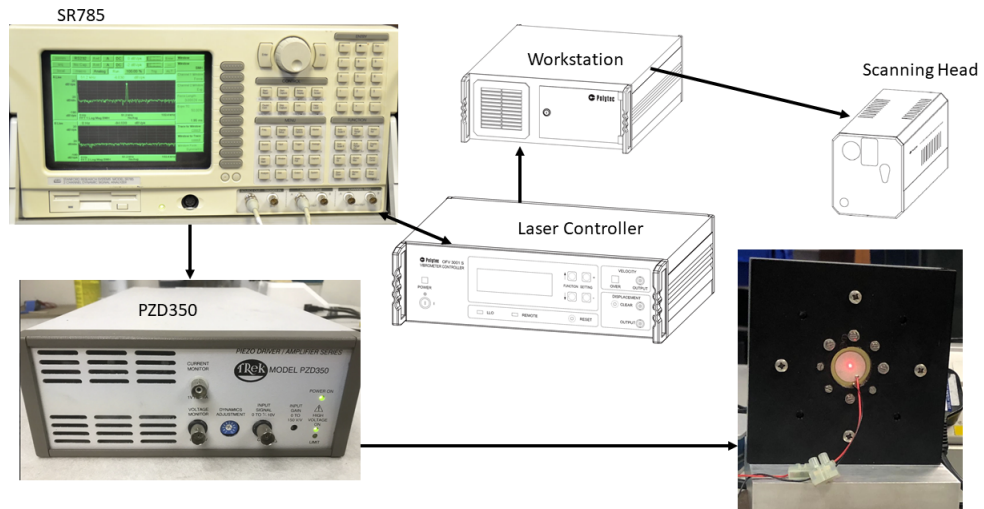


Figure 3.8: *Laser Operation Setup*

Table 3.2 presents the laser board acquisition specifications of PSV-300 laser displacement measurement system [111]. Displacement measurements are taken in mm/s/V which is then integrated in post-processing to obtain the peak displacement.

Table 3.2: PSV-300 Laser Board Acquisition Specifications

Parameter	Value
Velocity decoder	OVD-04
Measurements ranges (mm/s/V)	5/25/125
Maximum frequency	250 kHz
Filter	5/20/100 kHz
Data acquisition board	PCI-4451
Maximum bandwidth	40 kHz
Simultaneous input channels	2
Output channels	1

The maximum frequency which can be captured by the laser head and controller is 250 kHz (Table 3.2). The laser beam spot size on the contact surface is around 100 μm .

The laser controller was integrated to a Stanford Research (SR785) Dynamic Signal Analyser and Generator. SR785 is capable to send a continuous signal

to the piezoelectric disc in various frequency and voltage. Sinusoidal waveforms sent to the diaphragm via TREK PZD350A high-voltage piezo amplifier with an output voltage range of 0 to $\pm 350V$ peak AC. TREK piezo amplifier is an important piece of equipment within the testing campaign and investigated in detail in Section 3.5.

The measurements are taken with a sampling rate of 40 kHz for a sampling time of 1 second. This grants the satisfaction of Nyquist theorem (discussed in Section 3.1.2) as the maximum forcing frequency is 4 kHz [106].

The resolution of the measurements is $5 \frac{\mu m}{s}$. The amplitude error at the room temperature is $\pm 1.5\%$ of the root-mean-square of the reading.

To ensure uniform clamping, the screws are mounted using a digital torque screwdriver, Sealey 1/4" Hex with a torque range of 0.05 - 5 Nm. Eight screws are used to mount the clamping plates with 0.35 Nm of torque applied equally to all screws. The effect of the torque on the natural frequency is checked by varying the applied torque to the screws in the range of 0.20 Nm to 0.50 Nm. In the selected torque range, it is identified that the effect of the torque on the natural frequency was not significant.

3.5 Power Measurements

Electrical power is the product of voltage and current. For alternating current (AC) systems, the true power (also referred as actual power) is calculated by also taking into account the phase difference between the voltage and current signals.

The voltage and current are measured by connecting the TREK PZD-350A high voltage piezo amplifier to the analogue-to-digital converter (NI cDAQ-9171) connected to the computer (i.e., data acquisition software). Measurements for electrical power are taken simultaneously with jet velocity and in-cavity pressure measurements described in Section 3.6 and 3.7, respectively.

PZD350A have two output monitor sockets; one for voltage and one for current.

It is important to monitor voltage and current at the exit of the supply circuit. The voltage monitor have a ratio of 1/100 of the voltage output, so if the oscilloscope reads 200 mV the actual voltage is 20 V. The current monitor have a ratio of 0.05 V/mA thus; 1 V is 20 mA.

Figure 3.9 shows sample voltage and current data actuation at 2900 Hz at 20 V_p. The x-axis of Figure 3.9 is normalised with the period of oscillation to reflect 3 full cycles.

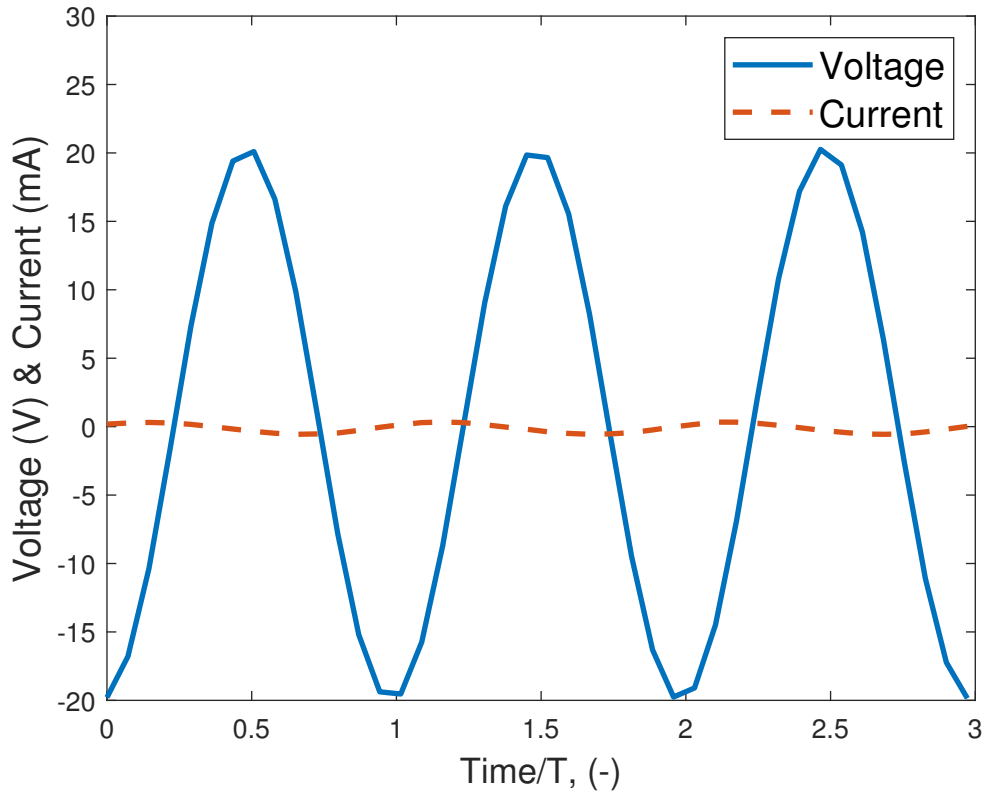


Figure 3.9: A Sample Data for Voltage and Current

Sampling rate is 40 kHz for both voltage and current signals. The sampling time is 5 seconds which results in a sample size of 200,000.

The voltage and current measurement have an uncertainty of $\pm 0.1\%$ and $\pm 1\%$, respectively.

3.6 Jet Velocity Measurements

For the jet velocity measurements mainly hot-wire anemometry is used which is an intrusive method in the flow measurements. Advantages and disadvantages

of the hot-wire anemometry are discussed in Section 3.9.

The hot-wire anemometry used in the experimental investigation are products of Dantec Dynamics (Denmark). MiniCTA 54T30 is used together with 55P11 probe. CTA stands for Constant Temperature Anemometer which is one of two anemometer type together with constant current. CTA systems are well-known, cost-effective and versatile. The probe is positioned in line with the orifice centre-line throughout the experiments. Dantec 55P11 probe consists of a platinum-plated tungsten wire of width 1.2 mm and diameter of $5 \mu\text{m}$.

MiniCTA is a single channel anemometer and can go up to 300 ms^{-1} of measurements in air [112]. The probe width is 1.2 mm which is equal or smaller than the SJA orifice diameters tested within this study and stands out as a significant advantage of using this probe type. The hot-wire probe is aligned over the centre of the exit plane. Figure 3.10 presents an illustration of the experimental setup. In the horizontal axis, the probe is placed as close as possible to the exit plane to sample the maximum possible jet velocity and to avoid velocity decays, corresponding to a downstream distance of $0.1 d_o$. The approach is identical to the experimental work of Gallas et al. [20], Amitay et al. [113, 114] and Persoons [94]. The position of the probe is set manually using a digital vernier caliper with resolution of $\pm 0.05 \text{ mm}$.

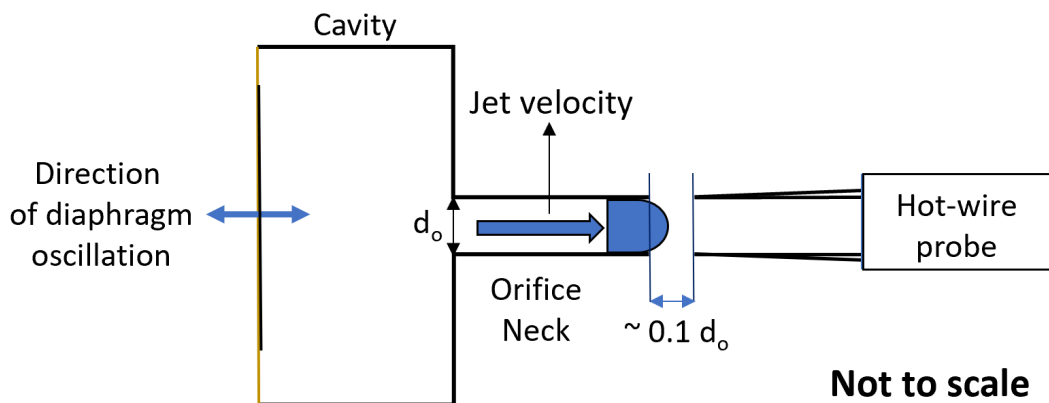


Figure 3.10: *Illustration of hot-wire probe positioning and setup*

Hot-wire calibration is conducted using a nozzle rig, standard K-type thermocouples to measure flow temperature and a Furness Control FC0510 micro-

manometer (a maximum velocity capability of 180 m s^{-1}) which read and convert air pressure into velocity. The manometer and hot-wire probe are placed next to each other. The data is taken simultaneously from the hot-wire and micro-manometer using the control computer.

The raw data is captured in voltage (V) and should be compensated for the variations in temperature (V_c) (i.e., temperature drift) by using the Equation 3.4.

$$V_c = \sqrt{\frac{T_w - T_o}{T_w - T_a}} V \quad (3.4)$$

Where T_w is the sensor hot temperature, T_o is the ambient reference temperature before calibration and T_a is the ambient temperature during acquisition. After compensating the raw voltage for the temperature drift, voltage can be converted into velocity by using the velocity data obtained in the calibration. It is a common practice to formulate the voltage calibration curve (to convert measured voltage to air velocity) of hot-wire with a fourth order polynomial (Eq. 3.5a) but Gomes [65] employed a fifth order polynomial (Eq. 3.5b). Therefore, both is considered to examine if the effect of increasing the order of polynomial is significant. Equations 3.5 show how the time-dependent voltage signal is converted into a velocity signal.

$$u(t) = p_1 V_c^4 + p_2 V_c^3 + p_3 V_c^2 + p_4 V_c + p_5 \quad (3.5a)$$

$$u(t) = p_1 V_c^5 + p_2 V_c^4 + p_3 V_c^3 + p_4 V_c^2 + p_5 V_c + p_6 \quad (3.5b)$$

Both polynomials are fitted to the measurements by using MATLAB 'polyfit' subroutine [115]. Fourth and fifth order polynomials are used to approximate the air velocity shown with Equation 3.5a - 3.5b.

Figure 3.11 presents the temperature corrected voltage measured with the hot-wire anemometry with respected to the air velocity measured. In the figure legend, 'Manometer Data' corresponds to the temperature corrected air

velocity reading of manometer, 5^{th} and 4^{th} order corresponds to the 5^{th} order polynomial and 4^{th} order polynomial, respectively. Hot wire is calibrated up to 100 ms^{-1} which is the maximum in-house nozzle velocity allowed. A fifth order polynomial fit is employed for the experimental results shown throughout the thesis.

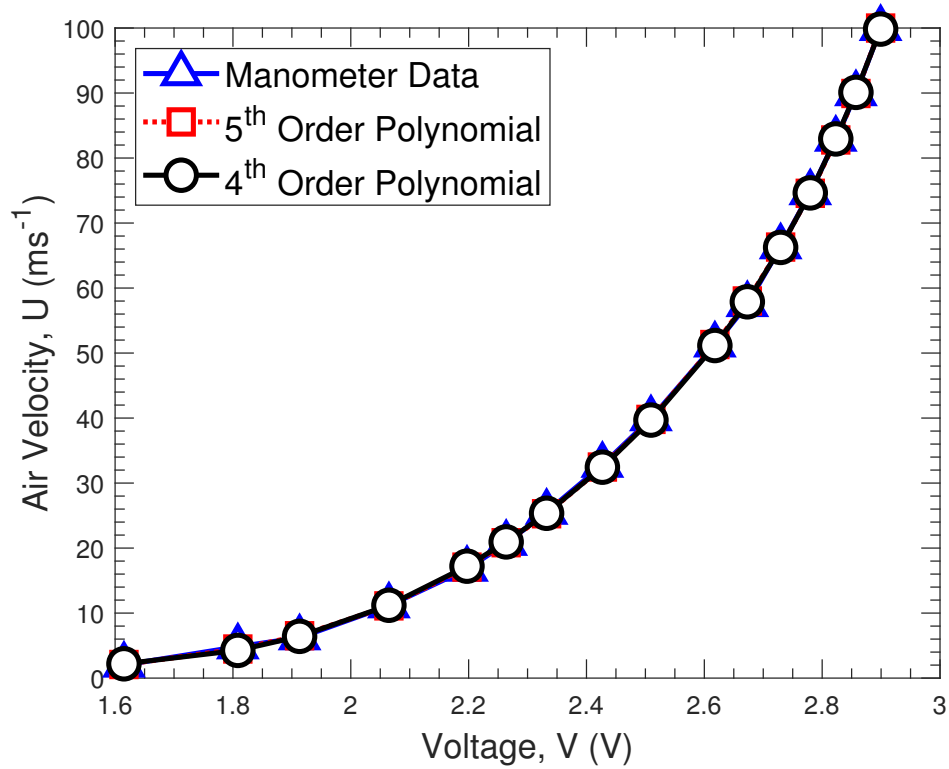


Figure 3.11: HWA Calibration Curve Fit with 4^{th} and 5^{th} Order Polynomials

It is identified that for the velocity measurement range of the miniCTA system used within this experimental campaign using either fifth and fourth order polynomials does make a significant difference.

The difference of the velocity at 99.9 ms^{-1} is 0.116 ms^{-1} (0.116%) and it is 0.470 ms^{-1} (0.47%) with 5^{th} and 4^{th} order polynomial fits, respectively.

The maximum sampling rate which a MiniCTA system can measure is 10,000 Hz at 50 ms^{-1} as indicated in the equipment manual [112]. The sampling rate increases with velocity and vice versa. Although an analogue-to-digital converter can digitize at higher sampling frequency (i.e., 40 kHz), the acquisition system does not measure the flow fluctuations at 40 kHz but only about 10

kHz [112].

The sampling time for each forcing frequency is 10 seconds to achieve 100,000 samples. The sampling frequency satisfies the Nyquist criteria (discussed in Section 3.1.2) given that maximum forcing frequency is 4,000 Hz in the tests. The equipment accuracy of the miniCTA hot-wire system is 3% together with the calibration and positioning error.

Figure 3.12 shows an example velocity signal for an actuation frequency (f) of 100 Hz. The signal is smoothed and peaks (marked with blue points) are detected so an ensemble average of peak values can be taken. The mean peak velocity is calculated by using this method throughout the thesis for the mean peak quantities.

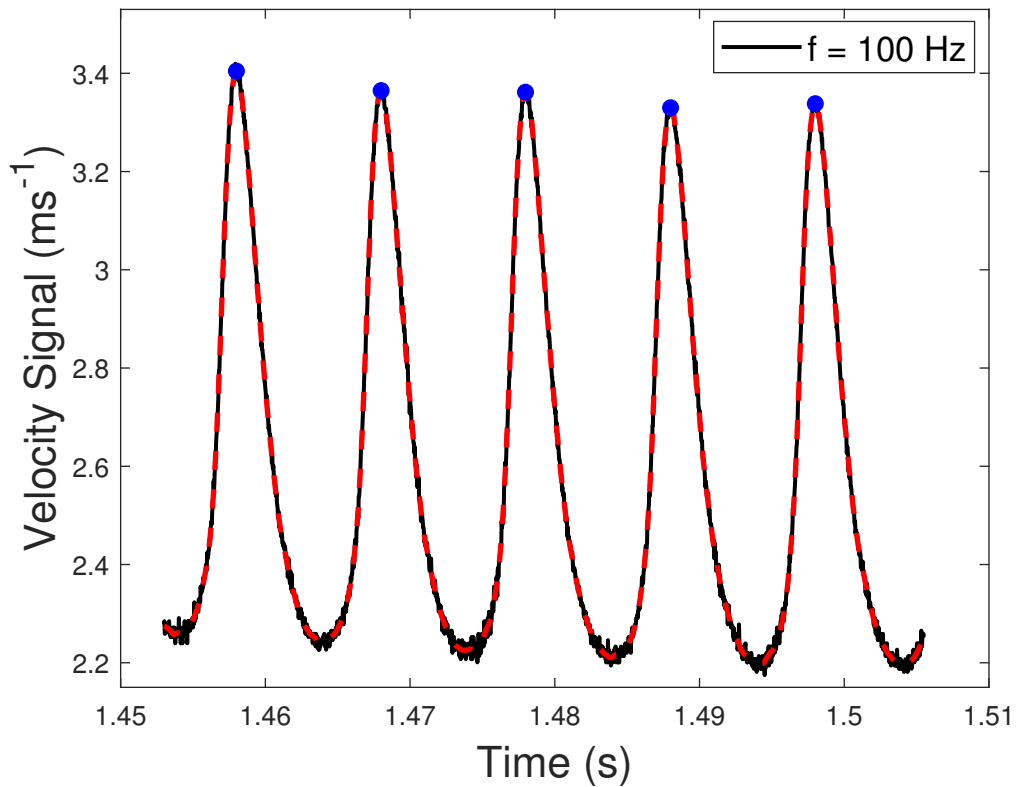


Figure 3.12: *A Sample Velocity Signal*

3.7 In-cavity Pressure Measurements

A pressure transducer is used to perform in-cavity pressure and jet velocity measurements.

A Meggit (formerly Endevco) pressure transducer, 8507C-5, is employed, with one of the smallest head diameters for research/industry applications. The cylinder-shaped head of the transducer has a diameter of 2.42 mm and can measure pressure in the range of 0 - 5 PSI (34.47 kPa). The sensor was factory calibrated, and its sensitivity was 77.81 mV/PSI (11.285 mV/kPa). The pressure transducer is connected to its 10V DC amplifier (Model 136) by a 9-pin connector. The output of the transducer is set to unity so the output is a direct measure of pressure (i.e., 10 V = 5 Psi).

In cavity pressure is measured by placing the probe sufficiently away from the orifice (i.e., $\approx 5d_o$). For the jet velocity measurements the transducer is placed to $0.1 d_o$ away from the orifice exit for consistency with the hot-wire measurements. Figure 3.13 presents the illustration of experimental setup of the pressure transducer with the hot-wire probe.

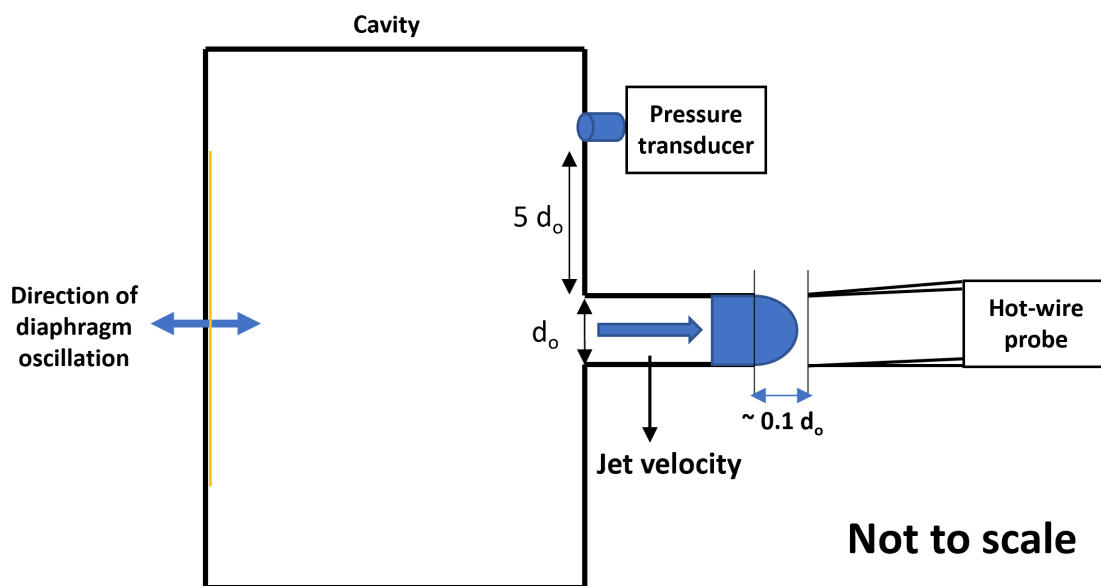


Figure 3.13: *Illustration of pressure transducer and hot-wire probe positioning and setup*

The resonance frequency of the 8507C-5 probe is 85kHz which is well above the sampling frequency. The DC amplifier unit is connected to a National Instruments DAQ (cDAQ-9171) board for data acquisition. The DAQ board have 4-channels and can sample up to 100k per second per channel. The amplifier is set up to send signals in PSI directly to the acquisition board. The

transducer accounts for the temperature drift automatically.

Figure 3.14 shows the pressure transducer and its amplification unit and it is taken from the manufacturer [116].



Figure 3.14: Meggit 8507C-5 Pressure Transducer and Model 136 DC Amplifier [116]

Figure 3.15 presents the CAD drawings of the probe.

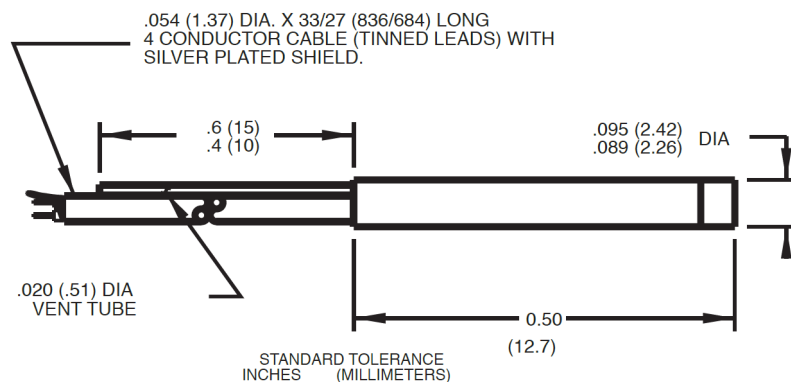


Figure 3.15: Meggit 8507C-5 Pressure Transducer Detailed Drawing [116]

Sampling rate is set as 40 kHz for both in-cavity pressure and jet velocity readings to satisfy Nyquist criteria (discussed in Section 3.1.2) given that the maximum actuation frequency is 4 kHz. The minimum sampling rate is 120,000 and maximum of 200,000. The jet velocity readings are mostly employed for high subsonic speeds where the supply voltage was high or the expected jet velocity was $+100 \text{ ms}^{-1}$.

The accuracy of the transducer is 11.285 mV/kPa which corresponds to ± 32.7 Pa at the full reading output of 10V and as a percentage error equals to $\pm 0.095\%$.

Figure 3.16 shows sample data for an in-cavity pressure reading. The x-axis of Figure 3.16 is normalised with the period of oscillation to reflect 3 full cycles.

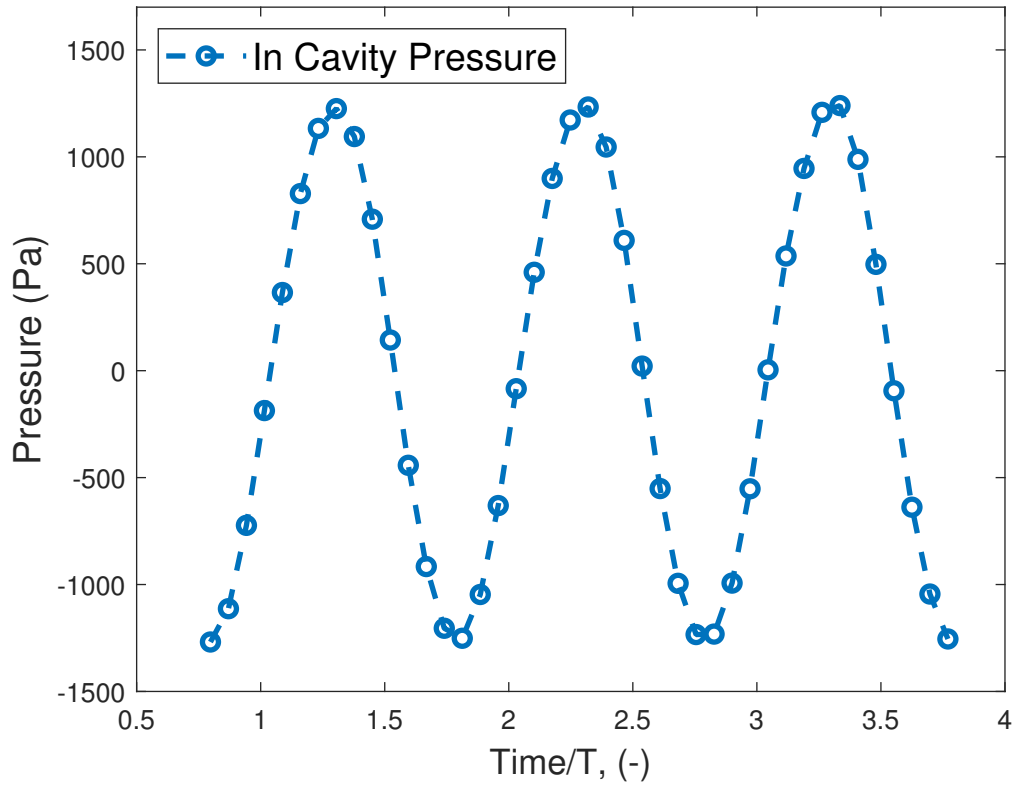


Figure 3.16: A Sample In-Cavity Pressure Data

3.8 Temperature Measurements

Temperature measurements during the operation of the actuators are taken both at the orifice exit and in the cavity.

K-type thermocouples (OMEGA) are connected to Keysight 34972A LXI data acquisition (i.e., data logger) which is controlled by a computer software (Agilent 34972A, USA). Three temperature measurements are taken simultaneously; room temperature, orifice exit and in-cavity temperature. The thermocouples gives a direct reading in degrees Celsius ($^{\circ}\text{C}$) with an uncertainty of $\pm 0.1\text{ }^{\circ}\text{C}$ ($\pm 0.5\%$ assuming 20°C is measured).

The temperatures for each actuation frequency and voltage is measured for 30 seconds where the actuator was switched off for the first 10 seconds and then switched on for 30 seconds and then stopped again. The sampling rate was 1

Hz.

Figure 3.17 shows sample temperature data, demonstrating the rationale behind the experiment. The presented data was captured during the commissioning trials of the experiment. The figure is included to give an insight into the temperature tests.

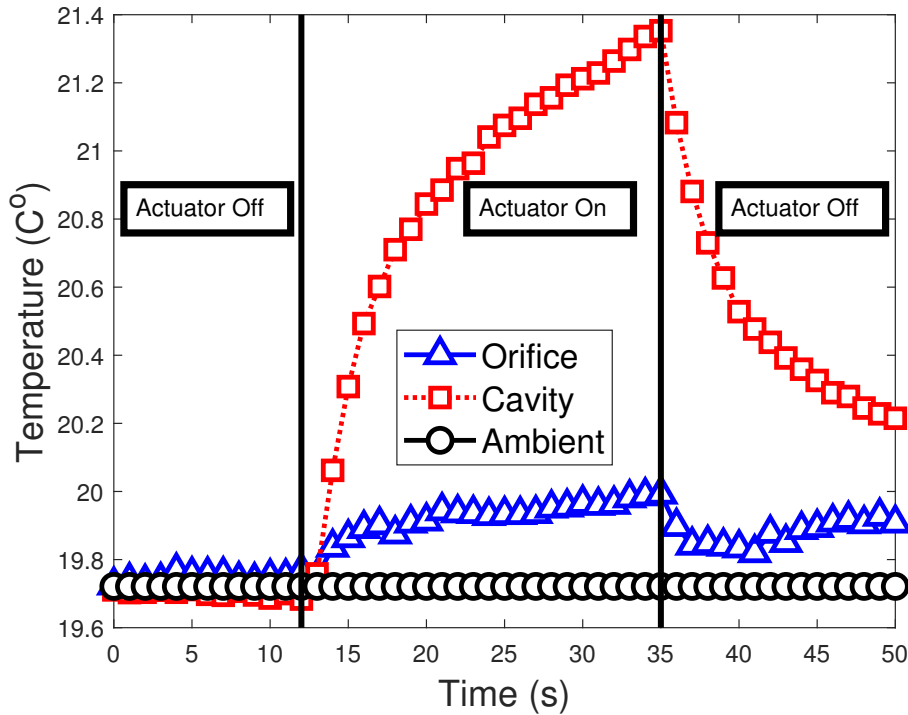


Figure 3.17: A Sample Data for Thermocouples Demonstrating the Operation

3.9 Discussion

For measuring the diaphragm displacement, the laser Doppler anemometer is a standard and high-accuracy technique. Nevertheless, the laser system used within the equipment was not up-to-date. Therefore, multiple simultaneous measurements could not be obtained. A single point measurement (at the diaphragm centre) is taken, but the software was not automated to target the centre. The centre was identified visually and targeted. Centre location was checked with a manual position sweep for the neighbouring points on the centre of the discs to identify the maximum deflection.

The jet-velocity is measured both with hot-wire anemometry and pressure

transducer depending on the velocity. The hot-wire probe is calibrated up to a maximum value of 100 ms^{-1} due to the in-house nozzle limitation and so it is recommended that the measured velocity should be less than 100 ms^{-1} [112]. The distance of the hot-wire from the orifice exit is aligned using a digital micrometre and is expected to introduce an uncertainty due to human error imparted by the eye alignment. The process used involves carefully moving the probe to the exit of the orifice and using a digital micrometre to measure the distance. The error due to misalignment is estimated to be $\pm 2.5\%$ for the similar orifice diameter and hot-wire probe in a selected study [65]. The hot-wire probe is very fragile and prone to fracture if it contacts with a surface. Therefore, the probe must be located over the orifice exit which ensures that the actual exit jet velocity is greater than the measured jet velocity.

Table 3.3 presents a summary of the measurement accuracy expressed as a percentage difference. The accuracy of the equipment used and measurements taken are similar to those of previously reported experimental studies [20, 58, 65, 81, 94, 117]

Table 3.3: Accuracy of the equipment used in the experimental campaign

Measurement-Units	Accuracy (\pm %)
Displacement (μm)	1.5
Hot-wire anemometry (ms^{-1})	3
Voltage Supply (V)	0.1
Current Draw (A)	1
Pressure (Pa)	0.1
Temperature ($^{\circ}C$)	0.5

No experimental flow visualisation method is used within the testing campaign. It was not possible to perform flow visualisation measurements experimentally, and where visualisations are needed modelling tools are used.

3.10 Summary

In this chapter, the experimental methods used throughout the thesis are described. Rather than having an experimental methods section, where an in-

house experiment is mentioned/used, all experimental methods are presented altogether.

A test bed for the clamping of the actuator is designed and manufactured to support both only-disc and SJA experiments. The design and manufacture of the clamping mechanism (i.e., groom-lip arrangement) and cavity-orifice arrangement is made within the existing capabilities of manufacturing laboratories. The piezoelectric diaphragms used are all off-the-shelf products except the custom-made single crystal piezoceramic actuators.

Two intrusive methods, hot-wire anemometry and pressure transducer and two non-intrusive methods, laser Doppler anemometry and power measurements, are employed within the experimental campaign. The experimental equipment and methods are selected based on the objectives of the study (defined in Chapter 1.3) which falls into two categories; evaluation of piezoelectric actuator's natural frequency and dynamic modal response, and performance of orifice-diaphragm next to (i.e., annexed) the piezoelectric actuator using different piezoceramic types and compositions.

The experimental techniques and apparatus are accurate and reliable to provide novel experimental data and to validate analytical/numerical models. The sampling rate and size are selected to satisfy the Nyquist criterion and to allow reliable data statistics (i.e., computation of the ensemble averaging and peak means) to be obtained. Exit jet velocity, in-cavity pressure, voltage supply and current draw are sampled simultaneously which made the experimental procedure more efficient (i.e., reducing testing time) and reliable (i.e., synchronous data is obtained).

Due to the soldering limitations (i.e., quality of soldering) the polycrystalline unimorph actuator could be tested up to the supply voltages of maximum 50

V_p . The single crystal unimorph actuators are limited to the supply voltage of 46 V as per its thickness and electric field; their tests are limited to $40 V_p$ to ensure avoiding fracture. The bimorph polycrystalline could go up to $80 V_p$. Therefore, the test overall campaign is limited by $40 V_p$ which is also important to minimize the induced noise and power consumption of SJA.

Piezoelectric diaphragm displacement measurements are used in Chapters 4-7. The hot-wire anemometry is used in Chapters 6-7 for the jet velocity measurements. In-cavity pressure and temperature measurements are used in Chapter 6. The voltage and current measurements are used in Chapter 7 to compute the electrical power consumption of the SJA.

Chapter 4

Theoretical Development and Experimental Validation of Natural Frequency and Mode Shape

4.1 Introduction

The modal analysis is the method used to analyse and characterise the vibration of linear structures and in this work it involved determining the natural frequencies, mode shapes and damping of the mechanical structure [47]. In the last two decades, there is a strong current interest in electro-mechanical transducers, in the form of sensors and actuators, in a number of areas in science and engineering, see e.g. [118]. In particular, there has been a wealth of research activities and publications on circular diaphragm-type piezoelectric laminates, which are widely used for sensing and actuation in micro-pumps, micro-motors, energy harvesters, acoustic devices, and other applications, e.g [38, 119, 120]. Significant progress has been made in the modelling and simulation of this type of devices, supported by substantial experimental validation programmes.

For a comprehensive understanding of piezoelectric diaphragm driven synthetic jet actuator, developing a sufficient knowledge regarding the frequency response of the diaphragm is vital. The highest output jet velocity is expected to occur around the first oscillation mode, called the mechanical resonance frequency. Within the fundamental frequency modes, the highest net transverse displacement is produced at the first mode [56]. Therefore, the investigation herein is limited to the first mode, which provides the highest net displacement that benefits the synthetic jet actuators performance. From a design perspective, accurate estimation the mechanical resonance frequency is essential for the actuator's sizing. In case of successful prediction of the natural frequency, SJA frequency response can be designed. It is likely that in a potential application, SJA would be driven at the natural frequency to get the maximum possible exit jet velocity. Therefore, being able to predict the natural frequency (and also the displacement) and to size the cavity-orifice arrangement accordingly, to maximise the exit jet velocity is important. Most research in the synthetic jet actuator field concentrates on the fluid dynamics aspects of the actuator or on obtaining high jet velocity. Therefore, the structural mechanics side of the SJA in which comes from the piezoelectric diaphragm is not studied in detail. The piezoelectric actuator can be classified as a thin plate as per the thickness to diameter ratio definition of Rao [121] which is $t/D < 0.05$ where t is the thickness of piezoceramic patch and the substrate layer and the D is the diameter of the substrate.

A typical circular plate piezoelectric actuator is a multi-layered axisymmetric laminate consisting of a stack with a passive substrate layer, one or more active piezoelectric layers, and other intermediate layers with electrodes and bonding film layers. In Figure 4.1, a simplified model is shown, with a substrate layer and one active layer of a smaller diameter on top of it. The piezoelectric actuator with a single layer of piezoceramic and substrate is called as unimorph piezoelectric actuator throughout the thesis. The actuator is usually supported around its circumference. When harmonic voltage potential is applied to the

upper active layer, its expansion (indicated in Fig. 4.1) and contraction due to piezoelectric effect [118] in radial and tangential directions induce a distributed bending moment along the circumference of the piezo-layer, causing periodic transverse displacements of the plate.

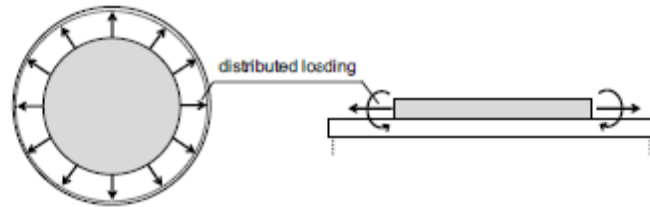


Figure 4.1: *Simplified model of a piezoelectric disc actuator with a substrate layer and single active upper layer*

In most applications of this type of actuators, the axisymmetric vibration modes are of importance, and this simplifies the analysis of their behaviour. Despite the significant research effort in the area of circular piezoelectric actuators [122, 123], it seems that some modelling aspects have not been adequately covered yet. When validating models against experimental measurements, the discrepancies between simulated results and experimental data tend to be attributed to uncertainties in clamping conditions and the level of energy dissipation, see e.g. [56, 57]. This is a sensible approach, however, there are some aspects in the modelling that seem to be poorly understood. It is thought that model refinements can bring the simulation results closer to the experimental data. For example, the sketch in Fig. 4.1 demonstrates that some in-plane extension-contraction is taking place in the plate structure in addition to plate bending. In the past, serious attempts were made to accommodate extensional behaviour in circular plates, by introducing models for coupled vibration [48], also in the static case, coupled extensional-flexural deformations were considered [54]. A recurring question in the studies that has not been resolved yet is about the role of the neutral plane (i.e., plane that does not undergo any extension) in bending for this type of laminate structures.

A specific objective of this chapter is to demonstrate that it is not necessary

to determine the position of a neutral plane in plate bending, as long as one consistently uses equations for coupled extensional-bending vibration, with reference to an arbitrary plane. Moreover, it is clear that for the configuration in Figure 4.1, there is no unique neutral plane for the stacked plate in the presence of asymmetric step changes in the plate thickness which implies that to obtain accurate natural frequency estimations coupled extensional-flexural vibrations might be important to account for. At the same time, the differences in vibrational behaviour for plates with symmetric and asymmetric steps is quantifiable by the adopted approach hereby.

The studies can be classified as static and dynamic cases where the actuation frequency is zero or very small when compared with the mechanical resonance in the static cases. The dynamic cases are high frequency forcing up to and beyond the first mechanical resonance.

The existing analytical models of circular piezoelectric plates for axisymmetric behaviour naturally split the solution into different regions along the plate radius and match state variables at boundaries with step changes in thickness and layers. This can lead to unnecessarily large systems of algebraic equations which may also possess ill-conditioned system matrices, see e.g. [54, 124] for the static case, or [56, 57] for a dynamic case example.

The analytical complexity in the dynamic case is increased further by the need to employ linear combinations of Bessel functions in the solution for each region. The aim of the present study is to obtain practically exact solutions by the use of the transfer matrix method [125], modified with the application of computed matrix exponentials [126], in order to avoid, or significantly reduce herewith the aforementioned analytical difficulties.

The rest of the chapter is organised as follows. Section 4.2 demonstrates and validates the lower order approach to identifying the resonance frequency of circular piezoelectric diaphragms. The classical plate transverse deflection equation which have solution involving with Bessel functions and transfer matrix method. The results obtained using the proposed analysis are compared with

selected experimental cases and results are presented to its potential for accurately modelling the experimental arrangement. Section 4.3 presents the equivalent theory with the uncoupled extensional-flexural deformation equations by employing matrix exponentials instead of Bessel functions. Experimental validation is presented just after the model presentation. Section 4.4 outlines the necessary equations of motion of a fully coupled extensional-flexural deformation of circular plates and presents them in a form suitable for the computation of transfer matrices; the emphasis is on the use of matrix exponentials. In Section 4.5, a special consideration of clamping is made based on the experimental results of a previously published work and in-house experimental cases. This is followed by a size sensitivity study in Section 4.6 to examine the effect of parameters on natural frequency. The discussions and overall conclusions are presented in Section 4.7 and Section 4.8, respectively.

4.2 Theory 1: Approach with CPT and TMM

An accurate estimation of the first mode of oscillation (i.e., fundamental frequency, f_m) of the piezoelectric actuator is challenging due to the complex structural dynamics of the step change in height (i.e., non-uniform thickness) of the plate which is usually overlooked in the field. The material properties of the passive plate and active plate are commonly not the same and the resultant plate is non-homogenous.

A theory is developed and applied using classical plate theory (CPT) to identify the fundamental frequency of Gomes [56]. The implementation method for the outer plate (i.e., only substrate) and inner plate (i.e., substrate and piezoelectric patch) was not accurate. The application of CPT is far from being a realistic physical foundation of the problem. The difference between fundamental frequency estimations and test results are addressed by introducing damping and clamping relaxation terms without a convincing explanation or physical background. The problems identified are listed below:

- The neutral plane of the composite section is in the middle of the substrate layer. This is not correct because the piezoelectric layer has a comparable stiffness to the substrate layer.
- The flexural stiffness of the substrate is assumed dominant and so the flexural stiffness of the piezoceramic layer is neglected.
- The overall flexural stiffness for the composite plate is assumed to be $D_s + D_p$ which is only valid if the neutral axis is in the middle of the substrate.
- By using the $D_p = \frac{E_p h_{pzt}^3}{12(1-\nu_p^2)}$, it is assumed that the substrate and piezoceramic layer are rigidly attached and there is no flexible bonding between them.

This section and the developed theoretical framework involves classical deflection equation for a circular plate with small deflections (i.e., classical plate theory or Kirchhoff theory) integrated with the transfer matrix method (TMM) formulation to account for the step-change in the thickness (i.e., piezoelectric patch). The problems identified in Gomes's study [56] are also addressed.

The specific objective of this section is to provide an accurate and easy-to-implement theory to calculate the fundamental frequency of the piezoelectric actuator. The relative simplicity of the model, when compared to the more advanced composite plate theory presented in Section 4.4 comes with the compromise of a slightly larger fundamental frequency difference between theory and experiment.

The developed theory should give an estimation which is accurate enough for the preliminary design of piezoelectric actuator in various applications including but not limited to piezoelectrical diaphragm driven synthetic jet actuator, micro-fluidic pump drivers or piezoelectric sensors.

The assumptions of the classical plate theory (CPT) theory presented are as follows [121]:

- Thickness to diameter ratio of the plate is in the order of $\approx O(0.03)$ [127].
- Transverse deflection compared to the thickness of the plate is small.
- The middle plane of the plate does not experience in-plane distortion [121].
- Shear deformation effects are neglected. Therefore, it is assumed, even after bending plane sections stays normal to the mid-surface.
- Transverse normal stress is small compared to the other stress components. Also, the transverse normal strain can be neglected under transverse loading.

The known limitations of the classical plate theory for transverse deflections are:

- Takes into account only the bending of the plate but not the axial forces/moments.
- Neutral plane is fixed, and there is a jump in neutral plane between the substrate and piezoceramic layer, which is not calculated.
- Radial displacement is assumed to be negligible.

4.2.1 Theory Derivation of CPT with TMM

The formulation starts with the classical deflection equation (Eq. 4.1) of the circular plates. Equation (4.1) is the statement of the equilibrium for linear bending in isotropic plate deforming in z-direction [121]. The derivation of Eq. 4.1 can be found in Reddy's book Chapter 5.2.1 [127]. Herein the formulation and corresponding derivation of equilibrium equations starts with an axisymmetric homogenous plate for the substrate plate. Then by using the transfer matrix method, the equations for a composite plate with attached

piezoceramic patch is obtained which provides an asymmetric step change in thickness.

$$D\nabla^4 w + \rho h \frac{\partial^2 w}{\partial t^2} = 0 \quad (4.1)$$

Where transverse displacement of the plate under load is w and D is the flexural rigidity. Density and thickness of the plate is represented by ρ and h , respectively. Also, ∇^2 is the Laplacian operator in polar coordinates and $\nabla^4 = \nabla^2 \nabla^2$.

$$\nabla^2 = \frac{\partial^2}{\partial r^2} + \frac{1}{r} \frac{\partial}{\partial r} + \frac{1}{r^2} \frac{\partial^2}{\partial \theta^2} \quad (4.2)$$

The flexural rigidity (D) is a measure of transverse deflection/bending and expressed as:

$$D = \frac{Eh^3}{12(1 - \nu^2)} \quad (4.3)$$

The displacement variable, w , can be expressed in polar coordinates space and time with the following equation, by separating time and space dependency

$$w(r, \theta, t) = W(r, \theta).T(t) \quad (4.4)$$

Assuming free vibrations for the axisymmetric plate, the motion can be expressed as using the angular frequency of vibrations ω

$$w = W \cos(\omega t) \quad (4.5)$$

Substituting Eq. (4.5) into Eq. (4.1) and re-arranging gives:

$$(\nabla^4 - k^4)W = 0 \quad (4.6)$$

Where k^4 is a non-dimensional wave parameter given by:

$$k^4 = \frac{\rho h \omega^2}{D} \quad (4.7)$$

Eq. (4.6) can be factorised as:

$$(\nabla^2 + k^2)(\nabla^2 - k^2)W = 0 \quad (4.8)$$

Assuming independence of θ (i.e., axisymmetric vibration), one may split the displacement vector as well by $W(r, \theta) = R(r) \cdot \Phi(\theta)$. The complete solution of Eq. 4.8 is the superimposition of the solutions of the following equations, $W(r) = W_1(r) + W_2(r)$ [128]:

$$\nabla^2 W_1 + k^2 W_1 = \frac{\partial^2 W_1}{\partial r^2} + \frac{1}{r} \frac{\partial W_1}{\partial r} + k^2 W_1 = 0 \quad (4.9a)$$

$$\nabla^2 W_2 - k^2 W_2 = \frac{\partial^2 W_2}{\partial r^2} + \frac{1}{r} \frac{\partial W_2}{\partial r} - k^2 W_2 = 0 \quad (4.9b)$$

The solutions of the Eq. 4.9a and Eq. 4.9b are given in the following forms of Bessel functions. J_0 and Y_0 is the Bessel functions of the zero order of the first and second kind, respectively.

$$W_1(r) = C_1 J_0(kr) + C_2 Y_0(kr) \quad (4.10a)$$

$$W_2(r) = C_3 I_0(kr) + C_4 K_0(kr) \quad (4.10b)$$

Where, I_0 and K_0 is the modified (hyperbolic) Bessel functions of the zero order of the first and second kind, respectively [128]. The full solution of the superimposed differential equations equals to the following expression [128].

$$W(r) = C_1 Y_0(r) + C_2 Y_0(kr) + C_3 I_0(kr) + C_4 K_0(kr) \quad (4.11)$$

Differentiation of Eq. 4.11 would result in the state variables such as the first derivative, Ψ , the second derivative is the radial bending moment M_r and the third derivative shear force, Q_r .

The mathematical operations regarding the differentiations of the Bessel functions are omitted to reduce the complexity of the chapter.

$$\Psi(r) = \frac{dW(r)}{dr} = -C_1 k J_1(kr) - C_2 k Y_1(kr) + C_3 I_1(kr) - C_4 k K_1(kr) \quad (4.12)$$

The bending moment have the following equation form

$$M_r(r) = D \left(\frac{d^2 W(r)}{dr^2} + \frac{\nu}{r} \frac{dW}{dr} \right) \quad (4.13)$$

From Eq. 4.10a:

$$\frac{\nu}{r} \frac{dW_1}{dr} = -\nu \frac{d^2 W_1}{dr^2} - \nu k^2 W_1 \quad (4.14)$$

From Eq. 4.10b:

$$\frac{\nu}{r} \frac{dW_2}{dr} = -\nu \frac{d^2 W_2}{dr^2} - \nu k^2 W_2 \quad (4.15)$$

Taking the derivatives and substituting Equations 4.14 and 4.15 into Equation 4.13 results in the following expression for the bending moment:

$$\begin{aligned} M_r(r) = & \frac{1}{2} D k^2 [(1 + \nu) J_0 - (1 - \nu) J_2] C_1 + \frac{1}{2} D K^2 [(1 + \nu) Y_0 \\ & - (1 - \nu) Y_2] C_2 - \frac{1}{2} D K^2 [(1 + \nu) I_0 + (1 - \nu) I_2] C_3 \\ & - \frac{1}{2} D K^2 [(1 + \nu) K_0 + (1 - \nu) K_2] C_4 \quad (4.16) \end{aligned}$$

The fourth state variable shear force, $Q_r(r)$, has the following form:

$$Q_r(r) = -D \frac{d}{dr} \left(\frac{d^2 W}{dr^2} + \frac{1}{r} \frac{dW}{dr} \right) = -D \left[\frac{d}{dr} \left(\frac{d^2 W_1}{dr^2} + \frac{1}{r} \frac{dW_1}{dr} \right) + \left(\frac{d^2 W_2}{dr^2} + \frac{1}{r} \frac{dW_2}{dr} \right) \right] \quad (4.17)$$

By using the equations 4.10a and 4.10b the $\frac{d}{dr}$ terms can be simplified to $-k^2 W_1$ and $-k^2 W_2$ for second order W_1 and W_2 terms respectively.

$$Q_r(r) = -Dk^3 (C_1 J_1 + C_2 Y_1 + C_3 I_1 - C_4 K_1) \quad (4.18)$$

The state variables which constitutes the state vector (displacement, spatial derivative of displacement, bending moment, shear force) is derived and it can be shown that the state variables at radius r are:

$$\begin{bmatrix} W(r) \\ \Psi(r) \\ M_r(r) \\ Q_r(r) \end{bmatrix} = \begin{bmatrix} A(r) \end{bmatrix} \cdot \begin{bmatrix} C_1 \\ C_2 \\ C_3 \\ C_4 \end{bmatrix}$$

$$\begin{bmatrix} A(r) \end{bmatrix} = \begin{bmatrix} J_0(kr) & Y_0(kr) & I_0(kr) & K_0(kr) \\ -kJ_1(kr) & -kY_1(kr) & kI_1(kr) & -kK_1(kr) \\ A_{31}(r) & A_{32}(r) & A_{33}(r) & A_{34}(r) \\ -Dk^3 J_1(kr) & -Dk^3 Y_1(kr) & -Dk^3 I_1(kr) & Dk^3 K_1(kr) \end{bmatrix}$$

The variables in the matrix are given below:

$$A_{31} = \frac{1}{2}Dk^2[(1 + \nu)J_0 - (1 - \nu)J_2]$$

$$A_{32} = \frac{1}{2}Dk^2[(1 + \nu)Y_0 - (1 - \nu)Y_2]$$

$$A_{33} = -\frac{1}{2}Dk^2[(1 + \nu)I_0 + (1 - \nu)I_2]$$

$$A_{34} = -\frac{1}{2}Dk^2[(1 + \nu)K_0 + (1 - \nu)K_2]$$

Now the matrices can be multiplied and iterated numerically to obtain the solution. The matrix multiplication of the two transfer matrices for the inner and outer plates govern the asymmetric step change in the thickness of the plate. Two transfer matrices are created one without the piezo (i.e., only substrate) then another with the piezo and substrate.

$$z_i(r) = A(r_i)\mathbf{C} \quad (4.19a)$$

$$z_{i+1}(r) = A(r_{i+1})\mathbf{C} \quad (4.19b)$$

If Equation 4.19a is inverted and substituted into equation 4.19b, the following can be obtained. This is a necessary step and it is important to note, the constants \mathbf{C} are not linked with the state variable.

$$\mathbf{C} = A^{-1}(r_i)z_i \quad (4.20a)$$

$$z_{i+1}(r) = A(r_{i+1})A^{-1}(r_i)z_i \quad (4.20b)$$

The boundary conditions should be prescribed to obtain the particular solution. For the centre of a circular plate, $Y_0(0)$ & $K_0(0)$ are infinite. Therefore, the constants become:

$$C_2 = C_4 = 0 \quad (4.21)$$

and the state vector reduces to:

$$z_{(r=0)} = \begin{bmatrix} W(r) \\ 0 \\ M_r(r) \\ 0 \end{bmatrix} \quad (4.22)$$

At the clamped ends, the deflection and its derivative is zero, so:

$$z_{(r=a)} = \begin{bmatrix} 0 \\ 0 \\ M \\ Q_r \end{bmatrix} \quad (4.23)$$

The determinant of the combined matrix with the appropriate boundary conditions should be equal to zero at the resonant frequencies.

Two transfer matrices are required for both piezoceramic patch and substrate. The overall transfer matrix is $U = U_s U_b$ where U_s is the transfer matrix for the piezoceramic patch and U_b is the transfer matrix for the substrate. The

transfer matrices for piezoceramic patch and substrate would have the same base elements for the 4×4 elements. However, the boundary conditions and numerical values are different.

For a homogenous plate with uniform thickness, the neutral plane is located at the half of the thickness, $z_d = t/2$ [127]. For the composite plate with variable thickness, the position of the neutral plane (z_d) does not simply lie in the half of the thickness. For a composite section the position of the neutral axis can be calculated by the following [129]:

$$z_d = \frac{E_{pzt}t_{pzt}^2 + E_s t_s^2 + 2E_s t_s t_{pzt}}{2(E_{pzt}t_{pzt} + E_s t_s)} \quad (4.24)$$

The plate bending stiffness (D_{bs}) is calculated with the following equation:

$$D_{bs} = \frac{E_{pzt}t_{pzt}^3}{12} + \frac{E_b t_s^3}{12} + E_{pzt}t_{pzt}(z_d - \frac{t_{pzt}}{2})^2 + E_s t_{pzt}(t_{pzt} + \frac{t_s}{2} - z_d)^2 \quad (4.25)$$

Figure 4.2 (diaphragm used corresponds to the Case 1 in Table 4.1) is included to give a visual understanding behind the calculation of frequency of oscillation modes. The x-intercepts are the resonant frequencies which are shown with circular markers. There are multiple resonant modes, however the main interest is the first mode only which also promotes highest net displacement as previously mentioned.

4.2.2 Results and Experimental Validation

In this section, the model results are compared with in-house experimental measurements for two selected cases of piezoelectric diaphragms. The information regarding the experimental procedure and apparatus can be found in Section 3.4.

Figure 4.3 shows the geometry of a unimorph piezoelectric diaphragm with the

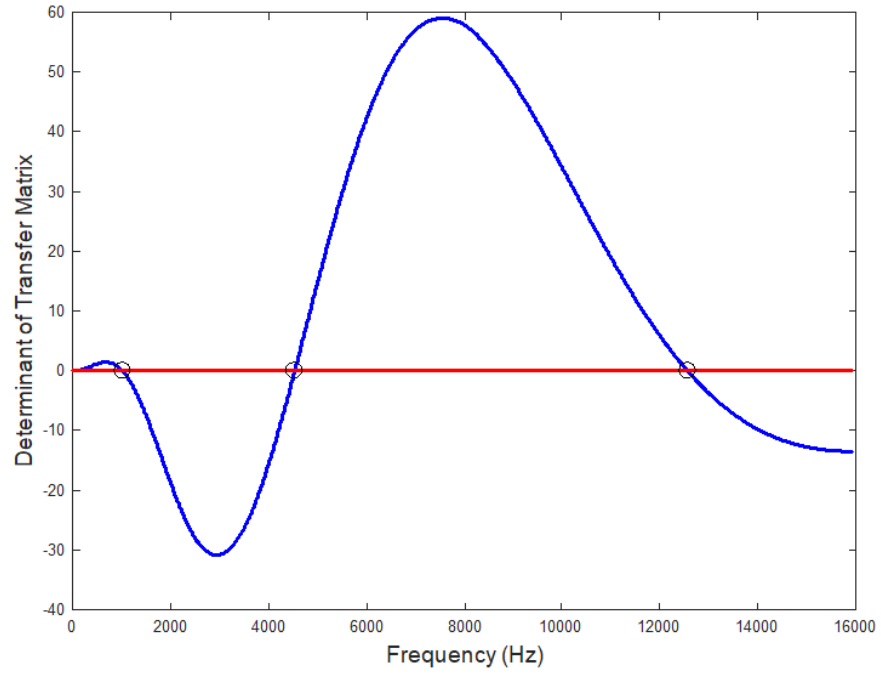


Figure 4.2: Natural Frequency determination with TMM

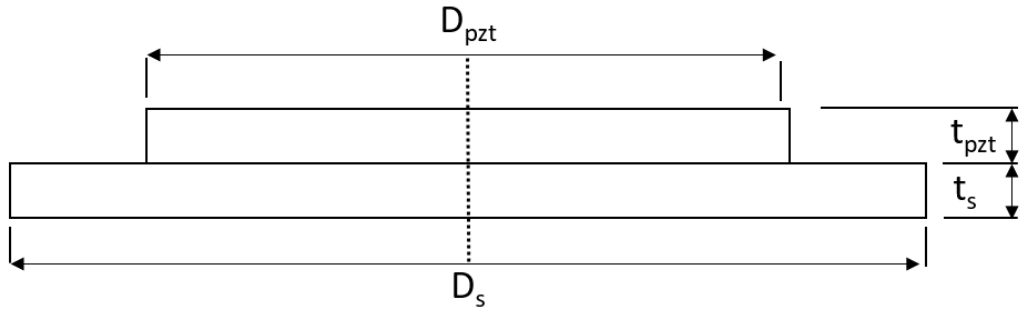


Figure 4.3: Configuration for the clamped stepped circular plate - with axisymmetric step

notation used for the validation cases.

The dimensions of the test cases are presented in Table 4.1. The last column shows the total thickness ratio ($t_{pzt} + t_s$) to the outer diameter of substrate, D_s . Both discs have a ratio of $t_{pzt} + t_s/D_s < 0.05$, are therefore classified as thin plates.

Table 4.1: Test cases for the theory validation

Case	D_s (mm)	D_{pzt} (mm)	t_{pzt} (mm)	t_s (mm)	$\frac{t_{pzt}+t_s}{D_s}$
1	27	19.8	0.13	0.15	0.010
2	27	19.8	0.23	0.22	0.015

Table 4.2 presents the material properties of the brass substrate and PZT-5A patch. The density (ρ), Young's modulus (E) and Poisson's ratio (ν) are presented. The material properties are provided by the manufacturer of the piezoelectric actuators, OBO Pro2 [107].

Table 4.2: Material Properties of the Piezoelectric Actuator

	ρ (kg/m^3)	E (Pa)	ν (-)
Brass (Substrate)	8500	110	0.34
Piezoelectric Patch (PZT-5A)	7500	60	0.32

Table 4.3 presents the resonance frequencies computed by the theory and detected by the experiments. The model results are computed for clamped conditions and the theory underestimated the experimental natural frequency in both cases. The percentage difference between experimental results and theory is 3.2% and 6.6% for Case 1 and Case 2, respectively. The difference in the estimation implies that the current inaccuracy cannot simply be explained by the error tolerance of the material properties (i.e., density or Young's modulus). The reported accuracy is acceptable for a rough approximation of the natural frequency. Nevertheless, it can be improved by taking into account extensional-flexural rigidity and lateral displacement of the diaphragm.

Table 4.3: Theoretical versus experimental results for the diaphragm's natural frequency

Case	f_m - Resonance frequency (Hz)		% Difference
	Theory	Experiment Unc. = $\pm 13Hz$	
1	1695	1751	3.2
2	2603	2787	6.6

4.3 Theory 2: Approach with Matrix Exponentials and TMM

The classical plate theory (CPT) application with transfer matrix method yielded acceptable result but there are differences between theory and exper-

iment which it would be desirable to reduce. The approach demonstrated in section 4.2 does not include any empirical terms and can be classified as a fully analytical model. Some of the constants in the equations lack physical meaning such as the wave parameter (k). Therefore, an alternative approach using the composite laminar plate theory for coupled extensional-flexural motion is developed as an alternative. The Bessel functions arising in the CPT model, can be written as matrix exponentials to remove those constants and reduce numerical effort. The rationale and the state vector assembly of the theory presented in this section is consistent with the theory presented in Section 4.2. Therefore, the natural frequency results computed by this theory and the previous one should be similar. This section can be considered to be a transition from the basic theory to a more advanced theory to introduce the reader to the matrix exponentials and discretization.

4.3.1 Formulation and Derivation of the Model

The equations of motion for free extensional-flexural axisymmetric vibration are written by employing stress force and moment resultants, and inertia terms [48]:

$$\frac{\partial n_r}{\partial r} + \frac{n_r - n_\theta}{r} = I_0 \frac{\partial^2 u}{\partial t^2} - I_1 \frac{\partial^3 w}{\partial t^2 \partial r} \quad (4.26)$$

$$\frac{\partial s_r}{\partial r} + \frac{s_r}{r} = I_0 \frac{\partial^2 w}{\partial t^2} \quad (4.27)$$

$$\frac{\partial m_r}{\partial r} + \frac{m_r - m_\theta}{r} - s_r = I_1 \frac{\partial^2 u}{\partial t^2} - I_2 \frac{\partial^3 w}{\partial t^2 \partial r}. \quad (4.28)$$

The assumptions of ignoring radial (n_r) and circumferential (n_θ) normal force resultant and lateral displacement (u) effectively decouples the system of equa-

tions. The set of equations reduces to:

$$\frac{\partial s_r}{\partial r} + \frac{s_r}{r} = I_0 \frac{\partial^2 w}{\partial t^2} \quad (4.29)$$

$$\frac{\partial m_r}{\partial r} + \frac{m_r - m_\theta}{r} - s_r = -I_2 \frac{\partial^3 w}{\partial t^2 \partial r} \quad (4.30)$$

Equations 4.29 and 4.30 can be manipulated to have a 4x4 transfer matrix in the form of the equations presented in 4.2.2. The stress resultants are dependent on the strain and curvature distributions in the plate. In axisymmetric plate bending with respect to the z -axis, it is convenient to introduce the change of displacement slope in radial direction ϕ in the reference plane $Ar\theta$, see Fig. 4.4(b). This dependent variable is related to the plate deflection w by

$$\phi = -\frac{\partial w}{\partial r} \quad (4.31)$$

and is also expressed in steady-state harmonic vibration by

$$\phi(r, t) = \Phi(r) \exp(i\omega t)$$

For steady-state harmonic vibration with frequency ω , each dependent variable, say $f(r, t)$, in the solutions of Eqs. (4.47-4.49) is represented in the form

$$f(r, t) = F(r) \exp(i\omega t) \quad (4.32)$$

with an amplitude function $F(r)$ governed by a system of ordinary differential equations after substitutions into (4.29-4.30).

From plate stress-strain relationships, the expressions for the internal force and moment resultants are readily obtained [48] for full set of coupled equations. The reduced set of equations become:

$$\begin{bmatrix} M_r \\ M_\theta \end{bmatrix} = \begin{bmatrix} K_0 & \nu K_1 \\ \nu K_1 & K_2 \end{bmatrix} \begin{bmatrix} \Phi/r \\ d\Phi/dr \end{bmatrix}, \quad (4.33)$$

where for the constants K_0 , K_1 and K_2 one has

$$\begin{aligned} K_0 &= \int_{z_1}^{z_2} \hat{E} dz = \hat{E}(z_2 - z_1) = \hat{E}h, \quad I_0 = \int_{z_1}^{z_2} \rho dz = \rho(z_2 - z_1) = \rho h, \\ K_1 &= \int_{z_1}^{z_2} \hat{E} z dz = \frac{1}{2} \hat{E}(z_2^2 - z_1^2), \quad I_1 = \int_{z_1}^{z_2} \rho z dz = \frac{1}{2} \rho(z_2^2 - z_1^2), \\ K_2 &= \int_{z_1}^{z_2} \hat{E} z^2 dz = \frac{1}{3} \hat{E}(z_2^3 - z_1^3), \quad I_2 = \int_{z_1}^{z_2} \rho z^2 dz = \frac{1}{3} \rho(z_2^3 - z_1^3), \end{aligned} \quad (4.34)$$

together with the integrals for the inertia constants, appearing in Eqs. (4.29-4.30). See Fig. 4.4(b) for the definition of the lower and upper bounds of integration and note that the plate thickness is designated by h .

From Hooke's law for isotropic material under axisymmetric conditions

$$\hat{E} = \frac{E}{1 - \nu^2}.$$

After the manipulation using Eq. 4.32, Equations 4.29 and 4.30 becomes as:

$$\frac{dS_r}{dr} + \frac{S_r}{r} = I_0 \omega^2 W \quad (4.35)$$

$$\frac{dM_r}{dr} + \frac{M_r}{r} - \frac{M_\theta}{r} - S_r = -I_2 \omega^2 \frac{dW}{dr} = I_2 \omega^2 \phi \quad (4.36)$$

By using Eq. 4.33, two more equations can be obtained to replace terms $\frac{d\Phi}{dr}$ and M_θ .

By taking the inverse of matrix in Eq. 4.33 the equation can be re-written as

$$\begin{bmatrix} \Phi/r \\ d\Phi/dr \end{bmatrix} = \begin{bmatrix} K_0 & \nu K_1 \\ \nu K_1 & K_2 \end{bmatrix}^{-1} \begin{bmatrix} M_r \\ M_\theta \end{bmatrix}, \quad (4.37)$$

From Eq. 4.37, two equations can be obtained:

$$\frac{d\Phi}{dr} = \frac{-\nu}{r}\Phi + \frac{1}{K_2}M_r \quad (4.38)$$

$$M_\theta = \frac{1-\nu^2}{r}K_2\Phi + \nu M_r \quad (4.39)$$

Eq. 4.38 can be used as a governing differential equation and Eq. 4.39 can be used to replace M_θ in Eq. 4.36.

4.3.2 Computational Model

This section presents the computational procedure and implementation strategy. The equations can be written in the form of $x' = Ax$ using the following ordinary differential equations. The prime ($'$), denotes d/dr .

$$\frac{dW}{dr} = -\Phi \quad (4.40)$$

$$\frac{d\Phi}{dr} = \frac{-\nu}{r}\Phi + \frac{1}{K_2}M_r \quad (4.41)$$

$$\frac{dM_r}{dr} = \left(\frac{1-\nu^2}{r^2}K_2 - I_2\omega^2\right)\Phi + \frac{1}{r}(\nu - 1)M_r + S_r \quad (4.42)$$

$$\frac{dS_r}{dr} = -I_0\omega^2W - \frac{1}{r}S_r \quad (4.43)$$

In the state-matrix form the derivatives can be expressed as:

$$\begin{bmatrix} W' \\ \Phi' \\ M_r' \\ S_r' \end{bmatrix} = \begin{bmatrix} 0 & -1 & 0 & 0 \\ 0 & -\frac{\nu}{r} & \frac{1}{K_2} & 0 \\ 0 & CK_2 - I_2\omega^2 & \frac{1}{r}(\nu - 1) & 1 \\ -I_0\omega^2 & 0 & 0 & \frac{-1}{r} \end{bmatrix} \begin{bmatrix} W \\ \Phi \\ M_r \\ S_r \end{bmatrix} \quad (4.44)$$

Where $C = \frac{1-\nu^2}{r^2}$.

The plates are discretised by separating them into outer region (only substrate layer) and inner region (substrate layer + piezoceramic layer) with 160 and 480 grid elements of uniform size, respectively.

It is a classical result [130] that for a homogeneous linear system of ordinary differential equations, with a vector of states $\mathbf{y}(r)$ and a constant system matrix \mathbf{A} , the unique solution to

$$\mathbf{y}' = \mathbf{A}\mathbf{y}, \quad \mathbf{y}(0) = \mathbf{y}_0 \quad (4.45)$$

is given by

$$\mathbf{y}(r) = \exp(\mathbf{A}r)\mathbf{y}_0. \quad (4.46)$$

From Eq. (4.46), it is clear that the transfer matrix \mathbf{T} is essentially the matrix exponential of $\mathbf{A}r$, when \mathbf{A} is a constant matrix.

4.3.3 Experimental Validation and Comparison with the CPT Model

Table 4.4 compares the results obtained by the theory and experiments. The selected test cases are identical those in Section 4.2.2.

Table 4.4: Theoretical versus experimental results for the diaphragm's natural frequency

	f_m - Resonance frequency (Hz)		% Difference
Case	Theory	Experiment Unc. = $\pm 13Hz$	
1	1698	1751	3.03
2	2607	2787	6.46

Table 4.5 compares the results obtained by the theories presented in this section and the previous one. The results obtained are very similar to those computed by the theory derived using Bessel functions which is presented in Section 4.2.

Table 4.5: Theoretical versus experimental results for the diaphragm's natural frequency

	f_m - Resonance frequency (Hz)		% Difference
Case	Theory 1 (Section 4.2)	Theory 2 (Section 4.3)	
1	1695	1698	0.18
2	2603	2607	0.15

4.4 Theory 3: Composite Plate Theory with Steps

The Kirchhoff's theory for a circular plate with Rayleigh rotatory inertia effect for a multi-layered heterogeneous circular plate is employed herewith. The assumptions are: (i) the material in each plate layer is elastic and mechanically isotropic; (ii) the strains and deflections are small, within the remit of linear theory of elasticity; (iii) only motions with displacements symmetrically distributed about the axis perpendicular to the circular plate through its centre are considered: an axisymmetric circular plate; (iv) the layers are perfectly bonded to each other; in addition, (v) the piezoelectric material is crystalline and poled along the normal to the plate surface; therefore, the plate in-plane strains are electro-mechanically transversely isotropic [118].

4.4.1 Theoretical model and computational procedure

The coupled extensional and flexural vibrations of a thin plate made of homogeneous and isotropic elastic material, with Young's modulus E , Poisson's ratio ν , and density ρ , are investigated by Kirchhoff-Love plate theory. Only a brief outline of the equations of motion is given in order to explain the model adopted for the analysis and to clarify the steps in the computational procedure. Details of the derivations of the equations of motion for circular plates can be found in standard textbooks, like e.g. [121, 131], and the references provided below. Since the investigation is motivated by applications to electro-mechanical actuators and sensors, only motions symmetric about an axis perpendicular to the plate centre are of interest.

With reference to Fig. 4.4, the axis of symmetry is the z -axis, the displacements $u(r, t)$, in the radial r -direction in a reference plane $Ar\theta$, and the deflections $w(r, t)$, in the z -direction, are functions of the position r and the time t . As a result of the axisymmetric behaviour assumption, the state variables of the

plate, like displacements, rotations, and internal forces and moments are all independent of the θ -coordinate.

Note that the reference plane is not in general coinciding with the middle plane of the plate, and u is dependent on the position of the reference plane $Ar\theta$, while w is not, based on the usual assumptions in thin plate theory.

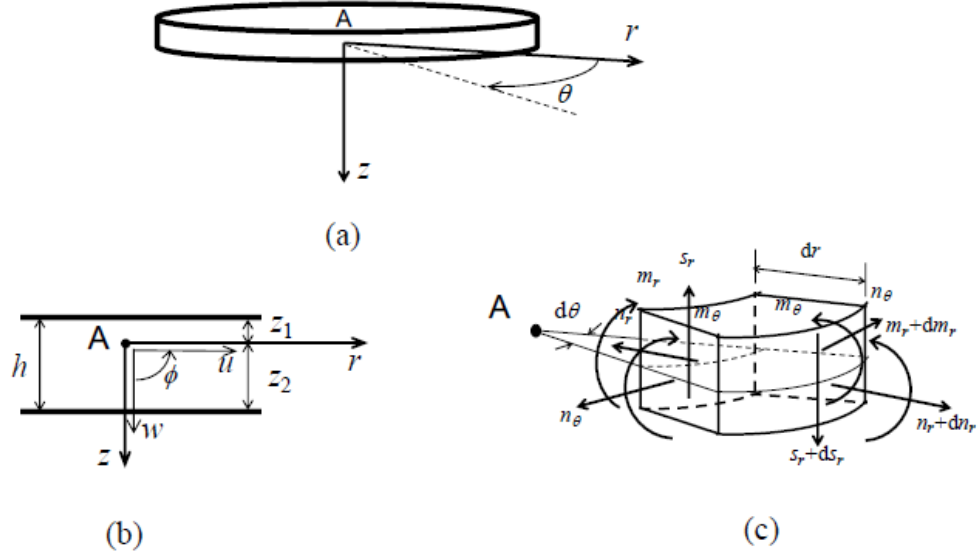


Figure 4.4: Convention for a coordinate frame and signs of internal forces in the circular plate model. (a) Plate coordinate frame. (b) Plate vertical cross-section. Note: the coordinate system $Ar\theta$ does not coincide with the plate mid-plane, in general. (c) Positive sign conventions for internal plate forces and moments.

The equations of motion for free extensional-flexural axisymmetric vibration [48] are written by employing stress force and moment resultants, and inertia terms:

$$\frac{\partial n_r}{\partial r} + \frac{n_r - n_\theta}{r} = I_0 \frac{\partial^2 u}{\partial t^2} - I_1 \frac{\partial^3 w}{\partial t^2 \partial r} \quad (4.47)$$

$$\frac{\partial s_r}{\partial r} + \frac{s_r}{r} = I_0 \frac{\partial^2 w}{\partial t^2} \quad (4.48)$$

$$\frac{\partial m_r}{\partial r} + \frac{m_r - m_\theta}{r} - s_r = I_1 \frac{\partial^2 u}{\partial t^2} - I_2 \frac{\partial^3 w}{\partial t^2 \partial r}. \quad (4.49)$$

Here, n_r and n_θ are radial and circumferential normal force resultants, m_r and m_θ are radial and circumferential moment resultants, and s_r is transverse

shear force resultant, see also Fig. 4.4(c) for the positive sign conventions. The inertia terms on the right-hand sides of Eqs. (4.47-4.49) contain cross-section constants I_0 , I_1 and I_2 .

With reference to Fig. 4.4, assume a laminate circular plate with layers of equal radii, and an arbitrary reference plane $Ar\theta$, for $z = 0$. The radial displacement u at any point with spatial coordinates (r, θ, z) is independent of θ , due to axisymmetry, and a linear function of the z -coordinate

$$u(r, z, t) = u_0(r, t) + z\phi, \quad (4.50)$$

where u_0 is the radial displacement at the reference plane, for $z = 0$, and ϕ is the displacement slope in radial direction. Whereas, the transverse displacement

$$w(r, z, t) \equiv w(r, t), \quad (4.51)$$

is independent of z . One can write for the displacement slope

$$\phi = -\frac{\partial w}{\partial r}. \quad (4.52)$$

The circumferential displacements vanish identically for axisymmetric plate motion.

The elastic strain components at the reference plane are expressed by

$$\varepsilon_r^0 = \frac{\partial u_0}{\partial r} \quad \text{and} \quad \varepsilon_\theta^0 = \frac{u_0}{r}, \quad (4.53)$$

while for the plate curvature, one has the following relationships

$$\kappa_r = -\frac{\partial^2 w}{\partial r^2} = \frac{\partial \phi}{\partial r} \quad \text{and} \quad \kappa_\theta = -\frac{1}{r} \frac{\partial w}{\partial r} = \frac{\phi}{r}. \quad (4.54)$$

Since Classical Laminate Plate Theory (CLPT) assumes linear strain distribution across the thickness, the transversely isotropic elastic strain in a plane, parallel to the reference plane with points of the same coordinate z , is described

in terms of the elastic strain at the reference plane, the plate curvature, and the elastic strain caused by the application of electric field E_f across an active layer

$$\begin{bmatrix} \varepsilon_r \\ \varepsilon_\theta \end{bmatrix} = \begin{bmatrix} \varepsilon_r^0 \\ \varepsilon_\theta^0 \end{bmatrix} + z \begin{bmatrix} \kappa_r \\ \kappa_\theta \end{bmatrix} - d_{31} E_f \begin{bmatrix} 1 \\ 1 \end{bmatrix}. \quad (4.55)$$

Here, d_{31} is the transverse piezoelectric constant at the plate point for the layer, which can be set to a zero value for a material layer without piezoelectric properties.

In each layer, from Hooke's Law for isotropic material in polar coordinates, the stresses in radial and circumferential directions are expressed by the strain through the corresponding Young's modulus E and Poisson's ratio ν in the form

$$\begin{bmatrix} \sigma_r \\ \sigma_\theta \end{bmatrix} = \frac{E}{1-\nu^2} \begin{bmatrix} 1 & \nu \\ \nu & 1 \end{bmatrix} \begin{bmatrix} \varepsilon_r \\ \varepsilon_\theta \end{bmatrix}. \quad (4.56)$$

It is assumed that the k -th layer in the laminate is located between a plane with coordinates $z = z_{k-1}$ and $z = z_k$ in the plate thickness direction. The internal forces and moments, acting on the plate are obtained by integrating the stresses through each layer thickness of the plate, and then summing up the resulting forces and moments over all available, assume n , layers, or

$$\begin{bmatrix} n_r \\ n_\theta \end{bmatrix} = \sum_{k=1}^n \int_{z_{k-1}}^{z_k} \begin{bmatrix} \sigma_r \\ \sigma_\theta \end{bmatrix} dz \quad \text{and} \quad \begin{bmatrix} m_r \\ m_\theta \end{bmatrix} = \sum_{k=1}^n \int_{z_{k-1}}^{z_k} \begin{bmatrix} \sigma_r \\ \sigma_\theta \end{bmatrix} z dz. \quad (4.57)$$

From CLPT stress-strain relationships, the expressions for the internal force and moment resultants are readily obtained [48, 54]

$$\begin{bmatrix} n_r \\ n_\theta \\ m_r \\ m_\theta \end{bmatrix} = \begin{bmatrix} A_{rr} & A_{r\theta} & B_{rr} & B_{r\theta} \\ A_{\theta r} & A_{\theta\theta} & B_{\theta r} & B_{\theta\theta} \\ B_{rr} & B_{r\theta} & D_{rr} & D_{r\theta} \\ B_{\theta r} & B_{\theta\theta} & D_{\theta r} & D_{\theta\theta} \end{bmatrix} \begin{bmatrix} \varepsilon_r^0 \\ \varepsilon_\theta^0 \\ \kappa_r \\ \kappa_\theta \end{bmatrix} - \begin{bmatrix} n_r^p \\ n_\theta^p \\ m_r^p \\ m_\theta^p \end{bmatrix}. \quad (4.58)$$

The constants A_{ij} ($i, j = r$ and θ) represent extensional stiffness, B_{ij} coupled extensional-bending stiffness, and D_{ij} bending stiffness, respectively. They can be expressed, by also considering symmetry relations, as follows

$$A_{rr} = A_{\theta\theta} = \sum_{k=1}^n \frac{E_k}{1 - \nu_k^2} (z_k - z_{k-1}), \quad (4.59)$$

$$A_{r\theta} = A_{\theta r} = \sum_{k=1}^n \frac{\nu_k E_k}{1 - \nu_k^2} (z_k - z_{k-1}), \quad (4.60)$$

$$B_{rr} = B_{\theta\theta} = \frac{1}{2} \sum_{k=1}^n \frac{E_k}{1 - \nu_k^2} (z_k^2 - z_{k-1}^2), \quad (4.61)$$

$$B_{r\theta} = B_{\theta r} = \frac{1}{2} \sum_{k=1}^n \frac{\nu_k E_k}{1 - \nu_k^2} (z_k^2 - z_{k-1}^2), \quad (4.62)$$

$$D_{rr} = D_{\theta\theta} = \frac{1}{3} \sum_{k=1}^n \frac{E_k}{1 - \nu_k^2} (z_k^3 - z_{k-1}^3), \quad (4.63)$$

$$D_{r\theta} = D_{\theta r} = \frac{1}{3} \sum_{k=1}^n \frac{\nu_k E_k}{1 - \nu_k^2} (z_k^3 - z_{k-1}^3), \quad (4.64)$$

where the index k in E_k and ν_k stands for the materials properties in the k -th layer of the laminate.

In Eq. (4.58), the radial and circumferential piezoelectric force resultants n_r^P and n_θ^P , and the radial and circumferential piezoelectric moment resultants m_r^P and m_θ^P , generated in the piezoelectric layers under potential (voltage) difference between the upper and lower layer surfaces, when the plate is fully constrained, are expressed by:

$$n_r^P = n_\theta^P = \sum_{k=1}^n \frac{E_k}{1 - \nu_k} E_f^k d_{31}^k (z_k - z_{k-1}), \quad (4.65)$$

$$m_r^P = m_\theta^P = \frac{1}{2} \sum_{k=1}^n \frac{E_k}{1 - \nu_k} E_f^k d_{31}^k (z_k^2 - z_{k-1}^2), \quad (4.66)$$

where the superscript k in E_f^k and d_{31}^k stands for the applied external electric field across the layer and the piezoelectric constant in the k -th layer of the laminate. It is clear that the contributions to forces and moments from non-

piezoelectric layers is zero, since $d_{31}^k = 0$ for such layers.

At this point, it is important to explain how the results obtained from Eqs. (4.65-4.66) radial and circumferential piezoelectric force and moment resultants are used in practical calculations. Bearing in mind the nature of strain and stress caused by the piezoelectric effect, the force and moment resultants are internal and do appear directly in the equations of motion because they balance themselves. They are in a self-equilibrium state and appear as equivalent external forces only at plate cross-sections when the piezoelectric layer changes thickness or has discontinuities. For example, with reference to the model schematically shown in Fig. 4.1, it is necessary to apply an equivalent external radial force n_r^P and moment m_r^P at the transition, in the radial direction, from a cross-section containing the active layer to a plate cross-section made of substrate material only. Also, note that n_r^P and m_r^P are mechanically distributed along the circumference at the step change in plate thickness.

The cross-section constants I_0 , I_1 and I_2 in the inertia terms on the right-hand sides of Eqs. (4.47-4.49) can be readily evaluated from

$$I_0 = \sum_{k=1}^n \rho_k (z_k - z_{k-1}), \quad (4.67)$$

$$I_1 = \frac{1}{2} \sum_{k=1}^n \rho_k (z_k^2 - z_{k-1}^2), \quad (4.68)$$

$$I_2 = \frac{1}{3} \sum_{k=1}^n \rho_k (z_k^3 - z_{k-1}^3), \quad (4.69)$$

where ρ_k is the mass density in the k -th layer of the laminate.

4.4.2 Derivation of the governing system of six first-order ODEs

For steady-state harmonic vibration with frequency ω , each dependent variable, say $f(r, t)$, in the solutions of Eqs. (4.47-4.49) is represented in the form

$$f(r, t) = F(r) \exp(i\omega t) \quad (4.70)$$

with an amplitude function $F(r)$ governed by a system of ordinary differential equations after substitutions into (4.29-4.30). Capital letters are in use, from now on throughout the derivation, for the amplitudes of the dependent variables U , W , N_r , N_θ , M_r , M_θ , and S_r , which are all functions of the radial position r , only.

The stress resultants are dependent on the strain and curvature distributions in the plate. In symmetric plate bending with respect to the z -axis, it is convenient to introduce the change of displacement slope in radial direction ϕ in the reference plane $Ar\theta$, see Fig. 4.4(b). This dependent variable is related to the plate deflection w by

$$\phi = -\frac{\partial w}{\partial r} \quad (4.71)$$

and is also expressed in steady-state harmonic vibration by

$$\phi(r, t) = \Phi(r) \exp(i\omega t).$$

For steady-state harmonic vibration with frequency ω , the internal force variables can be expressed by

$$\begin{bmatrix} N_r \\ N_\theta \\ M_r \\ M_\theta \end{bmatrix} = \begin{bmatrix} A_{rr} & A_{r\theta} & B_{rr} & B_{r\theta} \\ A_{\theta r} & A_{\theta\theta} & B_{\theta r} & B_{\theta\theta} \\ B_{rr} & B_{r\theta} & D_{rr} & D_{r\theta} \\ B_{\theta r} & B_{\theta\theta} & D_{\theta r} & D_{\theta\theta} \end{bmatrix} \begin{bmatrix} dU_0/dr \\ U_0/r \\ d\Phi/dr \\ \Phi/r \end{bmatrix}. \quad (4.72)$$

From the first and third scalar equations in Eq. (4.72), one has

$$\begin{aligned}
 \begin{bmatrix} dU_0/dr \\ d\Phi/dr \end{bmatrix} &= -\frac{1}{r} \begin{bmatrix} A_{rr} & B_{rr} \\ B_{rr} & D_{rr} \end{bmatrix}^{-1} \begin{bmatrix} A_{r\theta} & B_{r\theta} \\ B_{r\theta} & D_{r\theta} \end{bmatrix} \begin{bmatrix} U_0 \\ \Phi \end{bmatrix} \\
 &+ \begin{bmatrix} A_{rr} & B_{rr} \\ B_{rr} & D_{rr} \end{bmatrix}^{-1} \begin{bmatrix} N_r \\ M_r \end{bmatrix} \\
 &= -\frac{1}{r} \mathbf{M}^1 \begin{bmatrix} U_0 \\ \Phi \end{bmatrix} + \mathbf{M}^2 \begin{bmatrix} N_r \\ M_r \end{bmatrix}, \tag{4.73}
 \end{aligned}$$

with the derived matrices \mathbf{M}^1 and \mathbf{M}^2 independent of the radial coordinate r , and only dependent on the constants in the matrix linking force and kinematics variables in Eq. (4.72). Obviously, the last two matrices are related by

$$\mathbf{M}^1 = \mathbf{M}^2 \begin{bmatrix} A_{r\theta} & B_{r\theta} \\ B_{r\theta} & D_{r\theta} \end{bmatrix}.$$

The two differential equations in (4.73) directly provide the first and fourth equations in the overall system of six first-order ordinary differential equations, for the composite plate under coupled radial and bending vibration.

With Eqs. (4.47) and (4.49) under consideration, one needs the following two expressions combining force variables, for the second and fifth equations in the overall system of six first-order ordinary differential equations

$$\begin{aligned}
-\frac{1}{r} \begin{bmatrix} N_r - N_\theta \\ M_r - M_\theta \end{bmatrix} &= -\frac{1}{r} \begin{bmatrix} A_{rr} - A_{\theta r} & A_{r\theta} - A_{\theta\theta} & B_{rr} - B_{\theta r} & B_{r\theta} - B_{\theta\theta} \\ B_{rr} - B_{\theta r} & B_{r\theta} - B_{\theta\theta} & D_{rr} - D_{\theta r} & D_{r\theta} - D_{\theta\theta} \end{bmatrix} \begin{bmatrix} dU_0/dr \\ U_0/r \\ d\Phi/dr \\ \Phi/r \end{bmatrix} \\
&= -\frac{1}{r} \begin{bmatrix} p & -p & q & -q \\ q & -q & s & -s \end{bmatrix} \begin{bmatrix} dU_0/dr \\ U_0/r \\ d\Phi/dr \\ \Phi/r \end{bmatrix} \\
&= -\frac{1}{r} \begin{bmatrix} p & q \\ q & s \end{bmatrix} \begin{bmatrix} dU_0/dr \\ d\Phi/dr \end{bmatrix} + \frac{1}{r^2} \begin{bmatrix} p & q \\ q & s \end{bmatrix} \begin{bmatrix} U_0 \\ \Phi \end{bmatrix}. \tag{4.74}
\end{aligned}$$

After a substitution of the derivatives of U_0 and Φ with respect to r in the right-hand side of (4.74), from Eq. (4.73), one has

$$\begin{aligned}
-\frac{1}{r} \begin{bmatrix} N_r - N_\theta \\ M_r - M_\theta \end{bmatrix} &= \frac{1}{r^2} \begin{bmatrix} p & q \\ q & s \end{bmatrix} \left(\begin{bmatrix} A_{rr} & B_{rr} \\ B_{rr} & D_{rr} \end{bmatrix}^{-1} \begin{bmatrix} A_{r\theta} & B_{r\theta} \\ B_{r\theta} & D_{r\theta} \end{bmatrix} + \mathbf{I} \right) \begin{bmatrix} U_0 \\ \Phi \end{bmatrix} \\
&= -\frac{1}{r} \begin{bmatrix} p & q \\ q & s \end{bmatrix} \begin{bmatrix} A_{rr} & B_{rr} \\ B_{rr} & D_{rr} \end{bmatrix}^{-1} \begin{bmatrix} N_r \\ M_r \end{bmatrix} \\
&= \frac{1}{r^2} \mathbf{M}^3 \begin{bmatrix} U_0 \\ \Phi \end{bmatrix} - \frac{1}{r} \mathbf{M}^4 \begin{bmatrix} N_r \\ M_r \end{bmatrix}, \tag{4.75}
\end{aligned}$$

with \mathbf{I} as the unit 2×2 matrix. The derived matrices \mathbf{M}^3 and \mathbf{M}^4 are independent of the radial coordinate r again, and only dependent on the cross-section constants in the matrix linking force and kinematics variables in Eq. (4.72). The following relationships between the \mathbf{M} -matrices in (4.73) and (4.75) exist

$$\mathbf{M}^3 = \begin{bmatrix} p & q \\ q & s \end{bmatrix} (\mathbf{M}^1 + \mathbf{I}) \quad \text{and} \quad \mathbf{M}^4 = \begin{bmatrix} p & q \\ q & s \end{bmatrix} \mathbf{M}^2.$$

Before presenting the final transfer matrix \mathbf{A} , an appropriate pre-step of the derivation would be to present the boundary conditions of the plates. For a linear system of sixth order, there is a multitude of ways to select state variables and represent it by an equivalent system of first order differential equations, governed by different but equivalent system matrices \mathbf{A} . It is advantageous to consider six state variables in a vector \mathbf{y} directly linked with variables that appear in the boundary conditions for the plate. By using the boundary conditions, half of the values in the vector of the dependent variable \mathbf{y} are defined at $r = 0$, and half of the values in \mathbf{y} are prescribed at the plate circumference, for $r = a$, where a is the plate radius. Due to symmetry with respect to the z -axis, the boundary conditions at point A in Fig. 4.4, for $r = 0$, are always in the form

$$U(0) = 0, \quad \Phi(0) = 0, \quad \text{and} \quad S_r(0) = 0. \quad (4.76)$$

At the plate circumference, clamping

$$U(a) = 0, \quad W(a) = 0, \quad \text{and} \quad \Phi(a) = 0, \quad (4.77)$$

and simply-supported conditions

$$U(a) = 0, \quad W(a) = 0, \quad \text{and} \quad M_r(a) = 0, \quad (4.78)$$

are commonly used, or in some cases a simple support that allows extensional displacement

$$N_r(a) = 0, \quad W(a) = 0, \quad \text{and} \quad M_r(a) = 0. \quad (4.79)$$

For this reason, it is appropriate to have the following vector of state variables dependent on r

$$\mathbf{y} = [y_1 \ y_2 \ y_3 \ y_4 \ y_5 \ y_6]^T = [U \ N_r \ W \ \Phi \ M_r \ S_r]^T. \quad (4.80)$$

The required system of differential equations is obtained by expressing the derivatives

$$\mathbf{y}' = [y'_1 \ y'_2 \ y'_3 \ y'_4 \ y'_5 \ y'_6]^T = [U' \ N'_r \ W' \ \Phi' \ M'_r \ S'_r]^T, \quad (4.81)$$

in terms of the chosen state variables themselves. Here, the prime denotes $d(\)/dr$.

With reference to Eqs. (4.80-4.81), the system matrix linking the vector with derivatives of state variables to the vector of state variables is written in the form

$$\mathbf{A}(r) = \begin{bmatrix} -\frac{1}{r}M_{11}^1 & M_{11}^2 & 0 & -\frac{1}{r}M_{12}^1 & M_{12}^2 & 0 \\ \frac{1}{r^2}M_{11}^3 - I_0\omega^2 & -\frac{1}{r}M_{11}^4 & 0 & \frac{1}{r^2}M_{12}^3 - I_1\omega^2 & -\frac{1}{r}M_{12}^4 & 0 \\ 0 & 0 & 0 & -1 & 0 & 0 \\ -\frac{1}{r}M_{21}^1 & M_{21}^2 & 0 & -\frac{1}{r}M_{22}^1 & M_{22}^2 & 0 \\ \frac{1}{r^2}M_{21}^3 - I_1\omega^2 & -\frac{1}{r}M_{21}^4 & 0 & \frac{1}{r^2}M_{22}^3 - I_2\omega^2 & -\frac{1}{r}M_{22}^4 & 1 \\ 0 & 0 & -I_0\omega^2 & 0 & 0 & -\frac{1}{r} \end{bmatrix}. \quad (4.82)$$

Note that the third equation (third row in Eq. (4.82)) in the overall system of six differential equations comes from Eq. (4.71), while the sixth equation (sixth row in Eq. (4.82)) is based on Eq. (4.49).

4.4.3 Transfer matrix formulation

In the context of one-dimensional mechanical systems, the transfer matrix method [125] gives a relationship between state variables, like displacements and forces, at two different points on a structure. If one knows all variables at one point and assembles them into a vector \mathbf{y}_0 , a matrix multiplication of this vector by a transfer matrix $\mathbf{T}(\mathbf{r})$ yields the vector $\mathbf{y}(\mathbf{r})$ with all variables at

the other point

$$\mathbf{y}(r) = \mathbf{T}(r)\mathbf{y}_0 \quad (4.83)$$

In practice, only some of the variables are initially known at each point from boundary conditions. For a well-defined problem, it is possible to find all the variables at any point by using compatibility of displacements and force balance conditions at the boundaries.

As described in Section 4.3.2, for a homogeneous linear system of ordinary differential equations, with a vector of states $\mathbf{y}(r)$ and a constant system matrix \mathbf{A} , the unique solution to [130]

$$\mathbf{y}(r) = \exp(\mathbf{A}r)\mathbf{y}_0. \quad (4.84)$$

From Eq. (4.83), it is clear that the transfer matrix \mathbf{T} is essentially the matrix exponential of $\mathbf{A}r$, when \mathbf{A} is a constant matrix. If one has a direct and efficient computational procedure for the matrix exponential of $\mathbf{A}r$, a solution is readily achieved. Nowadays, the computation of functions of matrices is a mature subject in numerical mathematics [126] with a wealth of software implementations in commercial packages and open-source problem-solving environment. For example, the matrix exponential is available as standard function routines in MATLAB [115] and other commercial packages. One can argue in favour of closed-form analytical solutions but at the same time she/he must accept the fact that the modern matrix exponential solvers are practically providing exact solutions. Recently, this idea has been already discussed for beam vibrations [132]. Here, matrix exponentials are employed in the developed computational procedure with some additional considerations to reflect the dependence of the system matrix on r .

As shown in Eq. (4.82), it is necessary for circular plate vibration to deal with a more general system matrix \mathbf{A} , a function of the independent variable in the system of ordinary differential equations. This is a specific example of a linear system with variable coefficients, sometimes called in the mathematics

literature a non-autonomous linear problem (when time is the independent variable). It is leading to a problem formulation

$$\mathbf{y}'(r) = \mathbf{A}(r)\mathbf{A}(r), \quad 0 < r \leq a, \quad \mathbf{y}(0) = \mathbf{y}_0 \quad (4.85)$$

Naturally, a discretization scheme lends itself for dividing the variation range of r into relatively small intervals and assuming a constant system matrix \mathbf{A} at each interval. For n intervals of equal length Δr , or for $a = n\Delta r$, it is possible to employ a constant matrix computed from Eq. (4.82) at the mid-point in each interval. 100 and 50 intervals are used for the outer and inner plates, respectively. The effect of interval spacing (or number) is checked and is found insignificant. Bearing in mind Eq. (4.84), the state variables at each interval boundary are then computed from

$$\mathbf{y}_{j+1} = \mathbf{T}_{j+1}\mathbf{y}_j = \exp\{\mathbf{A}[(j + 1/2)\Delta r]\Delta r\}\mathbf{y}_j, \quad \text{for } j = 0, 1, \dots, n - 1. \quad (4.86)$$

The overall transfer matrix $\mathbf{T}(a)$ between the state variables at $r = 0$ and $r = a$ is obtained from

$$\mathbf{y}(a) = \mathbf{y}_n = \mathbf{T}(a)\mathbf{y}_0 = \mathbf{T}_n \dots \mathbf{T}_2 \mathbf{T}_1 \mathbf{y}_0. \quad (4.87)$$

The idea behind this approach for solving linear differential equations with variable coefficients was clearly presented in Chapter 7 of the pioneering monograph on matrix methods in dynamics [133], published at a time when numerical and symbolic computations by hand were still the norm. The method is also the simplest possible representation of the so-called Magnus integrator within the larger class of exponential integrators, see e.g. [134]. The properties of these integrators are carefully studied in numerical mathematics. The formal convergence and error bounds results are not necessary here because the computations are validated against experimental results for circular plates in Section 4.4.5. The transfer matrix method was applied to the pure bending

vibration of non-uniform circular plates by the application of a Runge-Kutta method in [50].

The 6×6 transfer matrix $\mathbf{T}(a)$ is used to obtain a frequency equation for finding the natural frequencies and the corresponding mode shapes. The boundary conditions at the centre of plate and at the circumference need to be considered. For axisymmetric vibration, at the centre of plate, based on Eq. (4.76), $y_1 = y_4 = y_6 = 0$ with y_2, y_3 and y_5 being generally non-zero at $r = 0$. Assuming a clamped plate at the circumference, one has from Eq. (4.77) $y_1 = y_3 = y_4 = 0$ with y_2, y_5 and y_6 non-zero at $r = a$. This information can be neatly incorporated into the solution process by transforming the overall transfer matrix for the plate into a 3×3 matrix \mathbf{T}_p by pre- and post-multiplication with two matrices based on the boundary conditions

$$\mathbf{T}_p = \mathbf{R} \mathbf{T}(a) \mathbf{L}, \quad (4.88)$$

where in this particular clamped plate case

$$\mathbf{L} = \begin{bmatrix} 0 & 0 & 0 \\ 1 & 0 & 0 \\ 0 & 1 & 0 \\ 0 & 0 & 0 \\ 0 & 0 & 1 \\ 0 & 0 & 0 \end{bmatrix} \quad \text{and} \quad \mathbf{R} = \begin{bmatrix} 1 & 0 & 0 & 0 & 0 & 0 \\ 0 & 0 & 1 & 0 & 0 & 0 \\ 0 & 0 & 0 & 1 & 0 & 0 \end{bmatrix}. \quad (4.89)$$

For free vibration analysis, the condition $\det(\mathbf{T}_p) = 0$ is a frequency equation for finding the natural frequencies. For each calculated natural frequency ω , a corresponding mode shape is obtained from a homogeneous system of algebraic equations with matrix \mathbf{T}_p , see [125] for more details. Standard root finding algorithms for transcendental functions enable the calculation of natural frequencies. Plates with other boundary conditions, like the conditions in (4.78-4.79), can be dealt with in a similar manner by appropriate \mathbf{L} and \mathbf{R}

matrices.

Up to this point, it has been assumed that a plate with a uniform thickness is considered. As stated in the Introduction, the focus of this investigation is on plates with step changes in the thickness. In particular, asymmetric step changes are of interest where the coupled extensional-flexural equations of motion are necessary for accurate calculations. In general, the transfer matrices from each uniform plate segment are multiplied in a specific order to obtain the overall transfer matrix for a plate with steps. Moreover, if a single reference frame is used across the whole stepped plate, the matching of state variables at the steps is automatically performed by multiplying the two transfer matrices for uniform plate segments at both sides of the step. Some more details of the computational procedure are given in Section 4.4.4 when natural frequency and mode shape calculations are explained.

4.4.4 Natural frequencies and mode shapes calculation

With reference to Subsection 4.4.3 and Fig. 4.3, the circular plate is divided into two regions: an inner region starting from the centre of plate to the step change in its thickness, $0 \leq r \leq a_1$; and, an outer region with $a_1 < r \leq a_0$. The plate has two layers in the inner region, passive and active (piezoelectric), while in the other region it is made of a single material without piezoelectric properties. By computing the cross-section constants according to the equations developed in 4.4.2, and by following the computation procedure in Subsection 4.4.3, one can obtain the transfer matrix T_1 for the inner region and the transfer matrix T_0 for the outer region, correspondingly. It is convenient to select a common reference plane, with e.g. $z = 0$, for both regions in the calculation of cross-section properties. In this way, the continuity of state variables at the boundary between the inner and outer regions is preserved by a simple multiplication of the corresponding transfer matrices. The overall

transfer matrix for the circular plate is then computed from

$$\mathbf{T} = \mathbf{T}_o(a_o) \cdot \mathbf{T}_i(a_i). \quad (4.90)$$

For a clamped plate, the determinant condition on the 3×3 matrix \mathbf{T}_p , obtained from (4.88), is employed in order to find the natural frequencies. Again, for each computed natural frequency ω , one corresponding mode shape can be obtained from a homogeneous system of algebraic equations with system matrix \mathbf{T}_p . As usual with mode shapes of vibration, one of the non-zero state variables at the centre of plate, y_2 , y_3 or z_5 , can be chosen arbitrarily, with the remaining variables computed from two of the available three equations. In most cases, it is preferable to have $y_3 = 1$, which corresponds to a unit displacement at the centre of plate.

It should be pointed out that both resonances and anti-resonances can be obtained by this method when using piezoelectric materials properties corresponding to close-circuited or open-circuited conditions [135] between the surfaces of the active layer.

4.4.5 Experimental Validation and Comparison with Previous Theory

Table 4.6 compares the results obtained by the theory and experiments. The selected test cases are identical to Section 4.2.2. The results obtained have shown a notable improvement towards matching the experimental natural frequency. Table 4.6 compares the results obtained by the theories presented in this section and the previous one with the experimental natural frequency.

Table 4.6: Theoretical versus experimental results for the diaphragm's natural frequency

Case	Theory 3 (Section 4.4)		Theory 2 (Section 4.3)		Experiment (Hz)
	f_m (Hz)	% Difference	f_m (Hz)	% Difference	f_m (Hz)
1	1780	1.66	1698	3.03	1751
2	2768	0.68	2607	6.46	2787

4.5 Clamping Effect on Natural Frequency: A Special Consideration

In Section 4.2, it is mentioned that Gomes studied the classical plate theory for piezoelectric composite actuator of various dimensions [56] without using transfer matrix method. The study made various assumptions that are difficult to justify. Also, it had problems regarding the implementation of equations including:

- Position of the neutral axis assumed at the middle of the substrate plate.
- The flexural stiffness for the piezoelectric layer (D_{pzt}) is assumed to be same as the substrate layer.
- Overall flexural stiffness in the composite section of the actuator is assumed to obey $D_s + D_{pzt}$, which is only right if the neutral axis is in the middle of the substrate.

Figure 4.5 is reproduced to demonstrate the geometry of a unimorph piezoelectric diaphragm with the notation used for the validation cases.

The details of the diaphragm composition such as diameter/thickness of active and passive layers, and material properties are obtained from the thesis of Gomes [65].

The dimensions of the test cases are presented in Table 4.8. The last column shows the total thickness ratio ($t_{pzt} + t_s$) to the outer diameter of substrate,

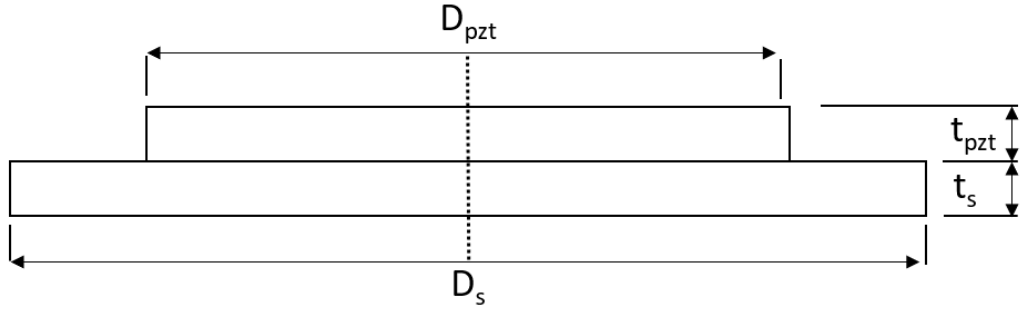


Figure 4.5: Configuration for the clamped stepped circular plate - with asymmetric step

Table 4.7: Material Properties of the Piezoelectric Actuator

	ρ (kg/m^3)	E (Pa)	ν (-)
Brass (Substrate)	8450	102	0.35
Piezoelectric Patch (PZT-5A)	7700	63	0.33

D_s . All discs have a ratio of $t_{pzt} + t_s/D_s < 0.05$, therefore, are classified as thin plates.

Table 4.8: Test cases for the theory validation

Case	D_s (mm)	D_{pzt} (mm)	t_{pzt} (mm)	t_s (mm)	$\frac{t_{pzt}+t_s}{D_s}$
1	15	10.5	0.11	0.10	0.014
2	20	13.5	0.14	0.10	0.012
3	27	18.7	0.13	0.15	0.010
4	27	18.8	0.21	0.22	0.016
5	35	23.4	0.24	0.24	0.014

Table 4.9 presents the resonance frequency computed by the theory and detected by the experiments. The theory results are produced for clamped conditions using Theory 1 and Theory 3. Theory 1 is used to represent the classical plate theory approach with TMM. It is already demonstrated that the computed Theory 2 results are very close to Theory 1, thus it is not employed in this particular analysis. Theory 3 is employed as it was shown to enhance accuracy of the computed natural frequency. The mean percentage difference between the experiment and theory is 9.1% and 3.9% respectively for Theory 1 and Theory 3. Except for the Case 1, results of the Theory 3 is highly accurate. The results have demonstrated the effectiveness of the theory developed over a set of different size diaphragm.

Table 4.9: Test case results with Gomes's experiments

Case	f_m - Resonance Frequency (Hz)			% Difference	
	Theory 1	Theory 3	Experiment Unc. = ± 50	Theory 1 & Expt.	Theory 3 & Expt.
1	3806	4068	4850	21.5	16.1
2	2252	2414	2450	8.1	1.47
3	1663	1752	1800	7.6	2.72
4	2494	2589	2600	4.1	0.42
5	1626	1720	1700	4.4	1.18

The difference between the theory and experimental result for Case 1 looks suspicious, the plate is thought to be over-clamped, effectively reducing the diameter of the piezoelectric actuator. Therefore, for this particular case, a FEM (Finite Element Method) with a commercial package is studied to double-check the experimental result. FEM is conducted using COMSOL Multiphysics with a 3-dimensional geometry [136]. On the other hand, under clamping of the diaphragm physically means that not full constraints are applied on the rotation at the boundaries.

Figure 4.6 presents the result of the FEM study which shows the 1st resonant mode and the deflection profile. The first mode of frequency is identified as 4046 Hz. To confirm the validity of the FEM, Case 5 is also studied and model computed the first mode of oscillation as 1719.5 Hz which is in good agreement with the experimental data of Gomes. Thus, it is suggested that the experimental data for Case 1 reported by Gomes was erroneous [56].

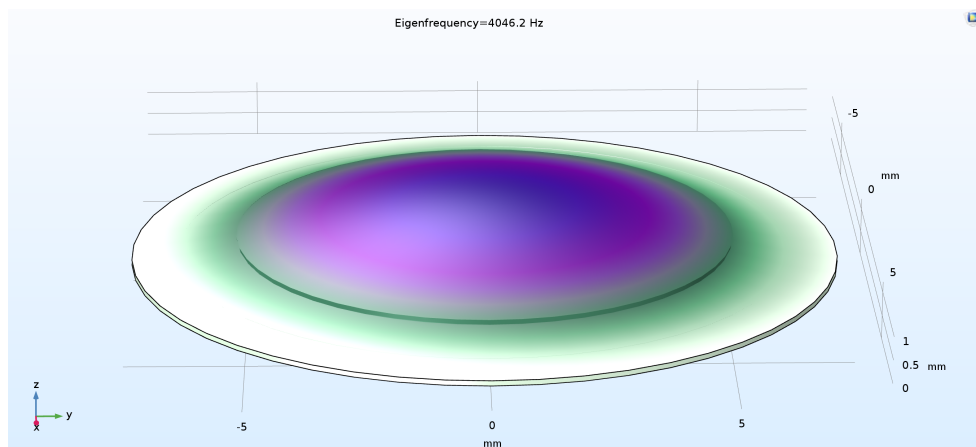


Figure 4.6: FEM model of a piezoelectric disc actuator for Case 1

Table 4.10 presents the theory and FEM result of Case 1. The percentage difference is %6.3 which agrees with the computations of other cases. FEM result regarding the Case 5 is presented for the reference of the reader. By using a standard computer, FEM solution is obtained in 3 seconds in which the Theory 3 presented results in approximately 10 seconds.

Table 4.10: Theoretical versus FEM results for the diaphragm's natural frequency

Case	f_m - Resonance frequency (Hz)		% Difference
	Theory 3	FEM	
1	4068	4046	0.5
5	1720	1719.5	0.03

Gomes [56] used a similar approach starting with the classical plate equation (Eq. 4.1) without employing TMM and assuming that the neutral plane is located at half of the thickness of the substrate. Without separating the diaphragm into inner and outer regions, such as our application, they obtained a percentage difference of %24 on average. Finally, Gomes introduced damping relaxation and edge relaxation parameters to refine the first results to reduce the difference of experiment and theory under %5. The physical validity of these parameters was not explained.

This application of classical plate theory and transfer matrix method demonstrates that the damping relaxation and edge relaxation parameters are not necessitated for the plate natural frequency calculations. Nevertheless, the importance of considering the extensional bending of the diaphragm, accurate computation/positioning of neutral planes and accurate flexural rigidity allocations of the plates are proved.

The percentage difference between the experiments (FEM for Case 1) and the theory is 6% without adding extra tuning parameter such as a clamping relaxation coefficient. The 6% difference can be explained by the facts that not accounting the radial forces and moments and the improper discontinuity (i.e., step change in thickness) modelling between the piezoceramic plate and the substrate.

For Case 1, over clamping of the plate is identified which is due to the relatively smaller diameter of the plate (i.e 15 mm) and equal torque applied as of the larger diameter plates. On the other hand, it is intuitive that as the actuator's outer plate diameter increases, the force/torque applied to each screw should increase as well as the number of screw-holes to persist fully clamped condition. Table 4.11 presents two size composition of two piezoelectric actuators used in the in-house experimental study with larger outer plate diameter.

Table 4.11: Test cases for the theory validation

Case	D_s (mm)	D_{pzt} (mm)	t_{pzt} (mm)	t_s (mm)	$\frac{t_{pzt}+t_s}{D_s}$
1	31	19.8	0.12	0.22	0.043
2	50	25	0.22	0.2	0.042

Table 4.12 presents the results for two larger diameter cases. Theory results are computed for simply supported boundary conditions. The experimental methods are consistent with the previous experimental results presented.

Table 4.12: Theoretical versus experimental results for the diaphragm's natural frequency - Simply Supported

Case	f - Resonance frequency (Hz)		% Difference
	Theory 3	Experiment Unc. = $\pm 13Hz$	
1	542	543	-0.2
2	371	355	-4.5

Table 4.12 reveals two important aspects regarding the model and experiments. Firstly, Theory 3 is capable of producing accurate results for simply supported cases as well as the clamped conditions. Secondly, the clamping condition of the plate plays a significant role on the natural frequency. Larger outer plate diameters should be clamped with more screws or higher torque should be applied each screw. Also, small absolute differences between the theory and experiments of the natural frequency can be attributed by slight under or over clamping of the plates.

4.6 Theoretical and Practical Insight

A parameter study may benefit accurate sizing of the sensor/actuator and demonstrate the parameter range capability of the theory developed, using Theory 3 to estimate the natural frequency. Some theoretical cases can be computed to understand the effect of different parameters on the natural frequency such as the effect of brass plate diameter, piezoelectric plate diameter and thickness composition.

Figure 4.7a, demonstrates the effect of varying substrate plate diameter (D_s) in which the piezoelectric plate diameter (D_{pzt}), substrate plate thickness (t_s), piezoelectric plate thickness (t_{pzt}) are kept constant as 19.8 mm, 0.2 mm and 0.2 mm, respectively. The results showed that the increasing substrate layer diameter reduces the natural frequency.

Figure 4.7b, demonstrates the effect of varying piezoelectric plate diameter (D_{pzt}) in which the substrate plate diameter (D_s), substrate plate thickness (t_s), piezoelectric plate thickness (t_{pzt}) are kept constant as 27 mm, 0.2 mm and 0.2 mm, respectively. The results showed that the increasing substrate layer diameter increases the natural frequency monotonically in $0.28 > \frac{D_{pzt}}{D_t}$. The natural frequency reduces insignificantly in the region where $0.1 - 0.28 < \frac{D_{pzt}}{D_t}$.

Figure 4.7c, demonstrates the effect of varying substrate plate thickness (t_s) in which the substrate plate diameter (D_s), piezoelectric plate diameter (D_{pzt}), piezoelectric plate thickness (t_{pzt}) are kept constant as 27 mm, 19.8 mm and 0.2 mm, respectively. The results showed that the increasing substrate layer thickness linearly increases the natural frequency.

Figure 4.7d, demonstrates the effect of varying piezoelectric plate thickness (t_{pzt}) in which the substrate plate diameter (D_s), piezoelectric plate diameter (D_{pzt}), piezoelectric plate thickness (t_{pzt}) are kept constant as 27 mm, 19.8 mm and 0.2 mm, respectively. The results showed that the increasing substrate layer thickness linearly increases the natural frequency between $0.5 < \frac{t_{pzt}}{t_b} < 3$ and beyond that a saturation is reached.

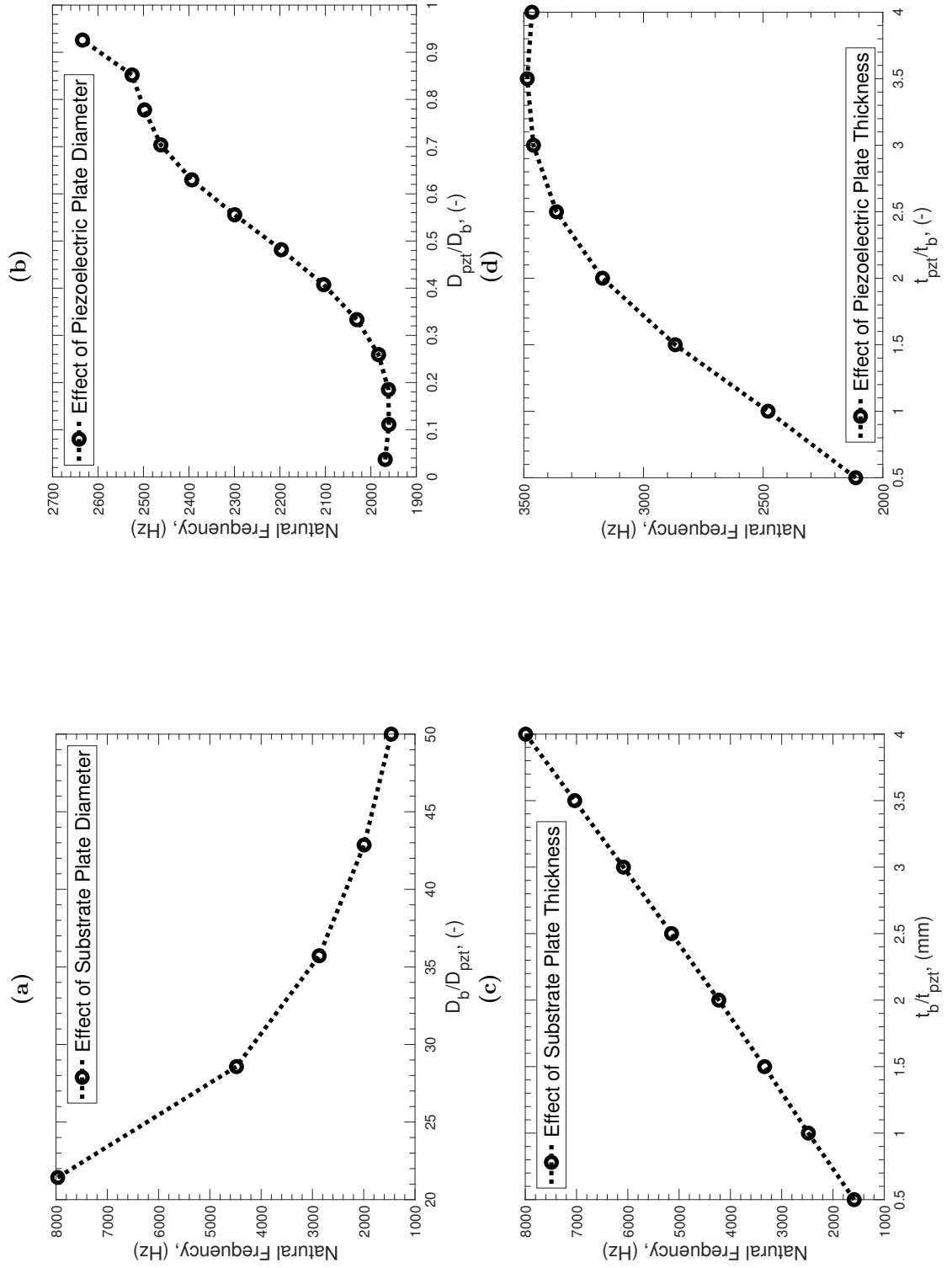


Figure 4.7: Effect of varying (a) Brass diameter (b) Piezoceramic diameter (c) Brass thickness (d) Piezoceramic thickness on Natural Frequency

4.7 Discussion

Table 4.13 presents a brief comparison of the three theories developed earlier in the previous sections. Analytical models and implementation methods are abbreviated and showed as sub-notes. The table compares the physical models, the size of the transfer matrix \mathbf{A} , discretization vectors for the inner and outer plates and the background of implementation method. The accuracy is the percentage difference between the computed natural frequency and in-house experimental data for the validation cases of clamped plates.

Table 4.13: A brief comparison of models

Theory	I-Section 4.2	II-Section 4.3	III-Section 4.4
Physical model	CPT ¹	Part EFT ²	Full EFT ²
Transfer matrix size (\mathbf{A})	4×4	4×4	6×6
Discretization	-	180 - 480	99 - 136
Implementation method	Bessel functions	ME ³	ME ³
Accuracy (%)	4.9	4.7	1.2
Run time (s)	0.43	0.15	0.18

Even though, the state vectors of the Theory 1 and Theory 2 are the same, approach and the constitutive equations behind the transfer matrices are different. As per accuracy row of Table 4.13, natural frequency computations of Theory 1 and 2 are close. Bessel functions are widely applied in many various studies including pioneering studies of Stavsky and Loewy [48], Sato and Shimizu [50] and also in Gomes's application of thin plate theory [56]. However, there is a significant novelty in the implementation of equations by using the matrix exponentials, which is computationally straightforward and reduces analytical effort. The significant improvement in the analytical models are introduced with the transition from Theory 2 to 3. When the lateral displacement, normal force resultant and circumferential force resultant are in-

¹Classical Plate Theory

²Extensional-Fluxural Deflection Composite Plate Theory

³Matrix Exponential

cluded the extensional and flexural vibration behaviour becomes coupled and also the additional rotatory inertial terms are taken into account. So that, the accuracy of natural frequency computations substantially increased. This implies the importance of coupling extensional & flexural equations and including rotatory inertia in which the change in the neutral plane position is also accounted at the step changes. The position of neutral axis is one of the recurring problems in the modelling of piezoelectric composite plates. The advantage of Theory 2 and 3, is the independence of the neutral plane. The reference plane can be selected as preferred at the cost of increasing the number of states and coupled equations.

For Theory 3, there can be a few plausible points to postulate the mean percentage difference of 1.2 compared with the experimental natural frequency and the model. In the model, the epoxy bonding layer (i.e. conductive adhesive) is not considered. The bonding layer is extremely thin in the order of 2-5 μm , thus its effect is very limited. The effect of considering the bonding layer on the natural frequency is demonstrated with an FEM study using COMSOL Multiphysics [136], using actuator geometry of Case 2 ($D_s = 27 \text{ mm}$, $t_{total} = 0.28 \text{ mm}$, see Table 4.8). When there is no bonding layer is modelled the natural frequency of the composite plate is $f_m = 1765.3 \text{ Hz}$. For the models using the bonding layer thickness of $3\mu\text{m}$, $5\mu\text{m}$ and $10\mu\text{m}$, the f_m is 1776.6 Hz, 1784 Hz and 1802.5 Hz, respectively. The increasing thickness of the bonding layer increases the natural frequency. Therefore, if the bonding layer thickness is $3\mu\text{m}$, its effect on the natural frequency is 11.3 Hz with a percentage difference of 0.64. The corresponding FEM results are presented in Figure 4.8. Therefore, it can be deduced that the bonding layer does not have a significant impact on the natural frequency computation of the model.

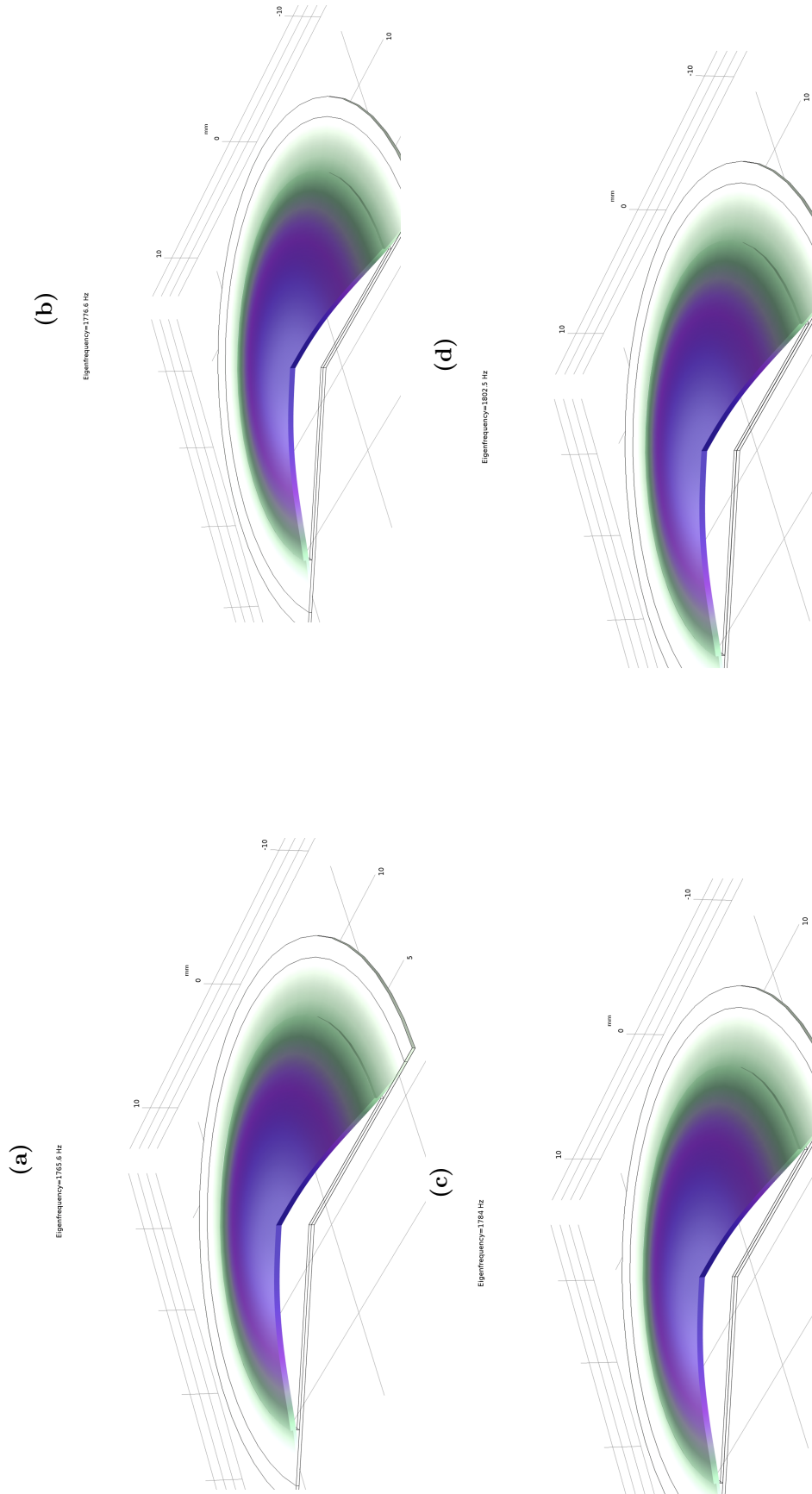


Figure 4.8: FEM Study on the variation of bonding layer thickness (a) $t_{bonding} = 0 \mu m$ (b) $t_{bonding} = 3 \mu m$ (c) $t_{bonding} = 5 \mu m$ (d) $t_{bonding} = 10 \mu m$

Other limitation of the analytical models, which may have effect on the natural frequency, is the assumption of isotropic material. The Young's modulus is assumed to be isotropic (as well as density and Poisson's ratio), however, Young's modulus could be anisotropic, in the form of a 6×6 elasticity compliance matrix. The anisotropic elasticity matrix can be manipulated to become isotropic [137].

4.8 Summary

Three theory has been introduced to obtain accurate natural frequency estimations for the thin inhomogeneous circular plates with stepped thickness. Introducing the transfer matrix method for the inner and outer plates as well as the exponential matrices have helped towards achieving an accurate (i.e., on average 1.5% compared to the experimental data) and efficient (i.e., code run-time less than 10 seconds) theory, to estimate the natural frequency of the piezoelectric actuator.

Theory 1, classical plate equation with Bessel functions, has been developed to show that the thin plate theory can provide acceptable level of confidence in natural frequency estimations in case of appropriate application. The method does not need to have tuning parameters (i.e., clamping or damping relaxation coefficients) to obtain acceptable level of accuracy in the natural frequency estimations. Due to the easy of implementation, Theory 1 is suggested as a preliminary tool for estimating natural frequency of composite piezoelectric actuators which synthetic jet actuator designers or similar could benefit.

Theory 2 is proposed to introduce the reader to the matrix exponentials instead of Bessel functions and discretization of the plates which is a novel aspect in the field. Theory 2 benefit from the reduced order flexural-extensional deflection equations of the thin plates. The accuracy obtained with the Theory 2 is similar to the Theory 1.

The difference between the second and third theory is the introduction of

extensional-flexural coupling and lateral displacements which improved the accuracy of the natural frequency estimations significantly. After implementing Theory 2, the computational procedure for the Theory 3 is straightforward. The results yields to accurate estimations of the natural frequency for both clamped and simply supported boundary conditions. As per the sensitivity analysis presented in Section 4.6 (Figures 4.7a - 4.7d), the parameter validity range (i.e., diameter, thickness) of the model is wide. Theory 3 is suggested for the pure structural mechanics researcher.

Table 4.14 presents a brief summary of the natural frequency estimations of theories developed. Case I-V is the validation cases of taken from the experimental study of Gomes [56] and Case VI-VII are in-house cases. Each case is listed with the outer diameter (shown with D in the table) and total thickness (t_t) of the piezoelectric actuator. The experimental natural frequencies (f_m) of the Gomes's cases and in-house cases are given in Table 4.9 and Table 4.4, respectively. The percentage differences (shown with %Diff. in the table) are calculated based on the experimental natural frequency. For Case I, FEM result is used for the percentage difference calculation as per the discussion made in Section 4.5. For eight cases, the mean percentage differences of natural frequency estimations are 5.9%, 5.5% and 1.3% for Theory I, Theory II and Theory III, respectively.

Table 4.14: Summary of Validation Cases Studied in the Chapter 4

Case	Diaphragm Size		Theory I		Theory II		Theory III	
	D (mm)	t_t (mm)	f_m (Hz)	%Diff.	f_m (Hz)	%Diff.	f_m (Hz)	%Diff.
I	15	0.21	3806	5.9	3813	5.8	4068	0.5
II	20	0.24	2252	8.1	2256	7.9	2414	1.5
III	27	0.28	1643	8.7	1666	7.4	1752	2.7
IV	27	0.43	2494	4.1	2498	3.9	2589	0.4
V	35	0.48	1626	4.4	1630	4.1	1720	1.2
VI	27	0.28	1695	3.1	1698	3	1780	1.7
VII	27	0.45	2603	6.7	2607	6.5	2768	0.7

By employing a finite element analysis, it is demonstrated that the adhesive bonding layer between the passive and active layers do not have a significant

effect on the natural frequency. The FEM analysis is accurate compared to the experiment and have a short run-time (i.e., less than 10 seconds) but it is not practical for a parameter sweep in case size of the piezo or substrate would be varied.

The structural models can be extended to study sandwich-layered actuators (i.e., bimorph piezoelectric actuator or multiple composite layers). In this chapter, the models are for the natural frequency estimation in the absence of a potential difference on the active layer. For the best purpose of synthetic jet actuator design and modelling, the forced vibrations under voltage load should be also studied. The dynamic response of the unimorph piezoelectric actuator under potential difference is investigated in the next chapter.

Chapter 5

Experimental Validation and Numerical Verification of Dynamic Response Modelling

5.1 Introduction

In Chapter 4, three analytical models are developed and validated against experimental data to identify accurate values for the natural frequency in free vibration of the piezoelectric thin circular plates. With the most advanced model derived, which accounted for the extensional-flexural rigidity and coupling between extensional and lateral displacement, accurate solutions for selected validation cases are obtained. In this chapter the dynamic response in the forced vibrations of a thin piezoelectric actuator under voltage load is studied. The model is extended to account for the voltage applied and the transverse piezoelectric coefficient to calculate the displacement profile. In order to calculate the displacement under the voltage load, the empirical damping term is also required. Therefore, different models of damping evaluation are also studied within this chapter.

Various studies under different settings are conducted to evaluate the displacement of piezoelectric actuators. Desphande [54] employed classical laminated

plate theory for the static deflections of multi-layered circular plates under voltage and pressure load. Hu studied forced vibrations of a circular diaphragm using Hamilton principle and the Rayleigh-Ritz principle and studied three diaphragms of same diameter and different thickness [59]. They obtained peak displacement results around 10% of the experimental data. However, their model assumes an approximate neutral axis calculation and is complex to implement. They have not studied how to evaluate mechanical damping term. Gomes studied the dynamic response of the actuator under voltage load using the classical thin plate equations combined with energy methods, obtaining peak displacement results of 50% off the experimental data [57]. Some studies considered the effect of both applied voltage and pressure to the disc [54, 58]. Herein, the frequency response analysis only concentrates on the displacement of the plates under voltage load due to the specific interest in the piezoelectrical driven synthetic jet actuator.

Therefore, it is required to study the forced dynamic vibration response of the thin plates using the theory presented in Chapter 4.4. The accurate estimation of the displacement of piezoelectric actuator will benefit the design and studies towards the performance enhancement of the piezoelectrical driven synthetic jet actuator.

In Section 5.2, the governing equations which also accounts for potential difference, transverse piezoelectric coefficient, and mechanical damping are presented. The experimental frequency response of selected cases are presented in Section 5.3. Damping models and damping evaluation are introduced in Section 5.4. Section 5.5 investigates the frequency response of the diaphragm under voltage load, and displacements are compared with in-house experimental data. Section 5.6 introduce a finite element method model, which is studied using COMSOL Multiphysics for additional verification of the displacement calculations and damping identification. The discussions are presented in Section 5.7, which is followed by the summary of the chapter in Section 5.8.

5.2 Formulation of the governing equations

In this section, derivation of the model used in the displacement calculations and assumptions are presented. The theory presented in this section, builds up on the theory presented in Chapter 4.4, as it is the most accurate theory compared with the experimental natural frequency based on the experimental validation of the selected in-house test cases. Referring to the expressions obtained and/or derived in Chapter 4.4.2, the key equations and relationships are re-written to avoid a discontinuity in the content flow of the current chapter.

Dynamic frequency response (i.e., active layer under potential difference/voltage load) computations the assumptions follows as: i) the piezoelectric plate have a resonance frequency of well below 1 MHz, therefore, it can be assumed as elastically isotropic [51], ii) Also, the voltage load is assumed to be uniformly distributed throughout the piezoelectric plate, iii) The piezoelectric patch is perfectly polarised along transverse, z-direction ($\langle 001 \rangle$), iv) Impact of the electrodes on the deflection is neglected v) effect of bonding layer on the transverse displacement is neglected as the base theory does not account for it.

Besides the modal parameters, as obtained by the procedure in Section 4.4.4, it is important to evaluate the steady-state response of the plate, when subjected to a harmonic variation in the electric field across the active layer. This is usually achieved by harmonically varying the electric potential difference between the upper and lower surfaces of the piezoelectric layer. The resulting vibration can be characterised by computing a frequency response function (FRF) for the displacement at centre of plate, as a function of the frequency of excitation ω , and by assuming a potential difference of unit magnitude, without any loss of generality.

From the classical laminate plate theory (CLPT) stress-strain relationships, the expressions for the internal force and moment resultants are readily obtained [48, 54]:

$$\begin{bmatrix} n_r \\ n_\theta \\ m_r \\ m_\theta \end{bmatrix} = \begin{bmatrix} A_{rr} & A_{r\theta} & B_{rr} & B_{r\theta} \\ A_{\theta r} & A_{\theta\theta} & B_{\theta r} & B_{\theta\theta} \\ B_{rr} & B_{r\theta} & D_{rr} & D_{r\theta} \\ B_{\theta r} & B_{\theta\theta} & D_{\theta r} & D_{\theta\theta} \end{bmatrix} \begin{bmatrix} \varepsilon_r^0 \\ \varepsilon_\theta^0 \\ \kappa_r \\ \kappa_\theta \end{bmatrix} - \begin{bmatrix} n_r^p \\ n_\theta^p \\ m_r^p \\ m_\theta^p \end{bmatrix}. \quad (5.1)$$

The constants A_{ij} ($i, j = r$ and θ) represent extensional stiffness, B_{ij} coupled extensional-bending stiffness, and D_{ij} bending stiffness, respectively. They can be expressed, by also considering symmetry relations, as follows

$$A_{rr} = A_{\theta\theta} = \sum_{k=1}^n \frac{E_k}{1 - \nu_k^2} (z_k - z_{k-1}), \quad (5.2)$$

$$A_{r\theta} = A_{\theta r} = \sum_{k=1}^n \frac{\nu_k E_k}{1 - \nu_k^2} (z_k - z_{k-1}), \quad (5.3)$$

$$B_{rr} = B_{\theta\theta} = \frac{1}{2} \sum_{k=1}^n \frac{E_k}{1 - \nu_k^2} (z_k^2 - z_{k-1}^2), \quad (5.4)$$

$$B_{r\theta} = B_{\theta r} = \frac{1}{2} \sum_{k=1}^n \frac{\nu_k E_k}{1 - \nu_k^2} (z_k^2 - z_{k-1}^2), \quad (5.5)$$

$$D_{rr} = D_{\theta\theta} = \frac{1}{3} \sum_{k=1}^n \frac{E_k}{1 - \nu_k^2} (z_k^3 - z_{k-1}^3), \quad (5.6)$$

$$D_{r\theta} = D_{\theta r} = \frac{1}{3} \sum_{k=1}^n \frac{\nu_k E_k}{1 - \nu_k^2} (z_k^3 - z_{k-1}^3), \quad (5.7)$$

where the index k in E_k and ν_k stands for the materials properties in the k -th layer of the laminate.

In Eq. (5.1), the radial and circumferential piezoelectric force resultants n_r^p and n_θ^p , and the radial and circumferential piezoelectric moment resultants m_r^p and m_θ^p , generated in the piezoelectric layers under potential (voltage) difference between the upper and lower layer surfaces, when the plate is fully constrained, are expressed by:

$$n_r^p = n_\theta^p = \sum_{k=1}^n \frac{E_k}{1 - \nu_k} E_f^k d_{31}^k (z_k - z_{k-1}), \quad (5.8)$$

$$m_r^D = m_\theta^D = \frac{1}{2} \sum_{k=1}^n \frac{E_k}{1 - \nu_k} E_f^k d_{31}^k (z_k^2 - z_{k-1}^2), \quad (5.9)$$

where the superscript k in E_f^k and d_{31}^k stands for the applied external electric field across the layer and the piezoelectric constant in the k -th layer of the laminate. It is clear that the contributions to forces and moments from non-piezoelectric layers is zero, since $d_{31}^k = 0$ for such layers.

Referring to Eqs. (5.8-5.9), in particular, a discontinuity in the state variables at the boundary between inner and outer regions arises under harmonic potential difference. The step change in the state variables can be represented by a vector $\mathbf{f} = [0 \ N_r^D \ 0 \ 0 \ M_r^D \ 0]^T$, containing the amplitudes of the harmonically varying force n_r^D and moment m_r^D resultants. At each frequency of excitation ω , a solution for the unknown state variables at the plate centre is computed from a non-homogeneous system of algebraic equations

$$\mathbf{T}_b \begin{bmatrix} N_r(0) \\ W(0) \\ M_r(0) \end{bmatrix} + \mathbf{R} \cdot \mathbf{b} = \mathbf{ZM}_{3 \times 1}, \quad \text{where} \quad \mathbf{b} = \mathbf{T}_O(a_O) \cdot \mathbf{f} \quad (5.10)$$

In order to obtain more realistic results from the physical point of view and to avoid numerical singularities in the solution of Eq. (5.10) at resonance frequencies, it is essential to incorporate some form of dissipation of mechanical energy in the model. Small, or weak, materials damping is assumed, and it is characterised by a loss factor η , constant across the whole frequency range of interest, in the sense described in classical vibration theory [138]. This assumption also means that the same damping ratio (factor) $\gamma = \eta/2$ is adopted for all plate modes of vibration. The following complex-valued wave-numbers can be introduced

$$k_r = \omega \left(\frac{I_0}{A_{rr}} \right)^{1/2} \left(1 - \frac{\eta}{2} i \right) \quad \text{and} \quad k_b = \left(\omega^2 \frac{I_0}{D_{rr}} \right)^{1/4} \left(1 - \frac{\eta}{4} i \right), \quad (5.11)$$

to describe analytically the damping mechanism in radial and bending vibra-

tions, correspondingly. Two of the elements in the system matrix in (4.82) require some modification to incorporate the damping in the model, or these matrix elements become

$$A_{21} = \frac{1}{r^2} M_{11}^3 - A_{rr} k_{\Gamma}^2, \quad \text{and} \quad A_{63} = -D_{rr} k_{\mathbf{b}}^4. \quad (5.12)$$

Note the two matrix elements reduce to the form shown in (4.82) when damping is neglected, or for $\eta = 0$.

Figure 5.1 presents a normalised radial displacement profile (i.e., mode shape for the first-mode of oscillation) for a sample piezoelectric actuator at the resonance frequency. At the clamped end (i.e., $r/R = 1$) the transverse displacement is zero and it increases monotonically towards the centre of the diaphragm where displacement reaches the maximum (i.e., $r/R = 0$).

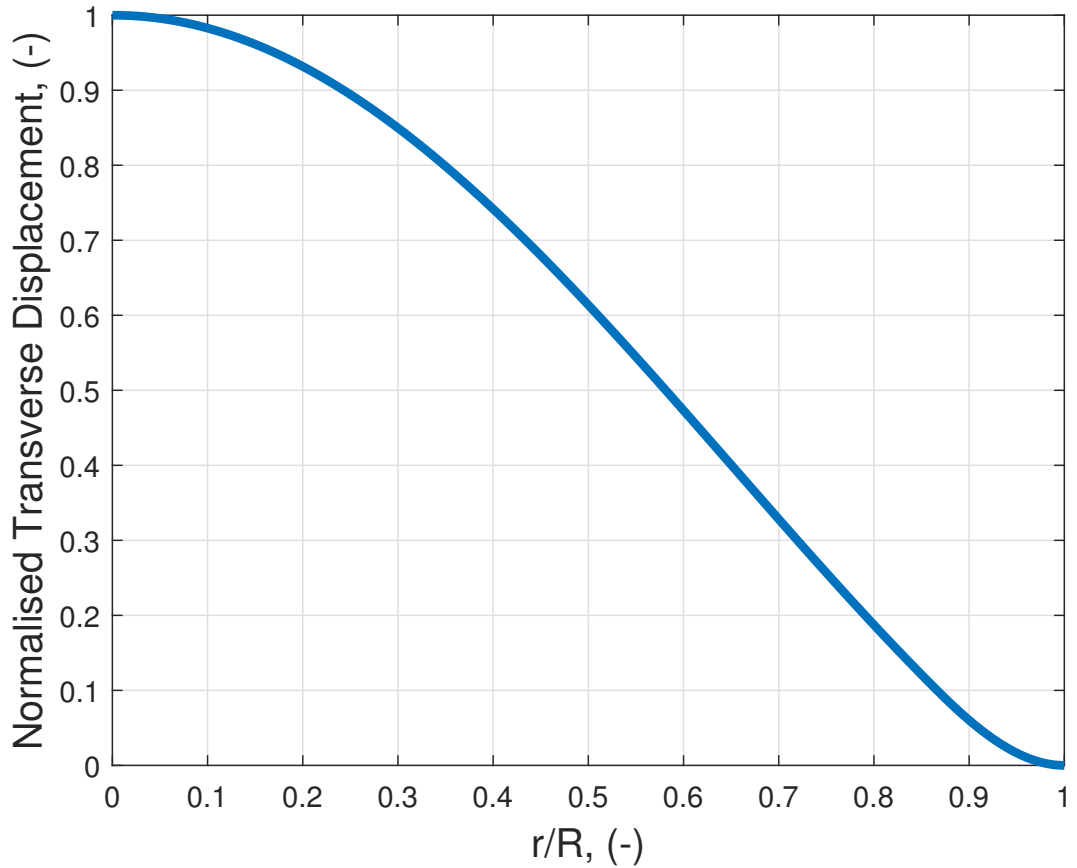


Figure 5.1: Radial displacement profile at resonant frequency

5.3 Experimental frequency sweep

In this chapter three different size of piezoelectric actuators are studied. The size and composition of the test cases (i.e. piezoelectric diaphragms) are shown in Table 5.1 with the peak supply voltage (V_p) used in the experiment.

Table 5.1: Test cases for the theory validation

Case	D_s (mm)	D_{pzt} (mm)	t_{pzt} (mm)	t_s (mm)	V_p (V)
1	27	19.8	0.13	0.15	20
2	27	19.8	0.22	0.23	20
3	35	25	0.2	0.1	20

Table 5.2 presents the material properties of the brass substrate and PZT-5A patch. The density (ρ), Young's modulus (E) and Poisson's ratio (ν) are presented. The material properties are provided by the manufacturer of the piezoelectric actuators, OBO Pro2 [107].

Table 5.2: Material Properties of the Piezoelectric Actuator

	ρ (kg/m ³)	E (Pa)	ν (-)	d_{31} (pm/V)
Brass (Substrate)	8500	110	0.34	-
Piezoelectric Patch (PZT-5A)	7500	60	0.32	180×10^{-12}

Figure 5.2 displays the dynamic response experimental measurements of the selected unimorph diaphragm as described in Chapter 3.4, at a constant voltage amplitude of $20 V_p$. It is previously calculated with appropriate theory and experimental results, the natural frequency varies with the diaphragm diameter and thickness composition. In all cases, the centre displacement increases, then reaches a peak at around the resonant frequency and reduces after the resonance. At relatively low actuation frequency, the transverse deflection is constant. After the resonant frequency, the centre deflection monotonically decays and reduces compared to the pre-resonance level. It can be inspected from Figure 5.2 that, in some cases secondary modes are observable; most notably in Case 3 with 35 mm outer plate diameter (around 1400 Hz). The relatively small diameter diaphragms are more tricky to clamp perfectly as reported earlier in Chapter 4.5, for Gomes's experimental data of 15 mm diameter disc.

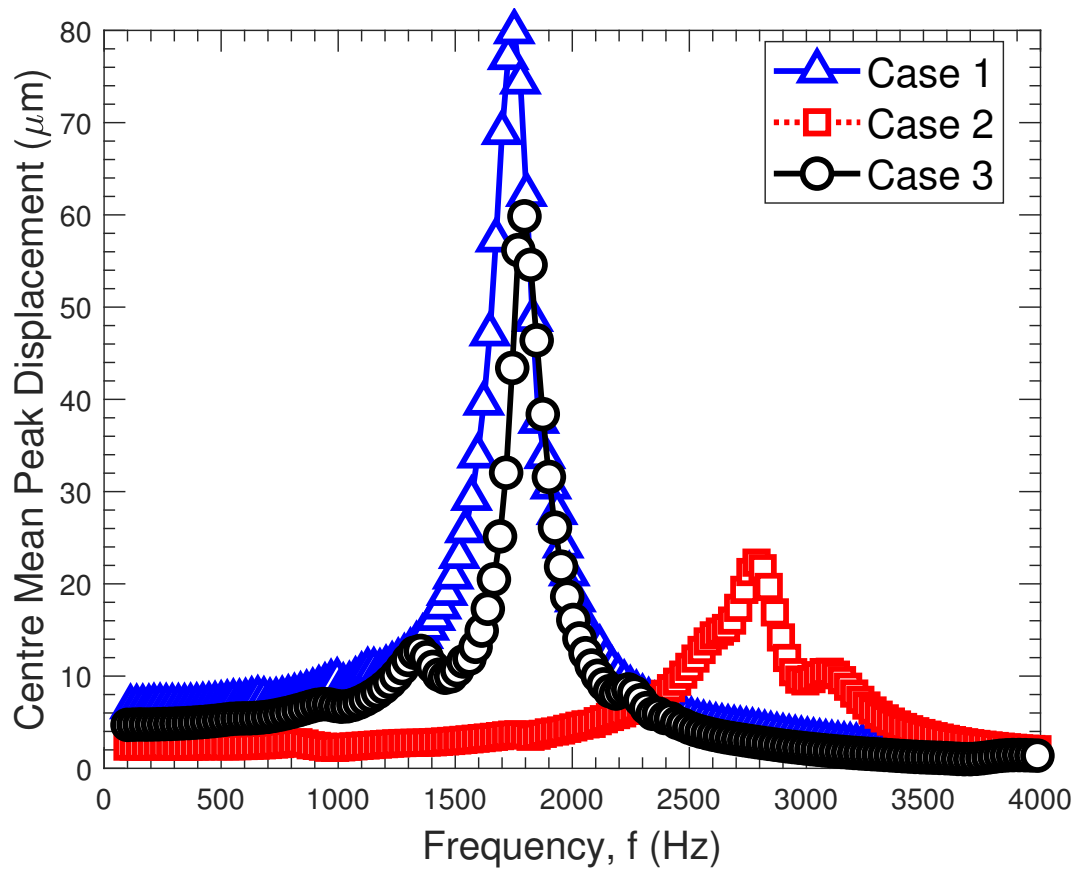


Figure 5.2: *Experimental Frequency Sweep of Selected Test Cases*

By using the selected test cases, similar inner and outer diameter cases can be compared which can be used to draw some key conclusions. The overall thickness and the peak displacement is inversely proportional as well. Also, the quasi-static deflection (i.e at low forcing frequency 100 Hz) is inversely proportional to the overall diaphragm thickness. Table 5.3 presents the displacement results at 100 Hz and at the resonance frequency (f_m) with the associated uncertainty in the experimental measurements.

Table 5.3: Results for the experimental centre displacement

FRF	Peak Mean Centre Displacement, Δ (μm)	
	100 Hz Unc. = $\pm 1.5\%$	f_m Unc. = $\pm 1.5\%$
Case 1	6.7	79.8
Case 2	2.2	22.3
Case 3	6.6	59.8

5.4 Identification of Mechanical Damping

The material damping (also referred as structural damping) restrains the vibratory motion of the piezoelectric composite plates and needs to be estimated for the dynamic response modelling. The damping can be classified as material (i.e., mechanical), damping due to the boundary condition and viscous damping. The material and boundary condition damping cannot be separated in this set of experiments. The viscous damping, which is caused by the interaction of the surrounding fluid and the plate, is negligible for the set of experiments presented in Section 5.3 [139, 140]. Nevertheless, the viscous damping, due to the interaction with an enclosed fluid medium (i.e., in the case of synthetic jet actuator) and plate under voltage (or pressure) load is not negligible.

For the evaluation of damping, using the experimental data, two different models are presented namely, the magnification factor and peak picking method, which also known as half-power method [47, 141]. The prior method is based on the displacement, and the latter relies on the accurate frequency identification of the natural peak and surroundings.

The magnification factor method is formulated in Munday and Farrar's Engineering Handbook [141] and employed for piezoelectric actuators [57], which is also an empirical method. The magnification factor (β) is a ratio of the quasi-static deflection ($\omega = 100Hz$) to the peak deflection. The quasi-static deflection is assumed at 100 Hz in which the inertial forces are negligible due to the low frequency forcing so that the forcing frequency satisfies, $f \ll f_m$ [142].

The damping identification is formulated as:

$$\beta = \frac{H(\omega_n)}{H(\omega_0)} \quad (5.13a)$$

$$\zeta_{mf} = \frac{1}{2\beta} \quad (5.13b)$$

The peak picking is a convenient and more widely used method in the damping

extraction of dynamic vibration research [143, 144]. This method uses the peak amplitude $H(\omega_n)$ and two frequency corresponding to the $\frac{H(\omega_n)}{\sqrt{2}}$ from either side of the $H(\omega_n)$.

$$\zeta_{hp} = \frac{\omega_2 - \omega_1}{2\omega_n} \quad (5.14)$$

Figure 5.3 presents a generic non-dimensional experimental FRF indicating the critical frequencies ($\omega_0, \omega_1, \omega_2, \omega_n$) used for the damping identification.

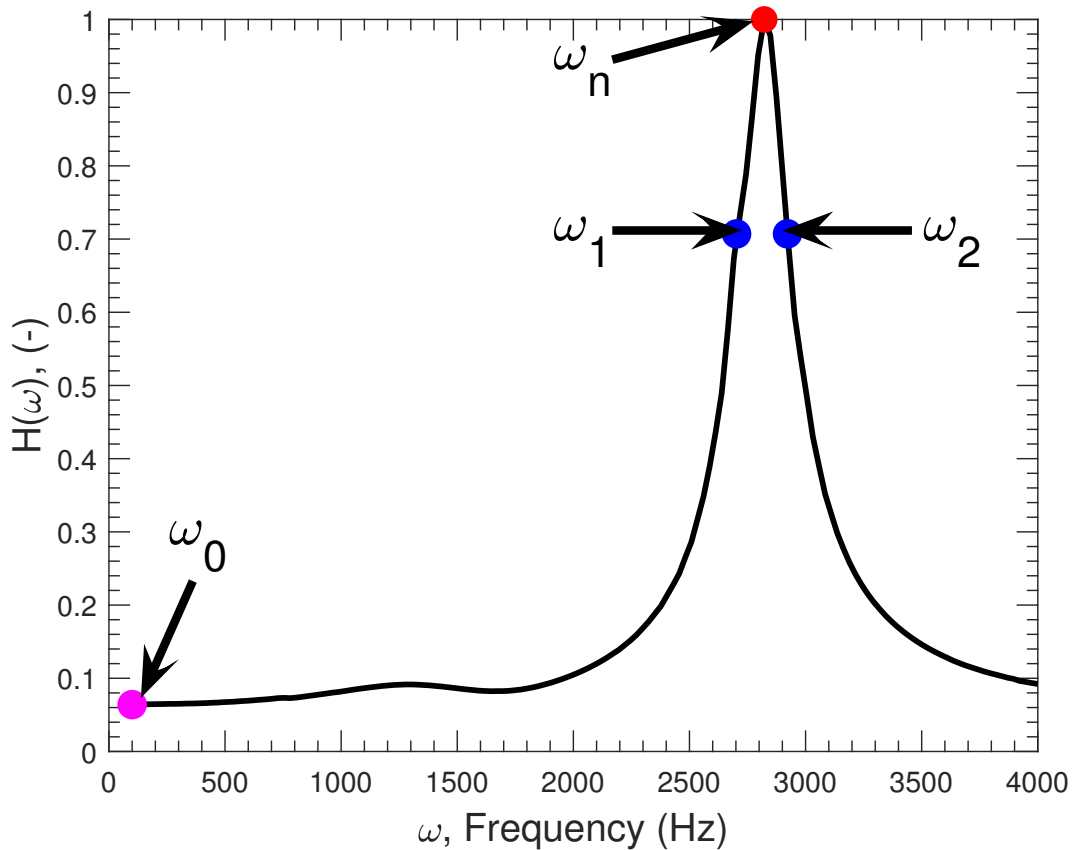


Figure 5.3: FRF illustration of the critical frequency parameters used in damping identification

Both damping models require accurate measurements of the dynamic response of the piezoelectric actuator which is assured by high resolution experimental equipment and multiple repeats of the experiments [47]. Both factors are assured as per the experimental apparatus and methods presented for dynamic response measurements in Chapter 3.4.

Damping models assume a single-input-single-output transfer function which is not accurate if the nearby oscillation modes contributes to the FRF. The

limitations of the half power method is the use of estimated half power points only and the half power frequencies (ω_1 & ω_2) are likely to need interpolation as measured data may not coincide that frequency points exactly. The interpolation is done by using MATLAB's *interp* built-in subroutine [115]. The half-power method equation is valid for small damping such as $\zeta < 0.1$. The average damping in the literature for the circular piezoelectric actuator is $\zeta \cong 0.03$, therefore the method should be in the valid region [59]. On the other hand, the magnification factor method is not widely used except the studies of Gomes [57, 65]. By Eq. 5.13, the magnification factor method requires accurate measurement of quasi-static displacement as well as the peak resonance displacement. The magnification factor method is valid to a higher range of damping ($\zeta < 1$) compared to the half power method [141]. Table 5.4 presents the structural damping identified by the damping models and the percentage difference between the values.

Table 5.4: Damping identification of the experimental FRF cases

Damping	$\zeta_{mf}(-)$	$\zeta_{hp}(-)$	% Difference
Case 1	0.042	0.041	2.4
Case 2	0.060	0.037	38.3
Case 3	0.057	0.040	29.8

No clear pattern between the damping ratios and the natural frequency or the diaphragm size is established. The half-power method is more established in the field and it is expected to work well in the damping range of $\zeta < 0.1$. However, half-power method is not applied in any piezoelectric actuator FRF study to the best knowledge of the author. The accuracy of the damping identification methods can be established by fitting both values from magnification factor method and half-power method to the experimental FRF.

5.5 Dynamic response model validation against experimental data

In this section, experimental and model results of dynamic frequency response are compared for three selected test cases (size and composition presented in Section 5.3). As per the previous section, both damping models are used for the purposes of comparison. For the validation cases of the dynamic response modelling, clamped boundary conditions for the piezoelectric actuators are considered.

Figure 5.4 presents the frequency response of the damping models and compared with the experimental data. Figure 5.4a presents the dynamic response for validation Case 1. The experimental result and computed FRF results are presented by using two different damping evaluated using alternative methods. In the legend of the figure ζ_{mf} and ζ_{hp} refers to damping identified by magnification factor method and half-power method, respectively. It is observed that both models fit to the experimental data and overall shape is accurately obtained by both of the damping models. The peak displacements at the resonant frequency is $79.8 \mu\text{m}$ measured experimentally, $83.9 \mu\text{m}$ and $86.0 \mu\text{m}$ computed using half-power method and magnification factor method, respectively. The percentage difference between the experimental peak centre displacement and the computed displacement using the damping obtained by half-power method is 4.8%, and it is 7.2% for the magnification factor method.

Figure 5.4b presents the dynamic response for validation Case 2. The experimental peak displacement at the resonant frequency is identified as $21.3 \mu\text{m}$. It is found that the damping obtained with the half-power method have overestimated the peak displacement at the resonant frequency around 50%. The damping obtained by the magnification factor have identified the peak as $25.0 \mu\text{m}$, with a difference of 17%.

Figure 5.4c presents the dynamic response for validation Case 3. The experi-

mental peak displacement at the resonant frequency is identified as $59.8 \mu\text{m}$. It is found that the damping obtained with the half-power method have overestimated the peak displacement at the resonant frequency around 40%. The damping obtained by the magnification factor have identified the peak as $67.1 \mu\text{m}$, with a difference of 12%.

To compare the accuracy of the damping methods the average percentage difference between the models and experiment can be quantified using the peak displacement at the natural frequency. The damping calculated with half-power method yielded a mean percentage difference of 31.6% in peak displacement estimation. The magnification factor method resulted in a mean percentage difference of 12%. As per the demonstrated test cases, the magnification factor method yields more accurate results for damping ratio calculations.

5.5.1 Experimental validation of the voltage sweep

The effect of sweeping potential difference is important to assess the performance of analytical FRF model. This study would also help identifying whether the non-linear voltage effects are important within the selected voltage range. Piezoelectric actuator of the Case 3 (in Section 5.5) is experimentally studied with peak supply voltages of 1 V, 10 V, 20 V, 30 V, 40 V and 50 V. Figure 5.5 presents the comparison of the analytical model computations and experimental centre displacement values versus the driving voltage. The damping used in the analytical model is extracted from the experimental result of each driving voltage using the magnification factor method. It is shown that the experimental centre displacement is consistently overestimated by the model with an average percentage difference of 8.2%. The increased drive voltage does not increase the overestimation and the peak displacement follows a linear trend against the driving voltage.

Therefore, up to $50 V_p$ ($100 V_{pp}$) non-linear effects due to the voltage is not observed. The piezoelectric diaphragm is within the limits of linear stiffness

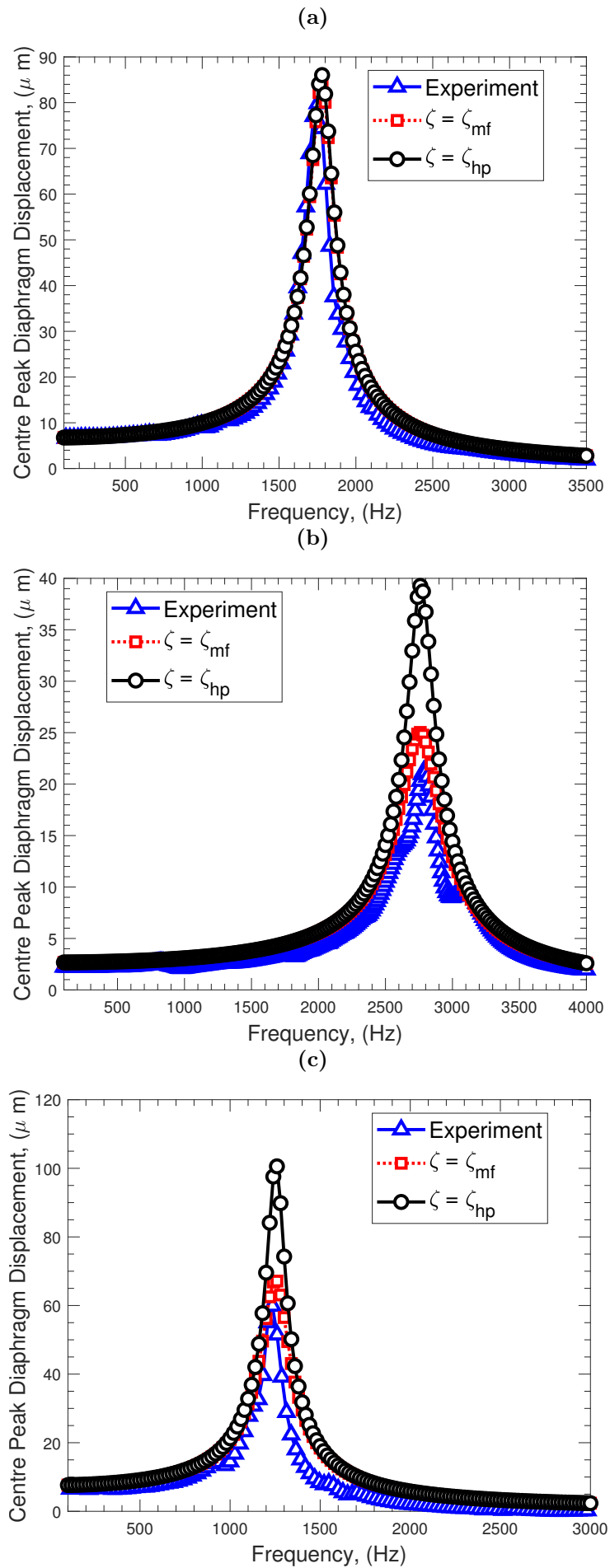


Figure 5.4: Dynamic Response modelling with two damping models (a) Case 1 (b) Case 2 (c) Case 3

and dielectric saturation is not expected. Also, the model have an acceptable accuracy of centre displacement estimations with the magnification factor damping extraction method.

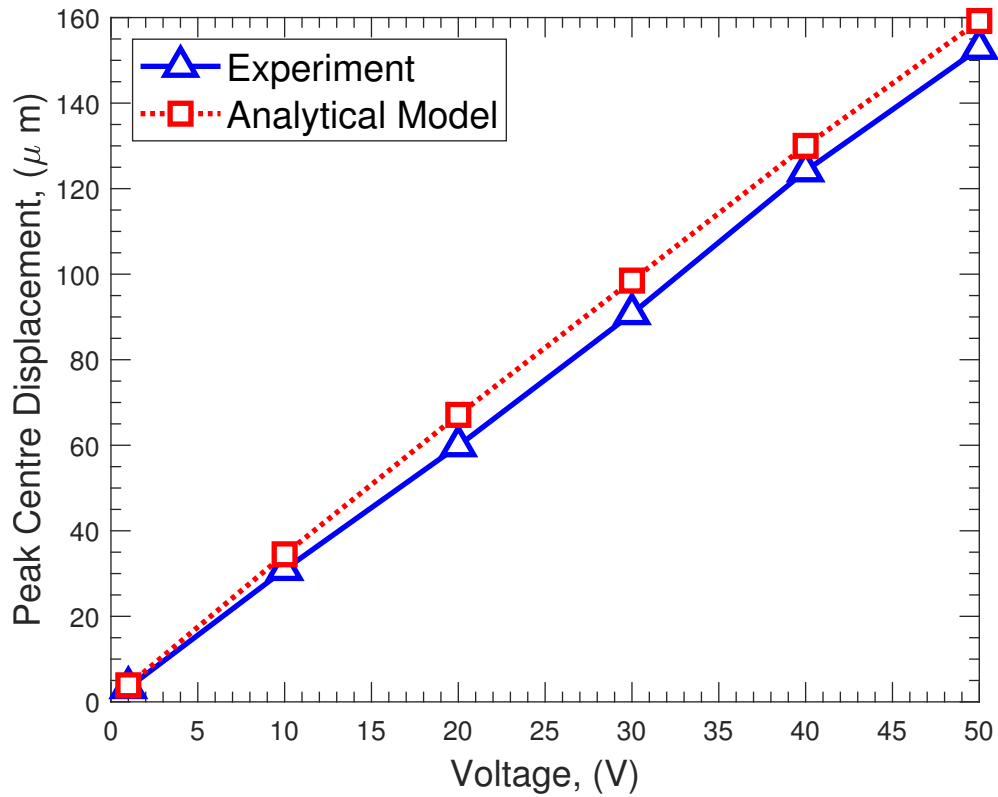


Figure 5.5: Piezoelectric actuator centre displacement versus the driving voltages

5.6 FEM of the Composite Piezoelectric Diaphragm

In this section finite element method (FEM) analysis of the piezoelectric actuator is studied. The aim of this study is to verify the damping ratio by using the values computed in Section 5.4 and prepare basis for a more advanced FEM to model a system which utilize piezoelectric diaphragm such as synthetic jet actuator (SJA). For the finite element model a commercial software, COMSOL Multiphysics (v 5.3a) is used [136]. FEM analysis of the piezoelectric diaphragms are conducted in the frequency domain.

5.6.1 Geometry and Equations

The circular unimorph piezoelectric actuator is axisymmetric, therefore a 2-D axisymmetric geometry is employed to reduce computational effort (i.e., solution time). Figure 5.6 presents the geometry of the plates. The top plate (grey) is the piezoceramic plate and the bottom plate (blue) is the brass substrate. The material properties are isotropic and consistent with the previously reported values in Table 5.2. Solid mechanics and electrostatics modules are employed to mimic the structural mechanics of the plates and voltage applied to the piezoceramic plate, respectively. Two physics interface are coupled to reflect the inverse piezoelectric effect.



Figure 5.6: 2-D axisymmetric geometry of the piezoelectric actuator

The equations behind the simulation use standard piezoelectric stress-strain relationships and linear deflection equation under force (\mathbf{F}). Force is due to the voltage applied to the piezoceramic layer and \mathbf{u} is the displacement vector.

$$-\rho\omega^2\mathbf{u} = \nabla \cdot \mathbf{s} + \mathbf{F}\nu e^{i\phi} \quad (5.15)$$

The strain tensor (\mathbf{s}) is computed by the following equation where the \mathbf{c}_e is the elasticity matrix, ϵ is the strain displacement of the piezoelectric patch. Electrical field (\mathbf{E}) and e^T is the piezoelectric constant which relates the stress applied to the mechanical strain.

$$\mathbf{s} = \mathbf{s}_0 + \mathbf{c}_e : \epsilon_l - \mathbf{e}^T \mathbf{E} \quad (5.16)$$

The strain is calculated by the following equations:

$$\epsilon = \frac{1}{2}(\nabla \mathbf{u}^T + \nabla \mathbf{u}) \quad (5.17)$$

The mechanical damping is modelled as isotropic structural loss factor in the elasticity matrix (\mathbf{c}_e). The elasticity matrix is multiplied with loss factor of $1 + i\eta_s$.

$$\mathbf{c}_e = (1 + i\eta_s)\mathbf{c}_e \quad (5.18)$$

5.6.2 Boundary Conditions and Mesh

The plate is fixed at the edge where displacement vector \mathbf{u} is set to zero. Triangular mesh element are used with maximum size of 0.0135 mm and minimum size of 0.00027 mm. The total number of mesh elements on the plates are 19364. The mesh convergence is checked and the mesh does not have a significant effect on the results, $\pm 1Hz$. The frequency sweep is conducted with 25 Hz interval starting from 100 Hz. The FEM computed solutions at least 1500 Hz beyond the mechanical resonance for each verification case.

The natural frequency is first identified by an eigenfrequency analysis then the frequency response functions are studied. Figure 5.7 presents an illustration of the eigenvalue analysis (corresponds to the validation Case 1 in the next section).

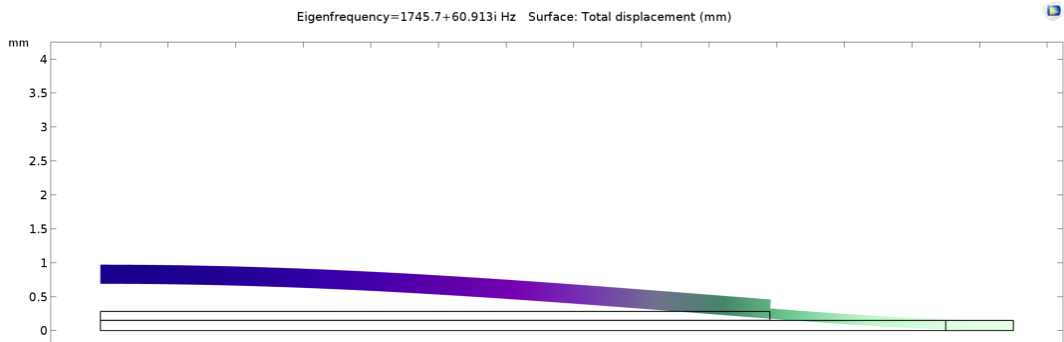


Figure 5.7: First-mode of oscillation with FEM analysis

5.6.3 Verification cases

The verification cases are the same as in Section 5.5. Therefore, the size composition and material properties are identical. For the damping coefficient of the FEM study, values obtained by magnification factor method are used.

Figure 5.8 presents the frequency response functions obtained using FEM and compared with experimental data. Figure 5.8a presents the FRF results of the experiment and FEM analysis with damping ratio of $\zeta = 0.042$. The resonant frequency is identified at 1750 Hz with a peak centre displacement of 82 μm , 2.5% difference in the displacement estimation. The resonance frequency match the experimental value. The diaphragm displacement reduces after the resonance to levels even under quasi-static conditions.

Figure 5.8b presents the FRF results of the experiment and FEM analysis with damping ratio of $\zeta = 0.06$. FEM model identified the resonance at 2775 Hz. The displacement corresponding the resonant peak is 22.9 μm with a difference of 0.6 μm compared to the experimental peak (percentage difference of 2.7%).

Figure 5.8c presents the FRF results of the experiment and FEM analysis with damping ratio of $\zeta = 0.057$. FEM model computed the resonance frequency at 1250 Hz with a peak centre displacement of 63.7 μm . The difference between the experimental peak displacement and the FEM model is 3.9 μm , percentage difference of 6.3%. In the experimental result, there is a fluctuation in the displacement signal, which can be due to a fluctuation in the laser signal or a secondary mode due to imperfect clamping. However, it does not have an impact on the peak displacement or on the damping calculations.

Table 5.5 presents the comparison of the peak centre displacement of FEM study and experimental results at the resonance frequency. The percentage difference between the experimental peak displacement and the FEM cases are 2.5%, 2.7%, and 6.3% respectively for Case 1, 2, and 3. The computations made by the FEM model verify the natural frequency of the diaphragm and the mechanical damping ratio computed using the magnification factor method.

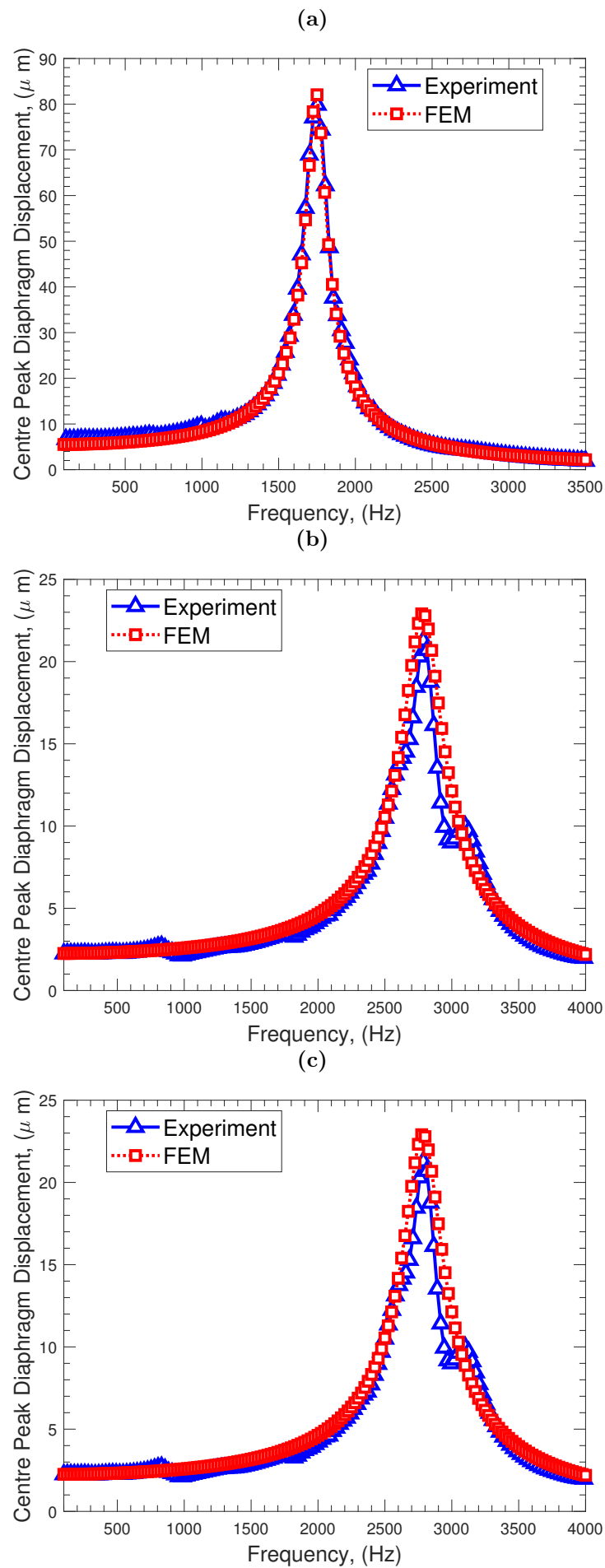


Figure 5.8: Frequency response function of FEM and experiment (a) Case 1 (b) Case 2 (c) Case 3

Even though, being an empirical method, it yields accurate displacement estimations both with FEM and analytical model presented in this chapter.

Table 5.5: Peak centre displacement by FEM and experiments at the resonant frequency

FRF	Peak Centre Displacement, Δ (μm)	
	FEM	Experiment Unc. = $\pm 1.5\%$
Case 1	82.0	79.8
Case 2	22.9	22.3
Case 3	63.7	59.8

5.7 Discussion

The mechanical damping identification is usually overlooked in the field and approximate values are used such as in studies of Hu and Sharma (i.e., $\zeta = 0.03$) [18, 59]. It is identified that damping extraction using the magnification factor method fit better to experimental curve for FRF model developed in this chapter. Traditionally, the half-power method implemented with a bandwidth of $\frac{H(\omega)}{\sqrt{2}}$ and applied likewise in this study. The half-power method was not implemented to the specific case of circular piezoelectric actuator but it is a commonly used technique in structural analysis [143, 145].

In addition, magnification factor method yields more accurate peak displacement estimations as it directly considers the peak displacement corresponding to the mechanical resonance frequency. The FRF model have a single term for the losses in an isotropic form. The potential reasons of the overestimation of the damping models; i) material may be anisotropic ii) additional dissipation mechanism due to piezoceramic element such as the dielectric loss factor [135] iii) imperfect clamping. In case the material is anisotropic the mechanical resonance frequency of the diaphragm would vary around $\pm 3\%$, based on the cases run using the FEM model. Nevertheless, assuming constant damping, the effect on the peak displacement is under 1%. Furthermore,

assuming transversely isotropic material is a common practice and yields accurate results of natural frequency estimations [58]. The dielectric loss factor (i.e., $\tan\sigma$) promotes mechanical power losses which could potentially affect the peak displacement. However, the supply potential difference (i.e., voltage) of the FRF test campaign is relatively low which limits the effects of dielectric loss. Within the experimental campaign, it is identified that imperfect clamping have a significant effect on the natural frequency and displacement profile. In order to avoid imperfect clamping, the screws are mounted using a torque-meter which ensures uniform clamping of the piezoelectric actuator. Therefore, effects of clamping on the peak displacement should be negligible. The magnification factor method resulted in more accurate results with an overestimation of 12% for three validation cases. The difference is thought to be due to the additional dielectric loss of the piezoelectric element. It should be noted that identification of the damping is not one of the primary interests of the present study, therefore, only linear models are employed. Non-linear material damping models such as Rayleigh damping could help towards the extraction of the damping from the experimental data. In particular, Rayleigh damping model is not studied within this context as it needs first two natural frequency to be experimentally obtained which is beyond the scope of the present study.

FEM model also provided accurate natural frequency computations and FRF's using the mechanical damping ratio established by magnification factor, compared to the experimental data. The mean percentage difference between the FEM model and the experiments over three validation cases is 4%. Analytical model consist of an efficient algorithm (solution time under 3 seconds) and could be implemented in any commercial or open-source software which can handle differential equations. On the other hand, the FEM model cannot be implemented via an open source software. A particular advantage of the FEM model is various clamping options such as asymmetric clamping.

The analytical FRF model is recommended for the structural mechanics re-

searchers who wants to assess the natural frequency and diaphragm displacement of piezoelectric actuators. A convenient way to assess the effects of actuator size composition, potential difference (i.e., voltage) and, transverse piezoelectric coefficient (d_{31}) is established.

In addition, the analytical model can compute the FRF in approximately 20 seconds in which for the FEM (3-D geometry) the solution time is around 600 seconds. Therefore, the analytical model developed have a significant advantage on the solution time and efficiency.

5.8 Summary

In this chapter, Theory 3 (presented in Chapter 4.4) which is the most advanced and accurate theory for the natural frequency computation is extended to account for the voltage load and material damping loss. Two damping identification methods are studied namely; magnification factor and half-power methods. It is identified that the magnification factor method yields more accurate results compared to the experimental FRF which is validated for three cases. The mean difference of the peak displacement computation and the experimental data is 6.9%, over three validation cases at $20 V_p$ supply voltage. The analytical FRF model also used to study a voltage sweep which showed that the increasing voltage does not have a adverse effect on the estimation accuracy. The analysis also helped to identify that until $50 V_p$, the piezoelectric diaphragm is within linear stiffness region.

An FEM model is also developed using COMSOL Multiphysics software and used for the verification of the analytical model. The FEM model has a mean accuracy of 4% at the peak displacement at the resonance compared to the experimental data over three validation cases.

Realistic models regarding the modal analysis of the piezoelectric actuator is demonstrated in the current chapter which builds up on the previous chapter. The analytical and FEM models are validated against experimental data and

demonstrated sufficient accuracy for further modelling. A potential application of the piezoelectric actuator would be the synthetic jet actuators (SJA).

Table 5.6 presents comparison of the peak displacement (i.e., corresponding to diaphragm mechanical frequency) of experimental data, developed analytical model and FEM analysis. Δ is the peak displacement in μm for each case and percentage difference (abbreviated as % Diff. in the table) of the model and FEM is compared with the experimental data. The mean percentage differences are 6.9% and 4.1% for the analytical model and FEM, respectively. The results presented are for 20 V_p of peak supply voltage.

Table 5.6: Summary of Validation Cases Studied in the Chapter 5

Case	Experiment	Model		FEM	
	Δ (μm)	Δ (μm)	% Diff.	Δ (μm)	% Diff.
1	79.8	7.2	86.0	82.0	2.8
2	22.3	2.6	22.9	23.0	3.1
3	59.8	10.8	67.1	63.7	6.5

Modelling of piezoelectric driven SJA attracts attention of the researchers for last two decades. Usually, the modal analysis of the piezoelectric actuator is overlooked and replaced by boundary conditions or assumptions. In the next chapter, synthetic jet actuator models based on the presented modal analysis (both analytical and finite element method) is developed to take advantage of the accurate modelling of the modal characteristics of the piezoelectric actuator. The analytical and FEM structural models needs to be combined with the fluidic-acoustic interaction to obtain accurate models of SJA.

Chapter 6

Extension and Experimental Validation of Physical Models for Synthetic Jet Actuators

6.1 Introduction

The synthetic jet actuator (SJA) is a compelling and challenging electromechanical-fluidic device due to the involvement of multi-physical disciplines (structural, acoustic, fluidic) and operational parameters (actuator geometry/size, diaphragm composition, actuation voltage and frequency) that motivate the need to have reliable modelling tools to minimise experimental testing time. The physical behaviour behind the actuator's operation should be studied in detail to understand the flow physics. A sufficient understanding of the isolated actuator would help develop modelling tools to assess and maximize the actuator's performance. High fidelity modelling of the isolated (i.e., on-bench) actuator would help towards the understanding of SJA, which would lead the focus of research towards the implementation of the actuator to an engineering application.

SJA's modelling efforts to-date can be classified into three categories: analytical, numerical, and lumped-element modelling (LEM). Within this project,

the modelling efforts focused on the two former types. Some authors, describe all models that are not computational fluid dynamics as lumped element models (LEM)[88]. The analytical and lumped-element models should be distinguished for a better understanding of the reader. Herein, the purely equation-based studies are referred to as analytical models. If the fluidic-acoustic-structural system was modelled using the idealisation of lumped elements such as mechanical (i.e., springs, dampers) or electrical (i.e., resistive, capacitive) elements, then they are referred to as an LEM study. LEM has a quick computation time and it is advantageous for parameter sensitivity studies; however, it does not have a comprehensive model of the piezoelectric diaphragm and may not necessarily provide accurate predictions of the jet velocity.

A fluid dynamics based analytical model of the synthetic jet actuator was studied by Sharma [18], in which the model constituted unsteady Bernoulli equation with continuity equation. The model employed a piston (i.e., moving wall) to emulate the piezoelectric diaphragm. By comparing orifice exit jet velocity results with Gallas's experimental jet velocity results [20], they obtained accurate match within 5% of the resonant peaks, achieving a better response than the original lumped element model presented by Gallas [20]. For a piezoelectric driven SJA, the diaphragm should be modelled so that the model can account for accurate mechanical resonance frequency and displacement profile. According to Sharma's model, the primary assumptions are that the mechanical resonance frequency and the force exerted (function of displacement) by the diaphragm are known [18].

De Luca and Girfoglio [69] used the governing equations of Sharma [18] and introduced a frequency coupling factor for increased resonance coupling strength with a tuning parameter. They pointed out that the resonant frequency and the force exerted cannot be known without further justifications, proposing:

- 1) A structural mechanics equation based on the dimensions and physical properties of the diaphragm substrate material (i.e., brass) to approximate the

mechanical resonance frequency of the diaphragm.

2) The force exerted by the diaphragm to be calculated based on the ratio of volume variation (ΔV) to uniformly distributed pressure load ($\frac{\Delta V}{p}$) then to be scaled with an electro-acoustic transduction coefficient (ϕ_a) which serves as a fitting parameter.

Nevertheless, De Luca and Girfoglio's [69] mechanical resonance equation is not accurate due to exclusion of the piezoceramic plate in the natural frequency calculation and the fitting parameter (ϕ_a) adds extra uncertainty to the model. Therefore, a more comprehensive approach for natural frequency modelling of the piezoelectric diaphragm is needed.

The first model presented in this study, called the fluidic dynamics based analytical model (hereafter referred to as analytical model), is adopted from the literature [18] and extended using the piezoelectric diaphragm model presented in Chapter 4. The so-called analytical model is an acoustic-fluid dynamics model integrated into a structural mechanics model of the piezoelectric diaphragm.

The SJA was also modelled using computational fluid dynamics (CFD) simulations, where Navier-Stokes equations are solved numerically. The main advantage of computational modelling is obtaining state variables at any point in the geometry and flow visualisation. Experimental flow visualisation techniques are challenging for an SJA. This is because it is difficult to get measurements to understand the flow physics inside the cavity. Therefore, the CFD simulation should be studied for more detailed quantitative and qualitative measurements. In the previous studies, the concentration was on the fluid-dynamics aspects of the actuator and flow visualisations [19, 102, 103]. The actuation mechanism was modelled as an oscillating wall boundary condition [101], or an inlet velocity boundary condition [102]. Without coupling a numerical piezoelectric diaphragm model with Navier-Stokes equations, the mechanical resonance cannot be known. Thus, CFD studies did not model the entire actuation frequency of the actuator. Usually, the studies are limited to a single actuation

frequency below the Helmholtz resonance frequency [19, 103]. Lv et al. also emphasized the importance of accurate modelling of the actuation mechanism for CFD models [70].

Another implication of using Navier-Stokes equations with the continuity equation and a turbulence model (if the flow is not laminar) is omitting the acoustics aspects of the actuator; Helmholtz resonance cannot be obtained.

Therefore, a CFD study should i) model the piezoelectric diaphragm to study the full spectrum of actuation frequency ii) capture flow visualisations at the mechanical resonance frequency iii) account for the pressure acoustics required to capture the Helmholtz resonance. The second model presented in this study is a multiphysics simulation developed within this project. The multiphysics model numerically computes coupled equations of viscous pressure acoustics with the structural mechanics of the piezoelectric disc.

The organisation of this chapter is as follows. In Section 6.2, the analytical model is studied, and selected cases are compared to experimental data in Section 6.3. In Section 6.4 the multiphysics model is introduced and also results are compared with selected experimental SJA cases. Numerical insights from the numerical models such as phase relationships, velocity and vorticity contours are investigated in Section 6.5. Then, the models, limitations and results are discussed in Section 6.6. Finally, in Section 6.7, a summary of the chapter is presented.

6.2 Analytical Modelling

In this section, the original model of Sharma [18] for a piston-based fluidic-acoustic analytical model is first reviewed. Hereafter, the model of Sharma is referred to as piston-based analytical model. The requirements for improvement of the existing model are evaluated for a piezoelectric diaphragm driven SJA. Then, the diaphragm driven SJA model is introduced which is a structural-fluidic-acoustic model.

6.2.1 Review of the piston-based fluidic-acoustic model

The fluidic-acoustic analytical model of SJA originates from the study of Sharma [18]. The model assumes a single degree-of-freedom mechanical system which is a piston-like (i.e., moving wall) excitation mechanism supported by a spring and damper for a Helmholtz resonator. The motion of the piston is coupled pneumatically to the cavity-orifice. This results in unsteady pressure fluctuations giving rise of fluid motion in the cavity and orifice. The fluid motion is modelled using an unsteady form of Bernoulli equation and continuity equation by assuming an isentropic process. Four differential equations are fed by different parameters, and they represent diaphragm displacement ($x_w(t)$), diaphragm velocity ($\dot{x}_w(t)$), pressure in the cavity ($p_i(t)$) and output jet velocity ($U(t)$).

The piston-based analytical model has the following assumptions:

- Driving force F_{ext} , applied by the piston, is known and it is a function of input voltage.
- Piezoelectric driven actuator behaves like a single degree of freedom mechanical system.
- Pressure inside the cavity is uniform except the near surroundings of the

orifice neck.

- Isothermal (constant temperature) and isentropic (adiabatic and reversible - no energy transformations occur due to friction or dissipative effects) process of the air contractions and expansions in the cavity.
- Cavity volume (V_o) is constant.

The piston-based analytical model consists of geometric, operational and fluid flow terms. The terms which appear in the governing equation block will be investigated in more detail below.

6.2.1.1 Effective Orifice Length

The orifice length needs to be corrected to account for the geometric end. Effective orifice length (l_e) is calculated by adding an inertia coefficient (C_I) based on orifice area (A_o).

$$l_e = l_o + C_I \sqrt{A_o} \quad (6.1)$$

An alternative expression for the effective orifice length is proposed by [69] and yields equivalent numerical values with Eq. 6.1. Δl_e was suggested as 0.62 and matches the values computed with Sharma's model for a circular orifice with sharp edges.

$$l_e = l_o + \Delta l_e \cdot d_o \quad (6.2)$$

Table 6.1 compares the numerical values of effective orifice length computed by Eq. 6.1 and Eq. 6.2 for the validation cases presented by Sharma [18] using C_I values of 0.705 and 0.86 for Case 1 and 2, respectively. The percentage difference between the two equations are 0.3% and 8% for Case 1 and 2, respectively. Therefore, Eq. 6.2 is adopted in this study to avoid the empirical C_I term in Eq. 6.1 which adds further uncertainty to the model.

Table 6.1: Comparison of effective orifice length equations

	Case 1 [18]		Case 2 [18]	
	Eq. 6.1	Eq. 6.2	Eq. 6.1	Eq. 6.2
Effective orifice length (mm)	2.681	2.673	1.48	1.36

6.2.1.2 Pressure Loss Term

The sudden contraction due to the flow motion from cavity to the orifice neck causes fluidic losses (K) which is expressed by $\beta_r (d_o/D_c)$ with C_d (orifice discharge coefficient). C_d is 0.6 for steady flow but for unsteady flow it varies cyclically and can be up to 0.88 [18].

$$K = \frac{1 - \beta_r^4}{C_d^2} \quad (6.3)$$

From a fluid dynamics perspective, the cavity and the orifice neck can be thought of as an unsteady pipe flow going through a sudden contraction. K value can be between 0.42 and 1 depending on the ratio of orifice diameter to cavity diameter. The piston-based analytical model used a value of $K=0.78$ for validation as its the best fit for the peak estimation of jet velocity [18].

6.2.1.3 Force Exerted By the Piston

Another term in the governing differential equations is F_{ext} , the force exerted by the piston to the fluid medium in the cavity. Equation 6.4a has the variables of forcing frequency (ω_f), mass of the diaphragm and the air in the cavity (m_t), acoustic piezoelectrical coefficient (D_a), applied voltage (V_{AC}) and piston surface area (A_w). Acoustic piezoelectric coefficient is given by Eq. 6.4b and it is a function of the fluid volume displaced by the piston (ΔV_0) and input supply voltage (V).

$$F_{ext} = \omega_n^2 m_t \frac{D_a V_{AC}}{A_w} \quad (6.4a)$$

$$D_a = \frac{\Delta V_0}{V_{AC}} \quad (6.4b)$$

6.2.1.4 Governing Differential Equations

The governing differential equations are given in the set of Equation 6.5 which consists of four coupled equations. The state vector consists of four variables which are x_w , \dot{x}_w , p_i and U as shown in Equation 6.5a.

Pressure contractions/expansions in the cavity-orifice arrangement is modelled using an isentropic contraction/expansion process together with the continuity equation by Equation 6.5b.

Equation 6.5c is employed for the acceleration of the orifice velocity. The fluidic (i.e., pressure) loss is a term that scales with (U^2) split into $|U|U$ to account for the positive velocity for expulsion and negative velocity for suction. The acceleration of the diaphragm modelled using the forced vibration with viscous damping equation is presented in Equation 6.5d.

Overall, the orifice-cavity arrangement is modelled using the unsteady continuity equation for air that undergoes an isentropic process for the expulsion and ingestion. The unsteady Bernoulli equation is coupled with the continuity equation and accounts for the sudden contraction due to the large d_o/D_c . The moving wall's motion is modelled with a second-order forced vibration equation with a viscous damping term.

$$p = \dot{p}_i dt, x_w = \dot{x}_w dt, \dot{x}_w = \ddot{x}_w dt, U = \dot{U} dt \quad (6.5a)$$

$$\dot{p}_i = \frac{\gamma A_w P_o}{V_o} \dot{x}_w - \frac{\gamma A_o P_o}{V_o} U \quad (6.5b)$$

$$\dot{U} = \frac{p_i}{\rho l_e} \dot{x}_w - \frac{K}{2l_e} |U|U \quad (6.5c)$$

$$\ddot{x} = \frac{F}{m_{wt}} \dot{x}_w - \frac{p_i A_w}{m_{wt}} 2\zeta_w \omega_w \dot{x}_w - \omega_w^2 x_w \quad (6.5d)$$

Figure 6.1 presents a schematic of the model used by Sharma in piston-based analytical model, showing its inputs and outputs [18].

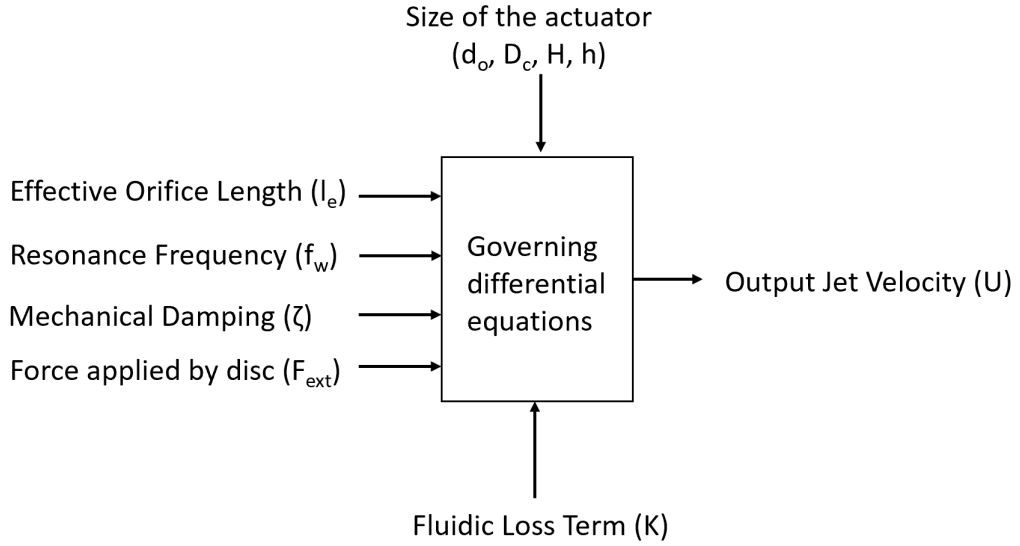


Figure 6.1: Block diagram of the piston-based analytical model

6.2.2 Improvement requirements of the piston-based analytical model

In the piston-based analytical model, the mechanical resonance frequency is an input, and it was not mentioned how the resonant frequency of the diaphragm should be obtained. This is the first point that needs to be addressed. The piston-based analytical model presented by Sharma [18] considers a piston rather than a piezoelectric diaphragm without addressing the following points. In their model, Sharma [18], proposed Equation 6.6 to calculate the mechanical resonance frequency. The stiffness term k_w is not related to the piezoelectric disc and it's not detailed how this term should be obtained. Therefore, the mechanical resonance frequency, f_m , which is a direct input to the model, is unknown before an experimental test.

$$\omega_n = \sqrt{\frac{k_w}{m_{wt}}} = 2\pi f_m \quad (6.6)$$

Secondly, the force exerted by the diaphragm (F_{ext}) is assumed to be known. However, to calculate F_{ext} , effective acoustic piezoelectric coefficient (D_a) is required, and that parameter is different for every diaphragm and supply voltage. Thus, D_a is an ill-defined parameter that needs a systematic approach

and stands out as a critical limitation of the piston-based analytical model.

Thirdly, the assumption that the piezoelectric disc behaves like a single-degree-of-freedom mechanical system (supported by spring and damper like a piston) should be investigated. This is a particular issue as the piston's deflection profile does not fully reflect the parabolic deflection profile of the piezoelectric diaphragm. Moreover, it does not take into account the composition of the piezoelectric diaphragm, material properties, and the way the diaphragm is clamped.

Equation 6.7 shows the alternative expression to replace the D_a term in the piston-based analytical model. The integral of displacement profile from centre ($r=0$) to the outer radius ($r=R_2$) of the diaphragm, divided by the supply voltage would produce a value for D_a .

$$D_a = \frac{\Delta V}{V_{AC}} = \frac{\int_0^{R_2} w(r) 2\pi r dr}{V_{AC}} \quad (6.7)$$

The analytical model aims to provide a quick measure of the output jet velocity. From a designer point of view, the ill-defined terms in the model complicate actuator design and test. The ideal analytical model should employ fundamental and easy-to-obtain parameters such as applied voltage and transverse piezoelectric coefficient, d_{31} , to calculate the force applied by the disc. This can be done by obtaining the natural frequency and displacement profile of the diaphragm from the structural model (presented in Chapter 5.2) to integrate Equation 6.7.

Other assumptions of uniform pressure distribution in the cavity (except the proximity of the orifice neck), isothermal and isentropic expansion/contraction and constant cavity volume ($\Delta V \ll \Delta V_o$) are acceptable for relatively small diaphragm displacement ($\frac{\Delta V_o}{\Delta V} < 0.1$). These assumptions should be re-considered for large transverse displacements ($\frac{\Delta V_o}{\Delta V} > 0.1$), which would be the case in single crystal piezoceramic, bimorph diaphragm, or high supply voltage applications.

6.2.3 Diaphragm-based Analytical Model

The model can be extended by integrating the analytical piezoelectric diaphragm model which would take into account the composition of the diaphragm, clamping and calculate the force exerted by the diaphragm leaving the only empirical term as the mechanical damping.

The change from the wall like deflection to a diaphragm model is illustrated in Figure 6.2.

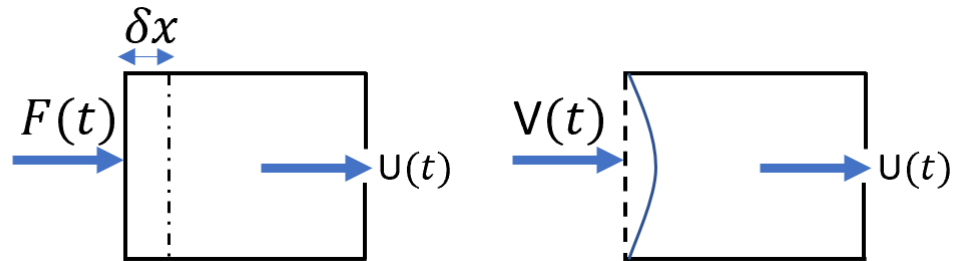


Figure 6.2: Wall deflection (piston-based analytical model) to diaphragm deflection (diaphragm-based analytical model)

The diaphragm-based analytical model consists of four ordinary differential equations (see Equation 6.5) and integrated to structural mechanics model of the piezoelectric diaphragm. A block diagram of the diaphragm-based analytical model is presented in Figure 6.3. The structural mechanics model is linked to the fluidic-acoustic model to input mass of the diaphragm, natural frequency of the diaphragm, mechanical damping and force applied by the diaphragm.

Figure 6.4 presents a non-dimensional transverse deflection profile from the structural mechanics model. A small discontinuity is observed at $r/R = 0.733$ due to the step-change corresponding to the piezoceramic patch.

F_{ext} is computed by numerically integrating the area under the line to calculate the stroke volume as shown in Eq. 6.7.

The governing differential equations (Eq. 6.5) are reduced to first order form and solved using a 4th order Runge-Kutta scheme on MATLAB's differential equation solver [115]. A time-step of 5×10^{-5} second is used for a timespan of

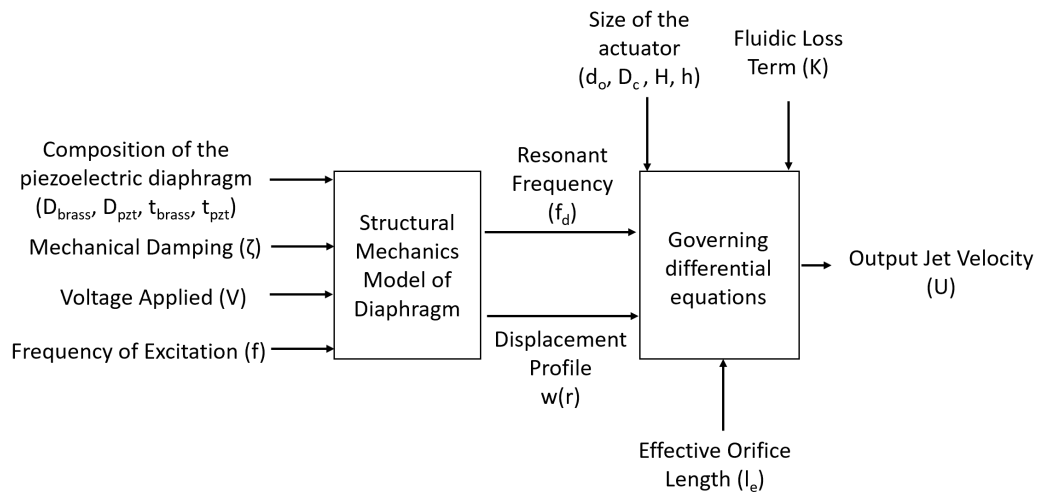


Figure 6.3: Block diagram of the diaphragm-based analytical model

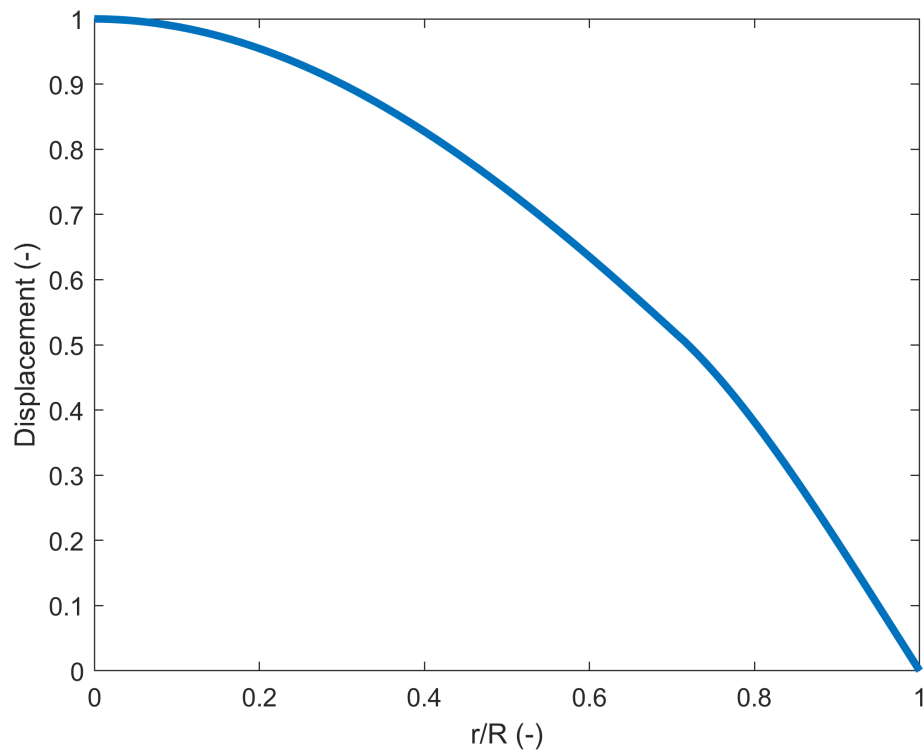


Figure 6.4: Deflection of the diaphragm from the structural model

1 second for each forcing frequency. MATLAB's 'ode45' sub-routine was employed for the simultaneous solution of the four ordinary differential equations. Initial conditions for all four state variables were set to zero and then iterated in time.

6.3 Validation of the Diaphragm-based Analytical Model

The diaphragm-based analytical model is validated against three sets of in-house experimental data throughout the actuation frequency envelope, to include cavity acoustic (i.e. Helmholtz) and diaphragm mechanical resonance and beyond. All validation cases utilise a opposite orifice-diaphragm configuration SJAs. Validation Case 1 and 2 have a common actuator geometry and size. They both employed the velocity-optimized actuator dimensions for a 27 mm diaphragm [66]. However, the piezoelectric actuator used in Case 1 and 2 are different, second case utilise a significantly thinner diaphragm. The performance of the dimensions are also confirmed within the experimental campaign run in this study which exhibits a bimodal frequency response. Validation Case 3 is designed to have a single dominant peak in the frequency response. All three cases benefit from opposite diaphragm-orifice configuration SJA design. The supply voltage is kept constant at $20 V_p$ for all validation cases.

Before proceeding to the validation cases, the methods and mathematical notation in the validation cases should be introduced. The displacement profiles are for the diaphragm mounted in the actuator, unlike the cases presented in Chapter 5.5. The displacement profiles relate to the centre of the diaphragm at all actuation frequencies. All presented quantities (diaphragm displacement, in-cavity pressure or output jet velocity) are calculated based on the positive peak averaging of the associated signals for both experiment and models. Peak averaging is a common method in the field as the time-average of synthetic jet quantities tend to zero [66, 81].

Figure 6.5 demonstrates a sample sinusoidal signal in which the peaks are marked with black dots. The positive peaks (i.e., black dots) are averaged to compute the mean peak quantity of the associated signal such as in-cavity pressure and exit jet velocity.

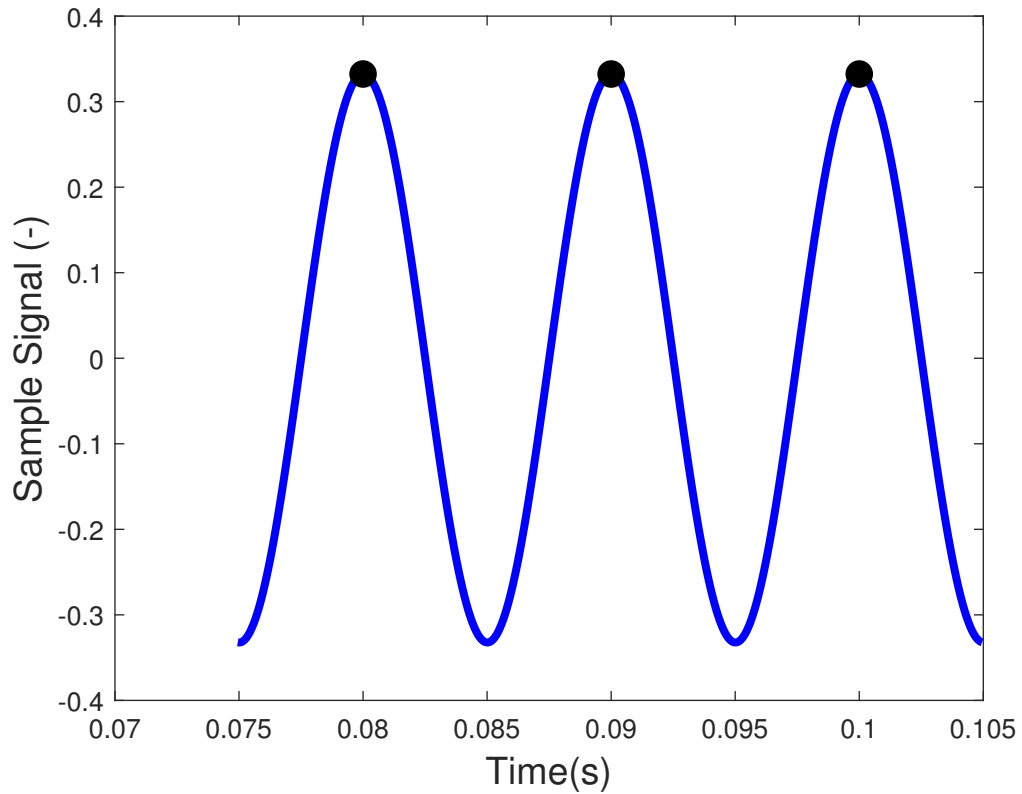


Figure 6.5: A Sample Signal and Peaks

6.3.1 Validation Case 1

Table 6.2 presents physical properties of the diaphragm and actuator, model parameters and expected resonance frequency of the first validation case. Helmholtz resonance frequency (f_h) is computed by Eq. 2.5, presented in Chapter 2.6.2 and the mechanical resonance frequency (f_m) of the diaphragm is computed by the structural mechanics model presented in Chapter 4.4.

Figure 6.6 presents the comparison between the peak centre diaphragm displacement of the model and experiment. The model matches experimental peak both in frequency and displacement magnitude (percentage difference of 1%). The peak displacement at the mechanical resonance is $15.8 \mu\text{m}$. A displacement increase around the Helmholtz resonance is observed which is due to increased pressure loading on the diaphragm. The model overestimated the diaphragm displacement by around $1 \mu\text{m}$. The displacement increases due to the cavity acoustic (i.e., Helmholtz) resonance at 1400 Hz which is around 400 Hz earlier than the theoretical cavity acoustic resonance given in Table 6.2.

Table 6.2: Validation Case 1 - Diaphragm and actuator size, model parameters and computed resonance frequency

Parameter	Value
D_{brass} (mm)	27
D_{pzt} (mm)	19.8
t_{brass} (mm)	0.22
t_{pzt} (mm)	0.23
d_{31} (m/V)	-180×10^{-12}
d_o (mm)	1.2
D_c (mm)	25
h (mm)	2.5
H (mm)	0.67
ζ (-)	0.0324
K (-)	0.78
F_{Ext} (N)	0.531
f_h (Hz)	1772
f_m (Hz)	2878

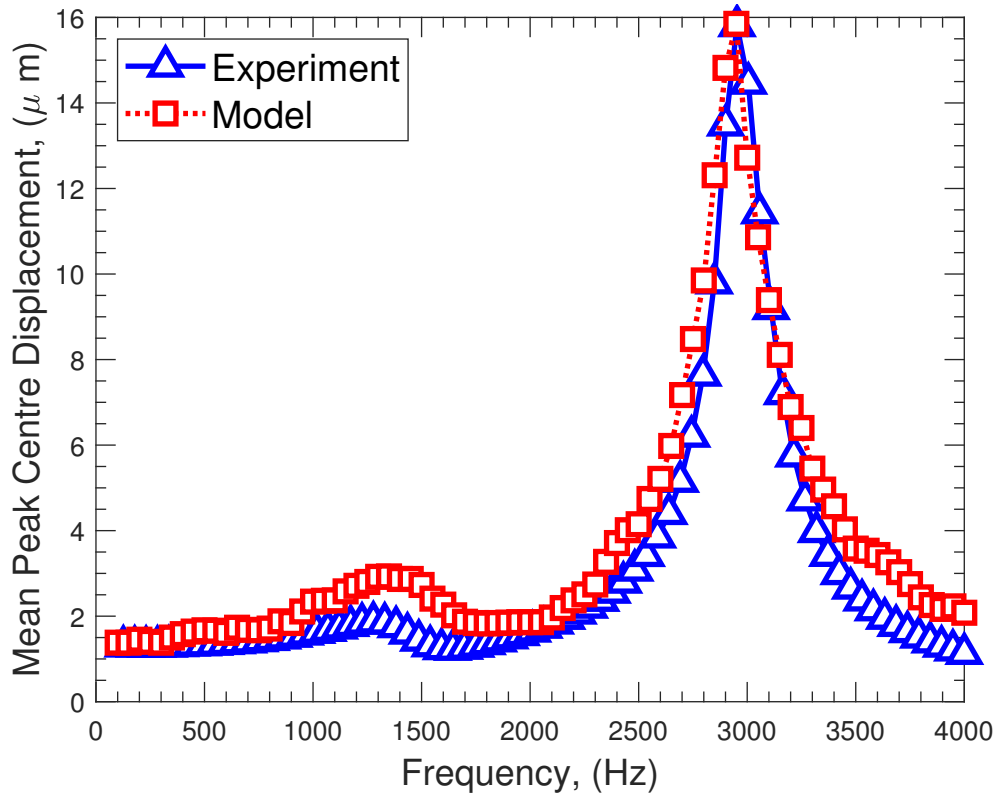


Figure 6.6: Validation Case 1 - Diaphragm displacement comparison of the model and experiment

Figure 6.7, compares the in-cavity pressure measured experimentally and predicted by the analytical model. It can be seen that the pressure in the cavity is over-calculated throughout the envelope of the forcing frequency. The over-

estimation is thought to be due to the assumption of an isentropic process. At the resonant peak which corresponds to 2900 Hz, the difference between the experiment and the model is 170 Pa, corresponding to a difference of 6.4%.

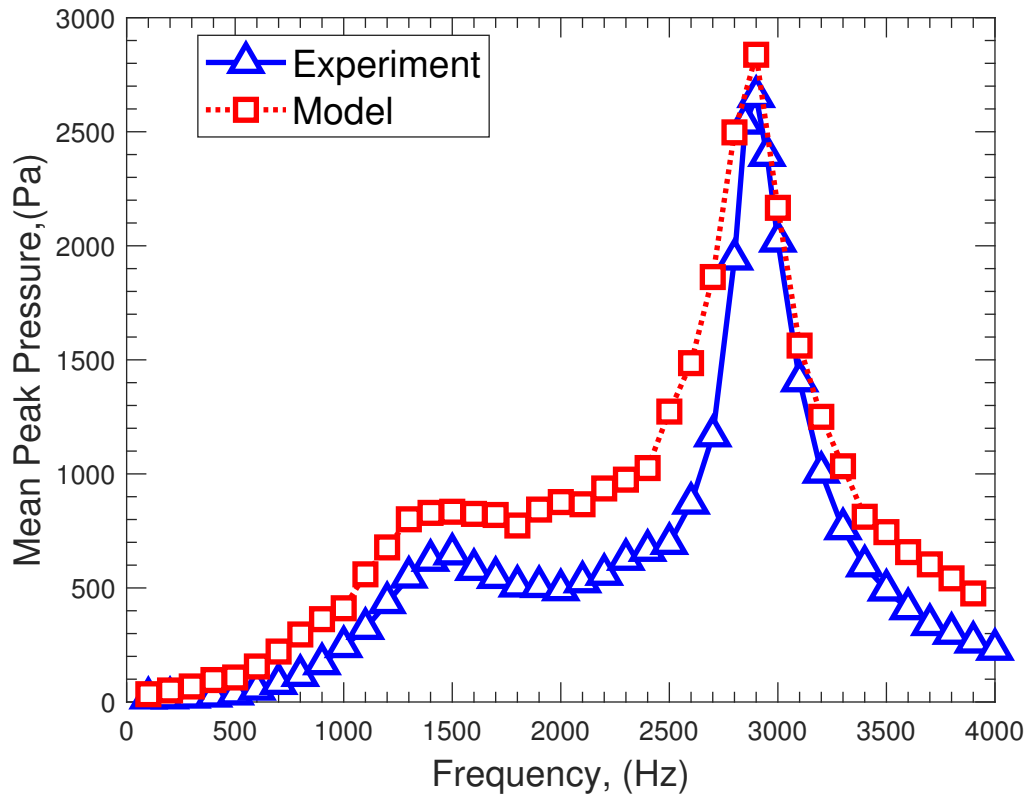


Figure 6.7: Validation Case 1 - Cavity pressure comparison of the model and experiment

Figure 6.8 presents the output jet velocity comparison of the analytical model and experimental data. The model matched the resonant peaks for their frequency position and velocity magnitudes with a significant overestimation in the middle actuation frequency region which is between the Helmholtz and mechanical diaphragm resonance. The middle actuation frequency region is partially influenced by both, and the present model does not account for the coupling between the two resonances. The actuation frequency plays an important role in the losses, and the fluidic loss term is used as a bulk parameter (constant for all actuation frequency) which gives a reasonable estimation for the peak jet velocity (corresponding to f_m). In this case, the particular jet velocity decreases in the middle region between two resonances is due to the increase in fluidic loss, in conjunction with the actuation frequency increase,

which is not attained at a resonance.

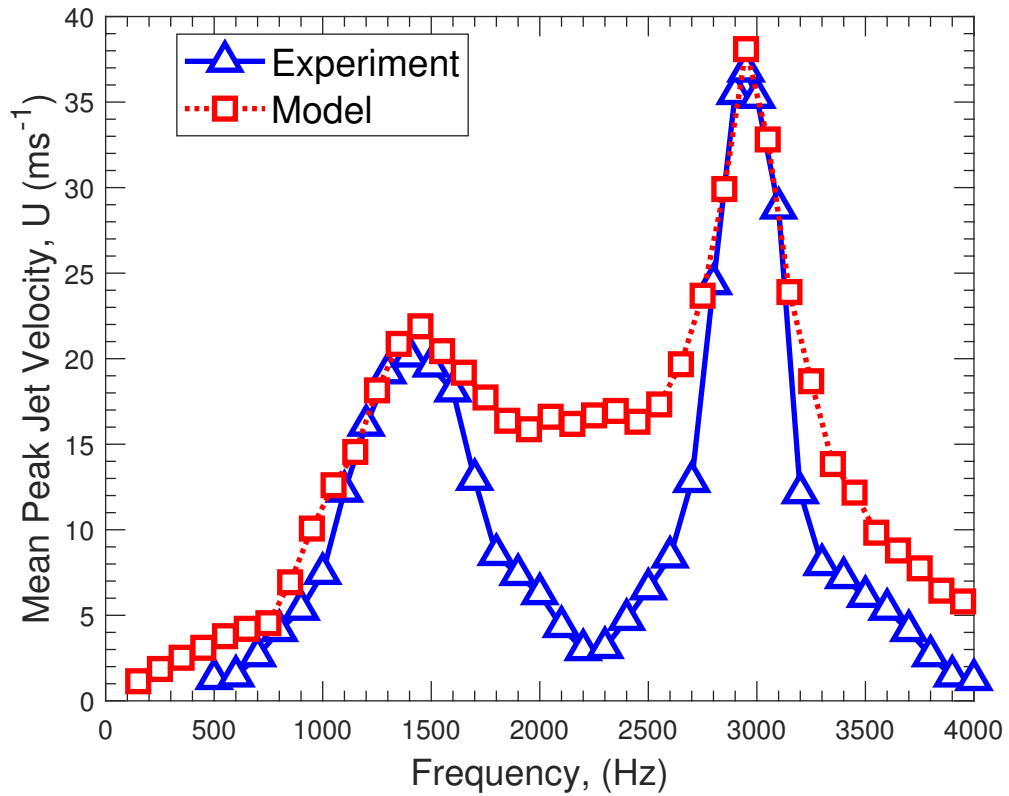


Figure 6.8: Validation Case 1 - Mean jet velocity comparison of the model and experiment

Table 6.3 compares the Helmholtz and mechanical resonance peaks identified by the model and their respective jet velocity. The calculated Helmholtz frequency (1701 Hz) is realised as 1400 Hz in the experiments, which is due to the shallow cavity employed for the study. The overestimation of the Helmholtz frequency is 18%, consistent with previously reported observations [66].

Table 6.3: Validation Case 1 - Comparison of model and experiment results at resonant frequency

Resonance frequency	Helmholtz		Mechanical	
	Model	Experiment	Model	Experiment
Frequency (Hz)	1350	1400	2950	2950
Jet Velocity (ms^{-1})	22.6	20.1	37.3	36.8

6.3.2 Validation of Isothermal Operation Assumption

It is mentioned in Section 6.2.1, that the model assumes isothermal expansion and contraction during in the ejection and suction cycles of the piezoelectric diaphragm. The validity of the assumption was not checked experimentally. Also, temperature measurements regarding the cavity and orifice exit is often not reported in the literature. Figure 6.9 presents the change in the SJA temperature at $20 V_p$ which actuates at the mechanical resonance frequency of the diaphragm.

For the first five seconds the actuator is switched off and then the voltage is applied for 10 seconds. After the first 5 seconds of actuation, a thermal equilibrium is reached in the cavity with a ΔT of 0.65° Celsius. Outside the orifice, the temperature is reduced by -0.3° Celsius of ΔT . After 10 seconds, the temperature at the orifice exit starts to increase which exceeds the initial temperature.

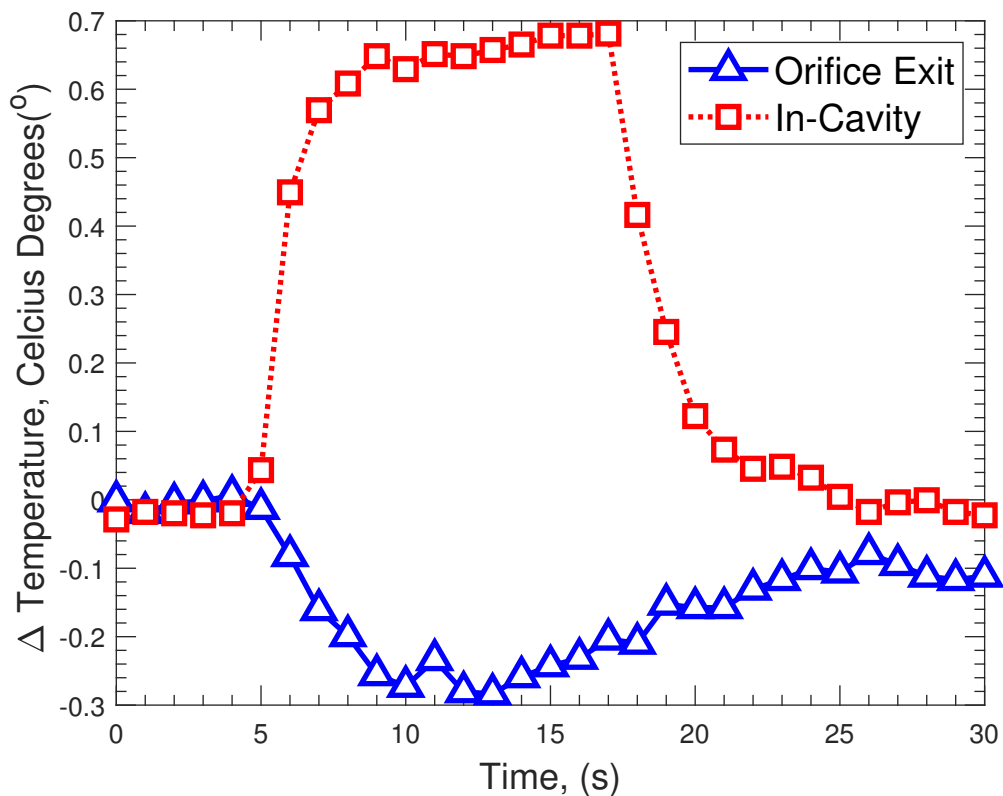


Figure 6.9: Temperature measurements of the in-cavity and orifice exit at the resonance frequency

The temperature profile of other actuation frequencies does not provide significant change in the temperature, and are not reported. Therefore, it can be deduced that the temperature change both in-cavity and orifice exit is not significant. The assumption regarding isothermal process is verified and not expected to break the validity of the model for this supply voltage. The experimental temperature data presented in section is representative for the other two validation cases and therefore not presented separately.

6.3.3 Validation Case 2

The second validation case employs the same actuator (i.e., cavity-orifice) with a different diaphragm. The substrate diameter (i.e., brass diameter) and piezoceramic diameter are the same as Validation Case 1, but the total thickness is 38% less.

Table 6.4 presents the dimensions, physical properties of the diaphragm and actuator and resonance frequency calculations. The resonance frequency calculations reveals that the frequency of the Helmholtz and diaphragm mechanical resonance are much closer and only 8 Hz away from each other. This is expected to amplify the output jet velocity of the actuator. Nevertheless, it should be noted that the calculated frequency values of the Helmholtz and diaphragm mechanical resonance are for the isolated cases (i.e., only Helmholtz resonance or only diaphragm). The resonance frequencies may vary due to the non-linear interaction of the cavity acoustic resonance and the diaphragm mechanical resonance.

Figure 6.10 presents the centre peak displacement of the diaphragm obtained using the model and experiment. It is observed that the displacement corresponding to the cavity acoustic resonance is identified at 1200 Hz according to the model and at 1300 Hz in the experiment. The mechanical resonance of the diaphragm is located at 2400 and 2440 Hz in the model and experiment (1.7%), respectively. It is noticeable that the agreement provided by the

Table 6.4: Validation Case 2 - Diaphragm and actuator size, and model parameters

Parameter	Value
D_{brass} (mm)	27
D_{pzt} (mm)	19.8
t_{brass} (mm)	0.15
t_{pzt} (mm)	0.13
d_{31} (m/V)	-180×10^{-12}
d_o (mm)	1.2
D_c (mm)	25
h (mm)	2.5
H (mm)	0.67
ζ (-)	0.036
K (-)	0.78
F_{Ext} (N)	0.647
f_h (Hz)	1772
f_m (Hz)	1780

structural model is closer to experiment than that for the diaphragm mechanical resonance frequency. The experimental peak centre diaphragm is $1.36 \mu\text{m}$ larger than the model's prediction, corresponding to a percentage difference of 7.4%. The SJA diaphragm displacement response which possess two resonant peaks is similar to that reported by Krishnan and Mohseni [146].

Figure 6.11 presents the mean peak jet velocity of the model and the experiment. The thinner disc employed would have a larger peak centre displacement thus a higher jet velocity at the resonant frequency. The Helmholtz (i.e., acoustic cavity) and mechanical resonances are located accurately with differences in jet velocity of $(-)$ 4.4 ms^{-1} and 1.25 ms^{-1} , respectively. The percentage difference between the experimental and computational peaks are -11.8% and 2.4% for Helmholtz and mechanical resonance, respectively.

Similar to Validation Case 1, the middle actuation frequency region between the acoustic cavity resonance and the mechanical diaphragm resonance is over-estimated. The coupling mechanism due to the resonances is not taken into account by the current model. The computations are done based on the detection of frequency and associated jet velocity for the resonance frequency. It can be suggested that the bulk parameter of fluidic loss (K) is higher in the

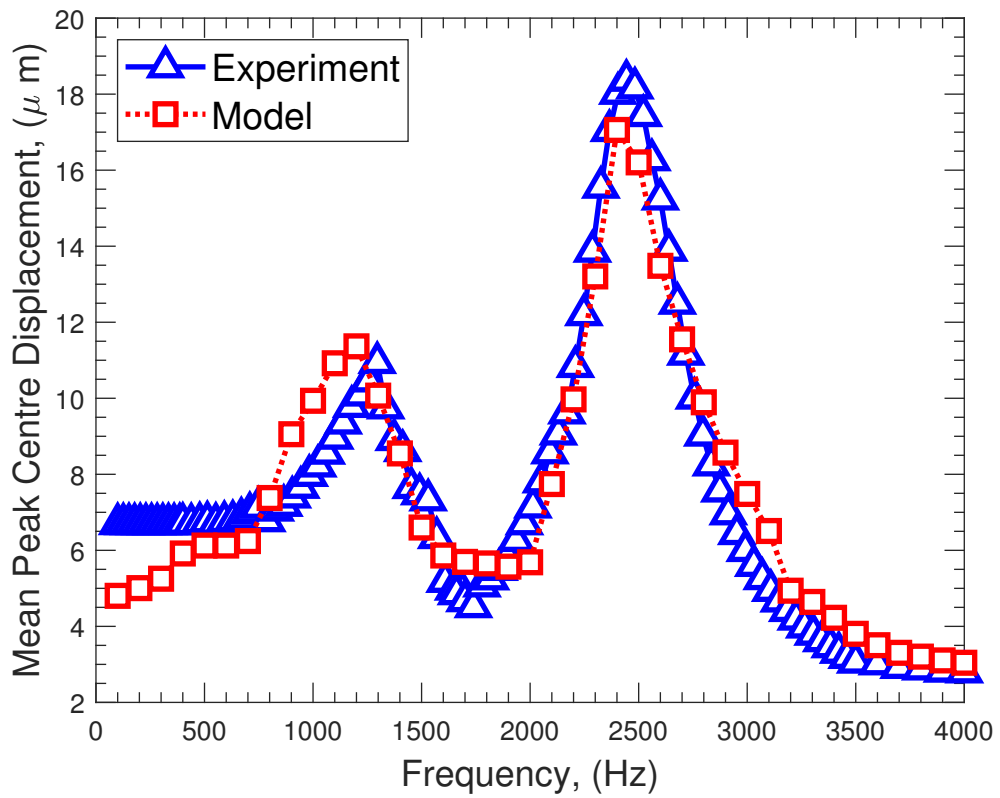


Figure 6.10: Validation Case 2 - Diaphragm displacement comparison of the model and experiment

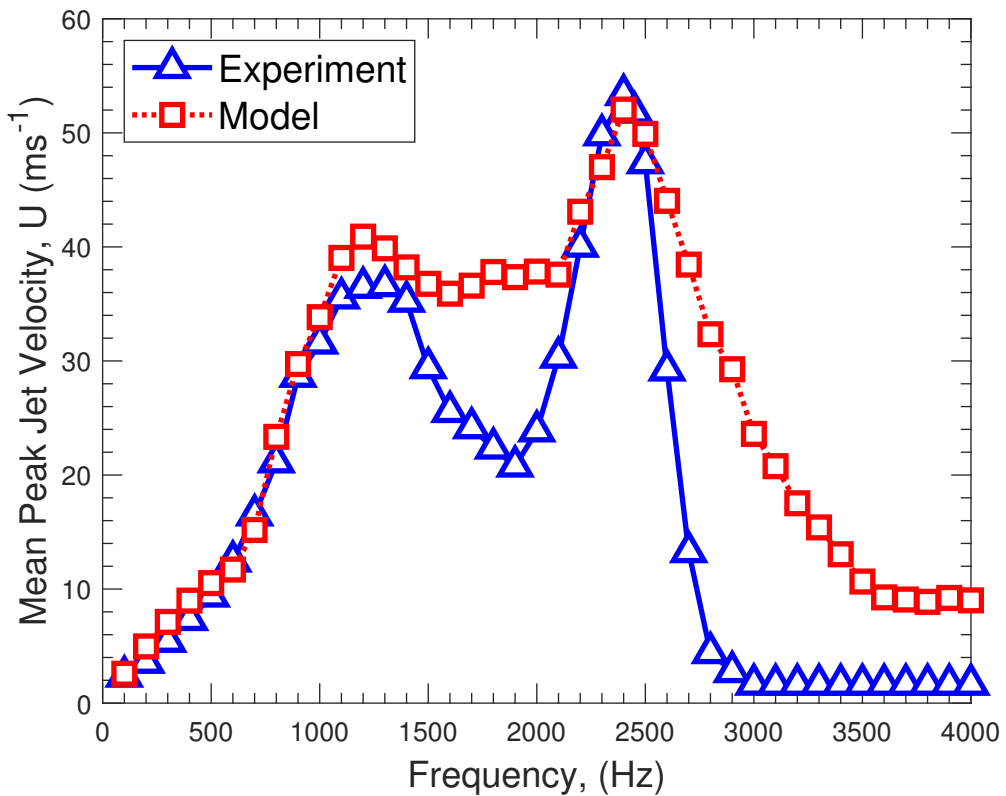


Figure 6.11: Validation Case 2 - Mean peak jet velocity comparison of the model and experiment

middle region as the actuation frequency in the region promotes higher losses. However, the actuation frequency between 1500 Hz & 2200 Hz; is not under the influence of any resonance frequency and therefore, does not turn into a higher jet velocity. A similar problem is also observed after 2600 Hz where the fluidic loss increase due to the increased actuation frequency.

Table 6.5 presents the frequency and corresponding jet velocity of the Helmholtz and mechanical resonance.

Table 6.5: Validation Case 2 - Comparison of model and experiment results at resonant frequency

Resonance frequency	Helmholtz		Mechanical	
	Model	Experiment	Model	Experiment
Frequency (Hz)	1200	1300	2400	2400
Jet Velocity (ms^{-1})	40.9	36.6	52.1	53.4

This experiment and its validation have two aspects worthy of being noted. Firstly, the thinner diaphragm employed produces a higher displacement (nearly four times of the 'disc-only' cases compared to the diaphragm used in Validation Case 1). Thus, higher peak jet velocity is obtained, which the model matched with an acceptable difference, especially at the resonant frequencies. The diaphragm displacement response on the actuator has a large damping due to increased viscous effects, compared to the 'only-disc' cases. The jet velocity corresponding to the Helmholtz resonance velocity is relatively high, both in the experiment and the model.

Two resonance frequencies, Helmholtz (i.e., cavity acoustic) and diaphragm mechanical, are close to each other in theory. However, it is observed that the cavity acoustic resonance has taken place at 1300 Hz (expected at 1770 Hz) and the mechanical diaphragm frequency at 2400 Hz (expected at 1780 Hz). The relative positioning of the resonance frequencies are similar to Gallas's [20] observation of the acoustic and mechanical resonance frequency.

For clarification and obtaining a broader understanding regarding the case 2, the analytical model is used with the same geometry but with a more stiff di-

aphragm. Assuming a natural frequency of 10 kHz is sufficiently away from the calculated Helmholtz resonance. This should fully decouple the interaction between two resonances. Figure 6.12, shows the exit jet velocity of model for the decoupled resonance frequencies. The Helmholtz resonance is located at 1800 Hz and the mechanical resonance is located at 10 kHz as per the input resonance frequency. The output jet velocity corresponding to the resonance peaks are 8 ms^{-1} and 40 ms^{-1} corresponding to the cavity acoustic and diaphragm mechanical resonance, respectively. Thus, in validation case 2, the coupling of the two resonance frequencies, enhanced the velocity of both acoustic cavity resonance and diaphragm mechanical resonance.

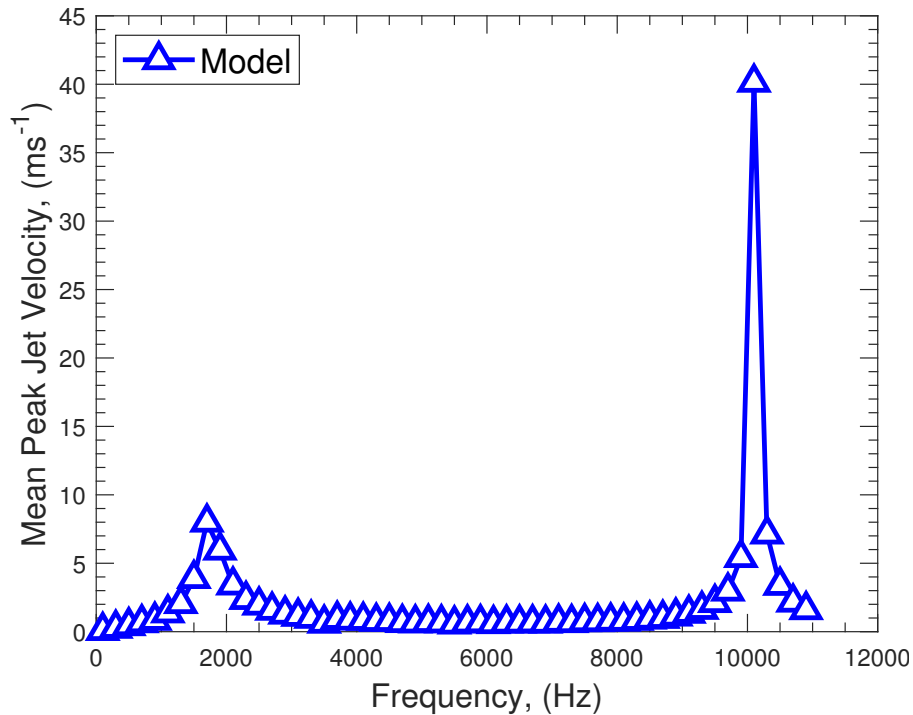


Figure 6.12: Validation Case 2 - Stiff Diaphragm with $f_m = 10 \text{ kHz}$

By using a thicker (stiffer) piezoelectric actuator, the cavity acoustic and diaphragm mechanical resonances can be separated. Thus, the case demonstrated with the stiff diaphragm shows even though a single dominant peak frequency response is not obtained (which was expected as per the resonance frequencies presented in Table 6.4), the jet velocity is enhanced due to the theoretically matching resonance frequencies. This case, together with the other two validation cases, are discussed in Section 6.6.

6.3.4 Validation Case 3

Validation Case 3 employs a larger diaphragm diameter of 35 mm and is designed to have a single modal response rather than a bimodal response like in the prior validation cases. A similar experiment was conducted [20], but that study did not reveal critical experimental results such as diaphragm displacement profile and power efficiency.

Validation Case 1 and 2 have helped towards developing an understanding for a design towards a single modal frequency response of the SJA. Placement of the resonant frequencies close to each other should be carefully investigated. In validation Case 1, the 'theoretical' difference between the resonant peaks ($f_m - f_h$) is 1100 Hz and, 8 Hz in validation Case 2. In this particular case, the difference between the two resonant frequencies are designed to be 700 Hz. The actuator size and important parameters of the analytical model are summarized in Table 6.6 together with the calculated resonance frequencies.

Table 6.6: Validation Case 3 - Diaphragm and actuator size, and model parameters

Parameter	Value
D_{brass} (mm)	35
D_{pzt} (mm)	25
t_{brass} (mm)	0.2
t_{pzt} (mm)	0.1
d_{31} (m/V)	-180×10^{-12}
d_o (mm)	0.84
D_c (mm)	33
h (mm)	0.84
H (mm)	4.65
ζ (-)	0.03
K (-)	0.78
F_{Ext} (N)	0.412
f_h (Hz)	552
f_m (Hz)	1256

To assess the performance of the model, peak centre displacement of the diaphragm and the mean peak jet velocity are compared. It should be noted that the actuation frequency range, for this validation case, is limited from 100 Hz to 2500 Hz which is sufficient to cover well beyond the resonance frequency, as

2500 Hz = $2 \times f_m$. The frequency sweep of the diaphragm displacements of the experiment and analytical model are compared in Figure 6.13.

The resonant frequency computed by the integrated analytical model match with the experimental peak. The peak centre displacement is $46.5 \mu\text{m}$ and $44.3 \mu\text{m}$, in the model and experiment, respectively. The peak displacement is overestimated by $2.2 \mu\text{m}$ from the model, corresponding to a percentage difference of 4.7%.

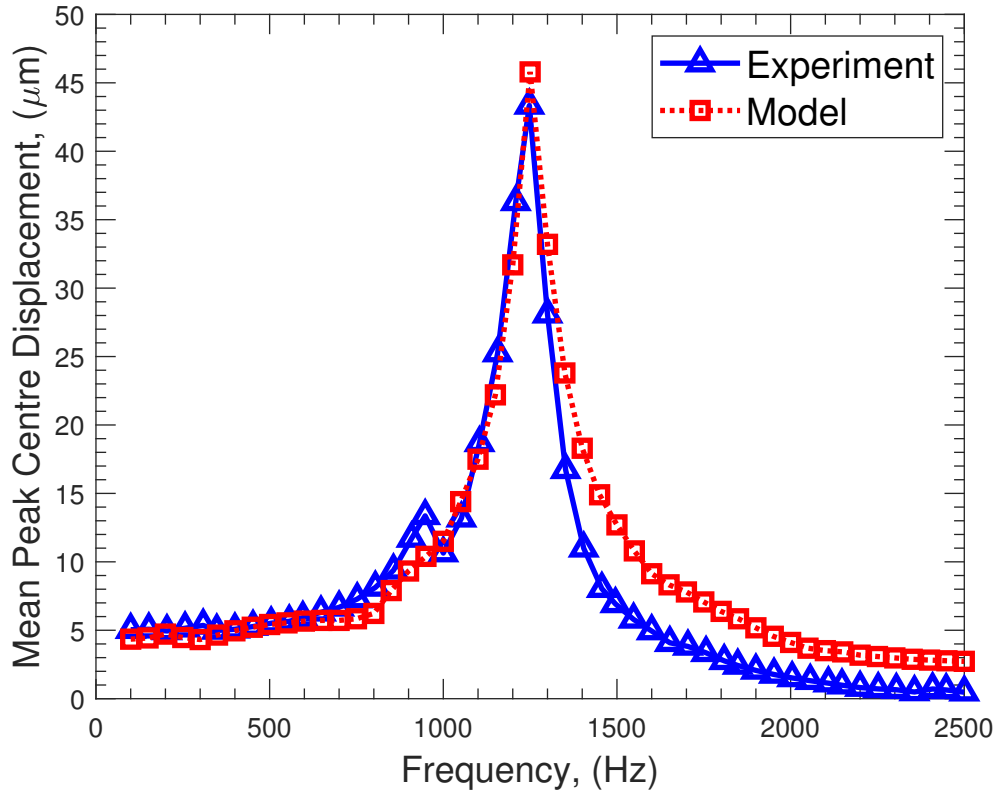


Figure 6.13: Validation Case 3 - Diaphragm displacement comparison of the model and experiment

Figure 6.14 presents the computed output jet velocity computed by the analytical model and obtained experimentally. Firstly, the peak jet velocity at the resonance matches with the experimental value with a difference of 0.6 ms^{-1} , corresponding to a percentage difference of 1.1%. As per the design goal of this actuator and diaphragm thickness selection, a single dominant peak is obtained. By inspecting the jet velocity frequency sweep, it can be observed that the cavity acoustic resonance is suppressed or damped.

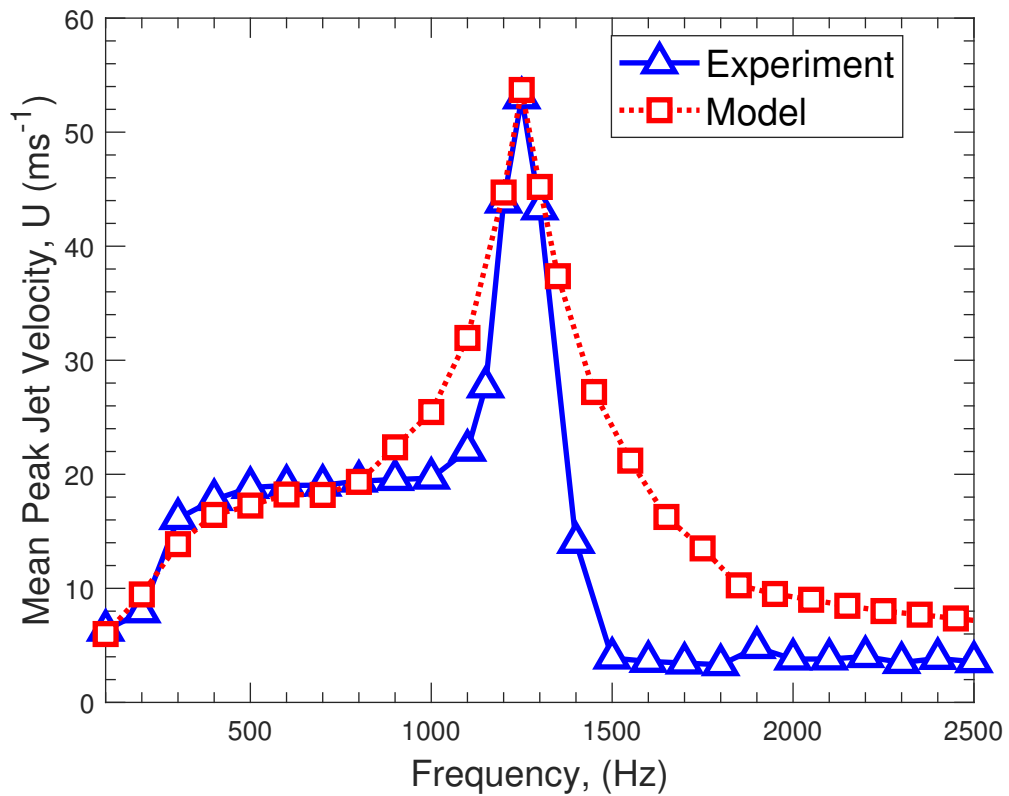


Figure 6.14: Validation Case 3 - Peak Jet Velocity Comparison of the model and experiment

Table 6.7 compares the results of model and experiment for the single modal resonant frequency and their respective jet velocity, for the single visible peak.

Table 6.7: Validation Case 3 - Comparison of model and experiment results at resonant frequency

Resonance frequency	Model	Experiment
Frequency (Hz)	1250	1250
Jet Velocity (ms ⁻¹)	53.7	54.3

In this case, the theoretical Helmholtz resonance frequency and the diaphragm mechanical resonance are 700 Hz away from each other. It is observed that the peak corresponding to the cavity acoustic resonance is not visible but blended into the mechanical diaphragm resonance which takes place at the expected frequency. In validation Case 1, where a bimodal response is identified, the difference between the two resonant frequencies was 1500 Hz. When the same actuator is used with a thinner diaphragm of mechanical resonance frequency of

2400 Hz, the frequency response became bimodal with cavity acoustic resonant taking place at 1000 Hz (therefore, $f_m - f_h = 1400$ Hz). From this investigation it is evident that bringing resonances closer would result in a higher peak jet velocity response. This is an observation in which the conditions of the other cases (i.e., Validation Case 2) is not the same. The suppression of the peak associated with the cavity acoustic resonance is further investigated in Section 6.6.

6.4 Multiphysics Modelling

Compared with the analytical model, the modelling of SJA can adopt a more sophisticated approach; multiphysics modelling. The quick computational time of the analytical model can be sacrificed to obtain more complex data, alter the geometry without a requirement to tune the parameters, and have good quality flow visualisations, enabling one to understand and comment on the flow physics of the actuator.

6.4.1 Mathematical Model - Pressure Acoustics with Viscosity

The finite element model equations of the piezoelectric actuator is given in Chapter 5.6 which is coupled with the pressure acoustic equations given in this section. An unsteady pressure, due to the oscillation of the diaphragm, inputs to the air medium in the cavity.

The set of equations used in this study adopts a pressure based approach with viscous flow. COMSOL Multiphysics [136] employs finite element methods for the discretization of the equations. If no fluidic loss and thermal conduction is assumed for a physics problem, then the solution can be reached by solving Euler's equation (inviscid momentum equation) and continuity equation.

$$\frac{\partial \mathbf{u}}{\partial t} + (\mathbf{u} \cdot \nabla) \mathbf{u} = -\frac{1}{\rho} \nabla p \quad (6.8)$$

$$\frac{\partial \rho}{\partial t} + \nabla \cdot (\rho \mathbf{u}) = 0 \quad (6.9)$$

Pressure acoustics is coupled with thermo-viscous acoustic physics to enable the computation of the viscosity and related losses.

Re-arranging the equations with linear perturbations yields the following equation which is an expression of the wave equation for sound waves in a lossless medium:

$$\frac{1}{\rho c^2} \frac{\partial^2 p}{\partial t^2} + \nabla \cdot \left(-\frac{1}{\rho} (\nabla p - \mathbf{q}_d) \right) = Q_m \quad (6.10)$$

The pressure term can be approximated by a time-harmonic wave with:

$$p(\mathbf{x}, t) = p(\mathbf{x}) e^{i\omega t} \quad (6.11)$$

The wave equation for acoustic waves reduces to an inhomogeneous Helmholtz equation where Q_m term is the monopole domain source (radiates sound isotropically equally in all directions) and q_d is the dipole domain source (does not radiate sound isotropically):

$$\nabla \cdot \left(-\frac{1}{\rho} (\nabla p - \mathbf{q}_d) \right) - \frac{\omega^2 p}{\rho c^2} = Q_m \quad (6.12)$$

A loss term in terms of a damping coefficient (d_a) can be added as a first order time derivative:

$$\frac{1}{\rho c^2} \frac{\partial^2 p}{\partial t^2} - d_a \frac{\partial p}{\partial t} + \nabla \cdot \left(-\frac{1}{\rho} (\nabla p - \mathbf{q}_d) \right) = Q_m \quad (6.13)$$

For compressible flow, full set of linearised Navier-Stokes equations are solved together with the continuity equation. This equation is used at the orifice neck and near surroundings where the effects of viscosity dominates the flow

characteristics.

The effects of turbulence are simulated by an eddy viscosity coefficient, μ . The eddy viscosity approach for the turbulence closure problem is proved to be effective for oscillatory jets [147].

$$\rho_0 \frac{\partial \mathbf{u}_t}{\partial t} = \nabla \cdot \left[-p_t \mathbf{I} + \mu \left(\nabla \mathbf{u} + (\nabla \mathbf{u}_t)^T \right) - \left(\frac{2}{3} \mu - \mu_B \right) (\nabla \cdot \mathbf{u}_t) \mathbf{I} \right] \quad (6.14)$$

6.4.2 Geometry, Meshing and Time Domain Study

The diaphragm is modelled as two stack layers of piezoceramic patch and substratum. The cavity and orifice walls are hard-walls acoustically, and the no-slip condition is prescribed. The diaphragm motion inputs a boundary pressure load which turns into pressure fluctuations at the cavity and gives rise to fluid movement towards the outer domain via the orifice neck.

The outer domain is used for the flow visualisation and represents the quiescent conditions such as no pressure gradient presents in the outer space. It's dimensions are $20 \times d_o$ in the direction of flow (z -axis) and $20 \times d_o$ in the lateral direction (y -axis). This should be sufficient to avoid effects on the resulting jet [102]. The mesh is denser in the cavity and orifice neck where viscosity plays an important role and less dense at the outer domain.

Two configurations are studied within computational modelling of the actuator. Figure 6.15 shows the geometry and meshing for the opposite diaphragm-orifice configuration actuator. Figure 6.16 shows the geometry and an example meshing for adjacent orifice-diaphragm configuration actuator.

Table 6.8 shows results for jet velocities and the difference between three meshes applied with different mesh density. Mesh convergence is checked, and it is ensured it has minimal effect on the jet velocity computation. On top of the standard mesh, 'Boundary Layer Mesh' is also employed at the orifice neck for finer resolution at the walls. The boundary layer mesh consists of

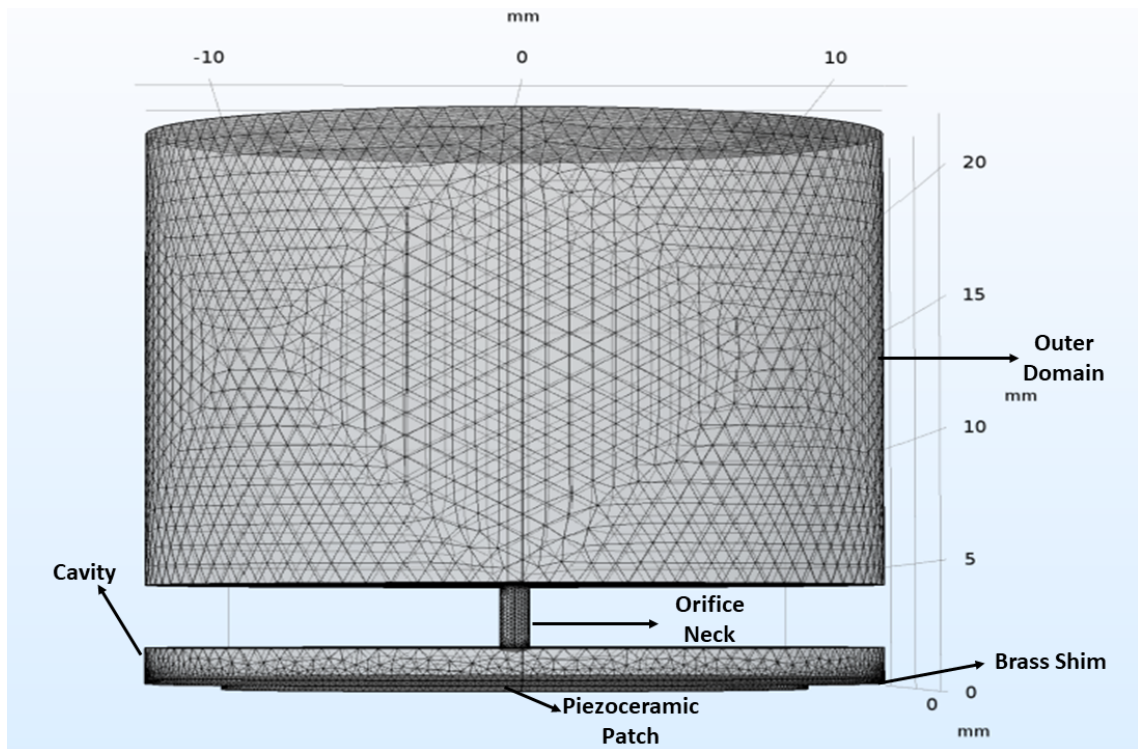


Figure 6.15: *Geometry, meshing and boundary conditions for opposite diaphragm-orifice configuration*

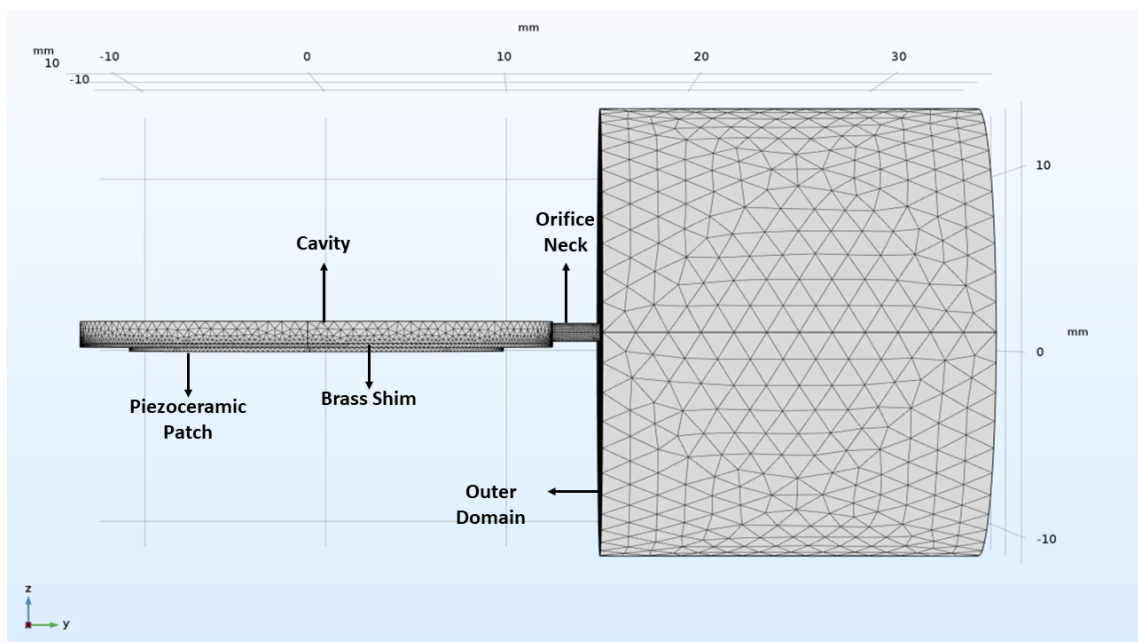


Figure 6.16: *Geometry, meshing and boundary conditions for adjacent diaphragm-orifice configuration*

triangular elements with higher resolution.

The frequency-domain study tends to have shorter computational time. Nevertheless, a time-dependent study is also essential to investigate the pressure, jet velocity and phase relationships. For the time-domain study, each forcing

Table 6.8: Simulation mesh convergence test

Mesh	Fine	Extra Fine	Extremely Fine
Number of Nodes	11990	21520	25564
Boundary Element	970	1120	1429
Min-Max			
Cell Size (mm)	0.00188 - 0.5	0.0005 - 0.25	6×10^{-6} - 0.0343
Jet Velocity (ms^{-1})	36.99	36.69	36.61

frequency is studied at least for 100 periods ($T = 1/f$), to ensure steady-state, with $1/(200f)$ time steps for each period which is found effective to capture both positive and negative peaks similar to the study of Jain et al. [102]. The computed results are collected by using spatial probes which records the data as the simulation runs.

6.5 Validation of the Multiphysics Model

The multiphysics model is validated against three sets of in-house experimental data throughout the actuation frequency envelope. Validation Case 1 utilized a 35-mm diaphragm with an opposite diaphragm-orifice configuration. Validation Case 2 is identical to the validation Case 1 of the analytical modelling. Validation Case 2 employed a velocity-optimized actuator dimensions for 27 mm diameter diaphragm by Gomes [66]. Validation Case 3 is an adjacent orifice-diaphragm configuration actuator. The supply voltage is kept constant at $20 V_p$ for all validation cases. The peak mean displacement and jet velocity definitions are consistent with the Section 6.3.

6.5.1 Validation Case 1

The first validation case uses a 35 mm diaphragm with a relatively shallow cavity. The diaphragm and actuator used for this study have the dimensions presented in Table 6.9.

Figure 6.17 presents the diaphragm deflection profile comparison of the model

Table 6.9: Validation Case 1 - Diaphragm and actuator size

Parameter	Value
D_{brass} (mm)	35
D_{pzt} (mm)	25
t_{brass} (mm)	0.30
t_{pzt} (mm)	0.28
d_{31} (m/V)	-180×10^{-12}
d_o (mm)	1.7
D_c (mm)	33
h (mm)	3.47
H (mm)	1
ζ (-)	0.03
f_h (Hz)	1268
f_m (Hz)	2250

and experiment, for the actuator clamped diaphragm. The resonance frequency difference is 37 Hz and the peak displacement difference is $0.1 \mu\text{m}$, corresponding to percentage differences of 1.7% and 0.2%, respectively. Figure 6.18 presents the jet velocity response comparison of the simulation and experiment. The figure is limited to 3000 Hz in which the jet velocity is sufficiently low (3% of the peak jet velocity). The jet velocity is calculated based on spatial average over the hot-wire probe's width.

The model exhibits a bimodal frequency response of jet velocity and accurately located the Helmholtz resonance frequency and velocity compared to the experiment. The mechanical resonance frequency also identified accurately, the jet velocity is overestimated by the model by 2.3 ms^{-1} , corresponding to a percentage difference of 8%.

Table 6.10 summarises the peak jet velocity obtained from experiment and the model for the resonant frequency.

Table 6.10: Validation Case 1 - Comparison of model and experiment results at resonant frequency

Resonance frequency	Helmholtz		Mechanical	
	Model	Experiment	Model	Experiment
Frequency (Hz)	1000	1000	2250	2250
Jet Velocity (ms^{-1})	15.1	14.0	30.6	28.3

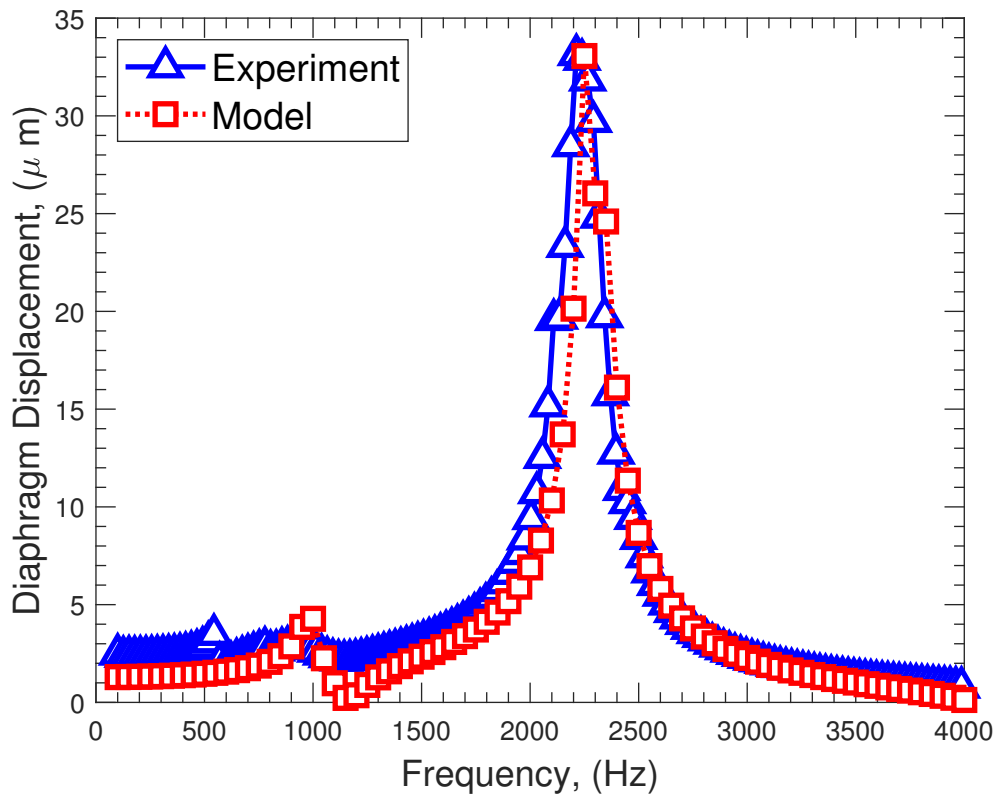


Figure 6.17: Case 1 - Diaphragm displacement comparison of the model and experiment

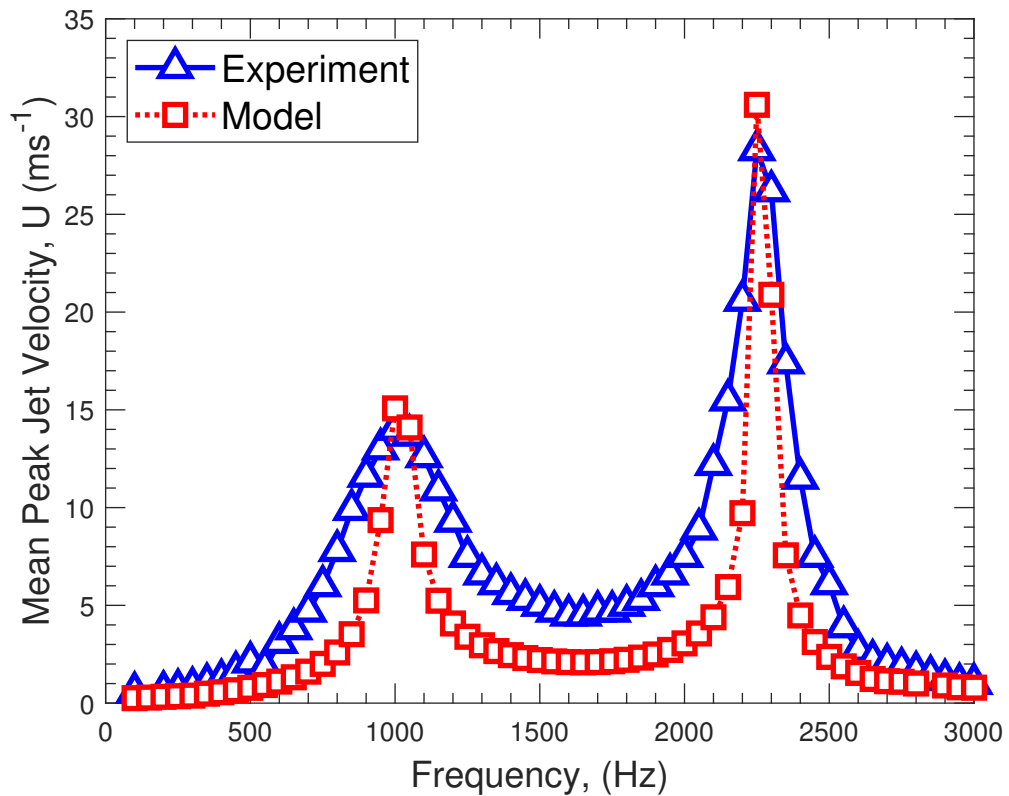


Figure 6.18: Case 1 - Mean peak jet velocity comparison of the model and experiment

6.5.2 Validation Case 2

Table 6.11 introduces the physical properties of the diaphragm, size of the actuator and the resonance frequencies for validation Case 2. Compared to the validation Case 1, the cavity diameter (-25%) and the orifice diameter (-40%) is smaller. Thus, the piezoelectric actuator size (both diameter and thickness) is also different.

Table 6.11: Validation Case 2 - Diaphragm and actuator size

Parameter	Value
D_{brass} (mm)	27
D_{pzt} (mm)	19.8
t_{brass} (mm)	0.22
t_{pzt} (mm)	0.23
d_{31} (m/V)	-180×10^{-12}
d_O (mm)	1.2
D_c (mm)	25
h (mm)	2.5
H (mm)	0.67
ζ (-)	0.0324
f_h (Hz)	1772
f_m (Hz)	2878

Figure 6.19 presents the comparison of model's diaphragm displacement profile with experimental data. The resonance peak at the mechanical frequency has accurately been captured around $15.9 \mu\text{m}$, the corresponding difference between the model and experiment is 1%. The model has overestimated the displacement around the cavity acoustic resonance by $0.5 \mu\text{m}$.

Figure 6.20 presents the jet velocity output comparison of the experiment and model. There is a 50 Hz difference in models evaluation of cavity acoustic resonance and diaphragm mechanical resonance frequencies. The cavity acoustic resonance takes places at 1400 Hz (experimentally) which is around 400 Hz below the calculated theoretical value. This observation is consistent with Section 6.3.1 and the potential reasons were mentioned.

The peak jet velocity at both peaks are estimated within $\pm 2.5 \text{ ms}^{-1}$. Both resonance peak velocities are covered within an acceptable tolerance and the

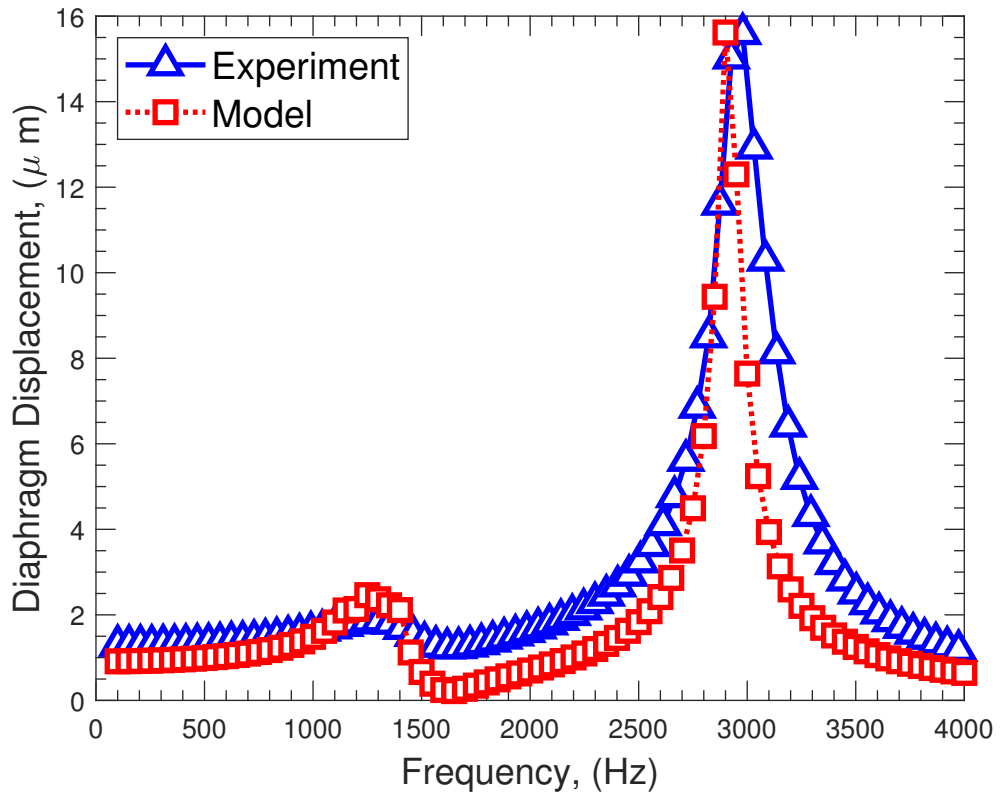


Figure 6.19: Case 2 - Diaphragm displacement comparison of the model and experiment

velocity drop in the middle region, between two resonance, is also captured.

Table 6.12 summarize the peak jet velocity output from experiment and the model for the resonant frequencies. The velocity resolution is within 5% for the jet velocity corresponding to the mechanical resonance.

Table 6.12: Validation Case 2 - Comparison of model and experiment results at resonant frequency

Resonance frequency	Helmholtz		Mechanical	
	Model	Experiment	Model	Experiment
Frequency (Hz)	1350	1400	2900	2950
Jet Velocity (ms^{-1})	17.5	20.1	34.7	36.8

Table 6.13 demonstrates the key non-dimensional parameters which govern the flow such as Stokes number, normalised Stroke length (L/d_o), Reynolds number based on the peak exit jet velocity ($Re_{\bar{v}}$) and Strouhal number (St).

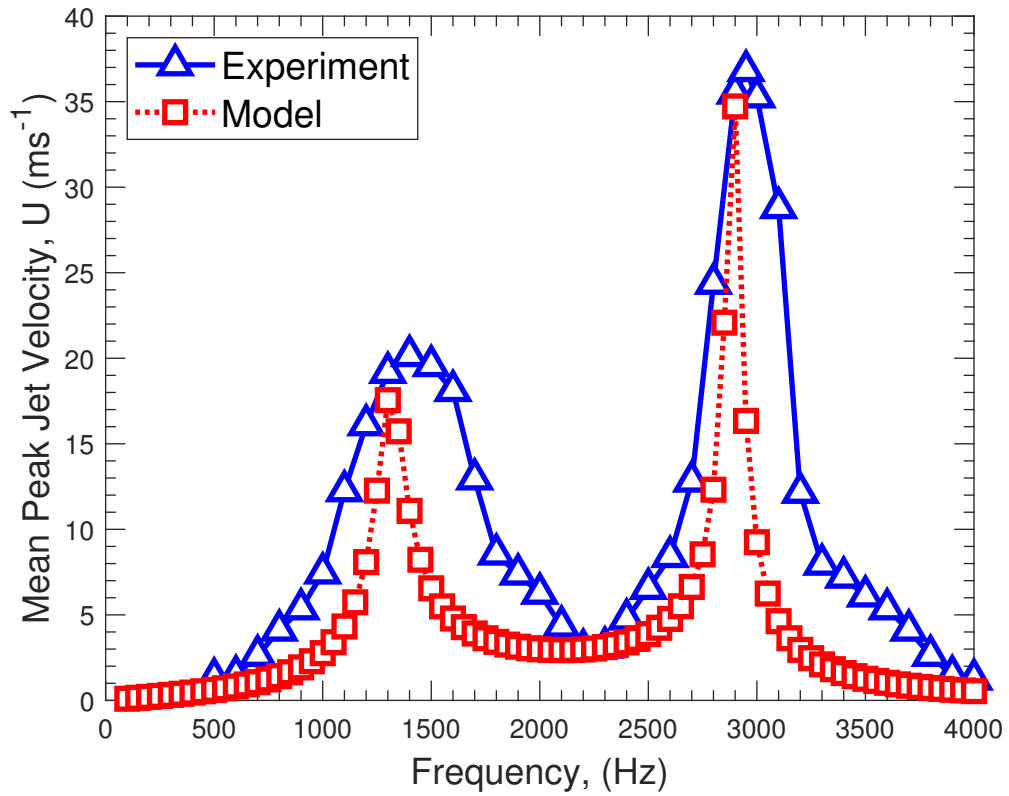


Figure 6.20: Case 2 - Mean peak jet velocity comparison of the model and experiment

Table 6.13: Key non-dimensional flow parameters at the mechanical resonance frequency

f_m	Experiment	Model
Stokes Number	41.7	42.0
$\frac{L}{d_o}$	1.67	1.78
$Re_{\bar{U}}$	926	1002
St	1.88	1.76

6.5.3 Time-domain Response and Phase Relationships

As previously mentioned, the multiphysics simulation has the advantage of flow visualisation, such as jet velocity and vorticity contours. One of the key property of the simulation is the visualisation of the velocity and vorticity fields to demonstrate the strength of the jet velocity after the detachment from the orifice. It is important to quantify the formation of the jet and vorticity at the diaphragm mechanical resonance frequency as many studies only studied actuation frequency at low actuation frequency; around or smaller

than Helmholtz frequency [19, 102, 103].

Before proceeding to the velocity and vorticity contours, the time-domain response of the actuator is studied to identify locations in which the flow visualisations are to be obtained. Then, the diaphragm locations are introduced in which the flow visualisations are presented.

The time-domain response of the actuator is studied to provide a broader understanding of the model. The results are presented for two frequency corresponding to the cavity acoustic resonance and diaphragm mechanical resonance. Figure 6.21 presents the normalised time-history data of jet velocity, in-cavity pressure, diaphragm displacement and diaphragm velocity. It can be observed that there is phase lag between the variables for both actuation frequencies.

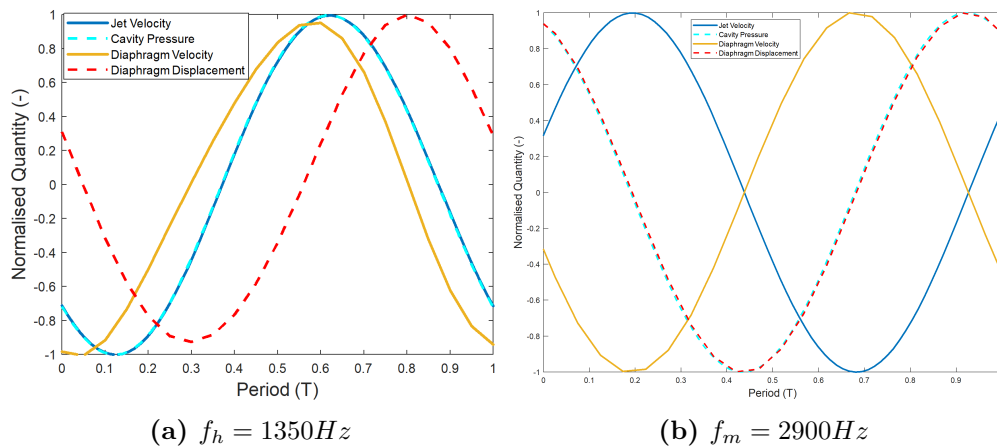


Figure 6.21: Normalised time-domain response of key variables

Figure 6.22 shows the positions of the diaphragm where flow visualisations of the actuator geometry are presented. Four positions are selected where the diaphragm is at peak expulsion, neutral position, peak suction and a quarter cycle away from the peak blowing.

The flow visualisations are presented when the SJA is excited at the mechanical resonance frequency of the diaphragm, therefore the flow compressibility is thought to be effective which increases the pressure loss hence reduce the exit jet velocity.

Compressibility of the air in the orifice-cavity originates from the exact solu-

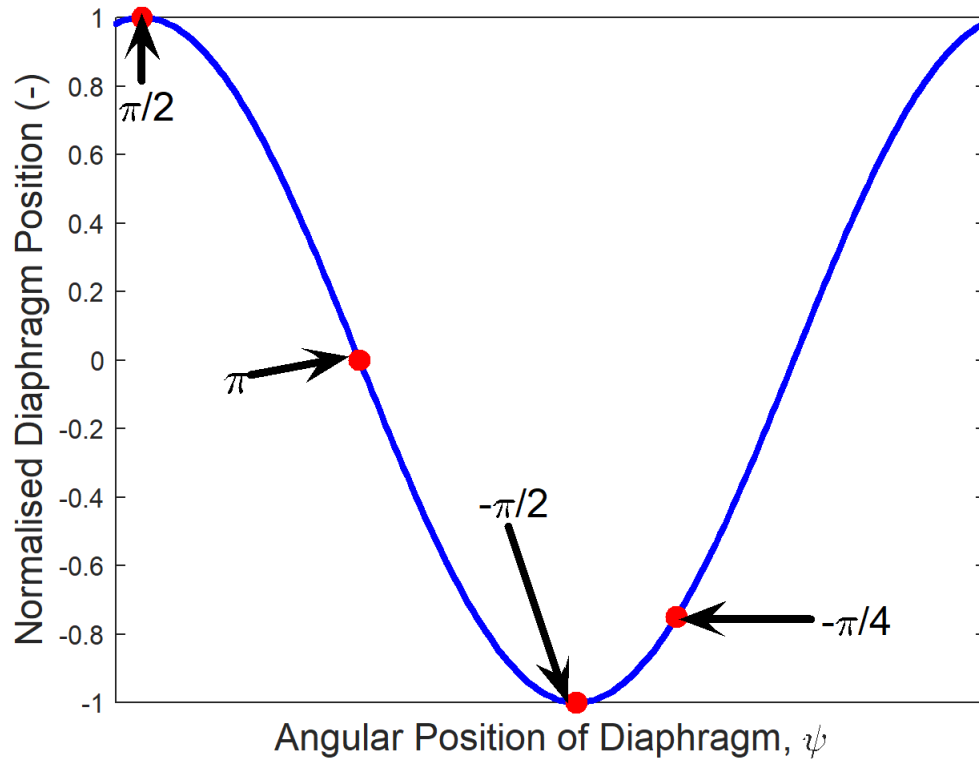


Figure 6.22: Diaphragm locations where flow visualizations are presented

tions of Navier-Stokes equations of channel flow with an oscillating pressure gradient which implies a phase difference between the pressure and velocity [81]. The compressibility effect results in non-linear fluid dynamic losses thus reduces the exit jet velocity [27]. The phase relationships are studied to get further information from the data regarding the compressibility effects. The phase between the diaphragm velocity and the jet velocity at the orifice exit is studied. Also, the phase difference between the cavity pressure and the jet velocity at the orifice exit is studied.

Figure 6.23 presents the phase relationships between the jet velocity at the orifice & diaphragm velocity and orifice jet velocity & internal cavity pressure. As per the suggestion of Sharma [18] with the fluid-dynamics analytical model, it is observed that the orifice jet velocity and diaphragm velocity are not in phase when actuation frequency is greater than the Helmholtz resonance frequency. Above the Helmholtz resonance (at 1350 Hz), the phase angle increase starts from around 1500 Hz. The phase between the diaphragm motion and

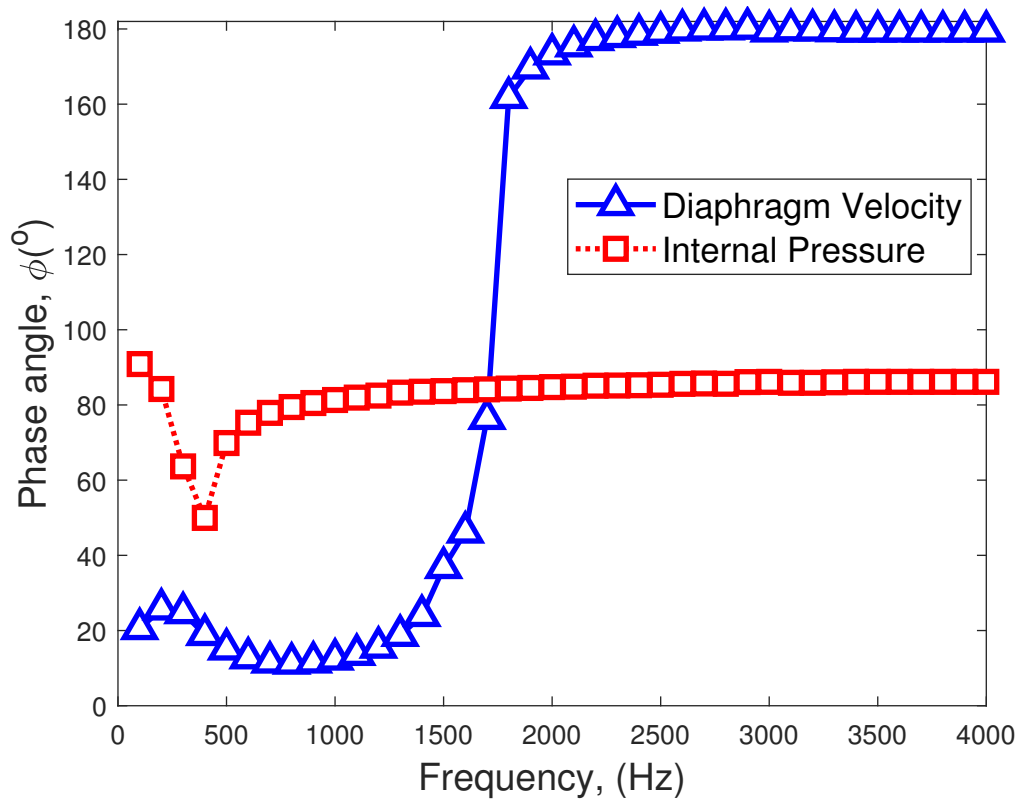


Figure 6.23: Case 2 - Phase angle relationships

jet motion becomes nearly anti-phase (reaching around 180°), until the end of actuation frequency range.

Phase angle starts increasing at the Helmholtz resonance and this implies that the flow is compressible for $f > f_H$. Thus, the flow becomes compressible until the end of the actuation frequency range.

Also similar to Sharma's computation for the opposite diaphragm-orifice case, the orifice jet velocity and internal pressure is nearly constant around 90° for most of the actuation frequency range. Referring back to Figure 6.21b, the diaphragm and orifice exit jet velocity is in anti-phase to each other.

6.5.4 Velocity Contours

Figure 6.24 shows velocity contours as per the diaphragm locations shown in Figure 6.22 at the diaphragm mechanical resonance frequency of 2900 Hz. Figure 6.24a shows two jet pockets in the cavity and roll up at the orifice neck edges. Figure 6.24b presents the jet formation and advection away from the

orifice which reduces with the distance from the orifice. Figure 6.24c shows a velocity contour during the peak of the expulsion cycle, as the diaphragm and jet is out-of-phase to each other. The expulsion cycle is important to present as it proves jet formation; jet is not sucked back into the orifice/cavity and advected in space. The large jet pocket is visible around $3 \times d_o$ away from the orifice exit in which the non-dimensional stroke length, L/d_o , is 1.78. Figure 6.24d shows the start of the re-formation of the jet in the cavity.

6.5.5 Vorticity Contours

As well as the velocity field contours, the vorticity field is also important to study to understand the flow behaviour. Vorticity contours help develop an understanding of the vortex formation in the cavity, orifice neck and outside of the orifice.

The specific importance of this actuator is its shallow cavity employed where the viscous effects are more dominant than a larger cavity height. The frequency of actuation is 2900 Hz which coincides with the mechanical resonance of the piezoelectric diaphragm.

Figure 6.25 shows the vorticity contours with respect to the diaphragm locations presented in Figure 6.22. Figure 6.25a shows the ejection cycle with respect to the orifice jet velocity. The initial vortex roll-up inside the cavity is captured. At the bottom of the orifice neck, the vortex roll-up is visible. At the top of the orifice neck, vorticity strength is increased, implying the formation to take place.

Figure 6.25b presents the formation and advection of anti-clockwise spinning vortices where the vorticity at bottom orifice neck is still significant. Due to the instantaneous neutral position of the diaphragm, the spin of the vortices are affected by their own inertia as there is no net momentum transfer from the diaphragm to the flow.

Figure 6.25c shows the peak instantaneous ejection of the diaphragm. The

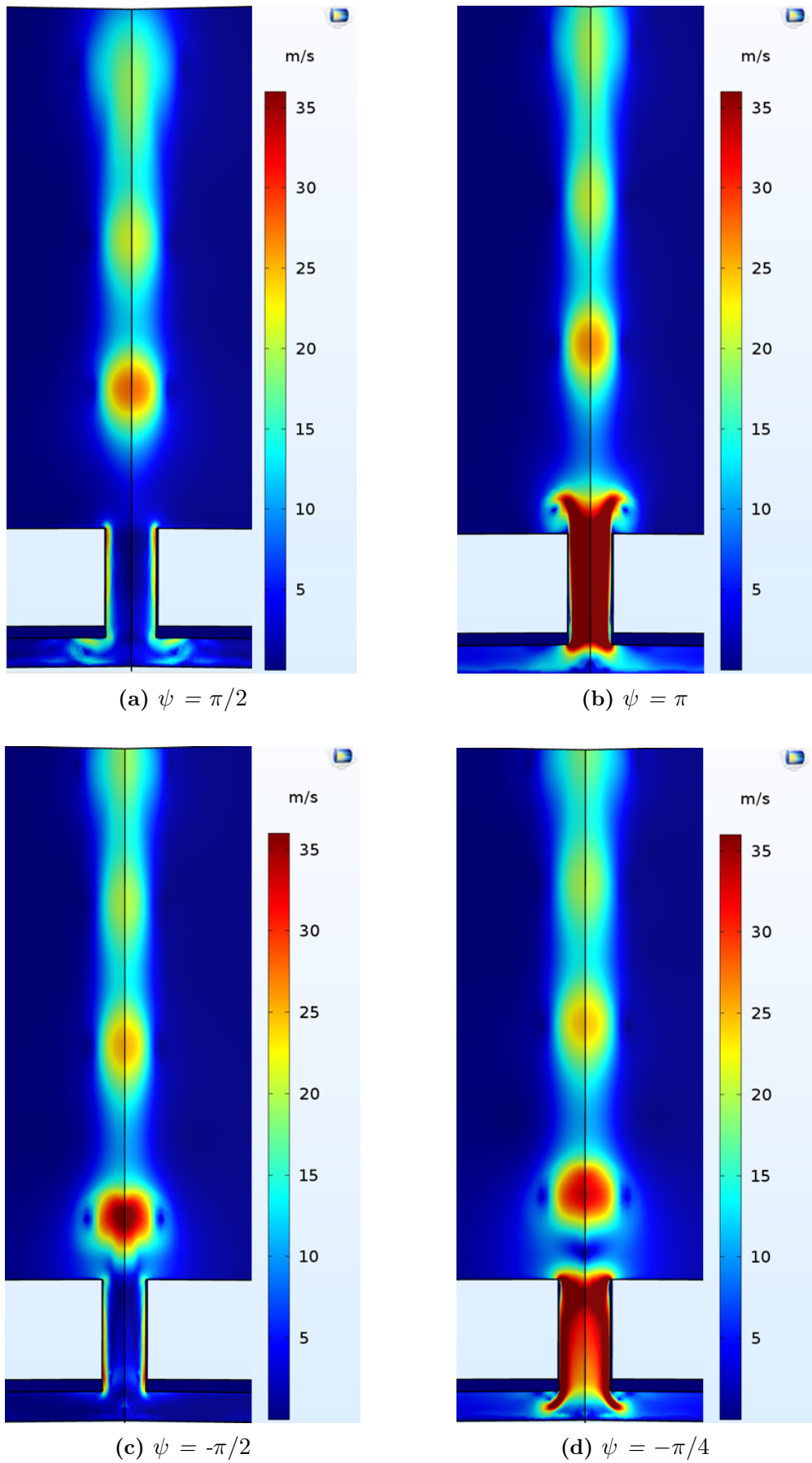


Figure 6.24: Numerical solutions for the validation Case 2 - Velocity Contours

formed vortex rings advected around $1 \times d_o$ away from the orifice exit and also spaced around $1.2 \times d_o$ in the lateral direction. Small vortex ring formation is visible at both top and lower edge of the orifice neck. Outer fluid is ingested back to the orifice neck causing the separation at the orifice neck.

Figure 6.25d shows the start of the re-formation of the vortex rings at the cavity and the advected vorticity with reduced strength at around $1.5 \times d_o$. A recirculation zone in the cavity is inspected due to the viscous fluid-structure interaction between the diaphragm and air. Also, it is showed that the vorticity is not sucked back into the cavity proving vortex formation.

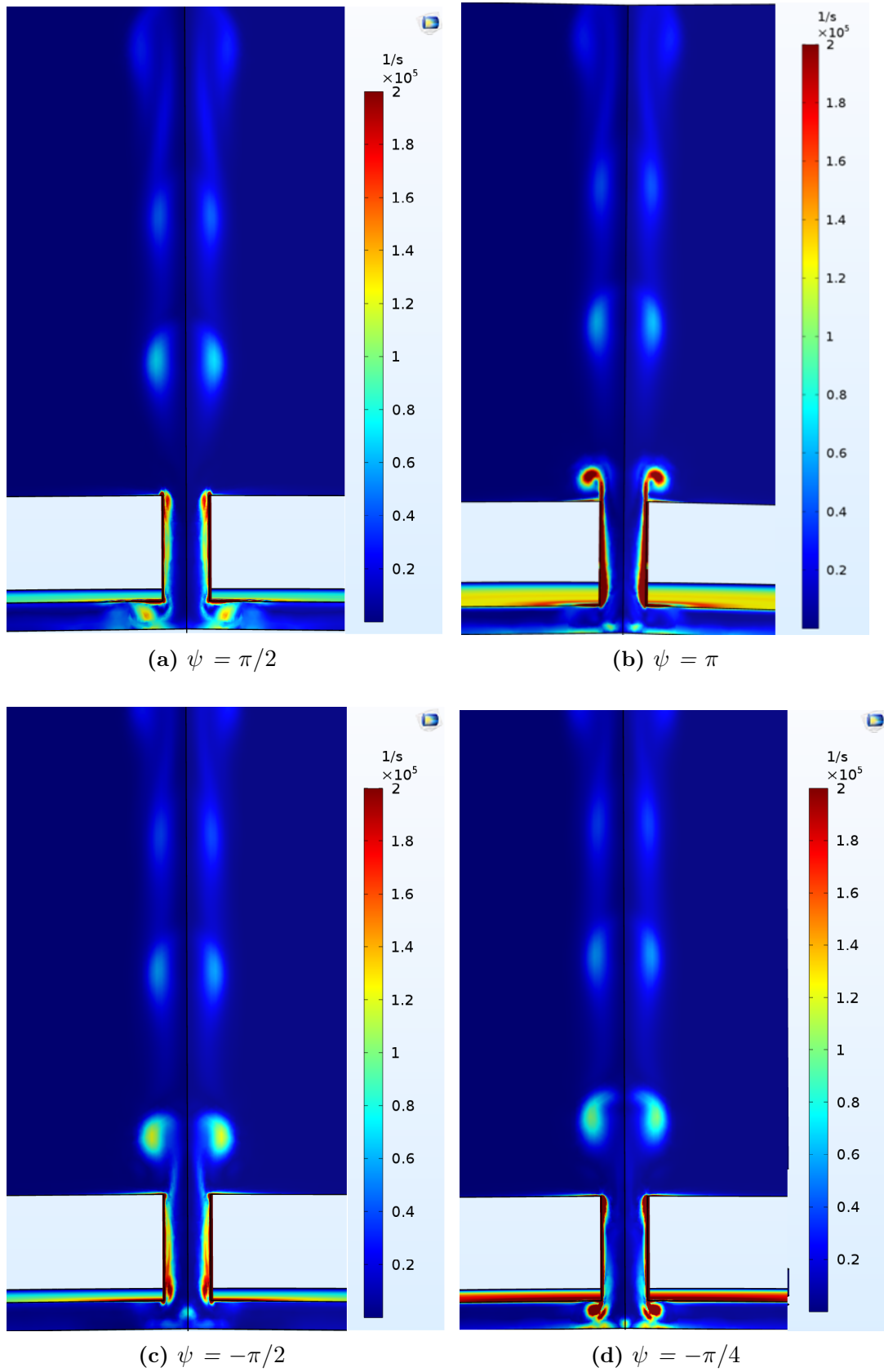


Figure 6.25: Numerical solutions for validation Case 2 - Vorticity Contours

6.5.6 Validation Case 3

This validation case investigates an adjacent orifice-diaphragm configuration actuator. The composition of the actuator geometry presented in Figure 6.16. The same piezoelectric diaphragm which was used for Validation Case 2 is employed for this case with a different actuator size, as presented in Table 6.14.

A design constraint of the adjacent orifice-diaphragm configuration is $d_o < H$.

Table 6.14: Validation Case 3 - Diaphragm and actuator size

Parameter	Value
D_{brass} (mm)	27
D_{pzt} (mm)	19.8
t_{brass} (mm)	0.22
t_{pzt} (mm)	0.23
d_{31} (m/V)	-180×10^{-12}
d_o (mm)	1.0
D_c (mm)	25
h (mm)	2.5
H (mm)	1.2
ζ (-)	0.0324
f_h (Hz)	1089
f_m (Hz)	2878

Figure 6.26 compares the experimental peak centre displacement with the model. The model matches the experiment both in resonance frequency and displacement amplitude. The response of the experiment is more damped and underestimated for small frequency range (i.e., 100-2500 Hz).

Figure 6.27 shows the comparison between the model jet velocity computation with the experimental data. The cavity acoustic resonance frequency is theoretically ~ 1100 Hz and realized as 900 Hz. This is due to the non-linear frequency interaction of the SJA as previously mentioned. The jet velocity corresponding to the mechanical resonance identified accurately with a difference of 0.1 ms^{-1} . However, the jet velocity corresponding to the cavity acoustic resonance is underestimated by 5.1 ms^{-1} . This is due to the underestimation of diaphragm deflection at the associated frequency band.

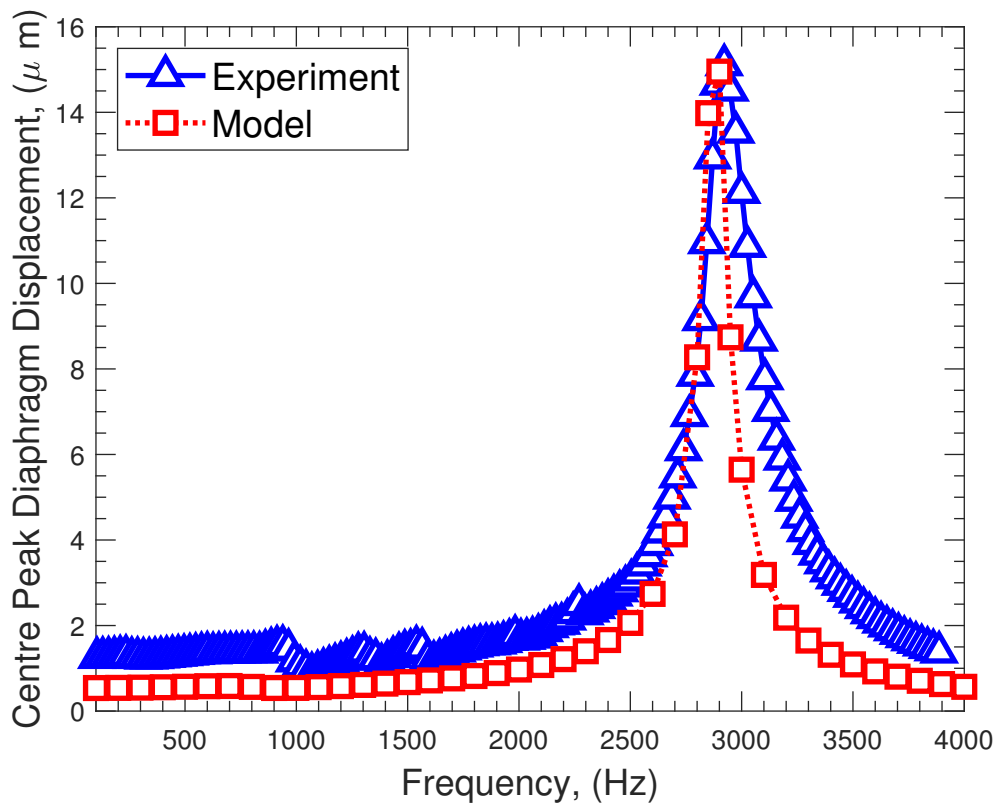


Figure 6.26: Case 3 - Diaphragm displacement comparison of the model and experiment

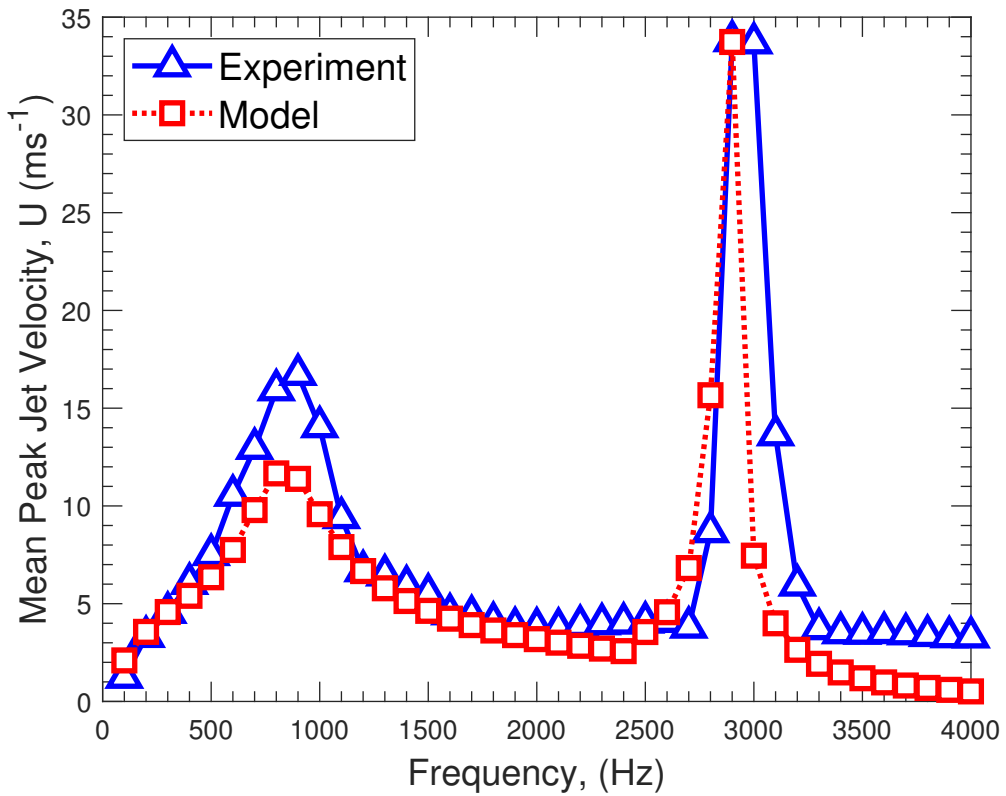


Figure 6.27: Case 3 - Mean peak jet velocity comparison of the model and experiment

Table 6.15 summarize the peak resonance response for model and experiment. The model has a shortcoming in the velocity corresponding to the cavity acoustic resonance due to a small diaphragm deflection computed for that actuation region. The mechanical resonance matches the experimental value both in terms of the actuation frequency and jet velocity. The experimental jet velocity peak has a broadband frequency (between 2900 Hz to 3000 Hz) in which the peak diaphragm displacement computation of the model has a narrower band.

Table 6.15: Validation Case 3 - Comparison of model and experiment results at resonant frequency

Resonance frequency	Helmholtz		Mechanical	
	Model	Experiment	Model	Experiment
Frequency (Hz)	800	900	2900	2900
Jet Velocity (ms^{-1})	11.6	16.7	33.7	33.8

The following table, Table 6.16, demonstrates the key non-dimensional parameters which govern the flow such as Stokes number, normalised Stroke length (L/d_o), Reynolds number based on the peak exit jet velocity ($Re_{\bar{U}}$) and Strouhal number (St).

Table 6.16: Key non-dimensional flow parameters at the mechanical resonance frequency

f_m	Experiment	Model
Stokes Number	34.7	34.7
$\frac{L}{d_o}$	1.35	1.33
$Re_{\bar{U}}$	516	509
St	2.33	2.37

6.5.7 Time-domain Response and Phase Relationships

The structure and the rationale behind this section is similar to Section 6.5.3 and concentrates on the adjacent synthetic jet. The phase relations are computed based on the diaphragm velocity and jet velocity and for internal cavity

pressure and jet velocity. Velocity and vorticity contours are also presented at the resonance frequency.

The time-domain response of the actuator is studied to provide a broader understanding of the model. The results are presented for two frequency corresponding to the cavity acoustic resonance and diaphragm mechanical resonance. Figure 6.28 presents the normalised time-domain data of jet velocity, in-cavity pressure, diaphragm displacement and diaphragm velocity. It can be observed that there is phase lag between the variables for both actuation frequency.

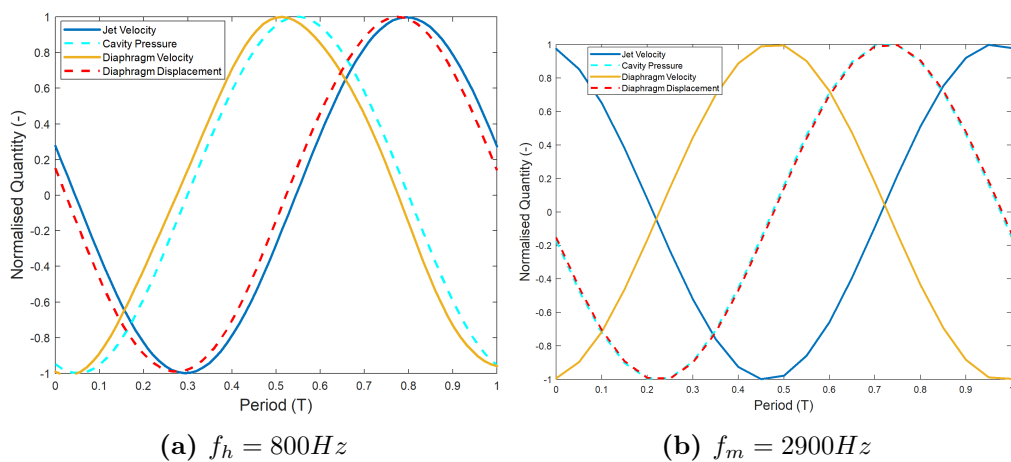


Figure 6.28: Normalised time-domain response of key variables

The phase relationships between the diaphragm's velocity and jet velocity is also studied for this case. The phase relationships are not widely studied for adjacent orifice-diaphragm configuration.

Figure 6.29 shows the results for the phase relationships based on the orifice exit velocity & diaphragm velocity and also with respect to cavity internal pressure.

Orifice jet velocity and diaphragm velocity tends to have an increasing phase angle as the actuation frequency increases and becomes nearly anti-phase (180°) around 1300 Hz. At the Helmholtz resonance frequency, the phase is around 110° . Given that the Helmholtz resonance is at 800 Hz this was expected which implies compressible flow after the Helmholtz resonance frequency. Comparing with the opposite orifice-diaphragm configuration the

phase angle increases more rapidly in frequency domain.

The orifice velocity and internal cavity pressure phase starts around 45° and tends to be around 80° as actuation frequency increases. This behaviour is similar to the opposite orifice-diaphragm configuration.

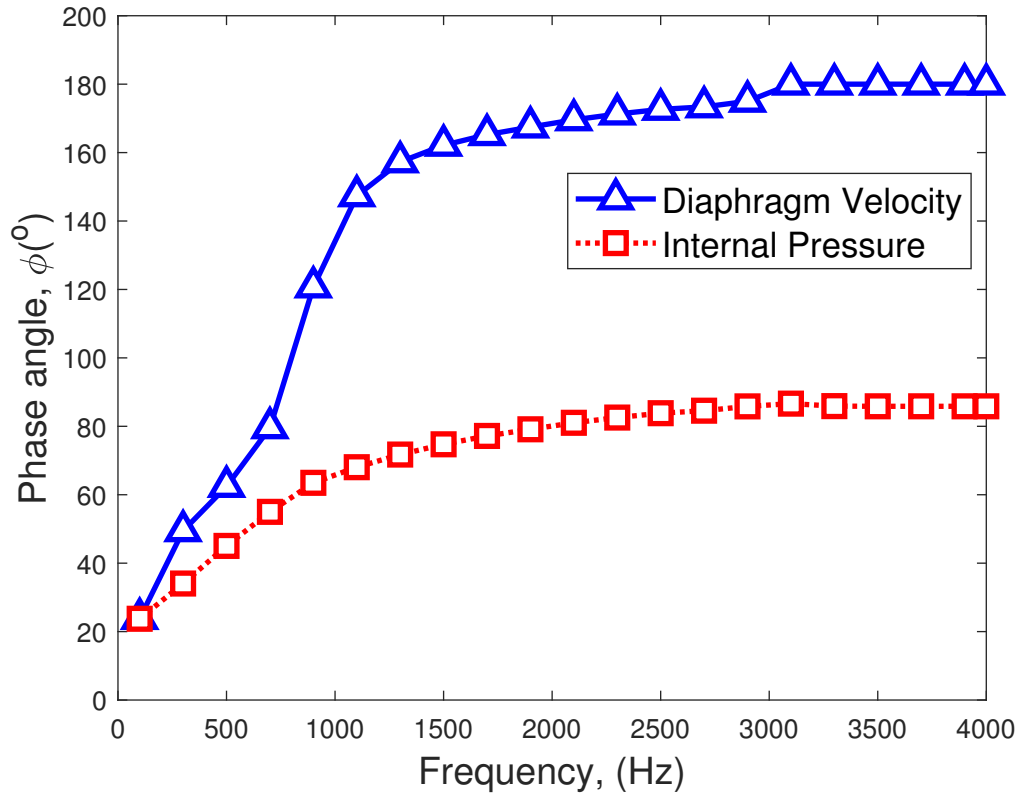


Figure 6.29: Case 3 - Phase angle relationships

6.5.8 Velocity Contours

Figure 6.30 is reproduced for convenience to show the positions of the diaphragm in which the flow visualisations are presented. Four positions are selected where the diaphragm is at peak expulsion, neutral position, peak suction and a quarter cycle away from the peak blowing.

All figures are plotted with the same legend scale to point out the differences. Also, the same scale used in the Figure 6.24. The frequency of actuation is 2900 Hz which coincides with the mechanical resonance of the piezoelectric diaphragm.

Figure 6.31a presents the maximum instantaneous expulsion where the di-

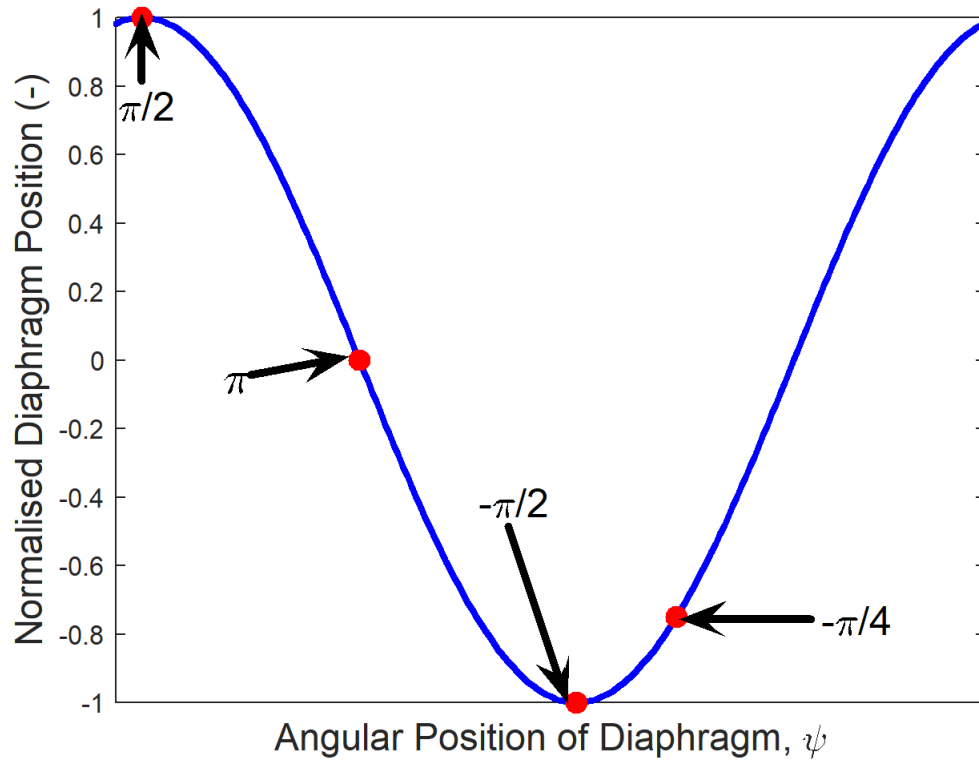


Figure 6.30: Diaphragm locations where flow visualizations are presented

aphragm is totally out of phase with respect to the cavity. An advected jet pocket with reduced velocity is visible at $1.5 \times d_o$. However, some of the fluid started to get ingested back in the cavity.

Figure 6.31b shows relatively high velocity at the orifice neck walls and lower velocity at the orifice exit due to the neutral position of the diaphragm. Instantly, the flow is not energised by the diaphragm and a low velocity is ejected out of the orifice. Flow separation is observed at the orifice neck towards the outer domain.

Figure 6.31c presents the maximum expulsion cycle as the diaphragm and orifice are out-of-phase with respect to each other. A dominant expulsion is observed with the disappeared separation at the orifice neck due to high energy forcing of the flow. The jet velocity gradually decreases after $1 \times d_o$. In the cavity, velocity increase from cavity to the orifice neck is visible.

Figure 6.31d shows the advection of the jet which is spread around $2 \times d_o$ from the orifice exit plane. Due to the position of the diaphragm the overall

momentum of the jet flow is reduced.

6.5.9 Vorticity Contours

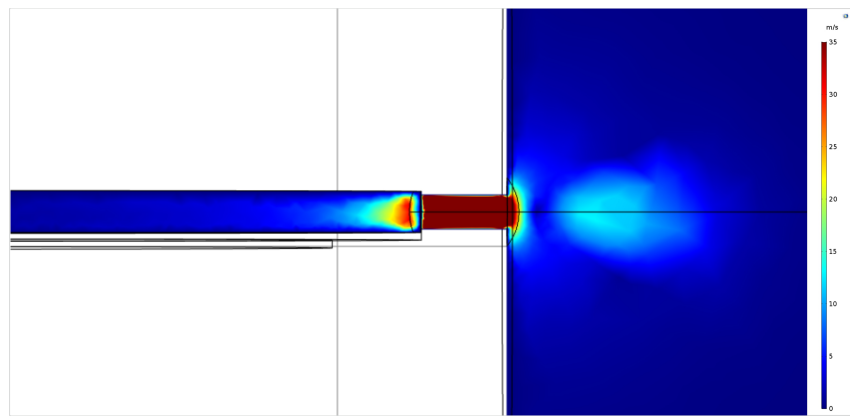
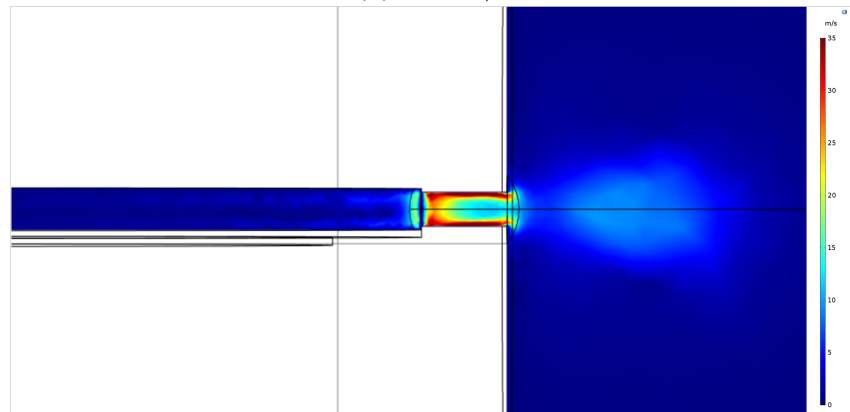
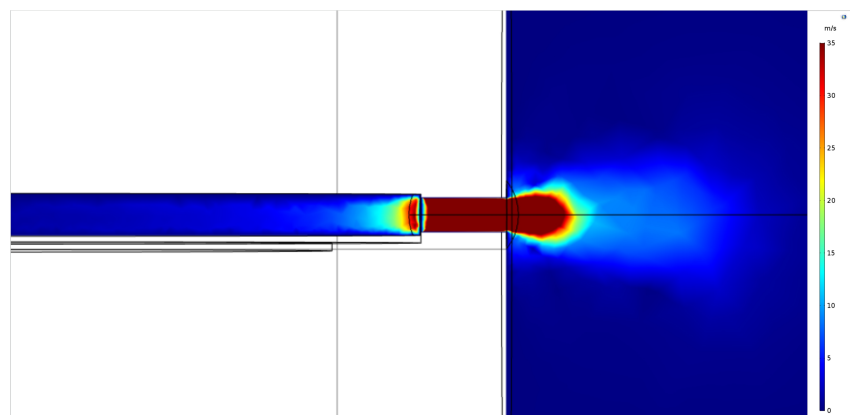
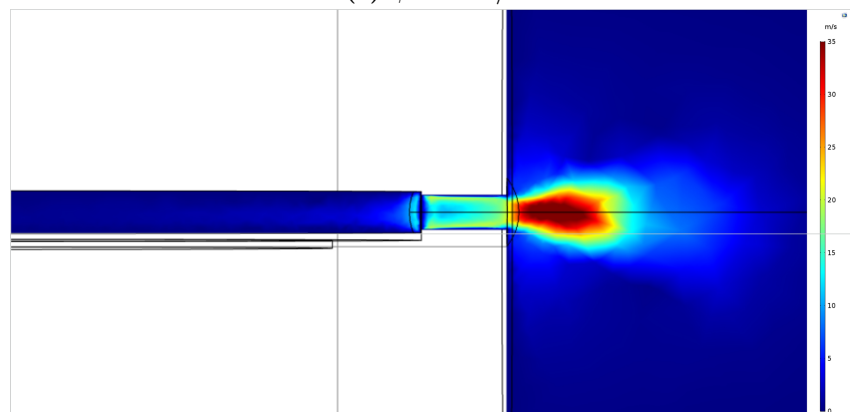
Vorticity plots are investigated to detect the potential vortex formation in the cavity, orifice neck and outer domain. Diaphragm motion is consistent with the previous plots and shown in Figure 6.22. The legend scale is set to be half of the Figure 6.25 for better visualisation. The frequency of actuation is 2900 Hz which is the mechanical resonance of the diaphragm. The vorticity roll-up and strength is reduced compared to Case 2 due to lower Stokes and Stroke numbers for this case.

The calculated Stokes number and non-dimensional stroke length is sufficient for the roll-up outside the orifice neck [78]. However, the vorticity field in the cavity is negligible except for the proximity of the cavity-orifice neck connection.

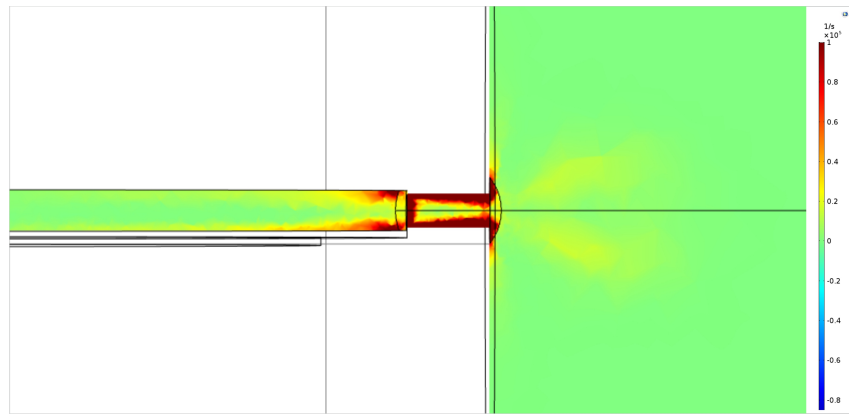
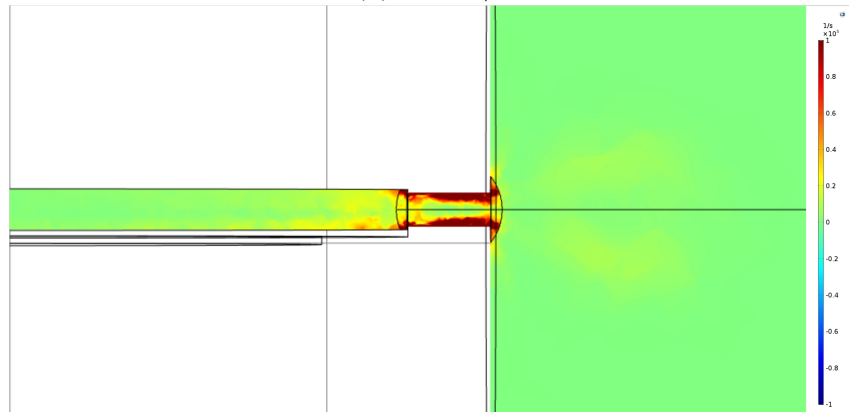
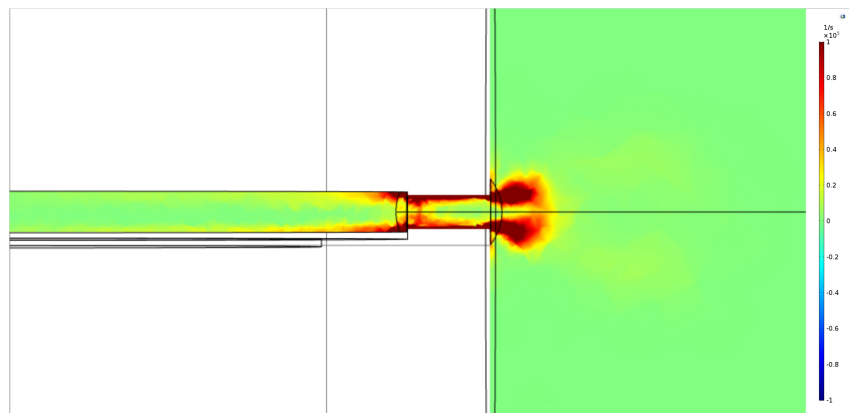
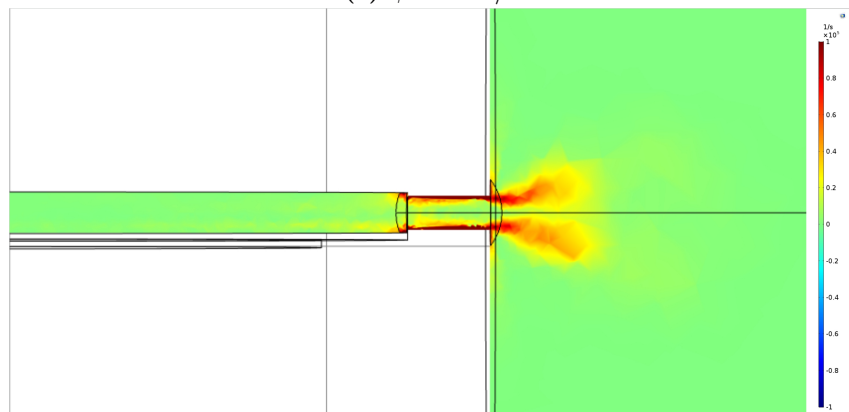
Figure 6.32a represents the bottom-most position for the ingestion and shows the vorticity entrainment within the cavity and separation in the orifice neck. Small re-circulatory zones are identified at the cavity-orifice neck connection due the geometric contraction. Due to the phase relationship between the orifice jet velocity and diaphragm,

Figure 6.32b shows the vorticity field where the diaphragm is instantaneously neutral. The vorticity at the orifice is further reduced due to the momentum loss of the flow.

Figure 6.32c shows the maximum expulsion of the orifice with the appearance of two vortex rings at the orifice exit. The vortex strength is persisted for nearly $1.2 \times d_o$ away from the orifice exit. The vortex rings are engaged at $1 \times d_o$ out of orifice due to the inertial and viscous losses as the fluid entrains. The counter-clockwise spinning vortex formation outside the orifice is a known pattern for the opposite configuration that is also valid for the adjacent design. Figure 6.32d shows the reduced vorticity strength both at the outer domain

(a) $\psi = \pi/2$ (b) $\psi = \pi$ (c) $\psi = -\pi/2$ (d) $\psi = -\pi/4$ **Figure 6.31:** Numerical solutions for the validation Case 3 - velocity contours

and at the orifice neck due to the diaphragm position which starts to ingest the vortex field again.

(a) $\psi = \pi/2$ (b) $\psi = \pi$ (c) $\psi = -\pi/2$ (d) $\psi = -\pi/4$ **Figure 6.32:** Numerical solutions for the validation Case 3 - vorticity contours

6.6 Discussion

The discussion section is separated into two parts; discussions for analytical model and multiphysics model as the validation cases and analysis slightly vary. Within this section, findings are discussed based on the observations made throughout the chapter in which unavoidably experimental results are also mentioned.

6.6.1 Discussion of SJA - Analytical Model

In the original previous paper of Sharma [18], where the acoustic-fluidic model is presented, the natural frequency of the diaphragm is assumed to be known as well as the acoustic piezoelectric coefficient (D_a , a measure of volume displaced by the diaphragm), which are both non-trivial to compute.

The fluidic-acoustic analytical model is integrated with the piezoelectric actuators structural analytic model (developed and presented in Chapter 4.4-Chapter 5.2) for natural frequency and displacement computation, making the overall model a structural-acoustic-fluidic analytical model (referred to as analytical model hereafter) with the only empirical term being mechanical damping of the piezoelectric composite diaphragm (ζ). The equation regarding the effective orifice length calculation is replaced with another equation to reduce the parameter uncertainty (C_I) in the model.

It is observed that the integrated model performed well, at least within the determined performance criteria of this study for the modelling accuracy goals in terms of estimation peak jet velocity and associated actuation frequency. Compared with the piezoelectric diaphragm peak displacement results (presented in Chapter 5.3), two key findings should be mentioned. Firstly, the peak centre displacements are reduced due to the annexed cavity-orifice arrangement causing added damping and stiffness. Also, due to the added mass of air and orifice acoustic mass, the resonance frequency has shifted.

Three validation cases are selected to show the evolution from a bimodal frequency response of output jet velocity to a single modal, which can be classified as a dominant peak response. Even though, the idea of having a single dominant peak in the frequency response was mentioned by several studies including [18, 66, 69], only experimental data was obtained by [20]. It can be stated that the relative positioning of the resonance frequencies are verified as the same actuator geometry is employed using two different piezoelectric composite diaphragms. Gallas stated that for a given actuator geometry the following equation should hold [20]:

$$f_1 \times f_2 = f_h \times f_m \quad (6.15)$$

In Eq. 6.15, f_1 and f_2 are the realized resonant frequency and f_h and f_m are the calculated resonance frequency.

The results of the multiplications suggest that in Case 1, there is a significant difference but in Case 2, the multipliers are nearly equal. This implies that the formula proposed by Gallas is only valid provided that the 'theoretical' resonant frequency values are matching or in the close proximity.

Table 6.17: ($f_1 \times f_2$) vs ($f_h \times f_m$)

	Case 1	Case 2	Case 3
$f_1 \times f_2$ (Hz^2)	4060000	3154160	1562500
$f_h \times f_m$ (Hz^2)	5099816	3120000	693312

On the other hand, in a more recent work, Chiatto et al. defined a particular criterion to assess the damping of the SJA as given in Eq. 6.16 [148]. According to this criterion, if Eq. 6.16 is satisfied, then the device works as an overdamped oscillator and does not show a jet velocity peak at the cavity acoustic (i.e., Helmholtz) resonance frequency. Otherwise, the SJA is underdamped and reveals a bimodal exit jet velocity response.

$$\frac{\bar{U}}{\omega_h d} \geq \frac{1}{K} \frac{2 l_e}{\pi d_o} \quad (6.16)$$

For the Validation Case 1 presented for the diaphragm-based analytical model, Equation 6.16 does not hold, thus the system is underdamped and exhibits a bimodal exit jet velocity response. However, the equation holds for the Validation Case 3 and the SJA exhibits a single modal frequency response. This result implies that it is not only possible to explain the frequency response of the actuator by the relative positions of the Helmholtz and diaphragm mechanical resonance frequency, but also with the damping of the device.

The main deficiency of the fluidic-acoustic model is the employment of a single pressure loss term (K). Regarding the K term, there are different approaches and values used in different previous studies. In the validation cases, the K parameter is used as 0.78 for all three validation cases, similar to the original paper of Sharma [18]. The K value used within this study has proven accurate results for the jet velocity corresponding to the resonant frequency peaks. Nevertheless, it overestimated the middle actuation frequency region in between acoustic cavity resonance and diaphragm mechanical resonance (for Validation Cases 1 & 2) due to the fact that those frequencies are high enough to promote additional pressure loss but not associated with a resonance to turn that into output jet velocity. The overestimation problem in the intermediate frequency region is also observed in the LEM study of Gallas [20]. For a bimodal frequency response actuator, employing multiple K parameters (i.e., K value might differs with respect to the actuation regimes) could reduce the overestimation of jet velocity. Equation 6.17 demonstrates a proposed (i.e., empirical) model for multiple K parameters.

$$K = \begin{cases} 0.78, & \text{if } f \approx [f_h, f_m] \\ 1, & \text{if } f \not\approx [f_h, f_m] \end{cases} \quad (6.17)$$

K = 0.78 would be employed for resonant peaks (i.e., f_h and f_m) and another

value of K to be used for the intermediate actuation frequency region. Herein, to demonstrate the concept, $K = 1$ is proposed as an arbitrary value for the intermediate frequency region and beyond mechanical resonance.

The structural-fluidic-acoustic model presented here now used to model the opposite diaphragm-orifice configuration SJA. For the adjacent configuration SJA, the K parameter should also take the bending of the flow during the discharge into account. The bending of the flow would cause extra pressure loss which should be reflected via the K parameter. According to the steady pipe flow theory, the bending can be accounted by adding 0.2 to the existing K [149]. However, for the adjacent synthetic jet, the model requires more experimental data such as with different orifice and cavity size adjacent SJA to empirically identify the pressure loss.

With this model, one other limitation is the geometry independence such as slanted-edge orifice, rounded-edge orifice, orientation of the orifice and geometry of the orifice (i.e circular or rectangular). All listed potential changes of cavity-orifice arrangement should be taken into account through the K parameter, which is a limiting factor. On the other hand, to model a bimorph composite piezoelectric actuator driven synthetic jet, the structural model should be adapted for that type of actuator.

The validation cases are all presented for supply voltage of $20 V_p$. Therefore, the assumptions regarding the isothermal cycles of expulsion and ingestion and neglecting friction losses do not impact the computations.

6.6.2 Discussion of SJA - Multiphysics Model

Typically, a CFD study has a geometry in which the Navier-Stokes equations (linearised or with a turbulence model) are solved together with the continuity equation by assuming a boundary condition case, such as sinusoidally vibrating wall with a fixed amplitude [19, 97, 103]. Nevertheless, such an approach would not help towards achieving the fully accurate frequency range of the

piezoelectrical diaphragm driven synthetic jet actuator for two reasons:

1) An inlet boundary condition does not reflect the proper deflection profile of the composite piezoelectric diaphragm. Besides, the amplitude of the oscillation needs to be an input to the model.

2) Acoustic cavity resonance and its coupling with diaphragm mechanical resonance cannot be obtained as Navier-Stokes equations do not involve any terms for acoustics.

Therefore, the multiphysics model presented involves proper modelling of the piezoelectric diaphragm which inputs pressure load (i.e., pressure fluctuations due to the motion of the diaphragm) to the cavity-orifice arrangement modelled with acoustic pressure equations.

Both opposite and adjacent orifice-diaphragm configurations are studied in the validation cases to take the advantage of the multiphysics model. Another important feature of the multi-physics simulation is the flow visualisation used to obtain contour plots of jet velocity and vorticity field.

In the actuation frequency region between the cavity acoustic resonance and mechanical diaphragm resonance, the jet velocity response of the multiphysics model is more accurate compared to the analytical model. This is due to the combined proper modelling of the diaphragm displacement and fluidic losses. The only empirical term in the model is the damping coefficient associated to the diaphragm. As per the previous analysis in Chapter 5.3, an average value for diaphragm damping can be employed as 0.03. Nevertheless, in this study true mechanical damping values obtained from the experiments are used.

The effect of adding cavity-orifice arrangement to the diaphragm reduces the peak diaphragm displacement and this is consistent with the structural-fluidic-acoustic analytical model. The reduction of the peak displacement is observed due to the added air and acoustic mass, as well as additional damping due to the air enclosed in the cavity-orifice arrangement.

Phase difference relations are also studied with the multiphysics model, which revealed that the adjacent orifice-diaphragm configuration tends to become

compressible after the Helmholtz resonance frequency earlier than the opposite configuration. The adjacent configuration's phase angle change reaches anti-phase (180°) more rapidly. Over the forcing frequency range, the effects of flow compressibility are more significant in an adjacent configuration actuator when compared to the opposite configuration, in which the compressibility is observed on an earlier frequency offset. This implies that compressible flow solvers should be used in a CFD study.

On the other hand, there is an ambiguity in the literature regarding the actuation frequency (f), in which compressibility effects become significant. Gallas claimed compressibility effects are important when the actuation frequency is greater than $0.5 \times f_H$ whereas Sharma suggested $f > f_h$ [75]-[18]. Based on the results obtained by the multiphysics simulation, flow starts becoming compressible when $f \approx f_h$ (initiates significant phase difference) and becomes fully-compressible (i.e., diaphragm velocity and exit jet velocity is out-of-phase to each other) when $f > f_h$.

At the mechanical resonance frequency, it is found that for both Validation Case 2 and 3, the Stokes number and non-dimensional Stroke length is sufficient for vortex roll-up [78]. Vorticity contours are studied, resulting in evidence of the vortex formation within the cavity for the opposite orifice-diaphragm configuration. Comparing the vorticity fields of the opposite and adjacent synthetic jets (presented in Figure 6.25 and Figure 6.32) reveals that the vorticity strength is halved for the adjacent synthetic jet. This is due to the change in the orifice-diaphragm configuration and increased cavity height. The fluid in the adjacent synthetic jet's cavity loses more pressure due the sudden bend and contraction when compared with the opposite synthetic jet.

In the adjacent orifice-diaphragm configuration case (i.e., Validation Case 3), vortex roll-up is visible in between the cavity and orifice-neck junction. However, vortex ring formation in the cavity is not observed. Two counter-clockwise spinning vortex appearance is documented at the orifice exit. Even though the adjacent synthetic jet actuator is more suitable to be used in an ar-

ray, significant reduction in the vortex strength is observed in this case. Thus, for a potential application of adjacent configuration SJA in arrays, the vortex strength should be studied. In this case, the Stokes number is relatively large, however, in an engineering application, it is likely that the orifice diameter will be reduced, causing the Stokes number also to reduce, which may result in no vortex roll-up. Therefore, both exit jet velocity and vortex formation/strength should be considered for a development towards an engineering application.

6.7 Summary

Models with two different approaches are studied for different synthetic jet actuator cases, which are then validated against experimental data. Outputs of the models are compared against experimental data separately for three validation cases each. The key properties of the validation cases and their agreement level with the experimental data is summarized in Table 6.18 which consists of the cavity diameter (D_c), total diaphragm thickness ($t_t = t_b + t_{pzt}$), experimental peak jet velocity (U_p) and % difference between the prediction of model and experimental peak jet velocity ($\%U_p$). The peak voltage applied to the piezoelectric actuator kept constant as $20 V_p$, for all presented cases.

Table 6.18: Summary of SJA Modelling Validation Cases for diaphragm-based analytical model and multiphysics model

	Diaphragm-Based Model				Multiphysics Model			
	$D_c(\text{mm})$	$t_t(\text{mm})$	$U_p(\text{ms}^{-1})$	$\%U_p$	$D_c(\text{mm})$	$t_t(\text{mm})$	$U_p(\text{ms}^{-1})$	$\%U_p$
I	25	0.45	36.8	1.4	33	0.58	28.3	8.1
II	25	0.28	53.4	2.4	25	0.45	36.8	5.7
III	33	0.30	54.3	1.1	25	0.45	33.8	0.3

The first model, namely the analytical model, is a combination of structural mechanics model and a acoustic/fluid dynamics based set of differential equations. The fluidic-acoustic dynamics model is extended to compute the accurate natural frequency of the piezoelectric diaphragm and to consider the proper transverse deflection profile of piezoelectric discs under AC voltage load,

resulting with a structural-fluidic-acoustic model.

The diaphragm-based analytical model considers all of the fundamental variables of the actuator (design and operational) and leaves the material damping of the diaphragm as the only unknown variable. The model has proven an acceptable match when compared with the in-house experimental data.

The percentage difference of the analytical model's jet velocity and the experiment at the mechanical resonance is 1.4%, 2.4% and 1.1% for Case 1, 2 and 3, respectively. For the Helmholtz resonance jet velocity, the percentage difference is 12.4%, 11.7% and 1.1% for validation Case 1,2 and 3, respectively. By the analysis of the selected test cases, it can be concluded that to have a single modal response of output jet velocity, the Helmholtz and mechanical frequency of the actuator and diaphragm should be considered carefully. Instead of designing the actuator to match the two resonant frequencies, the SJA should be designed as an overdamped oscillator. (Discussed in Section 6.6).

The second model utilizes a multiphysics approach, proving effective results for the diaphragm displacement and jet velocity across different validation cases. While providing an acceptable match for all the validation cases, slight shifts (± 100 Hz) in resonance frequency computations are observed.

The percentage difference of the multiphysics model's jet velocity and the experiment at the mechanical resonance is 7.1%, 5.7% and 0.3% for cases 1, 2 and 3, respectively. For the Helmholtz resonance jet velocity, the percentage difference is 1.4%, 12.9% and 30.5% for validation Case 1, 2 and 3, respectively. The Helmholtz frequency of the adjacent orifice-diaphragm configuration (Case 3) is underestimated by 100 Hz. The jet velocity corresponding to the Helmholtz resonance is also underestimated by 5.1 ms^{-1} . Nevertheless, the mechanical resonance frequency is identified accurately and the jet velocity matches the experimental value with a difference of 0.3%.

The computational model was used to obtain flow visualisation for velocity and vorticity. For the opposite diaphragm-orifice configuration, vortex formation in the cavity is observed unlike in the adjacent configuration. This implies that

the opposite configuration's near and far-field vortex strength is higher than the adjacent configuration. Therefore, for a potential flow control application, the opposite synthetic jet actuator is more likely to grant effectiveness. Also, it is found that the phase difference angle between the diaphragm's velocity and the orifice jet velocity is more dominant for the adjacent configuration.

From a practical point of view, the actuator would run at the resonant frequency at a potential engineering application; thus, estimating the resonant frequency and the corresponding jet velocity is the most critical point. Both models have covered the mechanical resonance jet velocity within $\pm 7\%$ difference (maximum of 2.3 ms^{-1}) for all validation cases.

Overall, the structural-fluidic-acoustic analytical model can be used as a tool to assess the jet velocity of synthetic jet actuator to model a potential design. It is a capable tool if parameter sweeps are to be conducted with a runtime less than one minute. The analytical model is optimised for opposite orifice-diaphragm configuration actuator, as per the validation cases presented. The multiphysics model has a longer run time (~ 12 hours for a 3D model), however, it is not only accurate but it also provides flow visualisations. In addition, multiphysics model can be used to simulate different configurations, such as adjacent orifice-diaphragm or twin diaphragm driven synthetic jet actuator.

Chapter 7

Investigation of achieving high jet velocity and power conversion efficiency

7.1 Introduction

This chapter mostly concentrates on experimental efforts through achieving high-subsonic synthetic jet velocity and high power conversion efficiency for potential flow control applications. For an efficient flow control application, the power spent on the actuation and the benefit gained from the control action should be carefully compared. Thus, achieving high-jet speed SJA is essential, but also power conversion efficiency should be considered and maximised. Less efficient SJA would require more input power to deliver the required jet velocity to match corresponding flight cross-wind velocity for aerospace applications. Therefore, a low-efficiency SJA requires a larger power supply which results in larger system mass, or less power available for other aircraft loads for a given power supply.

The actuator configuration is important for an engineering application as opposite orifice-diaphragm and adjacent orifice-diaphragm configurations might have different advantages and disadvantages. The overall size of the actua-

tor should be small enough in size to avoid modification requirements to the test object (i.e., aerofoil, square-back trailer) for flow control. Figure 7.1a and Figure 7.1b present opposite and adjacent configuration SJA in a small array, respectively, to demonstrate the sizing requirements. Figure 7.1a illustrates the use of three discs oscillating up and down and the formation of the jet. The embedment height of the opposite configuration is in the order of the cavity height in which the adjacent configuration requires order of diaphragm diameter. In addition, the distance between consecutive orifices is in the order of diaphragm diameter and cavity height for the opposite and adjacent configurations, respectively. Also, as per the illustration in Figure 7.1b, the adjacent configuration may use two diaphragms to discharge jets through three orifices which would increase the ratio of total fluidic power obtained to the electrical power spent. Furthermore, via anti-phase operation of the discs, the jet velocity can be enhanced and the noise output can be reduced [150].

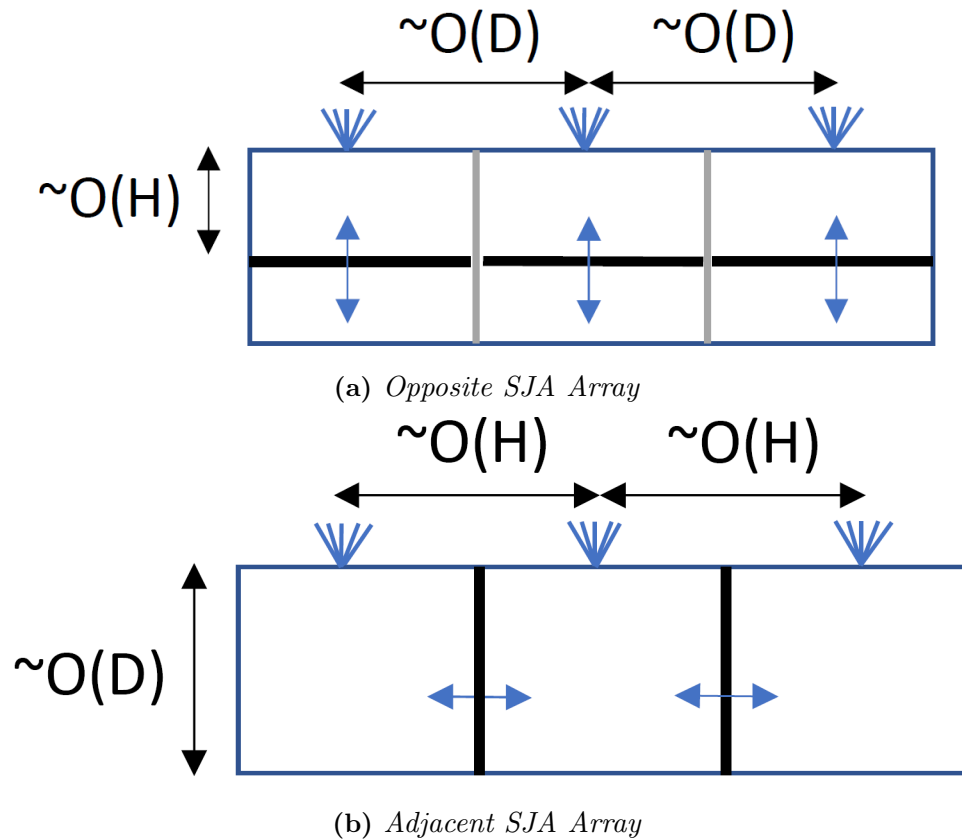


Figure 7.1: *Opposite and Adjacent Orifice-Diaphragm Configuration SJA Array*

By the experimental and modelling analysis done in Chapter 5 and Chapter 6, it is verified that increased transverse deflection of the diaphragm results in higher jet velocity, which is a known and intuitive concept. Also, it is known that increased supply voltage results in higher jet velocity and also higher current draw. Thus, electrical power consumption increases [66, 81]. However, an established relation between voltage, jet velocity and power consumption does not exist to the best knowledge of the author.

It is identified that there is a strong ambiguity in the literature regarding the definition of electric-to-fluidic power conversion efficiency. Therefore, it is also a necessity to compare definitions of different power conversion efficiencies found in the literature. The electric-to-fluidic power conversion efficiency is named as power conversion efficiency throughout the chapter.

The fluidic power of the actuator is a function of air density (ρ), orifice area (A_o) and peak exit jet velocity (U_p). The electrical power consumption is a function of the voltage supply (V) and current draw (I). For capacitive elements there is a phase difference (ϕ) between the voltage and current signals. The power conversion efficiency is a ratio of fluidic power (P_f) to the electrical power (P_e) expressed by:

$$\eta = \frac{P_f}{P_e} \quad (7.1)$$

Table 7.1, presents the ambiguity in the definition of the power conversion efficiency. To remove the uncertainty in the definition, one should be aware that the power conversion efficiency should be consistent throughout the calculations. If the electrical power is calculated for a whole period of oscillation, the jet velocity should be calculated for a whole period of oscillation as well. Therefore, the approach for calculation of the fluidic power is taken as the definition reported by Crowther and Gomes [27]. Even though, different notations are presented regarding the calculation of the electrical power, there seems to be a technical consistency in the literature. This is due to the prod-

uct integration of the time-dependent voltage and current is equivalent to the root-mean-squares of the phase matched voltage and current multiplication.

Table 7.1: Fluidic and electric power definitions in the literature

Study	Jet Velocity Scale	$P_f(W)$	$P_e(W)$
[27, 66]	$U_0^3 = \frac{5}{16}U_p^3$	$\frac{1}{2}\rho A_o U_o^3$	$\frac{1}{T} \int_0^T V(t)I(t)dt$
[86, 151]	N/A	$\frac{1}{2}\rho A_o U_p^3$	$\frac{1}{2}V_p I_p \cos(\phi + 1)$
[81]	$U_0 = \frac{U_p}{\pi}$	$\frac{1}{2}\rho A_o U_0^3$	$\frac{1}{T} \int_0^T V(t)I(t)dt$
[68]	$U_0 = \frac{2\bar{U}_p}{\pi}$	$\rho A_o U_0^2 c$	$V_{rms} I_{rms} \cos(\phi)$
[87]	N/A	$\frac{\rho A_o}{2T} \int_0^T U^3 dt$	$\frac{1}{2}V_p I_p \cos(\phi)$
[89]	$U_0 = \frac{U_p}{\pi}$	$\frac{\pi}{3}\rho A_o U_o^3$	$\frac{1}{T} \int_0^T V(t)I(t)dt$

Table 7.2 shows some of the experimental studies in the literature which achieved relatively high jet velocity. The table includes the year of publication, orifice (or slot size) and cavity diameter, voltage supply, peak jet velocity and electric-to-fluidic power conversion efficiency. As previously mentioned, the power conversion efficiency (η) is defined inconsistent across studies reported.

Table 7.2: A comparison of the experimental studies with key actuator dimensions, voltage supplied and achieved jet velocity and power conversion efficiency

Study	Year	d_o (mm)	D_c (mm)	V_p (V)	U_p (ms ⁻¹)	η (%)
[66]	2006	1.2	25	125	130	7
[27]	2006	1.2	25	45	70	14
[87]	2011	1x4	30	80	35	25
[86]	2014	1	27	50	38	15
[68]	2015	2	30.8	100	15	45
[88]	2015	5	80	35	25	65
[81]	2016	1x12	80	150	120	3.5
[81]	2016	1x12	80	150	211	N/A
[89]	2020	10	52.5	N/A	12	9
[9]	2020	2.5	35	100	100	3

Gomes and Crowther conducted actuator parameter studies for a 27 mm diaphragm and identified the optimum cavity height and depth for output jet velocity maximisation using unimorph polycrystalline piezoceramic actuator [27, 66].

In Chapters 4-5-6 only polycrystalline piezoceramic were employed. Nevertheless, it is known that polycrystalline material inherently has a low electro-mechanical coupling ratio (k_p), thus; it is not optimal for reduced electrical power consumption. It is identified that single crystal piezoceramic promotes a higher electro-mechanical coupling factor as shown in the numerical study of Rusovici and Lesieutre [100]. Lam et al. studied a single crystal piezoelectric micro-jet with working fluid of water [152]. The dimensions are quite different than SJA and involvement of liquid in the cavity differentiates from the scope of the current study. It has been shown that, for the same input voltage, the peak displacement of the single crystal ring is 15 times higher than the polycrystalline ring. Nevertheless, there is not a study which reveals the results of controlled experiments utilising common SJA dimensions and piezoelectric diaphragm size composition (i.e., equal diameter and thickness of substrate and piezoceramic). Single crystal piezoceramic diaphragm should be studied further with a controlled study to compare its performance with polycrystalline material. Single crystal and polycrystalline piezoelectric actuator of same dimensions are studied on common cavity-orifice arrangements in this chapter.

Another high-potential piezoelectric diaphragm type is the bimorph composite discs which may yield enhanced transverse deflections under relatively low voltage. Bimorph piezoelectric actuator promotes a larger transverse displacement as shown in the study of Yu et al. [153]. However, power conversion efficiency of bimorph piezoelectric driven SJA are not reported. Therefore, it can be anticipated that the displacement of the bimorph diaphragm would be higher than the unimorph diaphragm which would turn into jet velocity enhancement. Nevertheless, due to the involvement of two piezoceramic layers, it is likely that the current consumption of the bimorph would be higher than a unimorph actuator. Unimorph and bimorph driven SJA are studied on common actuator geometries to quantify the aforementioned performance metrics.

On the other hand, in Chapter 6 (Section 6.3.4) a single modal frequency response SJA was investigated in the validation case. As a result, the exit jet velocity enhancement was identified by devising the single modal frequency response. It was mentioned in Chapter 6 that the power conversion efficiency of single modal SJA should be studied. This is because it was not documented in previous studies, such as in Gallas's single modal response SJA [20]. In this chapter, the power conversion efficiency of the single modal SJA is also investigated.

This chapter consists of three individual studies on the performance of SJA such as diaphragm displacement, exit jet velocity and electric-to-fluidic power conversion efficiency. Section 7.2 presents the performance investigation of polycrystalline and single crystal piezoceramic driven SJA using common cavity-orifice geometry of two different configurations. Section 7.3 introduces the performance comparison of unimorph and bimorph piezoelectric driven SJA common cavity-orifice geometry of two different configurations. Section 7.4 delivers the performance investigation of the single modal frequency response SJA. The discussions are presented in Section 7.5, which is followed by the summary of the chapter in Section 7.6.

7.2 Comparison Between Polycrystal and Single Crystal Disc

7.2.1 Design of Experiments

This section investigates the effect of employing a polycrystalline (PZT-5A) and a single crystal (67% PMN- 33% PT) piezoceramic of identical sizes on common actuator geometry. Two actuator geometry configurations, namely opposite and adjacent orifice-diaphragm are studied.

The piezoelectric actuator with substrate and polycrystalline piezoceramic is abbreviated as PZT-5A diaphragm throughout the section. Likewise, the piezoelectric actuator of single crystal piezoceramic is abbreviated as PMN-PT diaphragm throughout the section.

The electric field of the single crystal piezoceramic is 2 kV/cm of the thickness, which limits the voltage supply to the single crystal actuator to 46 V. To ensure that single crystal piezoceramic made discs do not undergo fracture, the limit of the supply voltage is taken as 40 V. The polycrystalline diaphragm can take higher voltage due to higher electric field (i.e., $E_c = 12$ kV/cm), provided lead solders can resist. In order to ensure fair comparison, the voltage supply for the polycrystalline discs are limited to 40 V.

Table 7.3 presents the size and thickness compositions of the polycrystalline (PZT-5A) and single crystal (PMN-PT) piezoceramic actuators and their piezoelectric properties.

Table 7.3: Polycrystalline and single crystal actuator dimensions and properties

Parameter	PZT-5A	PMN-PT
D_{brass} (mm)	27	27
D_{pzt} (mm)	19.8	19.8
t_{brass} (mm)	0.22	0.22
t_{pzt} (mm)	0.23	0.23
d_{31} (pm/V)	-180	-560
k_p (-)	0.4	0.9
$\tan(\delta)$	2.0	0.6

7.2.2 Opposite Orifice-Diaphragm Configuration

The cavity-orifice size is consistent with the jet velocity optimised design of Gomes which is identified as a result of a comprehensive sensitivity analysis [66]. It is a known SJA design feature that cavity height is inversely proportional to the jet velocity [98, 154]. Shallow cavity promotes larger jet velocity due to the increased swept volume of the diaphragm compared to the volume of the cavity. Also, stronger vortex pair forms in the case of a shallow cavity design [98]. The ratio of the cavity height to the cavity diameter is 0.027 and the design can be classified as a pancake shape SJA (i.e., $H/D_c < 0.5$).

Table 7.4 presents the size of cavity-orifice and the operational parameters.

Table 7.4: Cavity-orifice arrangement size and operational parameters

Parameter	PZT-5A	PMN-PT
d_o (mm)	1.2	1.2
D_c (mm)	25	25
h (mm)	2.5	2.5
H (mm)	0.67	0.67
f (Hz)	100-4000	100-4000
V_p (V)	20-30-40	20-30-40

7.2.3 Diaphragm Displacement

The mean peak centre diaphragm displacement measurements are presented in this section. The displacement of the diaphragm is proportional to the jet velocity, therefore, it is an important measure of piezoelectric actuator performance. Figure 7.2a presents the voltage sweep over the forcing frequency range of the PZT-5A diaphragm. The peak displacement at the resonant frequency is $15.8 \mu\text{m}$, $24.1 \mu\text{m}$ and $32.2 \mu\text{m}$ for $20 V_p$, $30 V_p$ and $40 V_p$, respectively. Figure 7.2b presents the voltage sweep over the forcing frequency range of the PMN-PT diaphragm. The peak displacement at the resonant frequency is $47.9 \mu\text{m}$, $60.5 \mu\text{m}$ and $82.7 \mu\text{m}$ for $20 V_p$, $30 V_p$ and $40 V_p$, respectively. It is observed that the PMN-PT diaphragm gives approximately three times more peak centre displacement than the PZT-5A diaphragm.

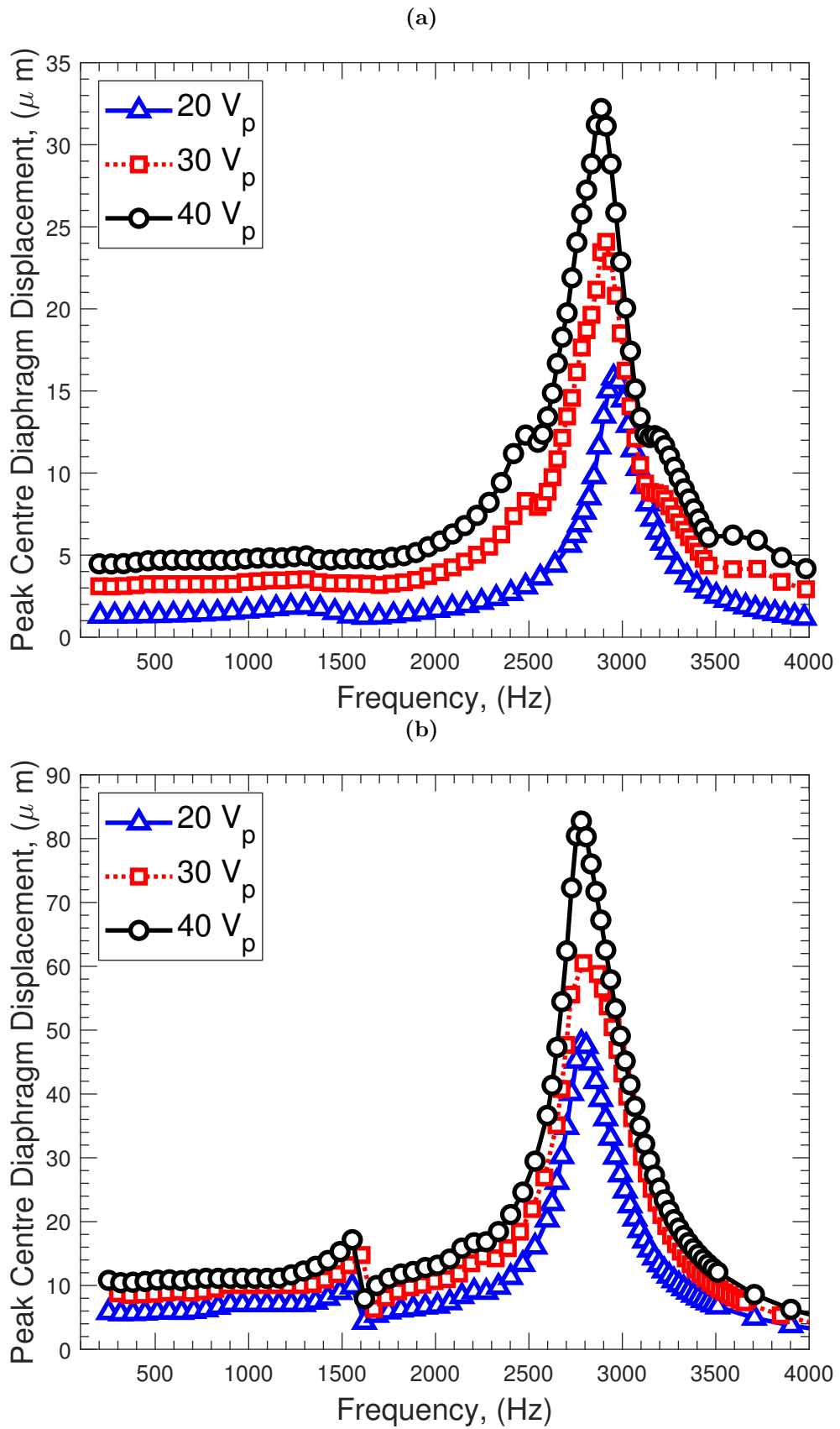


Figure 7.2: *Opposite Configuration SJA - Centre peak diaphragm displacements of SJA (a) PZT-5A diaphragm driven SJA (b) PMN-PT diaphragm driven SJA*

7.2.4 Jet Velocity

The exit jet velocity stands as the primary performance criteria of the SJA and it is measured at the orifice exit plane. Figure 7.3a presents the jet velocity measurements of the PZT-5A diaphragm. The double peak occurrence, due to the cavity acoustic and diaphragm mechanical resonance, is observed for all three supply voltages.

The jet velocities corresponding to the cavity acoustic and diaphragm mechanical resonance increase with the supply voltage. The jet velocity corresponding to the cavity acoustic resonance of the PZT-5A diaphragm are 20.1 ms^{-1} , 26 ms^{-1} and 34 ms^{-1} for 20 V_p , 30 V_p and 40 V_p , respectively. The mean peak jet velocity corresponding to the mechanical resonance is 36.8 ms^{-1} , 49.9 ms^{-1} and 65.0 ms^{-1} for 20 V_p , 30 V_p and 40 V_p , respectively.

Figure 7.3b presents the jet velocity measurements of the PMN-PT diaphragm. The jet velocity corresponding to the cavity acoustic resonance of the PMN-PT diaphragm are 45.0 ms^{-1} , 55.6 ms^{-1} and 64.4 ms^{-1} for 20 V_p , 30 V_p and 40 V_p , respectively. The mean peak jet velocity corresponding to the mechanical resonance is 70.7 ms^{-1} , 86.1 ms^{-1} and 99.5 ms^{-1} for 20 V_p , 30 V_p and 40 V_p , respectively. The jet velocity of the PMN-PT diaphragm driven SJA is two times more than the PZT-5A with supply voltage of 20 V_p , but the amplification decreases with the increasing voltage. On the other hand, the exit jet velocity corresponding to the cavity acoustic resonance of the PMN-PT actuator is approximately equal to the mechanical resonance jet velocities of the PZT-5A diaphragm.

The fluidic/pressure losses scale with U_p^2 , therefore the increase of jet velocity with voltage is non-linear. The potential reasons for this are the compressibility effects, voltage dependent piezoceramic saturation/dissipation and the increased pressure loading acting on the diaphragm. The cavity acoustic resonance increase with the voltage linearly in both cases where the viscous and compressibility effects are less. Detailed discussion is given in Section 7.5.

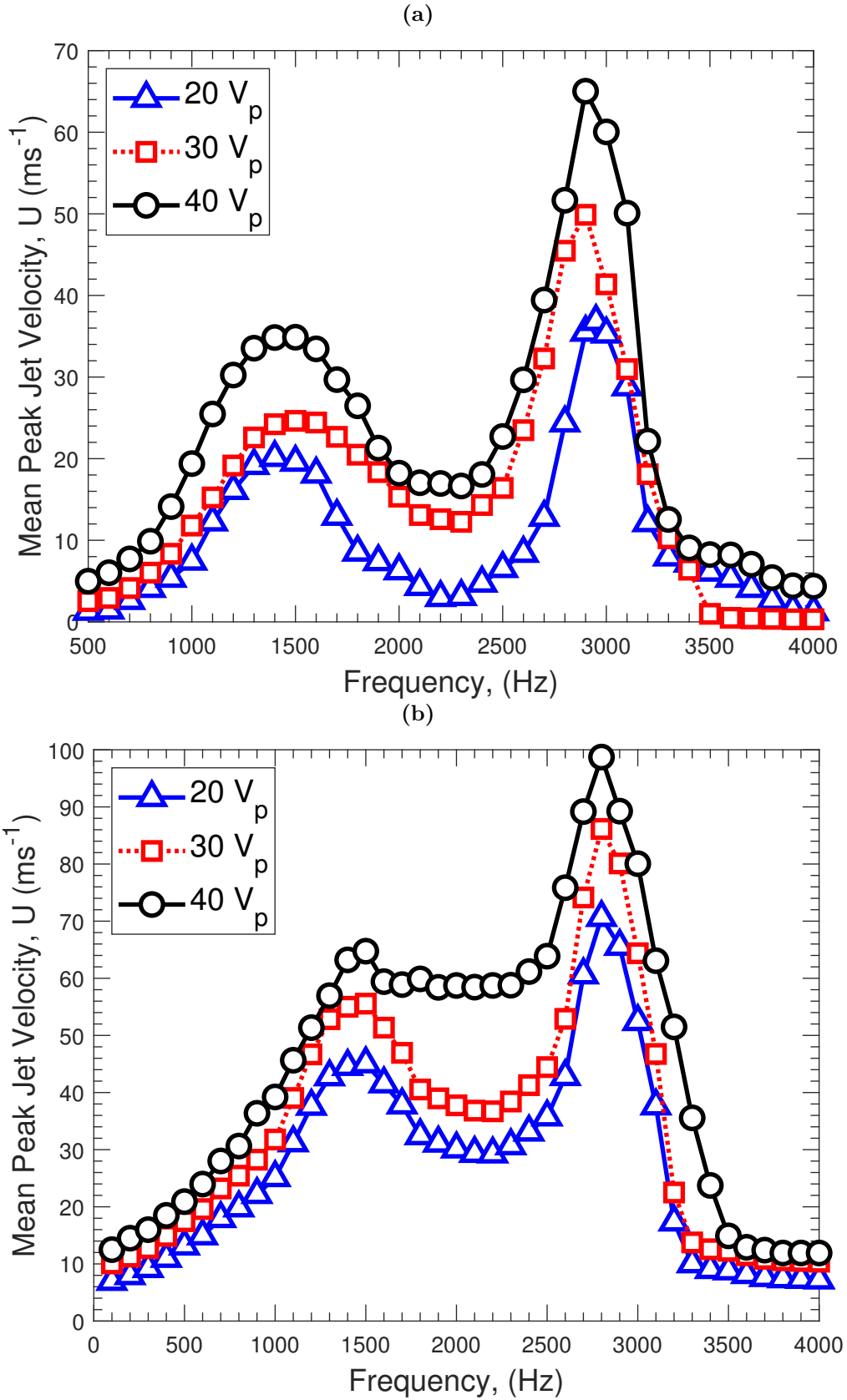


Figure 7.3: Mean Peak Exit Jet Velocity (a) PZT-5A diaphragm driven SJA (b) PMN-PT diaphragm driven SJA

7.2.5 Current Draw

Real-time acquisition of voltage and current is required to be able to calculate the power consumption of the SJA. Figure 7.4a presents the current drawn by the PZT-5A diaphragm actuator. The peak current consumption of the PZT-5A diaphragm is 11.2 mA, 14.4 mA, 20 mA for supply voltages of $20 V_p$, $30 V_p$ and $40 V_p$, respectively.

Figure 7.4b presents the current drawn by the PMN-PT diaphragm driven SJA. It is identified that the PMN-PT diaphragm consumes approximately twice as much of the current drawn by the PZT-5A diaphragm. The PMN-PT diaphragm has a peak current consumption of 24.4 mA, 36 mA, 45.9 mA for supply voltages of $20 V_p$, $30 V_p$ and $40 V_p$, respectively. The peak current consumption coincides with the resonant frequency for both diaphragms.

It should be noted that the peak current drawn by the PMN-PT diaphragm shifts -100 Hz at $40 V_p$ with the resonant peak. This change is thought to be due the increased displaced volume in the cavity which changes the relative positions of cavity acoustic and diaphragm mechanical resonance.

Another important feature of the piezoelectric diaphragm is their capacitive nature. The piezoceramic acts as a capacitor and stores power which causes a difference between the reactive ($V(t)I(t)$) and true power ($V(t)I(t)\cos(\phi)$). It is known that the true power of the actuator is relatively small compared to its reactive power [68]. To understand the power characteristics of the diaphragms, the phase difference (ϕ) between the time-dependent voltage and current signals are computed.

Figure 7.5 presents the power factor (i.e., cosine of phase difference) for the PZT-5A and PMN-PT diaphragms. The power factors are presented for a single voltage (i.e., $20 V_p$) for both diaphragm type which is representative across all supply voltages.

The power factor characteristics for the diaphragms indicates that at the resonant frequency, the capacitive nature of the diaphragm tends to be reactive.

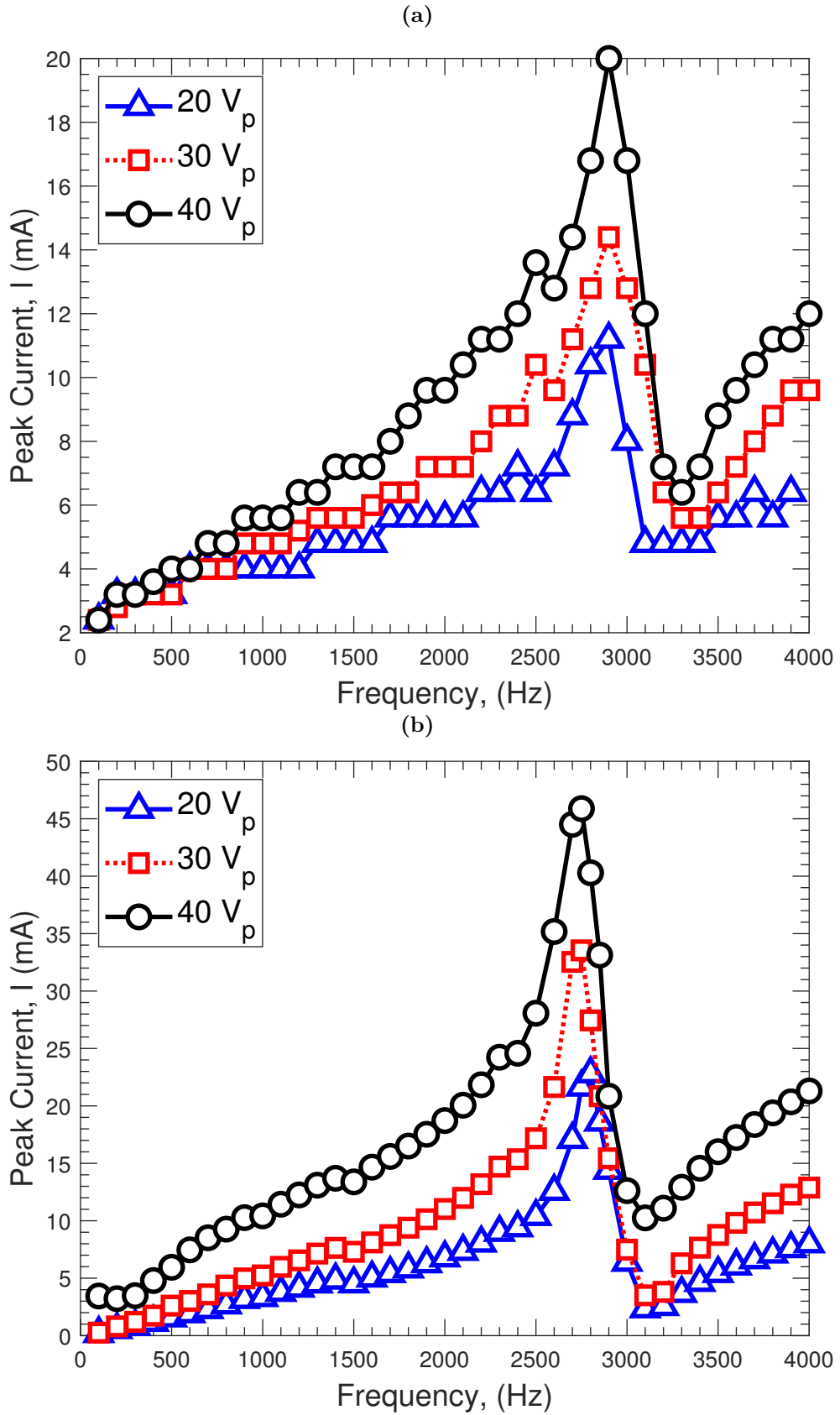


Figure 7.4: *Opposite Configuration SJA - Mean Peak Current Draw of SJA (a) PZT-5A diaphragm driven SJA (b) PMN-PT diaphragm driven SJA*

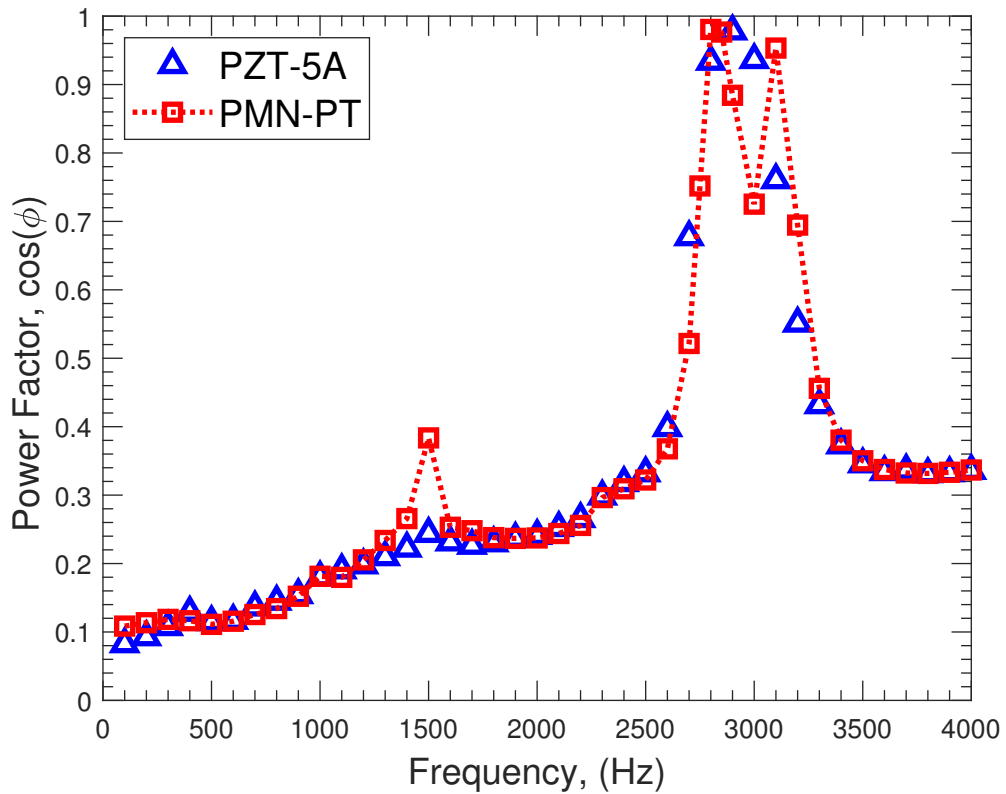


Figure 7.5: Power factor ($\cos \phi$) of PZT-5A and PMN-PT diaphragms

The PZT-5A diaphragm has a single peak of power factor at the resonant frequency. PMN-PT diaphragm exhibits a double peak occurrence of the power factor; first one at the mechanical resonance frequency and the second one 300 Hz beyond the resonant frequency. It should be noted that smaller peaks of the power factor are also related to the frequency corresponding to the cavity acoustic resonance which implies that the resonance drives the capacitive nature of the disc to become more reactive.

7.2.6 Electric-to-Fluidic Power Conversion Efficiency

In the introduction of this chapter, the different definitions regarding the power conversion efficiency are presented. For the analysis of the results, the approach proposed by Crowther and Gomes [27] is adopted which stands out as the most representative model. Thus, instantaneous jet velocity, $u(t)$, is modelled using the following expression using an expression for a biased sinusoid with the peak velocity (U_p):

$$u(t) = \frac{U_p}{2}(1 - \cos(\omega t)) \quad (7.2)$$

The fluidic power (P_f) over a cycle is then:

$$P_f = \frac{1}{2}\rho A_o u(t)^3 = \frac{1}{2}\rho A_o \left(\frac{1}{T} \int_0^T u(t)^3 \right) = \frac{1}{2}\rho A_o \left(\frac{5}{16} U_p^3 \right) \quad (7.3)$$

The power calculation is done by integrating the product of voltage and current over a period oscillation, then ensemble averaging over many (+5000) cycles.

Figure 7.6a presents the power conversion efficiency of PZT-5A diaphragm. The peak power conversion efficiency is identified at the cavity acoustic resonance which has relatively high jet velocity and low current consumption. At 20 V_p , the power conversion efficiency of cavity acoustic and diaphragm mechanical resonances are approximately equal. The increasing voltage decreases the efficiency at around diaphragm mechanical resonance and increases about the actuation frequency around cavity acoustic resonance. The reasons of this are thought to be due to more dominant compressibility effects and fluidic losses which limits the jet velocity and increase in both voltage supply and current draw.

Figure 7.6b presents the power conversion efficiency of PMN-PT diaphragm. The power conversion efficiencies at the mechanical resonance frequency is 39.5%, 30.7% and 23.0% corresponding to the supply voltages of 20 V_p , 30 V_p and 40 V_p , respectively. At the mechanical resonance and neighbouring frequencies, the power conversion efficiency reduces with the increasing supply voltage. At the actuation frequency around the mechanical resonance, the power conversion efficiency is bimodal, due to the double peak occurrence of the power factor shown in Figure 7.5. This is caused by the linear increased in the current consumption, increased compressibility effects and fluidic/pressure losses with increasing voltage which results in insufficient peak exit jet velocity to sustain the conversion efficiency levels attained by the lower supply voltages.

Frequencies around the cavity acoustic resonance, promotes an increased jet velocity with relatively lower increase of the current consumption, compared to the mechanical resonance frequency. Therefore, the efficiency is conserved with increasing voltage. In the middle region between the two resonance peaks, it is observed that the power conversion efficiency and the voltage supply is inversely proportional. This is due to the low jet velocity and high current consumption at $20 V_p$ which then alternates by lower current increment but a higher jet velocity with the increasing supply voltage.

When the power conversion efficiency of the PZT-5A and PMN-PT driven SJA is compared, it is observed that in both cases; the cavity-acoustic resonance dominated region promotes the largest power conversion efficiency. PMN-PT diaphragm introduced approximately a threefold increase in the power conversion efficiency across all supply voltages when peak efficiency ratios are compared.

Table 7.5 presents the peak power conversion efficiency and corresponding peak exit jet velocity for both diaphragm types. The table consists of power conversion efficiency (η) and peak exit jet velocity (U_p). In the table, peak conversion efficiency and peak jet velocity is presented regardless the supply voltage. The peak efficiency for the PZT-5A and PMN-PT are presented with their corresponding jet velocity and vice versa.

Table 7.5: Comparison of peak power conversion efficiency values

	PZT-5A		PMN-PT	
	η (%)	U_p (ms ⁻¹)	η (%)	U_p (ms ⁻¹)
Peak Efficiency	33.2	33.5	72.2	63.2
Peak Jet Velocity	16	65.1	23	99.5

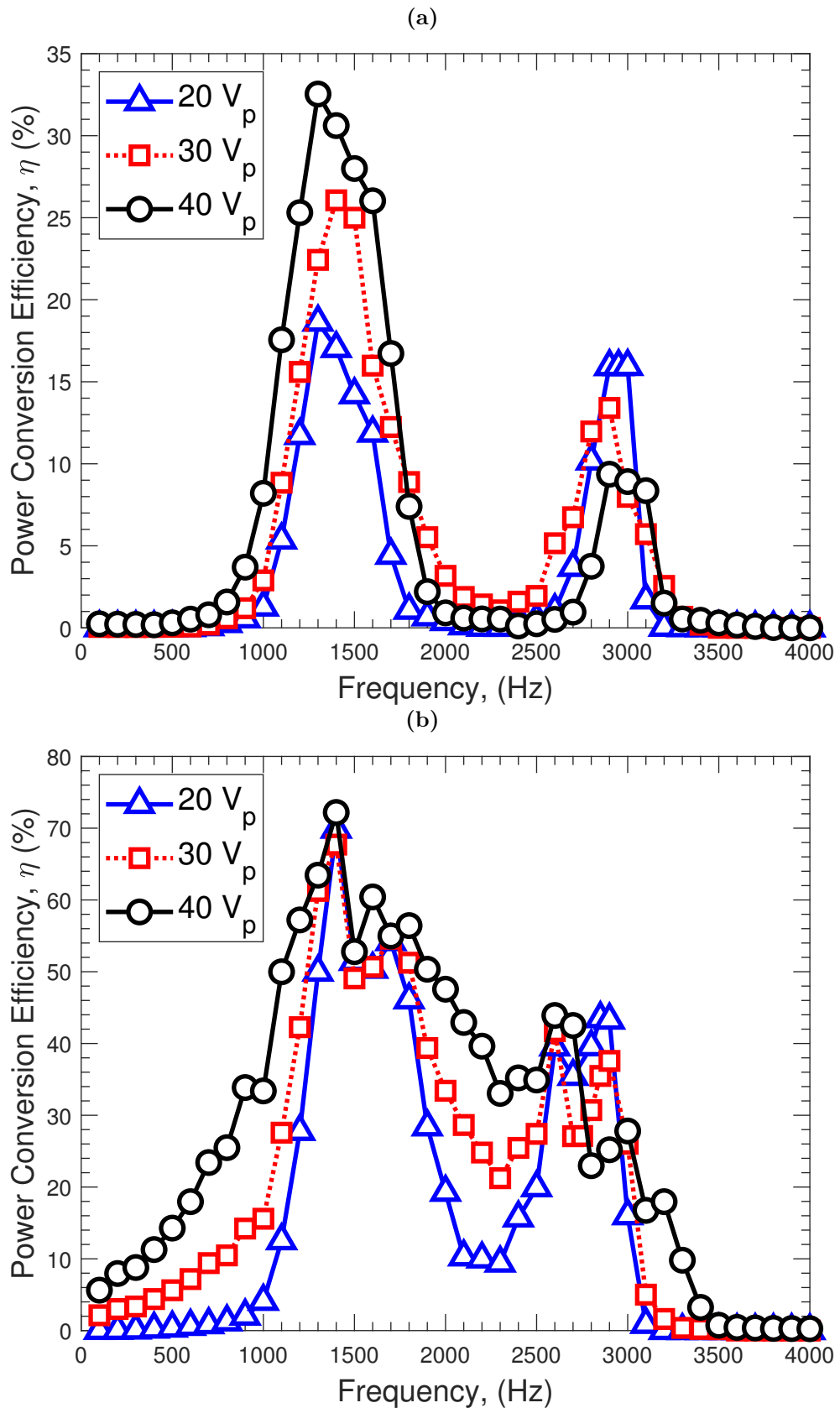


Figure 7.6: *Opposite Configuration SJA - Power Conversion Efficiency (a) PZT-5A diaphragm driven SJA (b) PMN-PT diaphragm driven SJA*

7.2.7 Adjacent Orifice-Diaphragm Configuration

The adjacent orifice-diaphragm configuration is the second type of orifice-cavity arrangement studied within this chapter. The adjacent orifice-diaphragm configuration is thought to be useful for potential flow control applications in an array design. Hereafter, the adjacent orifice-diaphragm configuration is named as adjacent SJA. In an array of SJA, adjacent design have the advantage of having closer distance between two consecutive orifices, around $\approx O(H)$, which is required to grant effective flow control over a surface. To note, in opposite configuration SJA array, the spacing between consecutive orifice distance is $\approx O(D_c)$ which is around 20 times more than the adjacent SJA array.

The adjacent orifice-diaphragm have an increased pressure loss term due to the bending of the flow during the discharge (ejection) phase which is likely to result in reduced jet velocity, compared to the opposite configuration. Also, the increased pressure loss can be explained by the smaller net cavity volume change in this configuration. Additionally, there is a design constraint that the cavity height must be larger than the orifice diameter, $H > d_o$. Therefore, the cavity height (H) have to increase compared to the design used in the previous section. As previously mentioned, the cavity height is inversely proportional with the maximum output jet velocity. The orifice diameter is reduced to 1.0 mm to minimize the cavity height and to increase the jet velocity.

The constraint applied to the decision of the orifice neck height is the other important design parameter. It is known that a short orifice neck ($h/d_o < 0.75$) causes flow separation in the up-stream (inner lips of the orifice) which does not reattach. The flow marginally reattaches at around ($h/d_o \approx 0.75$) and should become a fully developed flow if ($h/d_o > 0.75$) is satisfied [65]. It is also known that the acoustic resistance of the circular orifice is proportional to the length of the orifice and scales inversely proportional with the d_o^4 , such as; $R_o = C \frac{h}{d_o^4}$ where C is $\mu/2\pi$. Therefore, there should be a compromise between increasing

the orifice neck length (h) and increasing the acoustic orifice resistance to start being detrimental.

Orifice neck length is selected based on multiphysics simulations for 2.0, 2.5 and 3.0 mm in which resulted in the peak jet velocity (at the mechanical resonance frequency) of 31.5 ms^{-1} , 33.9 ms^{-1} and 30.9 ms^{-1} , respectively. Therefore, the orifice neck length is selected as 2.5 mm.

The organisation of this section is similar to the previous section. The results are presented for the jet velocity, current drawn and power conversion efficiency. The diaphragm displacement measurements are not presented due to similarity with the previous results.

The dimensions of the cavity-orifice size and the diaphragms are presented in Table 7.6. The operational parameters which are actuation frequency and voltage supply is also displayed.

Table 7.6: Cavity-orifice arrangement size and operational parameters

Parameter	PZT-5A	PMN-PT
d_o (mm)	1.0	1.0
D_c (mm)	25	25
h (mm)	2.5	2.5
H (mm)	1.2	1.2
f (Hz)	100-4000	100-4000
V_p (V)	20-30-40	20-30-40

7.2.8 Jet Velocity

Figure 7.7a presents the mean peak jet velocity results of PZT-5A diaphragm for $20 V_p$, $30 V_p$ and $40 V_p$ of supply voltage. It is observed that the cavity acoustic resonance is located at 900 Hz and the diaphragm mechanical resonance is identified at 2900 Hz. The exit jet velocity corresponding to the cavity acoustic resonance is 16.7 ms^{-1} , 24.9 ms^{-1} and 32.9 ms^{-1} . The peak jet velocity at the diaphragm mechanical resonance is 33.8 ms^{-1} , 46.1 ms^{-1} and 58.3 ms^{-1} for $20 V_p$, $30 V_p$ and $40 V_p$, respectively.

Figure 7.7b presents the mean peak jet velocity results of PMN-PT diaphragm

for $20 V_p$, $30 V_p$ and $40 V_p$ of supply voltage. It is observed that the cavity acoustic resonance is also located at 900 Hz and the diaphragm mechanical resonance is identified at 2800 Hz. The exit jet velocity corresponding to the cavity acoustic resonance is 31.1 ms^{-1} , 40.0 ms^{-1} and 52.5 ms^{-1} . The peak jet velocity at the diaphragm mechanical resonance is 61.9 ms^{-1} , 74.2 ms^{-1} and 90.3 ms^{-1} for $20 V_p$, $30 V_p$ and $40 V_p$, respectively.

PMN-PT diaphragm promotes 2 times more jet velocity at $20 V_p$ in which the ratio reduces to 1.5 times at $40 V_p$. The adjacent configuration SJA resulted in jet velocity reduction for both diaphragm types compared to the opposite configuration SJA.

7.2.9 Current Draw

Figure 7.8a presents the current drawn by the PZT-5A diaphragm driven actuator. It is identified that the PMN-PT diaphragm consumes approximately twice as much of the current drawn by the PZT-5A diaphragm. The peak current consumption of the PZT-5A diaphragm is 13.6 mA, 15.6 mA, 21.3 mA for supply voltages of $20 V_p$, $30 V_p$ and $40 V_p$, respectively.

Figure 7.8b presents the voltage supplied and current drawn by the PMN-PT diaphragm actuator. The PMN-PT diaphragm have a peak current consumption of 25.1 mA, 40 mA, 51.2 mA for supply voltages of $20 V_p$, $30 V_p$ and $40 V_p$, respectively. The peak current consumption coincides with the resonant frequency for both diaphragms.

It is observed that the current consumption has increased around 10% at the adjacent SJA compared to the opposite SJA. This is thought to be due to the increased pressure loading on the disc due to the reduced volume of the cavity and less fluid discharge due to the adjacent orifice-diaphragm configuration.

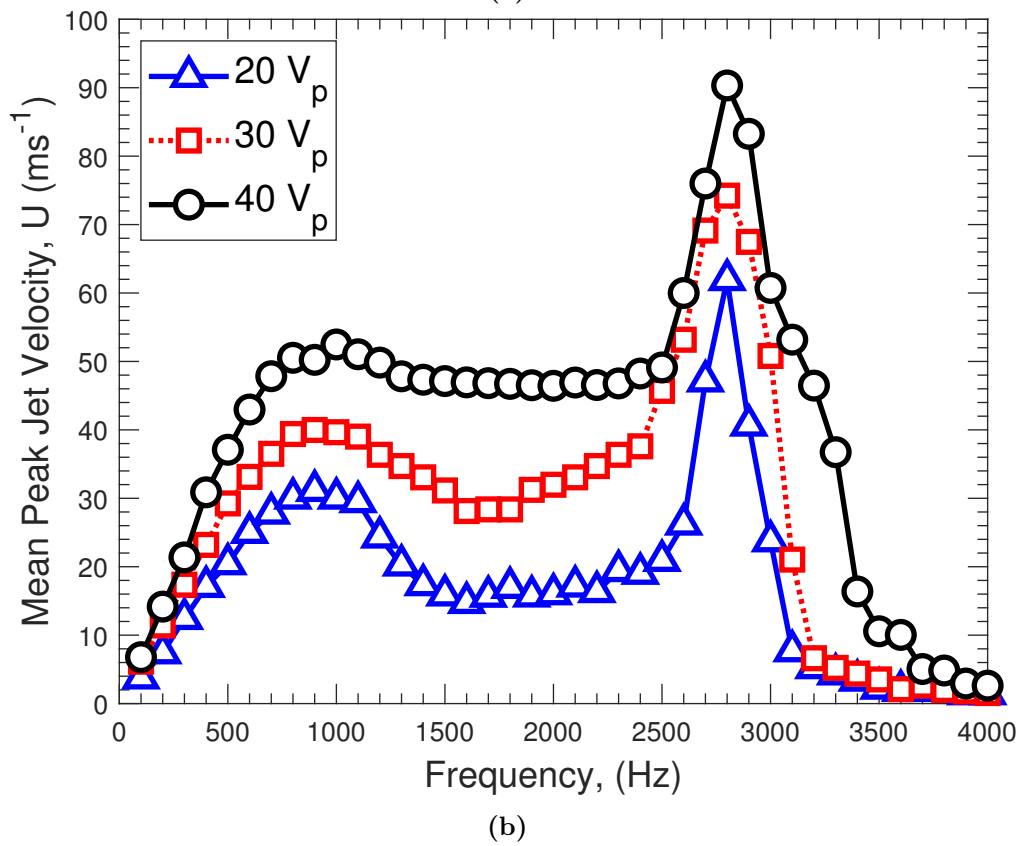
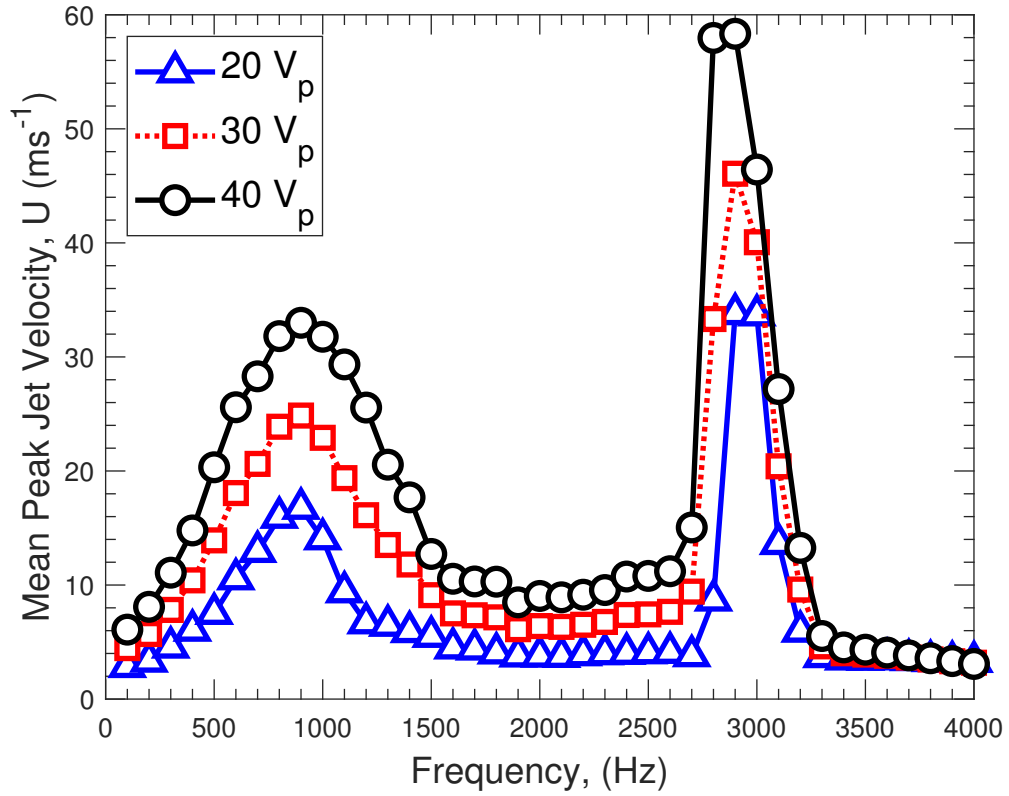


Figure 7.7: Adjacent Configuration SJA - Mean Peak Exit Jet Velocity (a) PZT-5A diaphragm driven SJA (b) PMN-PT diaphragm driven SJA

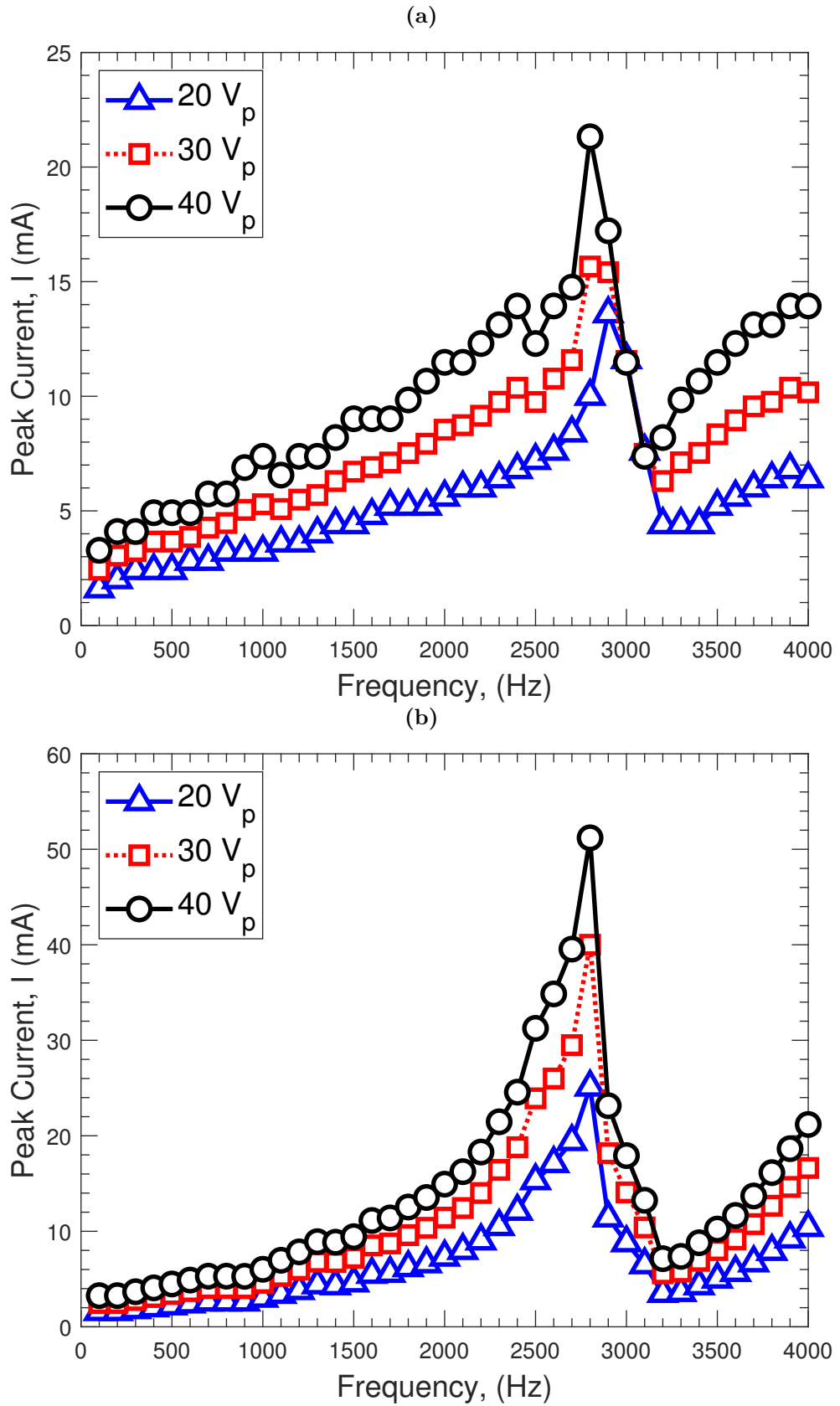


Figure 7.8: Adjacent Configuration SJA - Mean Peak Current Draw (a) PZT-5A diaphragm driven SJA (b) PMN-PT diaphragm driven SJA

7.2.10 Electric-to-Fluidic Power Conversion Efficiency

The power conversion efficiency calculation procedure is the same as Section 7.2.6. Figure 7.9a presents the power conversion efficiency for PZT-5A diaphragm. The power conversion efficiencies at the mechanical resonance frequency is 8.0%, 12.8% and 17.6% corresponding to the supply voltages of $20 V_p$, $30 V_p$ and $40 V_p$, respectively. At the mechanical resonance and neighbouring frequencies, the power conversion efficiency increases with the increasing supply voltage. This trend is similar to the result of opposite SJA. The efficiency corresponding to the cavity acoustic resonance has increased compared to the opposite configuration due to cavity acoustic resonance taking place on lower forcing frequency, with less current consumption.

Figure 7.9b presents the power conversion efficiency for PMN-PT diaphragm. The power conversion efficiency at the mechanical resonance frequency is 38.0%, 28.6% and 19.2% corresponding to the supply voltages of $20 V_p$, $30 V_p$ and $40 V_p$, respectively. The trend between the efficiency and voltage at the mechanical resonance is also similar to the opposite synthetic jet. The peak efficiency values at the mechanical resonance frequency is reduced for increasing voltage due to the additional pressure losses prescribed by the adjacent configuration. Also, with the incremental voltage, the increase in jet velocity is not sufficient to preserve the conversion efficiency rate. Another point regarding the power conversion efficiency decrease is due to the orifice diameter reduction in adjacent SJA compared to the opposite SJA (from 1.2 mm to 1.0 mm). The jet velocity at the surrounding frequencies of the cavity acoustic resonance promote an increased jet velocity as the supply voltage increases with relatively lower increase of the current consumption (compared to the current consumption increase in mechanical resonance frequency). Therefore, the efficiency is conserved with the increasing voltage.

Table 7.7 presents the peak power conversion efficiency and corresponding jet velocity for both diaphragm types. It should be noted that the peak jet velocity

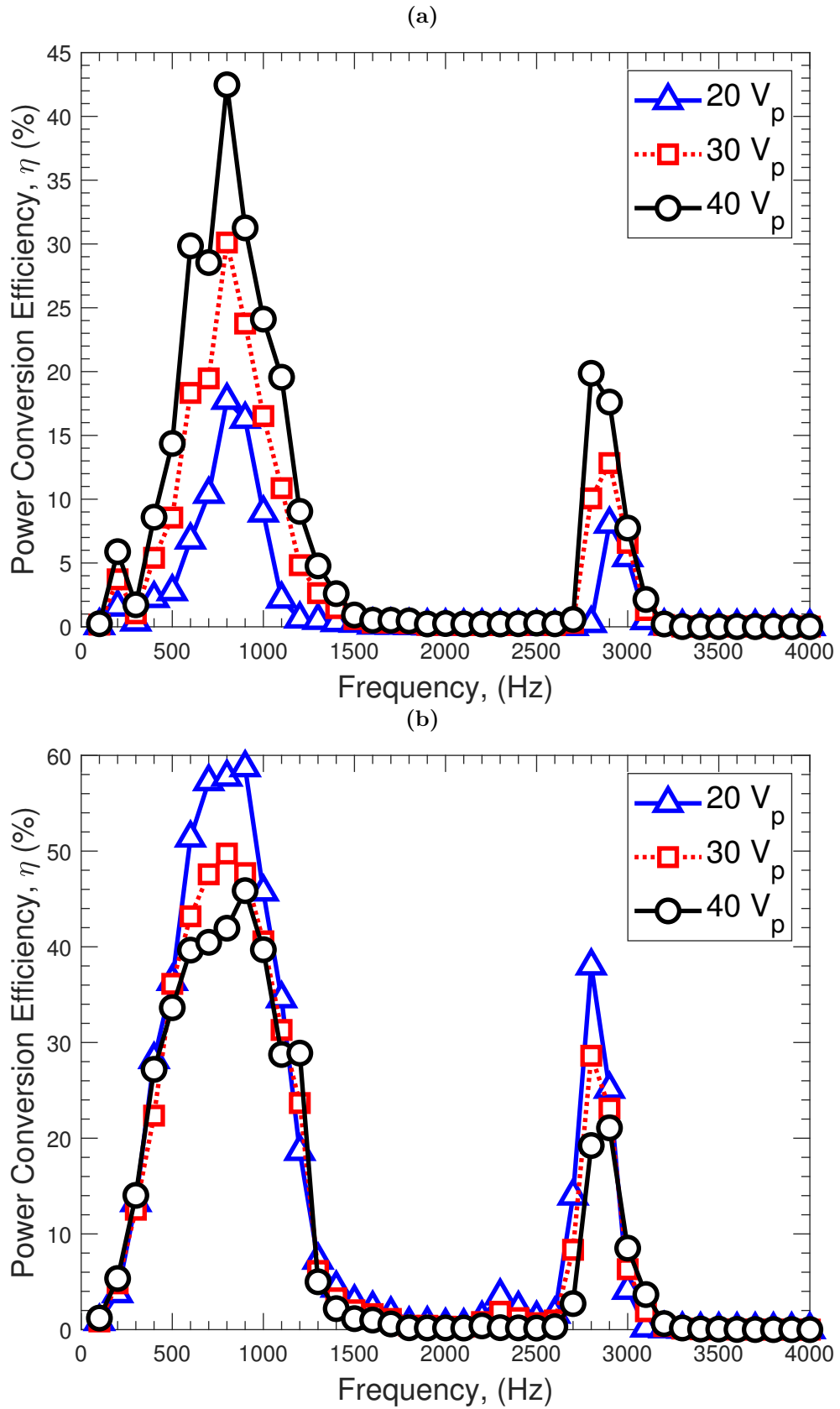


Figure 7.9: Adjacent Configuration SJA - Power Conversion Efficiency (a) PZT-5A diaphragm driven SJA (b) PMN-PT diaphragm driven SJA

and peak power conversion efficiency does not occur at the same actuation frequency. The table presents peak conversion efficiency and peak jet velocity regardless the supply voltage. The peak efficiency for the PZT-5A and PMN-PT are presented with their corresponding jet velocity and vice versa.

Table 7.7: Comparison of peak power conversion efficiency values

	PZT-5A		PMN-PT	
	η (%)	U_p (ms ⁻¹)	η (%)	U_p (ms ⁻¹)
Peak Efficiency	42.5	31.8	58.7	31.1
Peak Jet Velocity	19.9	58.0	19.2	90.3

7.3 Comparison Between Unimorph and Bimorph Disc

7.3.1 Design of Experiments

Bimorph diaphragm consists of two active layers and a passive layer and is known to provide a larger peak displacement than the unimorph piezoelectric actuator [153]. A bimorph diaphragm of total thickness 0.36 mm is compared with a unimorph diaphragm of total thickness 0.40 mm. Even though the piezoelectric actuators are not identical, due to the total thickness similarity, it is thought that a fair comparison is made. Same actuator size for the opposite and adjacent synthetic jets are employed. The rationale behind the sizing of the orifice-cavity arrangement was explained in the previous section, therefore is not repeated here. Table 7.8 presents the size and thickness composition of the unimorph and bimorph polycrystalline actuator and their piezoelectric properties.

Table 7.8: Polycrystalline unimorph and bimorph configuration actuator dimensions and properties

Parameter	Unimorph	Bimorph
D_{brass} (mm)	27	26
D_{pzt} (mm)	19.8	24.6
t_{brass} (mm)	0.20	0.1
t_{pzt} (mm)	0.20	0.13 (x 2)
d_{31} (pm/V)	-180	-175
k_p (-)	0.4	0.4

7.3.2 Opposite Orifice-Diaphragm Configuration

Table 7.9 presents size of cavity-orifice arrangement and operational parameters of the study. The dimensions and geometry of the actuator is identical to the opposite orifice-diaphragm configuration SJA presented in Section 7.2.2.

Table 7.9: Cavity-orifice arrangement dimensions and operational parameters

Parameter	Unimorph	Bimorph
d_o (mm)	1.2	1.2
D_c (mm)	25	25
h (mm)	2.5	2.5
H (mm)	0.67	0.67
f (Hz)	100-4000	100-4000
V_p (V)	20-30-40	20-30-40

7.3.3 Diaphragm Displacement

Figure 7.10a presents the peak centre diaphragm displacement of the unimorph diaphragm. The peak displacement is $29.4 \mu\text{m}$, $41.7 \mu\text{m}$ and $55.4 \mu\text{m}$ for $20 V_p$, $30 V_p$ and $40 V_p$, respectively. An increase is identified at the peak displacement of the unimorph diaphragm compared with the polycrystalline diaphragm used in Section 7.2.3, due to reduced total thickness.

Figure 7.10b presents the peak centre diaphragm displacement of the unimorph diaphragm. The peak displacement is $39.5 \mu\text{m}$, $55.9 \mu\text{m}$ and $74.7 \mu\text{m}$ for supply voltages of $20 V_p$, $30 V_p$ and $40 V_p$, respectively. The peak displacement of the bimorph diaphragm is comparable to the peak displacement of the single crystal diaphragm, presented in Section 7.2.3. Nevertheless, it should be noted

that the total thickness of the bimorph is 0.09 mm less than the single crystal actuator. As the voltage increases a shift of $\approx 100Hz$ of the mechanical diaphragm resonance is observed. This is due to the reduced effective volume of the cavity which modifies the Helmholtz resonance (i.e., cavity acoustic) and repositions the resonant peaks.

By inspecting the Figures 7.10a and 7.10b, it can be observed that the structural damping of the bimorph is larger than the unimorph piezoelectric actuator. This is thought to be due to the presence of double active layers of bimorph.

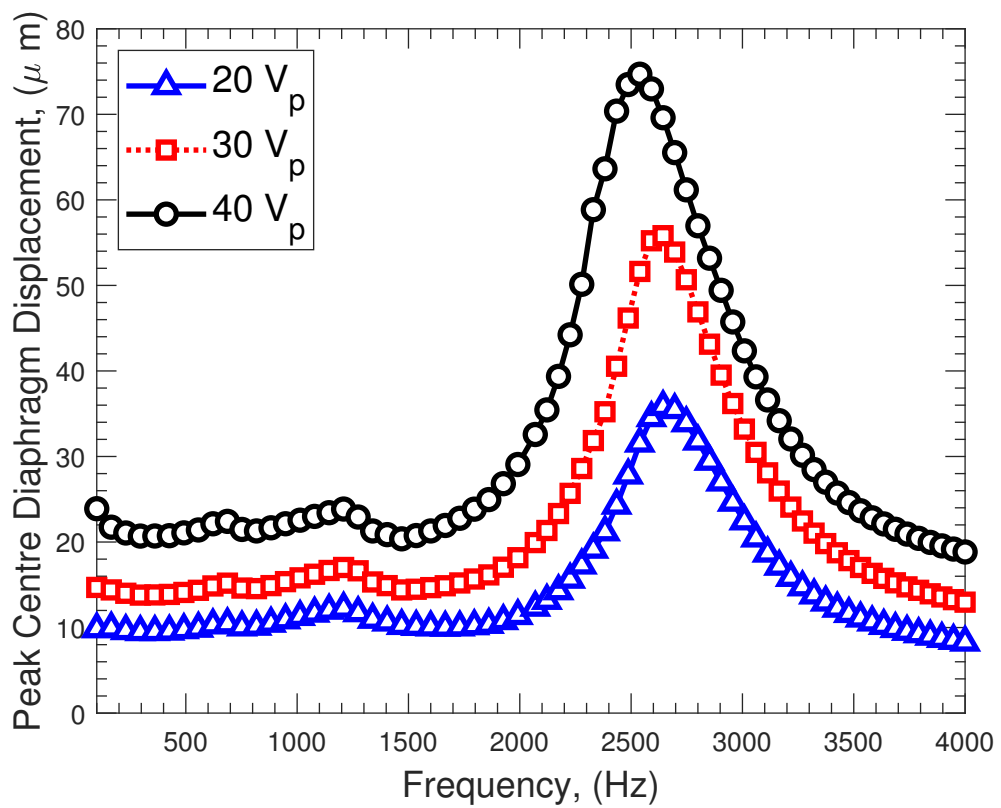
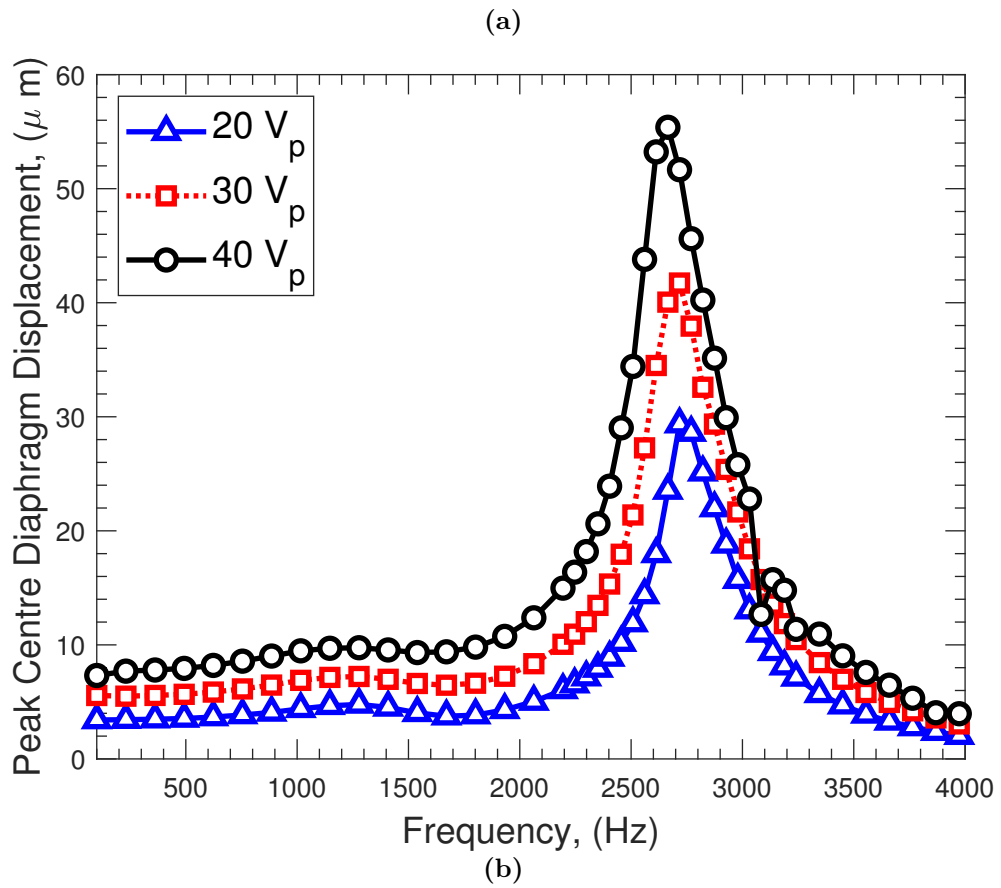


Figure 7.10: *Opposite Configuration SJA - Centre Peak Diaphragm Displacement*
 (a) *Unimorph diaphragm driven SJA* (b) *Bimorph diaphragm driven SJA*

7.3.4 Jet Velocity

Figure 7.11a presents the jet velocity measurements outside the orifice neck exit for the unimorph driven SJA. At the cavity acoustic resonance the peak jet velocity is 22 ms^{-1} , 30 ms^{-1} and 38 ms^{-1} at $20 V_p$, $30 V_p$ and $40 V_p$, respectively. The peak jet velocity corresponding to the mechanical diaphragm resonance is 43.8 ms^{-1} , 57.4 ms^{-1} , and 67.2 ms^{-1} for supply voltage of $20 V_p$, $30 V_p$ and $40 V_p$, respectively.

Figure 7.11b presents the jet velocity measurements outside the orifice exit for the bimorph driven SJA. At the cavity acoustic resonance, the jet velocity is 46 ms^{-1} , 60 ms^{-1} , 75 ms^{-1} at $20 V_p$, $30 V_p$ and $40 V_p$, respectively. The peak jet velocity corresponding to the mechanical diaphragm resonance is 63 ms^{-1} , 76.5 ms^{-1} , and 92.1 ms^{-1} for supply voltage of $20 V_p$, $30 V_p$ and $40 V_p$, respectively.

The cavity acoustic and mechanical diaphragm jet velocity of the bimorph is twice as much as the unimorph driven SJA. It is identified that the bimorph diaphragm promotes a broadband jet velocity response compared to the unimorph actuator driven SJA which exhibits a bimodal frequency response. This is due to the 3 times higher diaphragm displacement provided by the bimorph diaphragm at the low actuation frequency region (i.e., 100 - 2000 Hz).

At supply voltage of $20 V_p$, a small increase after the cavity acoustic resonance is visible which helps identifying the frequency of cavity acoustic resonance. At the higher voltages of $30 V_p$ and $40 V_p$, the cavity acoustic peak cannot be distinguished as the jet velocity response becomes unified. This is due to the large diaphragm displacement prescribed across the actuation frequency range and the jet velocity enhancement due to the cavity acoustic and mechanical resonance. Other factor causing the broadband jet velocity response is the shorter frequency spacing between the cavity acoustic resonance (i.e., 1600 Hz) and mechanical resonance (i.e., 2600 Hz) compared to the PMN-PT driven SJA presented in Section 7.2.2.

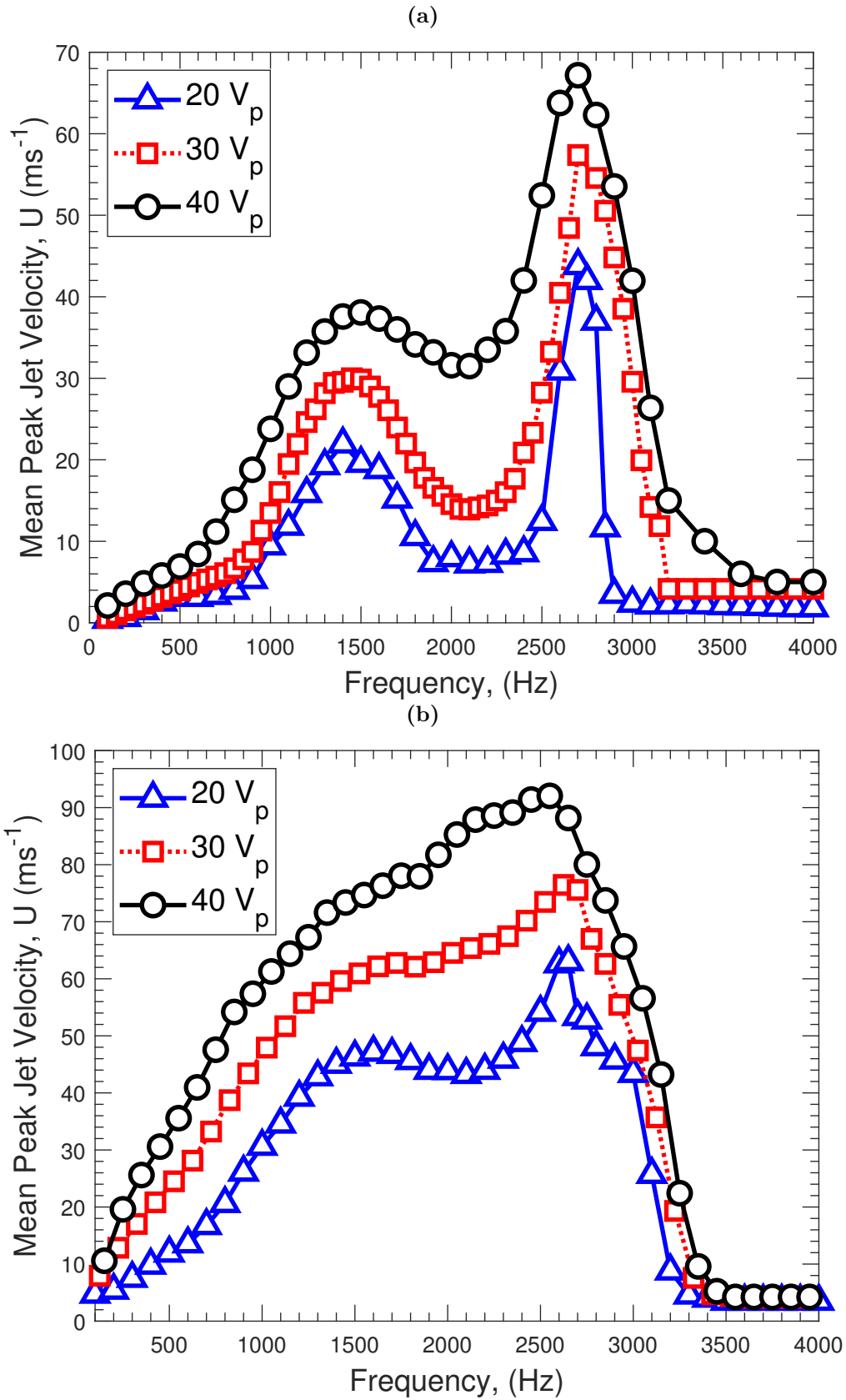


Figure 7.11: *Opposite Configuration SJA - Mean Peak Exit Jet Velocity (a) Unimorph diaphragm driven SJA (b) Bimorph diaphragm driven SJA*

7.3.5 Current Drawn

Figure 7.12a presents the current drawn by the unimorph diaphragm actuator. At the mechanical resonance frequency, the peak current consumption of the unimorph diaphragm is 9.6 mA, 14.4 mA, 19.5 mA for supply voltages of $20 V_p$, $30 V_p$ and $40 V_p$, respectively.

Figure 7.12b presents the voltage supplied and current drawn by the bimorph diaphragm actuator. It is identified that the bimorph diaphragm consumes approximately twice as much of the current drawn by the unimorph diaphragm. At the mechanical resonance frequency, the bimorph diaphragm have a peak current consumption of 50 mA, 74.8 mA, 103.5 mA for supply voltages of $20 V_p$, $30 V_p$ and $40 V_p$, respectively. The peak current consumption coincides with the resonant frequency for both diaphragms. The peak current drawn by the bimorph diaphragm is approximately 5 times more than the unimorph diaphragm around the mechanical resonance frequency. The peak current corresponding to the mechanical resonance frequency is approximately $2.5 \times V_p$ for all supply voltages. Beyond the resonance frequency region, the current consumption initially drops slightly and then increases significantly, scaling with $\cong V_p^{1.4}$.

7.3.6 Electric-to-Fluidic Power Efficiency

Figure 7.13a presents the power conversion efficiency for unimorph diaphragm. The power conversion efficiency corresponding to the diaphragm mechanical resonance decreases with the increasing voltage. At the cavity acoustic resonance dominated frequency region, the efficiency increases with the voltage. This is due to the relatively high increase of the jet velocity against the lower increase in current consumption at the corresponding frequency region.

Figure 7.13b presents the power conversion efficiency for bimorph diaphragm. It is identified that the power conversion efficiency reduces around the peak jet velocity (≈ 2600 Hz). Also, the increasing voltage reduces the efficiency

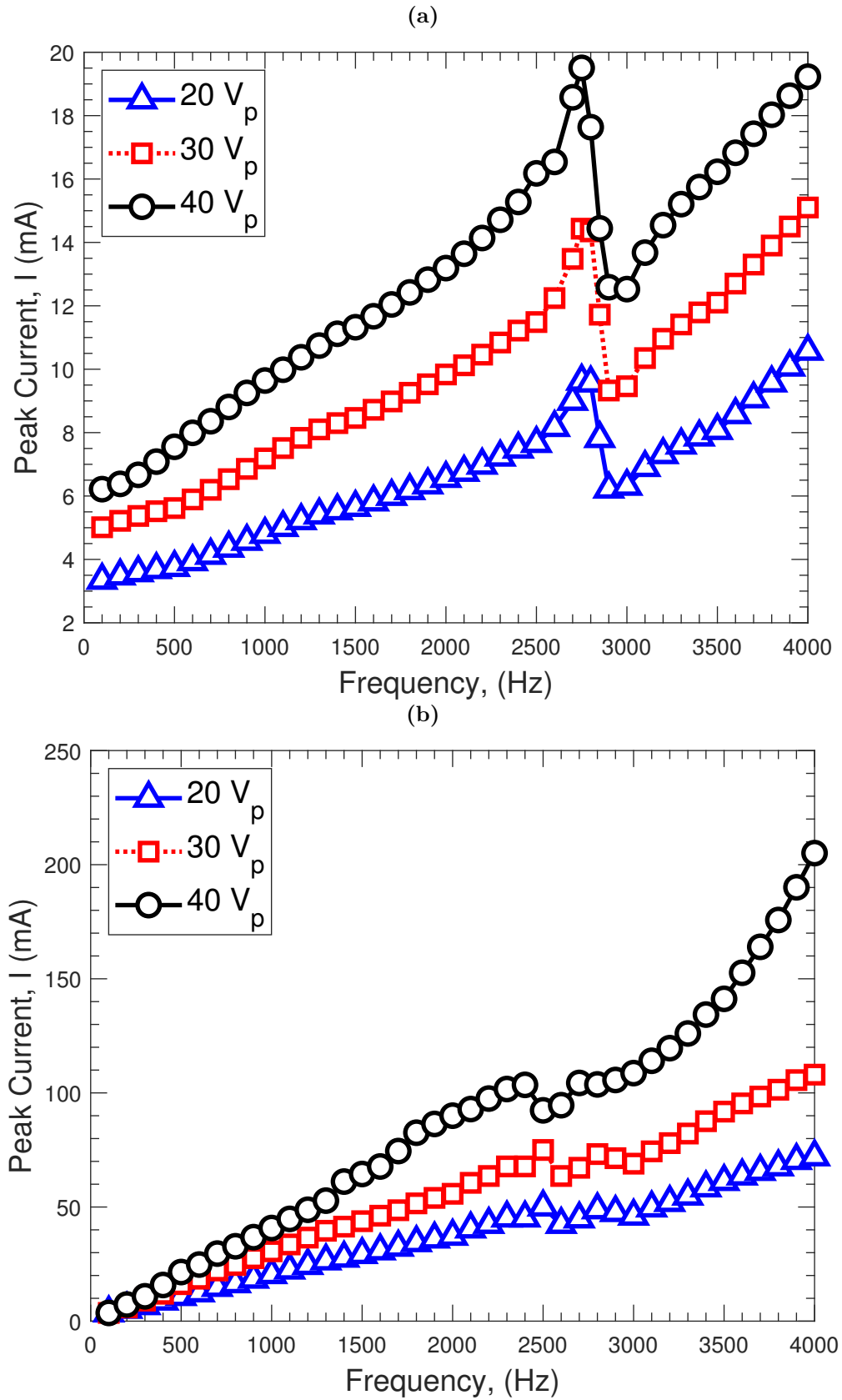


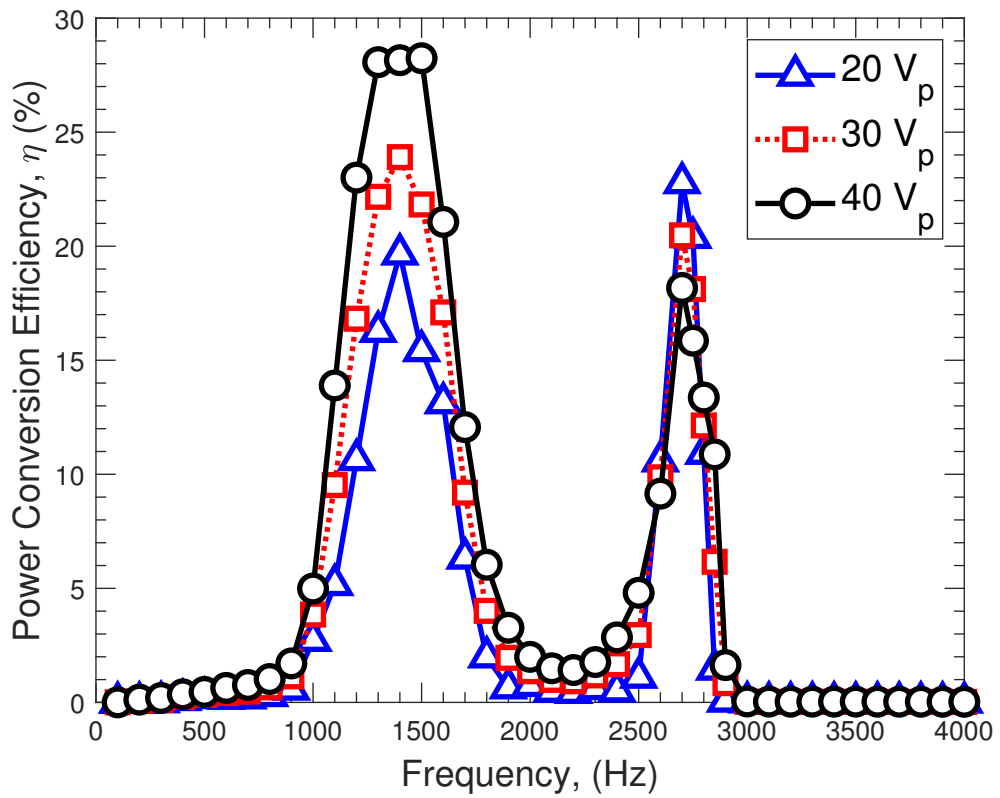
Figure 7.12: *Opposite Configuration SJA - Mean Peak Current Draw (a) Unimorph diaphragm driven SJA (b) Bimorph diaphragm driven SJA*

further at around the mechanical resonance frequency. The power conversion efficiency is larger at around cavity acoustic resonance frequency (≈ 1400 Hz). The peak conversion efficiency corresponds to lower actuation frequency as the voltage increase. This is due to the remarkable increase in current drawn with increasing voltage towards the diaphragm mechanical resonance which is not compromised by the jet velocity increase.

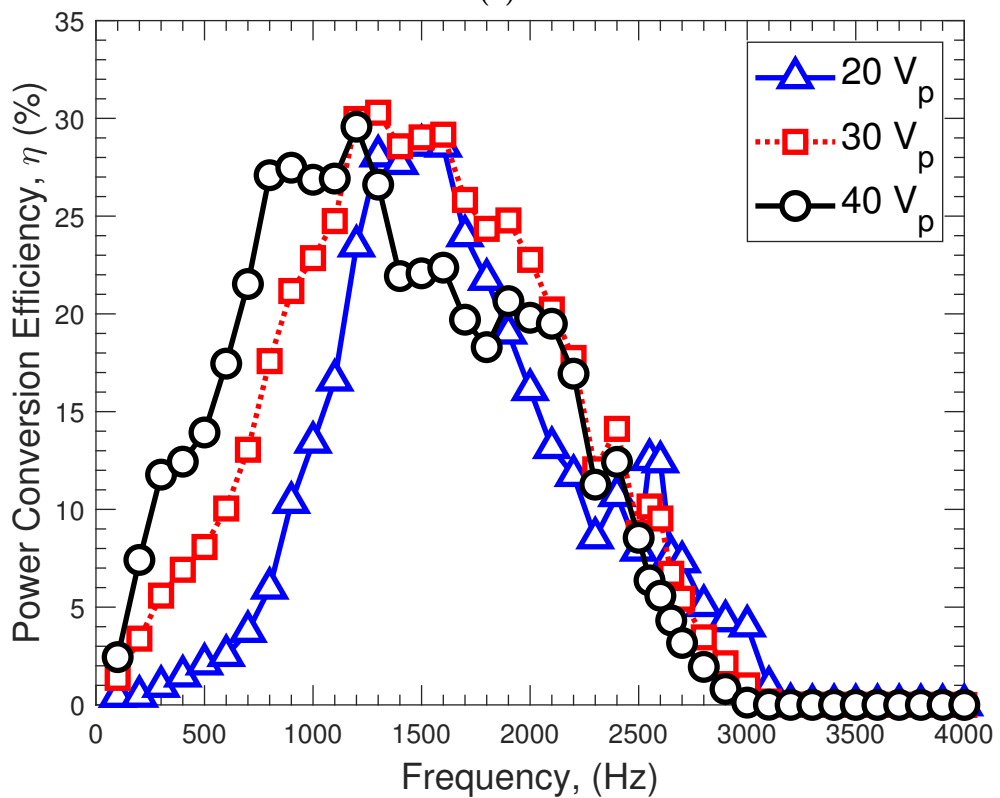
Table 7.10 compares the peak power conversion efficiency values and their corresponding jet velocity. In the table, peak conversion efficiency and peak jet velocity is presented regardless the supply voltage. The peak efficiency for the unimorph and bimorph piezoelectric actuators are presented with their corresponding jet velocity and vice versa.

Table 7.10: Comparison of peak power conversion efficiency values

Power Efficiency	Unimorph		Bimorph	
	η (%)	U_p (ms ⁻¹)	η (%)	U_p (ms ⁻¹)
Peak Efficiency	28.2	38.1	30.3	57.6
Peak Jet Velocity	18.2	67.2	6.4	92.1



(a)



(b)

Figure 7.13: *Opposite Configuration SJA - Power Conversion Efficiency of (a) Unimorph Driven SJA (b) Bimorph Driven SJA*

7.3.7 Adjacent Orifice-Diaphragm Configuration

In this section, the piezoelectric actuators used in the previous section is tested with adjacent orifice-diaphragm configuration SJA. Table 7.11 presents the size of the cavity-orifice arrangement and operational parameters of the experiments. The presentation of the results follows Section 7.3.2. The diaphragm displacement measurements are similar to the opposite synthetic jet actuator, therefore not presented in this section.

Table 7.11: Dimensions of cavity-orifice arrangement and operational parameters

Parameter	Unimorph	Bimorph
d_o (mm)	1.0	1.0
D_c (mm)	25	25
h (mm)	2.5	2.5
H (mm)	1.2	1.2
f (Hz)	100-4000	100-4000
V_p (V)	20-30-40	20-30-40

7.3.8 Jet Velocity

Figure 7.14a presents the jet velocity measurements outside the orifice exit. The peak jet velocity corresponding to the mechanical diaphragm resonance is 37.0 ms^{-1} , 51.1 ms^{-1} , and 62.7 ms^{-1} for supply voltage of $20 V_p$, $30 V_p$ and $40 V_p$, respectively. A bimodal frequency response is identified due to the presence of cavity-acoustic and diaphragm mechanical resonance .

Figure 7.14b presents the jet velocity measurements outside the orifice exit. The peak jet velocity corresponding to the mechanical diaphragm resonance is 54.5 ms^{-1} , 70.7 ms^{-1} , and 80.5 ms^{-1} for supply voltage of $20 V_p$, $30 V_p$ and $40 V_p$, respectively. The jet velocity response has a wide broadband for all supply voltages. The peak jet velocity is reduced around 10% for all supply voltages compared with the opposite orifice-diaphragm configuration's jet velocity presented in Section 7.3.2.

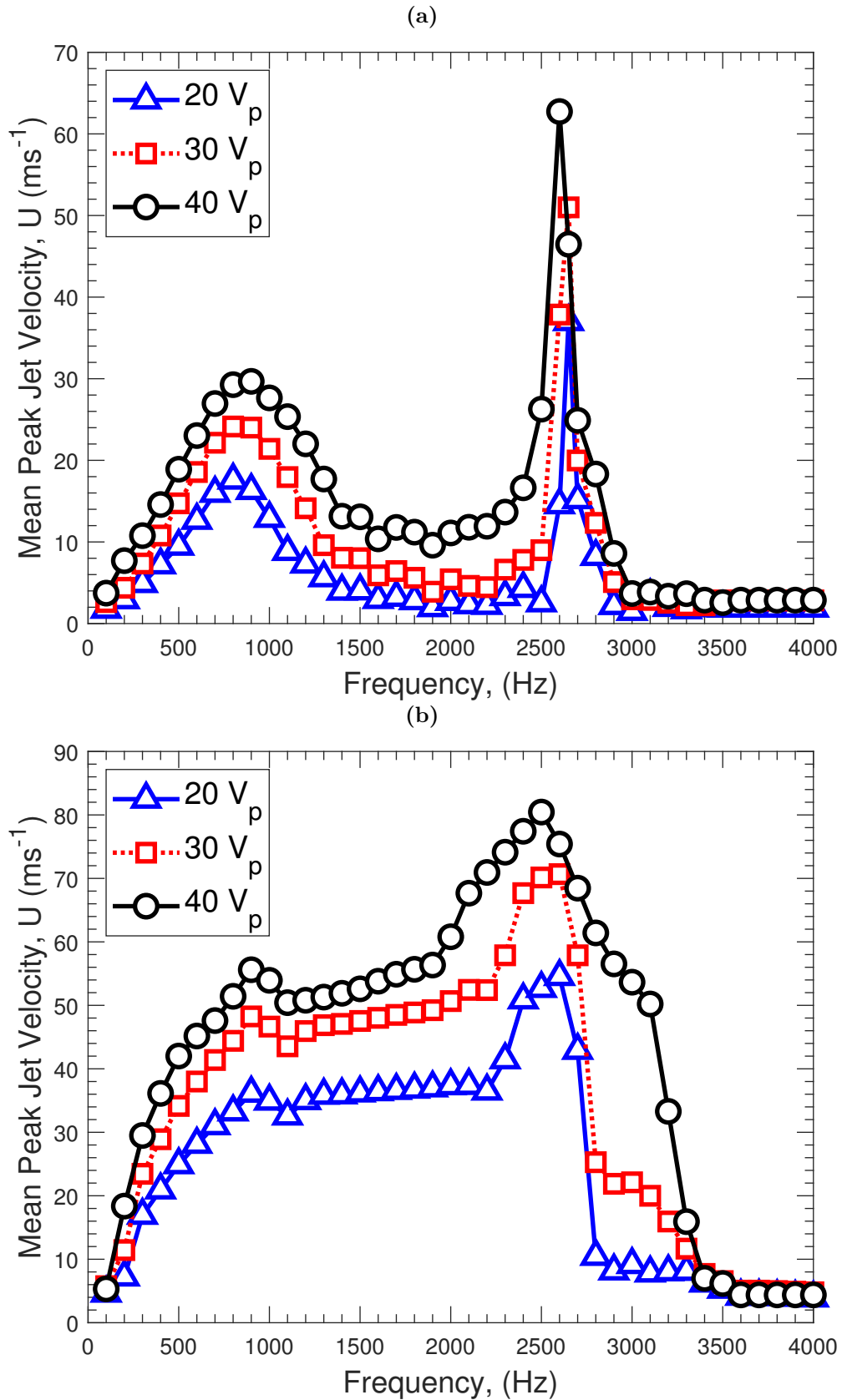


Figure 7.14: Adjacent Configuration SJA - Mean Peak Exit Jet Velocity (a) Unimorph diaphragm driven SJA (b) Bimorph diaphragm driven SJA

7.3.9 Current Drawn

Figure 7.15a presents the current draw by the unimorph diaphragm actuator. At the mechanical resonance frequency, the peak current consumption of the unimorph diaphragm is 7.7 mA, 11.3 mA, 15.0 mA for supply voltages of $20 V_p$, $30 V_p$ and $40 V_p$, respectively.

Figure 7.15b presents the current drawn by the bimorph diaphragm actuator. It is identified that the bimorph diaphragm consumes approximately twice as much of the current drawn by the unimorph diaphragm. At the mechanical resonance frequency, the bimorph diaphragm have a peak current consumption of 56.8 mA, 86 mA and 115.2 mA for supply voltages of $20 V_p$, $30 V_p$ and $40 V_p$, respectively. The peak current consumption coincides with the resonant frequency for both diaphragms. The peak current drawn by the bimorph diaphragm is approximately 7.5 times more than the unimorph diaphragm around the mechanical resonance frequency. The peak current is approximately $3 \times V_p$ for all supply voltages. Beyond the resonance frequency region, the current consumption increases significantly.

7.3.10 Electric-to-Fluidic Power Conversion Efficiency

Figure 7.16a presents the power conversion efficiency of the unimorph diaphragm. The peak conversion efficiency of the mechanical resonance frequency is 13.8%, 9% and 17.9% for peak supply voltages of $20 V_p$, $30 V_p$ and $40 V_p$, respectively. The conversion efficiency at the cavity acoustic resonance is 23.6%, 26.7% and 26.8% for peak supply voltages of $20 V_p$, $30 V_p$ and $40 V_p$, respectively.

Figure 7.16b presents the power conversion efficiency of the bimorph diaphragm. The peak conversion efficiency of at the mechanical resonance frequency is 6.5%, 6.5% and 5.1% for peak supply voltages of $20 V_p$, $30 V_p$ and $40 V_p$, respectively. The conversion efficiency at the cavity acoustic resonance is 21.4%, 20.9% and 17.3% for peak supply voltages of $20 V_p$, $30 V_p$ and $40 V_p$, re-

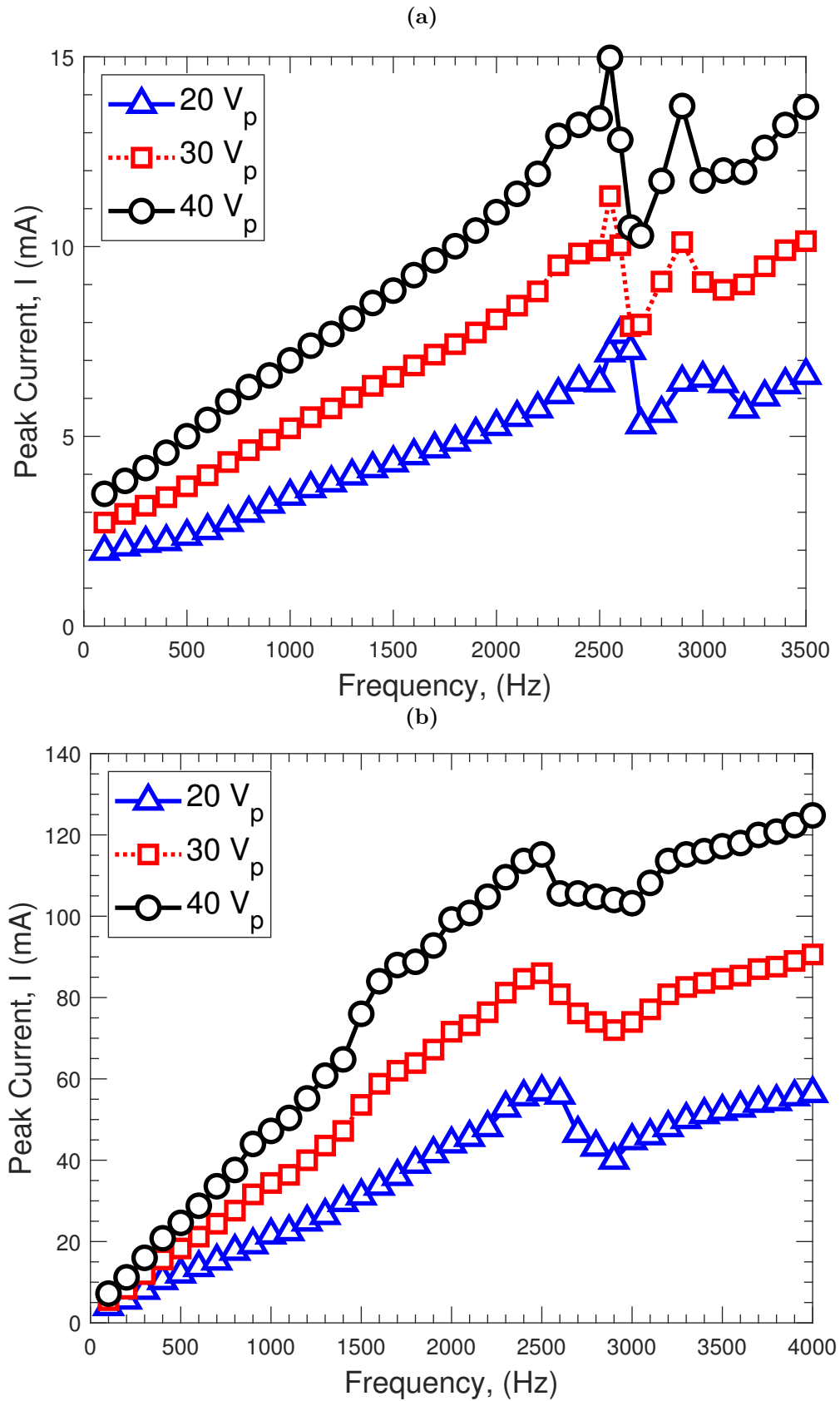


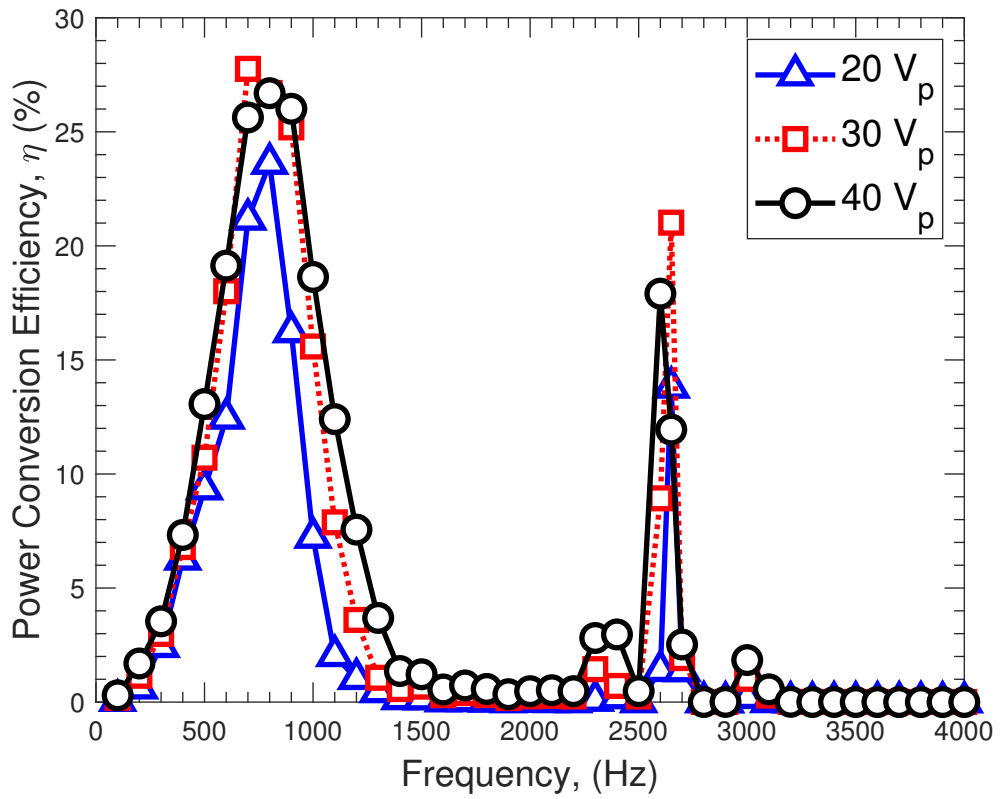
Figure 7.15: Adjacent Configuration SJA - Mean Peak Current Draw by (a) Unimorph diaphragm driven SJA (b) Bimorph diaphragm driven SJA

spectively. The results are aligned with the presented outcomes of the Section 7.3.6. The efficiency of the bimorph diaphragm is inversely proportional with the increasing voltage as the current consumption increases drastically compared with the jet velocity as explained in Section 7.3.9.

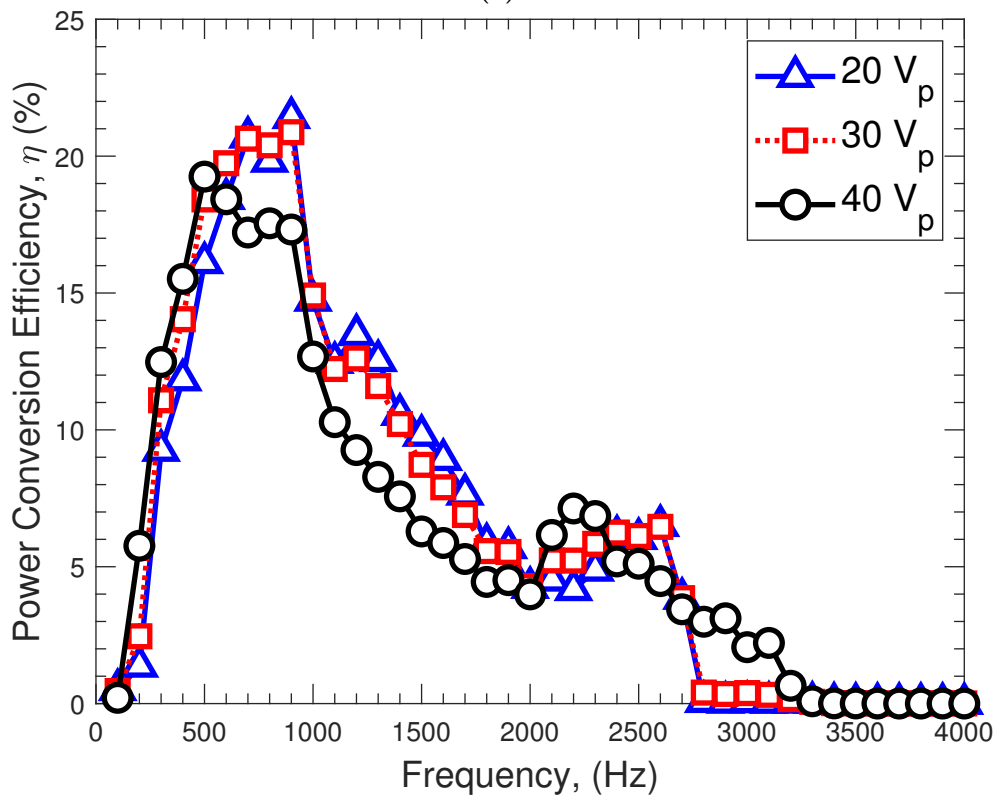
Table 7.12 presents the peak power conversion efficiency and their corresponding jet velocity for both diaphragm types. In the table, peak conversion efficiency and peak jet velocity is presented regardless the supply voltage. The peak efficiency for the unimorph and bimorph piezoelectric actuators are presented with their corresponding jet velocity and vice versa.

Table 7.12: Comparison of peak power conversion efficiency values

Power Efficiency, η (%)	Unimorph		Bimorph	
	η (%)	U_p (ms ⁻¹)	η (%)	U_p (ms ⁻¹)
Peak Efficiency	27.8	22.2	21.4	36.1
Peak Jet Velocity	17.9	62.7	5.1	80.5



(a)



(b)

Figure 7.16: Adjacent Configuration SJA - Power Conversion Efficiency (a) Unimorph diaphragm driven SJA (b) Bimorph diaphragm driven SJA

7.4 Single Modal Frequency Response SJA

Bringing the cavity acoustic and diaphragm mechanical resonances together to obtain a single modal jet velocity frequency response is a commonly mentioned [66, 90] topic but not thoroughly studied. Gallas et al. achieved a single modal frequency response SJA and showed the clear increase in jet velocity for an opposite orifice-diaphragm SJA configuration. Nevertheless, the efficiency of the SJA is not reported [20]. The single dominant peak is achieved by the heavy non-linear fluidic damping acting on the cavity acoustic resonance [90].

It is expected that for a single modal frequency response SJA, the output jet velocity as well as the power conversion efficiency would be relatively higher compared to the bimodal response SJA. A validation case is studied using the structural-fluidic-acoustic analytical model and compared with in-house experimental data, in Chapter 6.3.4. It was found there that the jet velocity was relatively high; exceeding 50 ms^{-1} at a supply voltage of $20 V_p$.

The present section utilises an opposite orifice-diaphragm configuration SJA. The exit jet velocity and power conversion efficiency of the single modal frequency response SJA is studied which employs a PZT-5A piezoceramic diaphragm. The results which are shown with "PZT-5A" legend in the figures are experimentally obtained. In addition, the diaphragm-based analytical model (developed in Chapter 6.2.3) is used to model an identical size PMN-PT piezoceramic diaphragm with the same cavity-orifice arrangement. The current consumption is assumed to behave in a similar trend with the PMN-PT diaphragm used in Section 7.2. Thus, the current draw is taken as the two times of the experimental PZT-5A driven SJA. The results which are shown with "PMN-PT" legend in the figures are obtained by the model and are hypothetical.

Table 7.13 presents the size of the piezoelectric actuator, electromechanical properties and the size of cavity-orifice arrangement.

Table 7.13: Piezoelectric diaphragm and cavity-orifice dimensions

Parameter	PZT-5A	PMN-PT
D_{brass} (mm)	35	35
D_{pzt} (mm)	25	25
t_{brass} (mm)	0.20	0.20
t_{pzt} (mm)	0.10	0.10
d_{31} (pm/V)	-180	-560
k_p (-)	0.4	0.9
d_o (mm)	0.84	0.84
D_c (mm)	33	33
h (mm)	0.84	0.84
H (mm)	4.65	4.65

7.4.1 Jet Velocity

Figure 7.17a presents the experimental jet velocity result of the PZT-5A diaphragm driven SJA and model computation by using PMN-PT diaphragm at supply voltage of $20 V_p$. The peak jet velocity of the PZT-5A diaphragm driven SJA is 53.5 ms^{-1} and 99 ms^{-1} for PMN-PT diaphragm driven SJA.

Figure 7.17b presents the experimental jet velocity result using the PZT-5A diaphragm driven SJA and model computation by using PMN-PT diaphragm at supply voltage of $40 V_p$. The peak jet velocity of the PZT-5A diaphragm driven SJA is 76.5 ms^{-1} and 143 ms^{-1} for PMN-PT diaphragm driven SJA.

It is observed that doubling the voltage resulted in an increase of jet velocity of 43% for PZT-5A and 30.8% for PMN-PT. This is due to the pressure losses scaled with the jet velocity and increase in jet velocity cause enhanced losses.

7.4.2 Current Consumption and Power Efficiency

Figure 7.18a presents the current drawn by the experimental PZT-5A diaphragm actuator and hypothetical PMN-PT diaphragm for supply voltage of $20 V_p$. The PMN-PT diaphragm is assumed to consume twice as much current of the PZT-5A based on the findings in Section 7.2. The peak current consumption by the PZT-5A diaphragm driven SJA is measured at the resonance frequency as 12.2 mA. Therefore, the peak current consumed by the

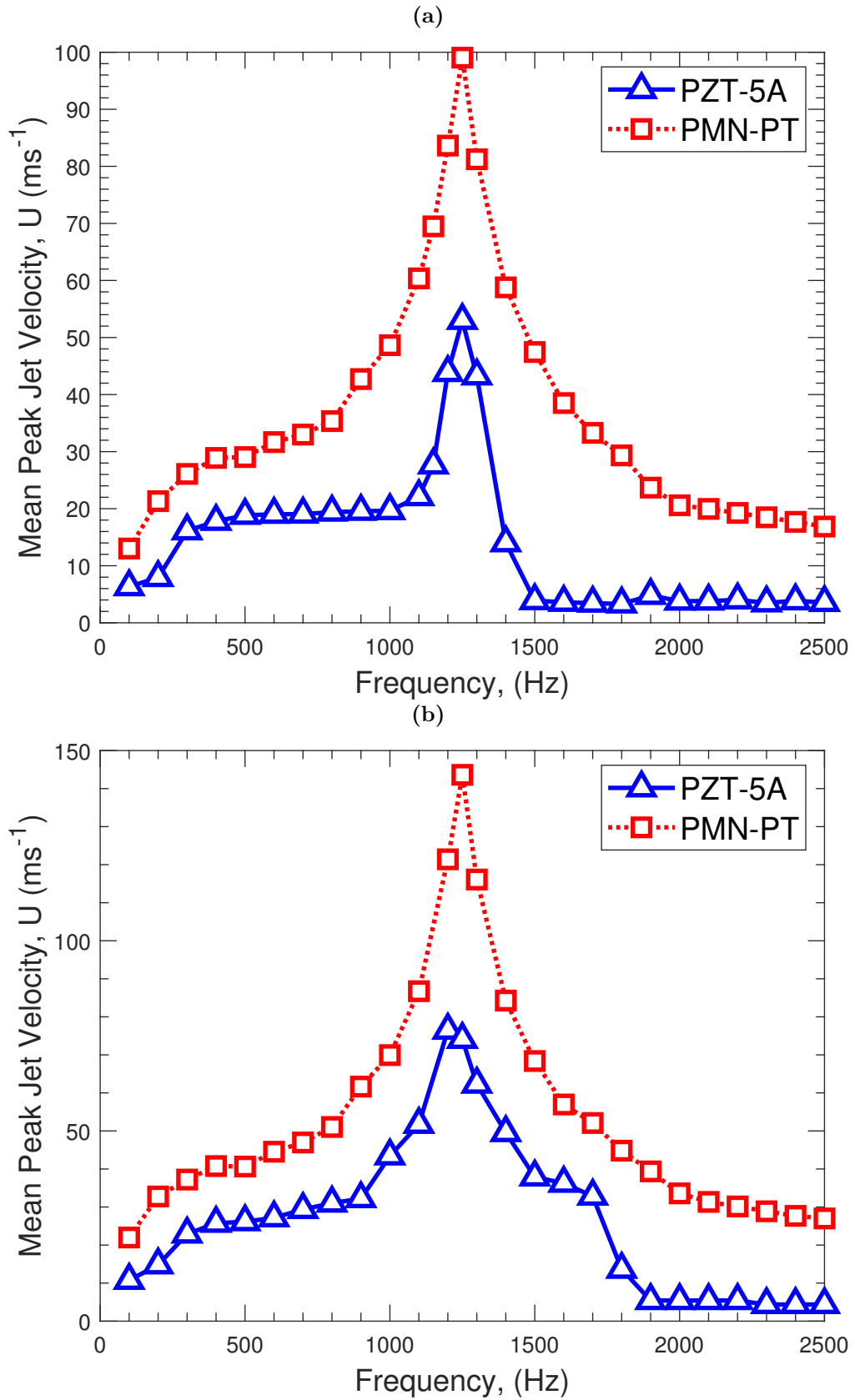


Figure 7.17: Mean Peak Exit Jet Velocity of the Single Modal SJA (a) PZT-5A and PMN-PT Driven SJA - 20 V_p (b) PZT-5A and PMN-PT Driven SJA - 40 V_p

PMN-PT diaphragm driven SJA is 24.4 mA at the resonance frequency.

Figure 7.18b presents the current drawn by the experimental PZT-5A diaphragm actuator and hypothetical PMN-PT diaphragm for supply voltage of $40 V_p$. The peak current consumption by the PZT-5A diaphragm driven SJA is measured at the resonance frequency as 25.9 mA. Therefore, the peak current consumed by the PMN-PT diaphragm driven SJA is 51.8 mA at the resonance frequency.

Figure 7.19a presents the power conversion efficiency comparison of the experimental PZT-5A driven SJA and hypothetical PMN-PT driven SJA at $20 V_p$ of supply voltage. PZT-5A driven SJA exhibits a peak efficiency of 36.2% at 1300 Hz at a jet velocity of 43.3 ms^{-1} . At the resonance frequency the power conversion efficiency is 30.2%, corresponding to a jet velocity of 53 ms^{-1} . For the hypothetical case of PMN-PT driven SJA, the peak efficiency is 59% corresponding to a jet velocity of 83.6 ms^{-1} .

Figure 7.19b presents the power conversion efficiency comparison of the experimental PZT-5A driven SJA and hypothetical PMN-PT driven SJA at $40 V_p$ of supply voltage. PZT-5A driven SJA exhibits a peak efficiency of 46.3% at 1300 Hz corresponding to a jet velocity of 62.3 ms^{-1} . At the resonance frequency the power conversion efficiency is 10%, corresponding to a jet velocity of 76.5 ms^{-1} . For the hypothetical case of PMN-PT driven SJA, the peak efficiency is 78.5% corresponding to a jet velocity of 116 ms^{-1} .

Table 7.14 presents the peak power conversion efficiency and their corresponding jet velocity for both diaphragm types, noting that the PZT-5A results are experimentally obtained and PMN-PT results are hypothetical by assuming PMN-PT diaphragm consumes two times more current than PZT-5A diaphragm and jet velocity is estimated by the structural-fluidic-acoustic model. It can be deduced that the single modal frequency response actuator contribute towards achieving higher power conversion efficiency. The PZT-5A diaphragm used in the experiments is 0.1 mm thicker than the one used in Gallas's configuration [20]. Using a thicker disc has an effect of increasing

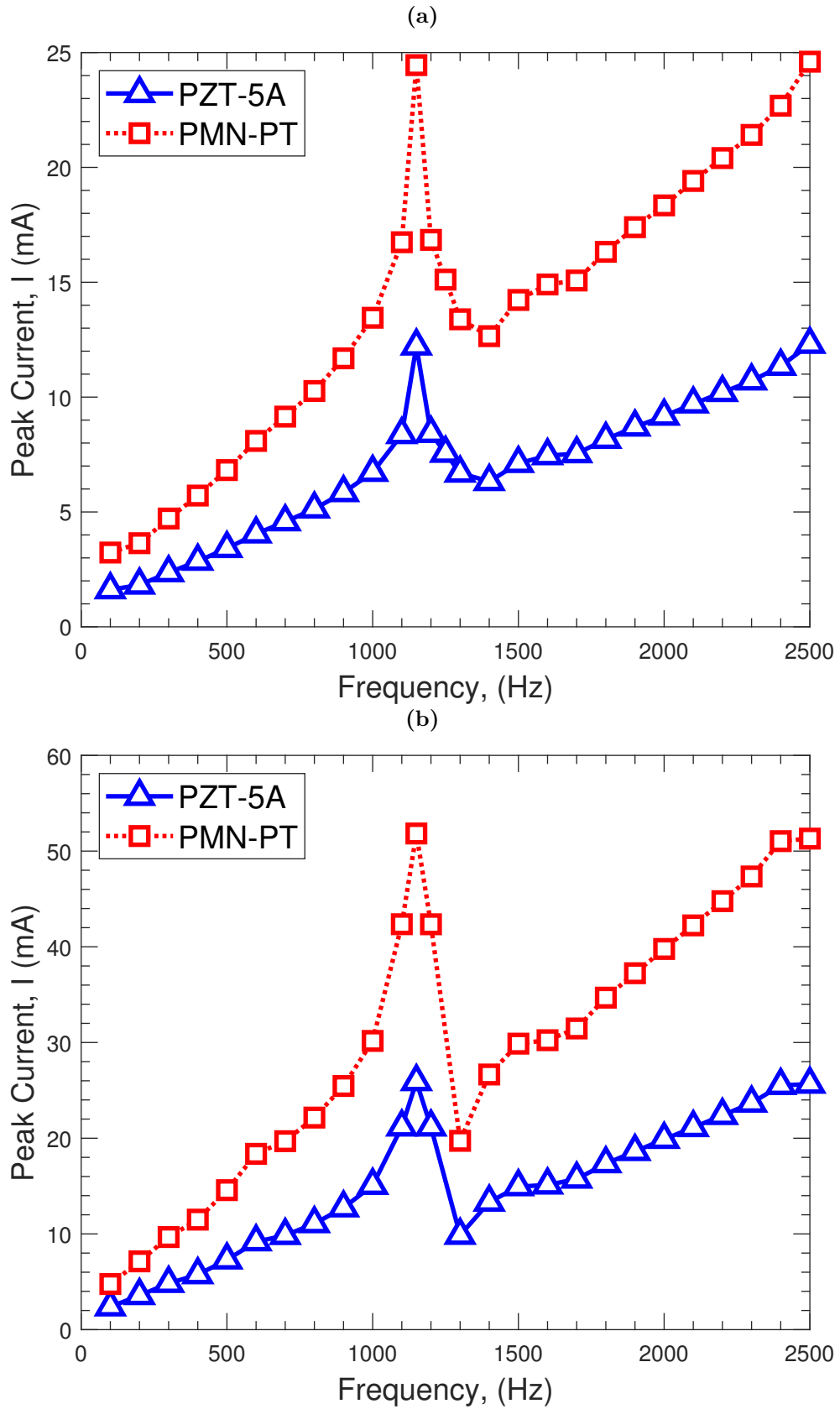


Figure 7.18: Mean Peak Current Draw of the Single Modal SJA (a) PZT-5A and PMN-PT Driven SJA - 20 V_p (b) PZT-5A and PMN-PT Driven SJA - 40 V_p

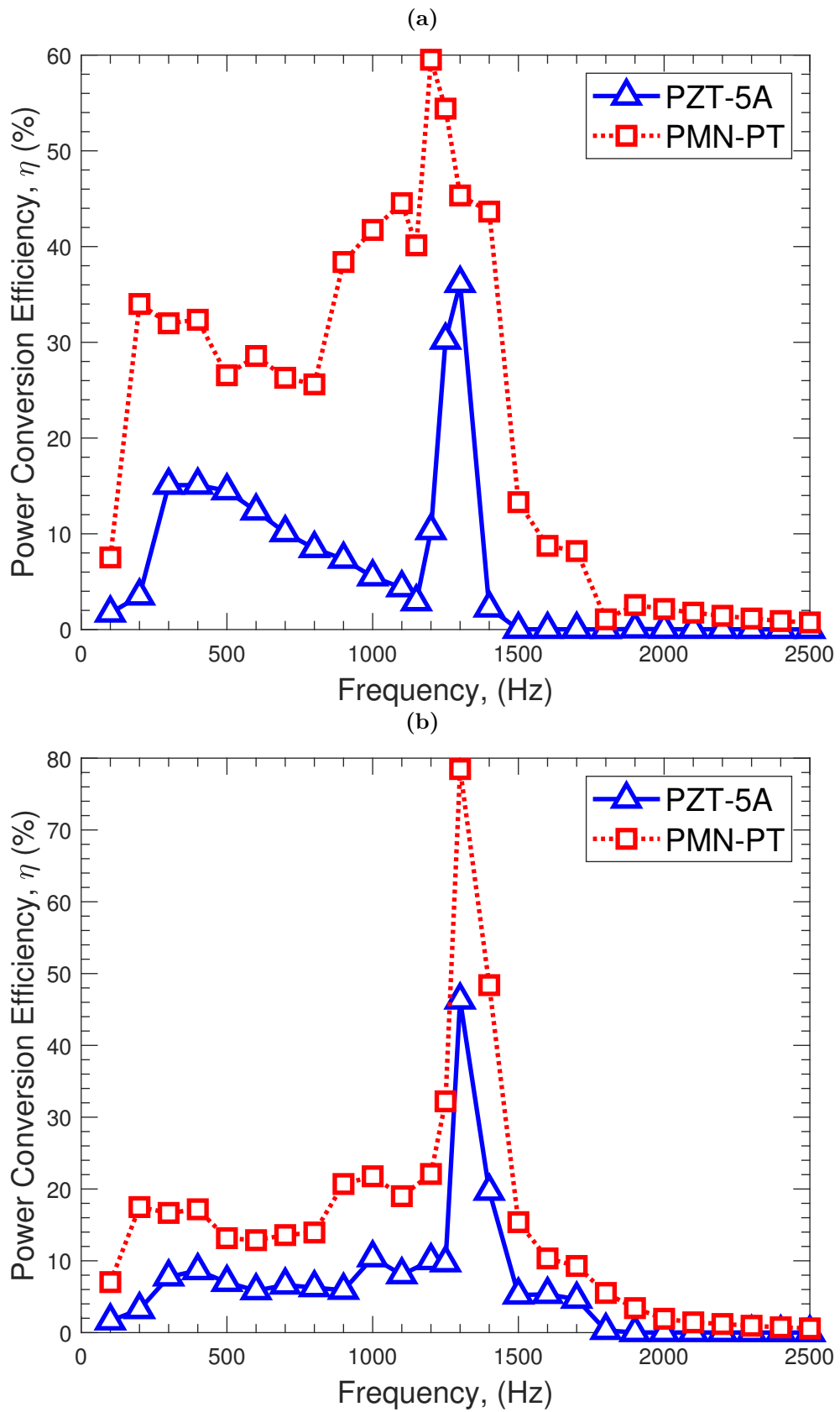


Figure 7.19: Power Conversion Efficiency of (a) Single Modal Response SJA - 20 V_p (b) Single Modal Response SJA - 40 V_p

Table 7.14: Comparison of peak power conversion efficiency values

Power Efficiency, η (%)	PZT-5A		PMN-PT	
	η (%)	U_p (ms ⁻¹)	η (%)	U_p (ms ⁻¹)
Peak Efficiency	46.3	62.3	78.5	116
Peak Jet Velocity	10	76.5	32.2	143.6

mechanical resonance frequency and reducing the jet velocity due to smaller displacement. Also, the current consumption is proportional to the actuation frequency. Thus, using a thinner piezoelectric diaphragm of similar composition would increase the power conversion efficiency further. Nevertheless, it is demonstrated (via both experiment and model) that the single modal frequency response SJA promotes an enhanced power conversion efficiency.

7.5 Discussion

7.5.1 Implications of the research

The rationale which drives the first study of this chapter is originated by the numerical study of Rusovici on SJA which is driven by polycrystalline and single crystal piezoelectric actuators [100]. The results imply that the single crystal (i.e., PMN-PT) piezoceramic driven SJA, due to the enhanced electromechanical coupling term (k_p), provides a significant enhancement for the electric-to-fluidic power conversion efficiency at low subsonic exit jet velocity range. Nevertheless, the study was not backed-up by an experimental investigation which motivated the work done in this chapter using single crystal piezoelectric actuators.

It is identified that the peak centre diaphragm transverse deflection of the single crystal piezoelectric diaphragm is three times larger than the polycrystalline diaphragm, for the same diaphragm supply voltage. Also, the current consumption of the single crystal is twice as much as the polycrystalline diaphragm. Therefore, the efficiency levels attained cannot be sus-

tained throughout the voltage sweep due to the lower increase of the fluidic power against the power consumed by the actuator. To distinguish the performance of the piezoceramic types better, the mechanical and fluidic power should be separated. Within the experimental campaign, it is identified that the mechanical power which is a function of the peak diaphragm displacement (i.e., volume swept) consistently increases with the increasing supply voltage. Also, the fluidic power (i.e., jet velocity) depends on the design of the actuator. Nevertheless, the fluidic power does not proportionally increase with the increasing supply voltage due to additional compressibility effects and pressure/fluidic loss.

When the voltage sweep of the "only disc" centre peak disc displacement presented in Chapter 5.5.1 is considered, it can be seen that the displacement of the diaphragm is within the limits of the linear stiffness region. Thus, for the voltage range investigated in the present chapter, effects of piezoceramic saturation/dissipation is likely to be negligible. Nevertheless, when the peak displacement results belonging to the SJA cases presented in Chapters 7.2.3-7.3.3 are investigated, it is identified that the linear stiffness is no longer valid. An interpretation for this pattern is the viscous damping acting on the diaphragm which increases with the voltage in addition to the material damping.

The experimental campaign using the single crystal-driven SJA have proven that a peak jet velocity of approximately 100 ms^{-1} and efficiency of 40% can be achieved, which stands out as a significant improvement in the field, compared to the cases listed in Table 7.2. Herein, the most significant limitation of the single crystal piezoceramic element employed is the electric field ($E_c = 2 \text{ kV/cm}$) which allows a maximum voltage supply of 45 V, limiting the study to 40 V of peak supply voltage to ensure that the diaphragm would not undergo plastic deformation/crack. By the procurement of a more advanced/robust single crystal piezoceramic, such as PIN-PMN-PT with an electric field of 5.0 kV/cm, peak supply voltage of 100 V would be possible to test. This would

further increase the exit jet velocity.

It is also demonstrated that changing the SJA configuration from opposite to adjacent orifice-diaphragm reduces the peak jet velocity by around 10%, due to two potential causes. Firstly, the cavity height used in the adjacent orifice-diaphragm configuration is around two times higher than the cavity height used in the opposite configuration SJA. Also, due to the bending of the flow during the ejection cycle, the pressure losses are increased in the adjacent configuration. This result is particularly important for a potential application as the spacing between adjacent orifices can be reduced without a significant jet velocity reduction. Maintaining short spacing between two adjacent orifices is important to grant effective flow control.

Bimorph polycrystalline diaphragm also provides a larger peak displacement with a significant current consumption compared to the single crystal and unimorph polycrystalline diaphragm. Therefore, they should be utilised in application cases where the power consumption is not a constraint.

Table 7.15 provides a comparison between the previously published work and the present study. The SJA power conversion efficiency definition is consistent with Gomes and Crowther's definition [27, 66] as the jet velocity measurement technique is the same as in the present study, both using 1-D hot-wire probe. In addition, the electric power computation technique is consistent with most of the present studies. It is also identified that, the electric power calculation techniques used by Jabbal [86] and Feero [68] yield equivalent results compared with the integration of current and voltage signals, multiplied by the period of oscillation. It is demonstrated that the power conversion efficiency improved significantly from 7% identified by Gomes[66] to 72% in the present study for halved jet velocity. A jet velocity of 70 ms^{-1} is attained by Crowther and present study with 14% and 43% power conversion efficiency, respectively. In the present study, the power conversion efficiency enhancement is provided by the utilisation of single crystal piezoelectric diaphragm.

Uchino suggests that the power conversion inefficiency of the piezoelectric ma-

Table 7.15: Comparison of the selected experimental research with present work

Study	Year	d_o (mm)	D_c (mm)	V_p (V)	U_p (ms^{-1})	η (%)
[66]	2006	1.2	25	125	130	7
[27]	2006	1.2	25	45	70	14
[87]	2011	1x4	30	80	35	25
[86]	2014	1	27	50	38	15
[68]	2015	2	30.8	100	15	45
[88]	2015	5	80	35	25	65
[81]	2016	1x12	80	150	120	3.5
[81]	2016	1x12	80	150	211	N/A
[89]	2020	10	52.5	N/A	12	9
[9]	2020	2.5	35	100	100	3
Present study	2021	1.2	25	40	63.2	72.2
Present study	2021	1.2	25	40	99.5	23
Present study	2021	1.2	25	20	71	43

terial is related to the stored mechanical energy of the piezoceramic material which acts like a spring [135]. For the enhancement of fluidic power, one also needs to consider the acoustic impedance matching of the piezo-actuator to the fluid. If a good match is realized, more than 90% of the mechanical energy can be transmitted from the transducer to the fluid. However, if the matching is not perfect, only 10 – 20% mechanical energy is transmitted to the fluid, and the remaining bounces back to the piezo-actuator [155]. The acoustic impedance between the air and the piezoelectric material or the substrate material is $\approx O(100,000)$. In case of injecting a thin layer of coating with a smaller impedance difference (i.e., PVDF, teflon), the electric-to-fluidic power conversion efficiency is thought to show a significant increase.

Within this study, limitations are present for the actuator design achievement towards a full-scale application. The scope of the study is limited to the single-diaphragm single-orifice design. Also, for a potential application, an adjacent orifice-diaphragm with double piezoelectric diaphragm would be employed for increased jet velocity such as in the study of Van Buren et al. [81]. Such a configuration with multiple diaphragm and orifice (such as two diaphragms to actuate through three orifices) is not studied. On the other hand, SJA produces

significant noise while operating which may create passenger discomfort during flight. The noise aspects are not considered within this study but a detailed investigation on the noise reductions by using lobed-orifices are presented in previous work [150].

7.5.2 Implications for industry

SJA can be used for various aerodynamic flow control (AFC) settings including i) horizontal wing flow separation control for fuel savings, ii) nacelle-pylon junction flow instability, which causes lift reduction [9] iii) aeroplane vertical tail which is oversized to ensure that in case of asymmetric thrust (i.e., engine failure or strong crosswind conditions) sufficient side force can be produced to balance the asymmetry [8]. In case of a successful AFC implementation, the rudder size could be reduced, which would enable smaller thus lighter weight vertical tail and reduced drag. Rathay et al. studied slot orifice SJA in small-scale vertical stabilizer models and obtained 20% side force increase at moderate rudder deflection angles [156, 157]. It is also reported that the efficiency of the SJA decreases with the increasing rudder deflection or sideslip angle due to the low momentum transfer of the actuator and therefore sweeping jets are nominated for the full-scale flight tests [8]. Nevertheless, the performance of the SJA array, such as the peak jet velocity output or the electric-to-fluidic power conversion efficiency is not reported. However, the peak jet velocity is calculated as 8.2 ms^{-1} with the given parameters and a momentum coefficient of 0.248%. Therefore, there is still a requirement for further justification of the performance metrics of the SJA.

Mooney et al. conducted an AFC study for horizontal tail and established the requirements of the two candidate flow control mechanisms; sweeping jet and synthetic jet [31]. They have evaluated the ratio of average jet velocity of the synthetic jet and free stream by using a non-dimensional momentum coefficient, which reads as:

$$C_\mu = \frac{2\rho_j n A_o U_j^2}{\rho_\infty U_\infty^2 S_v} \quad (7.4)$$

Mooney et al. estimates that an acceptable value of C_μ would be 0.5% for the jet velocity of the actuator for such a flow control application [31]. They assumed a free-stream low-speed condition of 130 knots (i.e., $U_\infty = 67 \text{ ms}^{-1}$) and a tail wing size of 470 ft^2 (i.e., $S_v = 43.7 \text{ m}^2$). The required number of actuators (n) is given as 200. On the other hand, the electrical power (P_e) required for the AFC should be limited to 450 kW due to the capability of auxiliary power units [31]. The air density terms can be neglected, and the jet velocity term (U_j) is linked to the peak jet velocity by $U_j = \frac{2U_{j,peak}\pi}{3}$ [31]. Thus, it could be suggested that the enhanced exit jet velocity of the actuator is equally important to achieve low power consumption (i.e., high power conversion efficiency). Therefore, one could define a ratio of the required fluid momentum coefficient and electric power consumption.

Three studies including the present study, Van Buren et. al [81] (i.e., highest exit peak jet velocity) and Feero et al. [68] (i.e., highest electric-to-fluidic power conversion efficiency reported) are compared for their momentum coefficient and power consumption. Figure 7.20 presents the aforementioned comparisons of momentum coefficient (Figure 7.20a) and power supply limits (Figure 7.20b). It is identified that the momentum coefficient, C_μ , is improved compared to the Feero's study but cannot attain level of Van Buren's study. This is mainly due to the lower orifice/slot area in the studies and not the peak exit jet velocity. On the other hand, it is identified that due to the power limitation of the auxiliary power unit, Van Buren's configuration can support up to 46 actuators where Feero's configuration can support 250+ actuators. The PMN-PT driven SJA of the present study can support up to 200 actuators. Even though the momentum coefficient obtained is not the current state-of-the-art, it is identified that the power consumption requirements together for the sufficient number of actuators are provided by the present study. This suggests that

further improvements are required especially for larger diameter (or slot area) orifice SJA to increase C_μ . It is anticipated that the enhancement of C_μ is possible by employing PIN-PMN-PT piezoceramic, which can support higher supply voltage (around 100 V for the size studied in Section 7.2).

The required momentum coefficient and the power supply limit can be divided to establish a new and integrated figure-of-merit of the SJA for a full-scale flight implementation. Figure 7.21 presents a ratio of calculation of C_μ divided by (P_e) for 200 actuators to satisfy the power supply requirement for 60 minutes of continuous operation. Three studies: Van Buren et. al [81] which is the highest peak exit jet velocity reported, Feero et al. [68] as it stands out as the highest power conversion efficiency reported and present study are compared. The present study is represented by the performance of PMN-PT driven SJA at highest jet velocity with 40 V_p supply voltage, presented in Section 7.2.2. By the calculation presented in Figure 7.21, it is identified that the momentum coefficient per the power consumed of the current study is evidently the most state-of-the-art value reported to-date. The momentum coefficient per the power consumed is improved by 130% compared to Van Buren et al. [81].

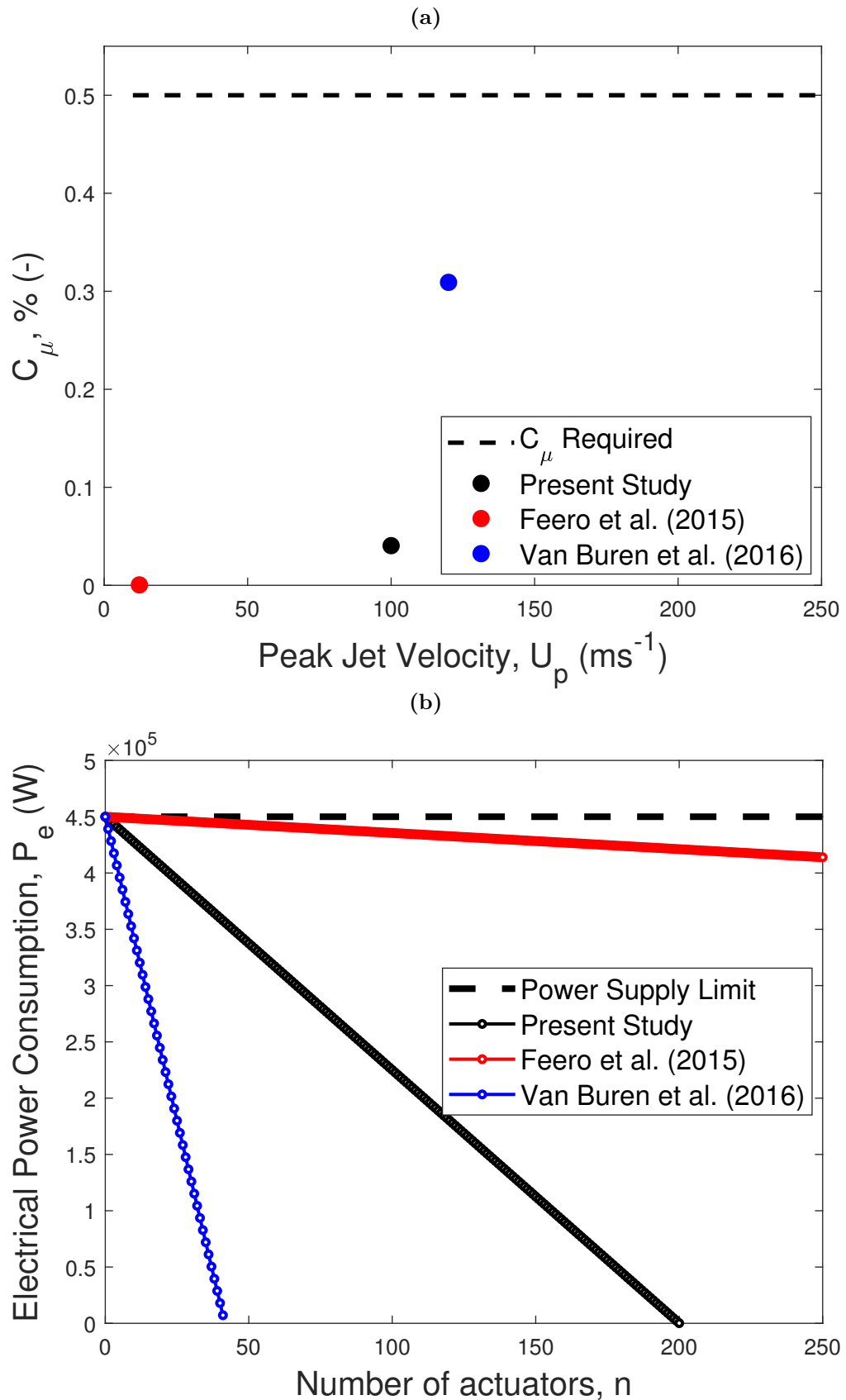


Figure 7.20: C_μ and power consumption requirement calculations for the conditions provided by Mooney et al. [31] (a) Peak jet velocity (U_p) versus the momentum coefficient C_μ (b) Number of actuators versus the power consumption

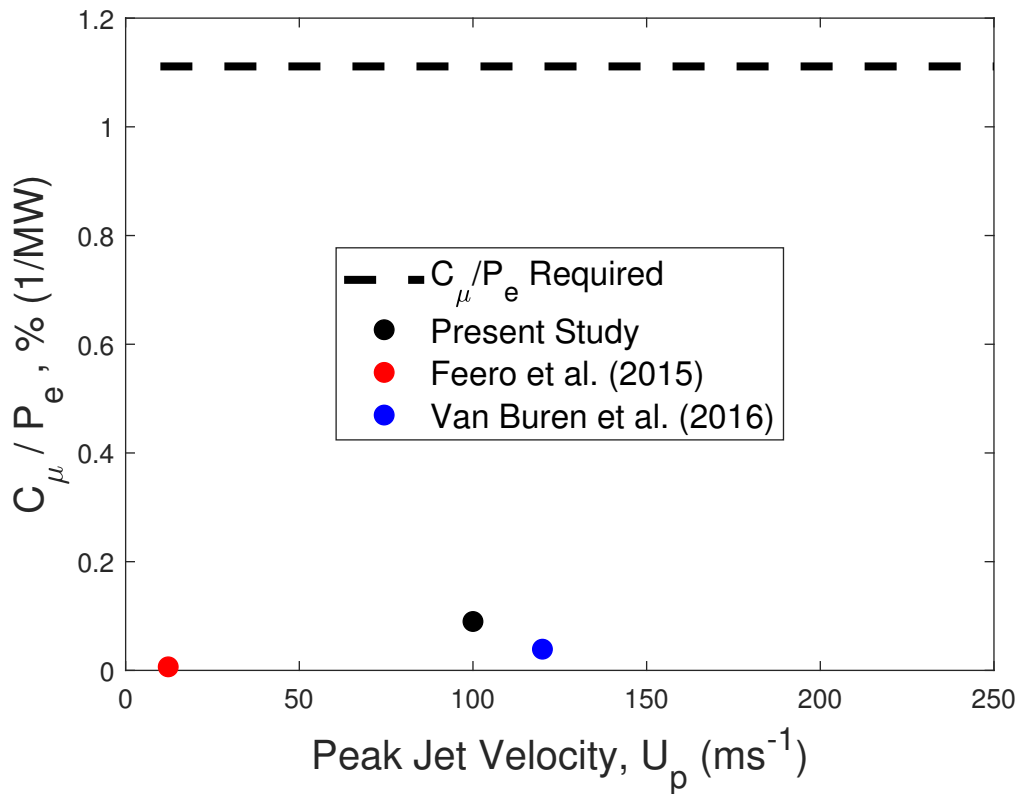


Figure 7.21: C_μ/P_e calculations for the conditions provided by Mooney et al. [31]

7.6 Summary

This chapter consists of three different studies. In the first study, the same dimensions of polycrystalline (PZT-5A) and single crystal (PMN-PT) piezoceramic elements with brass substratum are employed on common cavity-orifice dimensions. The experimental campaign involved both opposite and adjacent orifice-diaphragm configuration SJA, which may have different benefits depending on the geometry of application. The key outcomes of the experimental investigation are as follows:

- The peak centre diaphragm displacement of the PMN-PT diaphragm driven SJA is three times larger than the identical size PZT-5A diaphragm across all supply voltages (i.e., 20-30-40 V_p).
- Jet velocity exhibits a twofold increase (37 ms^{-1} to 71 ms^{-1}) when a single crystal diaphragm is employed at 20 V_p of supply voltage. With the supply voltage of 40 V_p , jet velocity of 99.5 ms^{-1} is achieved by the

PMN-PT diaphragm SJA, compared to the 65 ms^{-1} produced by the PZT-5A diaphragm SJA.

- Current consumption peaks around the mechanical resonance frequency for both diaphragm types, and increases proportionally with the voltage. The peak current consumption of the PMN-PT SJA is twice as much as that of the PZT-5A diaphragm SJA.
- Electric-to-fluidic power conversion efficiency tends to be larger at around cavity acoustic resonance frequency compared to the mechanical resonance for both diaphragms. A peak power conversion efficiency of 72.2% is achieved with the PMN-PT diaphragm, corresponding to a jet velocity of 63.2 ms^{-1} . With the PMN-PT diaphragm, a power conversion efficiency of 23% is achieved corresponding to a jet velocity of 99.5 ms^{-1} , which is a twofold increase of the power conversion efficiency compared to the PZT-5A diaphragm. The power conversion efficiency is inversely proportional to the voltage supply, as the fluidic power does not compromise the increase in electric power (i.e., both current consumption and voltage supplied increases). The time-dependent behaviour of the voltage and current signals revealed that the capacitive nature of the diaphragm tends to be reactive at the mechanical resonance frequency; power factor ($\cos(\phi)$) tends to 1.
- Adjacent orifice-diaphragm configuration SJA has a reduced peak jet velocity of approximately 10% for both diaphragm types across all voltages, compared with the opposite configuration SJA. The peak jet velocity with the PMN-PT diaphragm is 90 ms^{-1} at a supply voltage of 40 V_p . The current consumption has increased by around 10% compared to the opposite configuration due to the increased pressure loading on the diaphragm. A peak power conversion efficiency of 51.2% is achieved with the PMN-PT diaphragm corresponding to a jet velocity of 52.5 ms^{-1} . At the mechanical diaphragm resonance, the peak efficiency is 38% at a jet

velocity of 61.1 ms^{-1} .

The second study of this chapter compares similar dimensions of unimorph polycrystalline and bimorph polycrystalline piezoelectric diaphragms on common cavity-orifice dimensions in both opposite and adjacent orifice-diaphragm configuration SJA. The key outcomes of the experimental investigation is as follows:

- The peak centre diaphragm displacement of the bimorph diaphragm is 1.5 times larger than the unimorph diaphragm.
- Also, the jet velocity of the bimorph diaphragm shows a 1.5 times increase compared to the unimorph diaphragm.
- Current consumption peaks around the mechanical resonance frequency for both diaphragm types and increases proportionally with voltage. The current consumption of the bimorph has a fivefold increase compared to the unimorph diaphragm.
- The electric-to-fluidic conversion efficiency of the bimorph driven SJA is significantly lower than the unimorph due to the enhanced current consumption. The efficiency peaks at the cavity acoustic resonance driven actuation frequency region. The peak power conversion efficiency of the bimorph driven SJA is 30.3% corresponding to a jet velocity of 57.6 ms^{-1} . The peak efficiency of the unimorph driven SJA is 28.2% at a jet velocity of 38.1 ms^{-1} .
- Adjacent orifice-diaphragm configuration SJA has a reduced peak jet velocity of approximately 10% for both diaphragm types across all voltages. The peak jet velocity with the bimorph diaphragm is 80.5 ms^{-1} at a supply voltage of $40 V_p$ compared to the 62.7 ms^{-1} peak of the unimorph diaphragm. The current consumption has increased by around 10% compared to the opposite configuration, due to the increased pressure loading

on the diaphragm. Owing to the occurrence of the cavity acoustic resonance, the power conversion efficiency has increased at that actuation frequency region. At the cavity acoustic resonance, peak power conversion of 21.4% is achieved with the bimorph diaphragm, corresponding to a jet velocity of 36.1 ms^{-1} . At the mechanical diaphragm resonance the peak efficiency is 5.1% at a jet velocity of 80.5 ms^{-1} .

Even though the concept of single modal frequency response SJA is widely mentioned [66, 81] and stands out as a popular research topic in the field, there is not a significant data presentation except in Gallas's experiment focusing on the jet velocity [20]. The third study of the chapter investigates the single modal frequency response SJA; combining an experimental set of data for polycrystalline diaphragm and an hypothetical case of single crystal diaphragm using the structural-fluidic-analytical model for the jet velocity estimation. The key outcomes of the experimental investigation are as follows:

- Polycrystalline driven SJA experimentally achieved 53.5 ms^{-1} and 76.5 ms^{-1} with supply voltages of $20 V_p$ and $40 V_p$, respectively. The corresponding power conversion efficiency at the mechanical resonance is measured to be 30.2% and 10% at $20 V_p$ and $40 V_p$, respectively. The peak power efficiency is measured as 36.3% and 46.3% at $20 V_p$ and $40 V_p$, corresponding to jet velocities of 43.3 ms^{-1} and 62.3 ms^{-1} , respectively.
- By using the structural-fluidic-acoustic model developed in Chapter 6.2.3, a hypothetical single crystal diaphragm of the identical size of the polycrystalline diaphragm is assumed. The model is used to predict the jet velocity which resulted in 99 ms^{-1} and 143 ms^{-1} for supply voltages of $20 V_p$ and $40 V_p$, respectively.
- Assuming the current consumption is twice as much as the polycrystalline diaphragm throughout the actuation frequency envelope, the power conversion efficiency is calculated for the PMN-PT diaphragm. The peak

efficiency is 59% corresponding to a jet velocity of 83.6 ms^{-1} with a supply voltage of $20 V_p$. The peak efficiency is 78.5% at a velocity of 116 ms^{-1} and supply voltage of $40 V_p$.

Chapter 8

Conclusions

This conclusions chapter consists of three sections. First section is the review of the research objectives to demonstrate the research conducted. The second section is summary of main conclusions of the work, where the novel scientific contributions are highlighted. The third section is the recommendations for the future work.

8.1 Review of aim and objectives

Objective 1 *"To develop an accurate structural mechanics model of the uni-morph piezoelectric actuator to estimate natural frequencies of mechanical diaphragm"* is investigated in Chapter 4. Three theories for the natural frequency estimation of the piezoelectric actuator are derived and their performance of assessing the natural frequency of the piezoelectric actuator is comparatively demonstrated.

- Theory 1 - By employing transfer matrix method formulation, it is demonstrated that classical vibration theory can estimate the natural frequency of the piezoelectric actuator with an accuracy of $\pm 6\%$.
- Theory 2 - An equivalent theory by using reduced form of extensional-flexural deformation equations are developed using matrix exponentials instead of Bessel functions with a 4×4 transfer matrix. This change eases

the process and yields shorter implementation and solution time. The accuracy of the solution is the same as the prior theory. They both do not consider the coupled extensional-flexural deformations of the circular diaphragm.

- Theory 3 - With the full coupled extensional-flexural deformation equations, the transfer matrix has become a 6×6 and yielded a natural frequency estimation accuracy of the piezoelectric actuator of $\pm 1.5\%$ compared to the experimental data. The plausible explanations of the difference are thought to be the frequency resolution of the experimental program (i.e., frequency between two actuation modes), not considering the thin adhesive bonding layer between active and passive layers and using isotropic elastic compliance.

Objective 2 *"To extend the structural mechanics model to compute displacement of the piezoelectric diaphragm under potential difference and to verify results with a finite element method analysis"* is studied in Chapter 5. Theory 3, which stands out as the most accurate analytical model from Chapter 4 is extended to account for the potential difference that applies to the active layer of the piezoelectric actuator, which essentially, is the derivation of frequency response function.

- Damping is extracted by two different methods from the experimental data. It is identified that magnification factor method yields more accurate damping estimations than the half-power method and it fits the experimental data with an higher accuracy. Frequency response function is obtained and compared to the experimental data and a mean difference of 12% over three validation cases is obtained.
- A finite element method analysis is conducted to further verify the modal response of the analytical model and to prepare the basis for an FEM study of structural-fluidic-acoustic multiphysics model of the SJA. The

FEM model has an accuracy of 4% at the peak displacement at the resonance compared to the experimental data.

Objective 3 *”Extending analytical and finite element method based structural mechanics models to account for the fluidic and acoustic characteristics of the synthetic jet actuators. Essentially achieving a more realistic coupling between structural, fluidic and acoustic domains to compute diaphragm displacement, in-cavity pressure and exit jet velocity”* is studied in Chapter 6. Two types of models of SJA are studied to address both structural, acoustic and fluidic features of electromechanical device. The first model is obtained by integrating the frequency response function of the piezoelectric actuator subject to potential difference (derived and validated in Chapter 5) by a set of equations governing fluidic-acoustic side of the SJA. The second model is based on the FEM model of the piezoelectric actuator (developed and verified in Chapter 5) and coupled with the pressure acoustics and viscous flow equations using a commercial FEM software.

- The response of the piezoelectric actuator based analytical model is validated with three different experimental cases. The peak exit jet velocity, corresponding to the mechanical resonance frequency of the actuator, is computed with an average difference of 1.6%. The exit jet velocity corresponding to the cavity-acoustic resonance is computed with an average difference of 8.4% compared to the experimental data, over three validation cases.
- The response of FEM based multiphysics model is also validated with three different experimental cases. The peak exit jet velocity, corresponding to the mechanical resonance frequency of the actuator, is computed with an average difference of 4.3%. The exit jet velocity corresponding to the cavity-acoustic resonance has an average difference of 14.9% compared to the experimental data, over three validation cases.

Objective 4 "Conducting an investigation using experiment and extended analytical model to investigate and maximise the performance criteria (exit jet velocity and electric-to-fluidic power conversion efficiency) of different SJA configurations using different piezoceramic actuators" is studied in Chapter 7. The chapter consists of three different sub-studies. The first study investigates the effect of using identical dimension polycrystalline and single crystal piezoceramic on SJA performance: diaphragm displacement, exit jet velocity and electric-to-fluidic power conversion efficiency. For the comparison of the piezoelectric actuators contribution towards the performance, common SJA dimensions are used in both opposite and adjacent orifice-diaphragm configurations. The second study investigates the effect of using unimorph and bimorph polycrystalline piezoelectric diaphragms on SJA performance and the experimental comparisons and actuator configurations are consistent with the previous study. The third study of the chapter concentrates on the performance of the single modal frequency response SJA experimentally and it is harmonised by the diaphragm-based analytical model presented in Chapter 6.

- It is identified that single crystal piezoceramic driven SJA promotes a threefold increase of the peak centre diaphragm displacement, jet velocity and power conversion efficiency at $20V_p$, compared to the polycrystalline driven SJA. The power conversion efficiency drops as the supply voltage is increased due to the an increasing imbalance between the fluidic power and electrical power. In the cavity-acoustic resonance dominated actuation frequency region ($\eta=72\%$), the power conversion efficiency is higher than the mechanical resonance dominated actuation frequency($\eta=44.4\%$).
- At a peak supply voltage of $40 V_p$, the single crystal driven opposite configuration SJA has a peak exit jet velocity of 99.5 ms^{-1} ($\eta = 23\%$) compared with 65 ms^{-1} ($\eta = 16\%$) of the polycrystalline driven SJA. The adjacent orifice-diaphragm configuration SJA achieved 90 ms^{-1} ($\eta =$

19.2%) and 58 ms^{-1} ($\eta = 19.9\%$), with single crystal and polycrystalline, respectively, at a supply voltage of $40 V_p$.

- The bimorph driven diaphragm promotes 1.5 times larger transverse displacement compared to the unimorph driven diaphragm at the same supply voltage. However, it exhibits a large current consumption due to the employment of two active layers which results in lower power conversion efficiency. Opposite configuration SJA, driven with a supply voltage of $40 V_p$, achieved a peak jet velocity of 92.1 ms^{-1} ($\eta = 6.4\%$) and 67.2 ms^{-1} ($\eta = 18.2\%$) with bimorph and unimorph driven SJA, respectively. Adjacent configuration SJA achieved a peak jet velocity of 80.5 ms^{-1} ($\eta = 5.1\%$) and 62.7 ms^{-1} ($\eta = 17.9\%$) with bimorph and unimorph driven SJA respectively, with a supply voltage of $40 V_p$.
- Single modal frequency response SJA has a peak jet velocity of 62.3 ms^{-1} with a supply voltage of $20 V_p$ and a power conversion efficiency of 46.3% with a polycrystalline piezoceramic. The case is modelled using the diaphragm-based analytical model assuming a single crystal piezoceramic and it is estimated to have a jet velocity of 116 ms^{-1} with a power conversion efficiency of 78.5%.

8.2 Summary and Contributions

In this section, the main conclusions and contributions of this thesis are summarized.

- For the accurate modal analysis of the piezoelectric actuators which are essentially a stack of plates; the extensional-flexural deformations and their respective forces & moments cannot be neglected. Due to its relatively low thickness (compared to the active and passive layers), the effect of the adhesive bonding layer between active and passive plates does not contribute to the natural frequency significantly.

- The method of material damping identification is important for the frequency response functions and different methods result in large differences of the peak displacement compared to the experimental data. Magnification factor method, generally, yields accurate fit to the experimental data.
- Accurate identification of the natural frequency of the piezoelectric diaphragm leads to accurate models of the SJA. Also, the piezoelectrical driven SJA should be fully modelled (i.e., diameter/thickness and material properties of the piezoelectric diaphragm layers) to achieve an accurate response from the model. The only empirical term is the material damping of the diaphragm. Fluidic/pressure loss term varies significantly with the model employed. The cavity or chamber can be modelled as an inviscid medium. The fluidic losses become significant in the orifice neck and they should be modelled with viscous equations.
- The viscous damping acting on the piezoelectric actuator is significant and reduces the peak centre displacement by approximately 30%. The fluidic power should be carefully computed based on the exit jet velocity acquired (i.e., full sine wave or biased sinusoidal). The jet velocity does not increase proportionally with the supply voltage due to the increasing compressibility and viscous effects. Adjacent orifice-diaphragm configuration SJA, due to the increased viscous effects, promotes lower jet velocity than the opposite configuration.
- Current draw is a function of the actuation frequency and supply voltage. The cavity acoustic resonance frequency region has a higher power conversion efficiency due to the low power consumption compared to the mechanical diaphragm resonance frequency region, for all tested types/dimensions of piezoelectric actuator. A polycrystalline piezoceramic has a single peak of the power factor whereas single crystal piezoceramic has a double peak occurrence of the power factor around the

mechanical resonance frequency.

The main contributions and novel research points achieved are briefly given as follows:

- Matrix exponentials (instead of Bessel functions) with a transfer matrix method are used for the full extensional-flexural equations of the circular plates and an accurate natural frequency and peak displacement estimation is obtained.
- The modal analysis of the piezoelectric diaphragm replaced the simplified equations (to estimate natural frequency) and assumptions (for peak displacement) presented in the analytical and lumped element models existing in the literature. Diaphragm displacement and exit jet velocity estimations are accurately achieved with a piezoelectric diaphragm based SJA analytical fluidic-acoustic model.
- SJA Multiphysics model involved the modelling of the piezoelectric diaphragm and fluidic/acoustic features are developed. The coupling between the structural mechanics and acoustics of the SJA allowed the modelling of full actuation frequency envelope of the SJA, including cavity-acoustic and diaphragm mechanical resonance. Thus, the main shortcoming of the existing CFD models in the literature is resolved.
- It is identified that a single crystal piezoelectric actuator enhances the performance metrics of the actuator and yields high jet velocity and power conversion efficiency at relatively low supply voltages. This is likely to enable the implementation of the SJA technology to satisfy full-scale flight flow control tasks.

8.3 Recommendations for Future Work

The recommendations for the future work of SJA modelling and performance enhancement can be separated into two primary sections; quiescent conditions

and application cases.

- Acquiring a PIN-PMN-PT piezoceramic made actuator to test the high voltage response, such as beyond $40 V_p$. The experiment would investigate the exit jet velocity and the electric-to-fluidic power conversion efficiency of supply voltages up to 115 V as a PIN-PMN-PT piezoceramic has an electric field of 5.0 kV/cm (by assuming piezoceramic thickness of 0.23 mm, similar to the PMN-PT case studies).
- Matching acoustic impedance between the air and the piezoelectric actuator as discussed in Chapter 7.5. A thin layer to reduce the impedance mismatch between the air and piezoelectric actuator should be employed.
- Studying cases in which multiple piezoelectric actuators are discharged to orifices by in-phase and out-of-phase operation. For example, an array of actuators could be used to work out-of-phase to each other, which would maximise the cavity pressure in each chamber and consequently exit jet velocity.
- Implementing an array of SJA to test the control effectiveness on a small-scale vertical tail and wing with a small-scale wind tunnel test. The experiment should target quantification of the lift and drag forces on vertical tail model/wing with and without flow control action. The voltage supply and current consumption should be monitored and logged, as well as the forces acting on the vertical tail model/wing.

Bibliography

- [1] International Air Transport Association. IATA Website, 2021. URL <https://www.iata.org/>.
- [2] Hannah Ritchie. Climate change and flying: what share of global CO2 emissions come from aviation?, 2020. URL <https://ourworldindata.org/co2-emissions-from-aviation>.
- [3] Advisory Council for Aeronautics Research in Europe. Flight-Path 2050 Goals, 2020. URL <https://www.acare4europe.org/sria/flightpath-2050-goals>.
- [4] Directorate-General for Mobility and Transport (European Commission) and Directorate-General for Research and Innovation (European Commission). *Flightpath 2050 Europe's vision for aviation*. European Union, 2011. ISBN 9789279197246. doi: 10.2777/50266. URL <http://ec.europa.eu/transport/modes/air/doc/flightpath2050.pdf>.
- [5] Rachel Cooper. IATA approves resolution for global aviation industry to achieve net-zero carbon emissions by 2050, 2021. URL <https://www.climateaction.org/news/>.
- [6] J. Reneaux. Overview on drag reduction technologies for civil transport aircraft. In *ECCOMAS 2004 - European Congress on Computational Methods in Applied Sciences and Engineering*, number July, pages 1–18, 2004.
- [7] L. Anna, Marta Blangiardo, Lea Fortunato, Sarah Floud, Kees De Hoogh, Daniela Fecht, Rebecca E. Ghosh, Helga E. Laszlo, Clare Pearson, Linda Beale, Sean Beevers, John Gulliver, Nicky Best, Sylvia Richardson, and Paul Elliott. Aircraft noise and cardiovascular disease near Heathrow airport in London: Small area study. *BMJ (Online)*, 347(7928):9–12, 2013. ISSN 17561833. doi: 10.1136/bmj.f5432. URL <http://dx.doi.org/doi:10.1136/bmj.f5432>.
- [8] John C. Lin, Marlyn Y. Andino, Michael G. Alexander, Edward A. Whalen, Marc A. Spoor, John T. Tran, and Israel J. Wygnanski. An Overview of Active Flow Control Enhanced Vertical Tail Technology Development. *54th AIAA Aerospace Sciences Meeting*, 2016. doi: 10.2514/6.2016-0056. URL <http://arc.aiaa.org/doi/10.2514/6.2016-0056>.
- [9] Perez Weigel, Martin Schüller, André Gratias, Mathias Lipowski, Theodor Meer, and Michiel Bardet. Design of a synthetic jet actuator for flow

- separation control. *CEAS Aeronautical Journal*, 11(4):813–821, 2020. ISSN 18695590. doi: 10.1007/s13272-020-00479-2. URL <https://doi.org/10.1007/s13272-020-00479-2>.
- [10] Green Car Congress. Renault Altica: 44MPG Diesel Concept with Active Airflow Management, 2006. URL www.greencarcongress.com/2006/02/renault_altica_.html.
- [11] Greg Archer, Thomas Earl, Eoin Bannon, Julia Poliscanova, Nico Muzi, and Soifa Alexandridou. CO 2 Emissions From Cars: The facts. Technical Report August, European Federation for Transport and Environment AISBL, 2018. URL https://www.dbresearch.de/PROD/DBR_INTERNET_EN-PROD/PROD0000000000346332/CO2+emissions+from+cars:+Regulation+via+EU+Emissio.pdf.
- [12] Leonardo P. Chamorro, R. E.A. Arndt, and F. Sotiropoulos. Drag reduction of large wind turbine blades through riblets: Evaluation of riblet geometry and application strategies. *Renewable Energy*, 50(December 2018):1095–1105, 2013. ISSN 09601481. doi: 10.1016/j.renene.2012.09.001.
- [13] M. Jabbal, S. C. Liddle, and W. J. Crowther. Active flow control systems architectures for civil transport aircraft. *Journal of Aircraft*, 47(6):1966–1981, 2010. ISSN 15333868. doi: 10.2514/1.C000237.
- [14] Haohua Zong, Matteo Chiatto, Marios Kotsonis, and Luigi de Luca. Plasma synthetic jet actuators for active flow control. *Actuators*, 7(4):1–34, 2018. ISSN 20760825. doi: 10.3390/act7040077.
- [15] Roman Seele, Emilio Graff, John Lin, and Israel Wygnanski. Performance enhancement of a vertical tail model with sweeping jet actuators. *51st AIAA Aerospace Sciences Meeting including the New Horizons Forum and Aerospace Exposition 2013*, (January):1–18, 2013. doi: 10.2514/6.2013-411.
- [16] Avraham Seifert, Tom Shtendel, and Danny Dolgopyat. From lab to full scale Active Flow Control drag reduction: How to bridge the gap? *Journal of Wind Engineering and Industrial Aerodynamics*, 147:262–272, 2015. ISSN 01676105. doi: 10.1016/j.jweia.2015.09.012. URL <http://dx.doi.org/10.1016/j.jweia.2015.09.012>.
- [17] Mark Jabbal. Flow Control Actuators for the 2020 Civil Transport Aircraft. Technical report, Avert, 2009.
- [18] Rajnish N. Sharma. Fluid Dynamics-Based Analytical Model for Synthetic Jet Actuation. *AIAA Journal*, 45(8):1841–1847, 2007. ISSN 0001-1452. doi: 10.2514/1.25427. URL <http://arc.aiaa.org/doi/10.2514/1.25427>.
- [19] Paul Ziadé, Mark A. Feero, and Pierre E. Sullivan. A numerical study on the influence of cavity shape on synthetic jet performance. *International Journal of Heat and Fluid Flow*, 74(June):187–197, 2018.

- ISSN 0142727X. doi: 10.1016/j.ijheatfluidflow.2018.10.001. URL <https://doi.org/10.1016/j.ijheatfluidflow.2018.10.001>.
- [20] Quentin Gallas, Ryan Holman, Toshikazu Nishida, Bruce Carroll, Mark Sheplak, and Louis Cattafesta. Lumped Element Modeling of Piezoelectric-Driven Synthetic Jet Actuators. *AIAA Journal*, 41(2): 240–247, 2003. ISSN 0001-1452. doi: 10.2514/2.1936. URL <http://arc.aiaa.org/doi/10.2514/2.1936>.
- [21] Mike Zhang, Benjamin; Nudelman. Here’s the simple reason why planes have winglets, 2017.
- [22] Tyler van Buren, Edward Whalen, and Michael Amitay. Interaction between a vortex generator and a synthetic jet in a crossflow. *Physics of Fluids*, 27(10), 2015. ISSN 10897666. doi: 10.1063/1.4932359.
- [23] Louis N. Cattafesta and Mark Sheplak. Actuators for active flow control. *Annual Review of Fluid Mechanics*, 43:247–272, 2011. ISSN 00664189. doi: 10.1146/annurev-fluid-122109-160634.
- [24] Gilad Arwatz, Ilan Fono, and Avi Seifert. Suction and oscillatory blowing actuator modeling and validation. *AIAA Journal*, 46(5):1107–1117, 2008. ISSN 00011452. doi: 10.2514/1.30468. URL <https://doi.org/10.2514/1.30468>.
- [25] F Sonkaya, S Cadirci, and D Erdem. Flow Separation Control on NACA0015 Airfoil Using Synchronized Jet Actuator. 15(2):427–440, 2022.
- [26] Mathias Lipowski, Dennis Bäcker, and Fraunhofer Enas. Array of synthetic jets for large passenger aircraft. In *Proceedings of Aerospace Europe Conference 2020*, pages 1–8, Bordeaux, 2020.
- [27] W. J. Crowther and L. T. Gomes. An evaluation of the mass and power scaling of synthetic jet actuator flow control technology for civil transport aircraft applications. *Proceedings of the Institution of Mechanical Engineers. Part I: Journal of Systems and Control Engineering*, 222(5): 357–372, 2008. ISSN 09596518. doi: 10.1243/09596518JSCE519.
- [28] Geoff A. Slipher and James E. Hubbard, Jr. Description and characterization of an electroactive polymer synthetic jet actuator. *Electroactive Polymer Actuators and Devices (EAPAD) 2007*, 6524:65240I, 2007. ISSN 0277786X. doi: 10.1117/12.714144.
- [29] Yuanchang Liang, Yasuo Kuga, and Minoru Taya. Design of synthetic jet actuator based on FSMA composite. *Smart Structures and Materials 2005: Industrial and Commercial Applications of Smart Structures Technologies*, 5762:179, 2005. ISSN 0277786X. doi: 10.1117/12.600000.
- [30] Arvind Santhanakrishnan and Jamey D. Jacob. Flow control with plasma synthetic jet actuators. *Journal of Physics D: Applied Physics*, 40(3):637–651, 2007. ISSN 00223727. doi: 10.1088/0022-3727/40/3/S02.

- [31] H.P. Mooney, J.B. Brandt, D.S. Lacy, and E.A. Whalen. AFC-Enabled Vertical Tail System Integration Study. Technical Report March 2014, NASA, 2014.
- [32] Wenshi Cui, Hui Zhu, Chao Xia, and Zhigang Yang. *Comparison of Steady Blowing and Synthetic Jets for Aerodynamic Drag Reduction of a Simplified Vehicle*, volume 126. Elsevier B.V., 2015. doi: 10.1016/j.proeng.2015.11.224. URL <http://dx.doi.org/10.1016/j.proeng.2015.11.224>.
- [33] Maher Ben Chiekh, Jean Christophe Béra, and Michel Sunyach. Synthetic jet control for flows in a diffuser: Vectoring, spreading and mixing enhancement. *Journal of Turbulence*, 4(03):1–12, 2003. ISSN 14685248. doi: 10.1088/1468-5248/4/1/032.
- [34] Adeel Arshad, Mark Jabbal, and Yuying Yan. Synthetic jet actuators for heat transfer enhancement – A critical review. *International Journal of Heat and Mass Transfer*, 146:118815, 2020. ISSN 00179310. doi: 10.1016/j.ijheatmasstransfer.2019.118815. URL <https://doi.org/10.1016/j.ijheatmasstransfer.2019.118815>.
- [35] Rob Carter and Richard Kensley. Introduction to Piezoelectric Transducers. *Journal of Chemical Information and Modeling*, 53(9): 1689–1699, 2020. ISSN 1098-6596. URL <https://doi.org/10.1016/j.solener.2019.02.027><https://www.golder.com/insights/block-caving-a-viable-alternative/>
- [36] Katzir S. *The Discovery of the Piezoelectric Effect the Appearance of the Effect*. Springer, Dordrecht, 2006.
- [37] Hwang-Pill Kim, Woo-Seok Kang, Chang-Hyo Hong, Geon-Ju Lee, Gangho Choi, Jaechan Ryu, and Wook Jo. 5 - Piezoelectrics. In Olivier Guillon, editor, *Advanced Ceramics for Energy Conversion and Storage*, Elsevier Series on Advanced Ceramic Materials, pages 157–206. Elsevier, 2020. ISBN 978-0-08-102726-4. doi: <https://doi.org/10.1016/B978-0-08-102726-4.00005-3>. URL <https://www.sciencedirect.com/science/article/pii/B9780081027264000053>.
- [38] Maryam Hamlehdar, Alibakhsh Kasaeian, and Mohammad Reza Safaei. Energy harvesting from fluid flow using piezoelectrics: A critical review. *Renewable Energy*, 143:1826–1838, 2019. ISSN 18790682. doi: 10.1016/j.renene.2019.05.078. URL <https://doi.org/10.1016/j.renene.2019.05.078>.
- [39] Supratik Datta. Piezoelectric Materials: Crystal Orientation and Poling Direction, 2014. URL <https://www.comsol.com/blogs/piezoelectric-materials-crystal-orientation-poling-direction/>.
- [40] S. Waqar, L. Wang, and S. John. *Piezoelectric energy harvesting from intelligent textiles*. Elsevier Ltd., 2015. ISBN 9780081002230. doi: 10.1016/B978-0-08-100201-8.00010-2. URL <http://dx.doi.org/10.1016/B978-0-08-100201-8.00010-2>.

- [41] M. Kimura, A. Ando, and Y. Sakabe. Lead zirconate titanate-based piezo-ceramics. *Advanced Piezoelectric Materials: Science and Technology*, pages 89–110, 2010. doi: 10.1533/9781845699758.1.89.
- [42] X Jiang, F Tang, J T Wang, and T Chen. Growth and properties of PMN-PT single crystals. *Physica C*, 365:678–683, 2001.
- [43] Ju Hyun Yoo, Jae Il Hong, and Wenwn Cao. Piezoelectric ceramic bimorph coupled to thin metal plate as cooling fan for electronic devices. *Sensors and Actuators, A: Physical*, 79(1):8–12, 2000. ISSN 09244247. doi: 10.1016/S0924-4247(99)00249-6.
- [44] Ivan Giorgio, Luca Galantucci, Alessandro Della Corte, and Dionisio Del Vescovo. Piezo-electromechanical smart materials with distributed arrays of piezoelectric transducers: Current and upcoming applications. *International Journal of Applied Electromagnetics and Mechanics*, 47(4): 1051–1084, 2015. ISSN 13835416. doi: 10.3233/JAE-140148.
- [45] A. Erturk and D. J. Inman. An experimentally validated bimorph cantilever model for piezoelectric energy harvesting from base excitations. *Smart Materials and Structures*, 18(2), 2009. ISSN 1361665X. doi: 10.1088/0964-1726/18/2/025009.
- [46] M. Gul, O. Uzol, and I. S. Akmandor. An experimental study on active flow control using synthetic jet actuators over S809 airfoil. *Journal of Physics: Conference Series*, 524(1), 2014. ISSN 17426596. doi: 10.1088/1742-6596/524/1/012101.
- [47] Jimin He and Zhi-Fang Fu. 3 - Basic vibration theory. In Jimin He and Zhi-Fang Fu, editors, *Modal Analysis*, pages 49–78. Butterworth-Heinemann, Oxford, 2001. ISBN 978-0-7506-5079-3. doi: <https://doi.org/10.1016/B978-075065079-3/50003-6>. URL <https://www.sciencedirect.com/science/article/pii/B9780750650793500036>.
- [48] Raphael Yehuda, Stavsky;Loewy. Axisymmetric Vibrations of Isotropic Composite Circular Plates. *The Journal of the Acoustical Society of America*, 49:1542–1550, 1971. doi: 10.1121/1.1912531.
- [49] N. T. Adelman and Y. Stavsky. Flexural-extensional behavior of composite piezoelectric circular plates. *Journal of the Acoustical Society of America*, 67(3):819–822, 1980. ISSN NA. doi: 10.1121/1.383958.
- [50] C. Sato, H. and Shimizu. Transfer matrix analysis of non-linear free vibrations of circular plates with variable thickness. *Journal of Sound and Vibration*, 97(4):587–595, 1984.
- [51] Shifeng Li and Shaochen Chen. Analytical analysis of a circular PZT actuator for valveless micropumps. *Sensors and Actuators, A: Physical*, 104(2):151–161, 2003. ISSN 09244247. doi: 10.1016/S0924-4247(03)00006-2.

- [52] Yuanlin Hu, Xin Liang, and Wen Wang. Deflection of circular diaphragm-type piezoactuators coupling with gas compression in micropumps. *Microsystem Technologies*, 23(12):5329–5341, 2017. ISSN 09467076. doi: 10.1007/s00542-017-3355-3.
- [53] Suryanarayana A.N Prasad, Quentin Gallas, Stephen B. Horowitz, Brian D. Homeijer, Bhavani V. Sankar, Louis N. Cattafesta, and Mark Sheplak. Analytical Electroacoustic Model of a Piezoelectric Composite Circular Plate. *AIAA Journal*, 44(10):2311–2318, 2006. ISSN 0001-1452. doi: 10.2514/1.19855. URL <http://arc.aiaa.org/doi/10.2514/1.19855>.
- [54] Mandar Deshpande and Laxman Saggere. An analytical model and working equations for static deflections of a circular multi-layered diaphragm-type piezoelectric actuator. *Sensors and Actuators, A: Physical*, 136(2): 673–689, 2007. ISSN 09244247. doi: 10.1016/j.sna.2006.12.022.
- [55] Melih Papila, Mark Sheplak, and Louis N. Cattafesta. Optimization of clamped circular piezoelectric composite actuators. *Sensors and Actuators, A: Physical*, 147(1):310–323, 2008. ISSN 09244247. doi: 10.1016/j.sna.2008.05.018.
- [56] Luis Teia Gomes. Effect of damping and relaxed clamping on a new vibration theory of piezoelectric diaphragms. *Sensors and Actuators, A: Physical*, 169(1):12–17, 2011. ISSN 09244247. doi: 10.1016/j.sna.2011.04.005.
- [57] Luis Teia Gomes. Dependency between amplitude and modeshape on vibrating diaphragms. *Sensors and Actuators, A: Physical*, 173(1):66–74, 2012. ISSN 09244247. doi: 10.1016/j.sna.2011.10.017.
- [58] Yuanlin Hu, Hao You, and Wen Wang. Non-linear deflection of a circular diaphragm-type piezoactuator under loads of voltage and pressure. *Sensors and Actuators, A: Physical*, 268:91–100, 2017. ISSN 09244247. doi: 10.1016/j.sna.2017.11.006. URL <http://dx.doi.org/10.1016/j.sna.2017.11.006>.
- [59] Yuanlin Hu, Xin Liang, and Wen Wang. A theoretical solution of resonant circular diaphragm-type piezoactuators with added mass loads. *Sensors and Actuators, A: Physical*, 258:74–87, 2017. ISSN 09244247. doi: 10.1016/j.sna.2017.02.029. URL <http://dx.doi.org/10.1016/j.sna.2017.02.029>.
- [60] Jonne Jeyalingam. *Towards the Noise Reduction of Synthetic Jet Actuators Using Lobed Orifices*. PhD thesis, Brunel University London, 2018.
- [61] James Lighthill. Acoustic streaming. *Journal of Sound and Vibration*, 61(3):391–418, 1978. ISSN 09354964. doi: 10.1007/s001620050068.
- [62] S. G. Mallinson, C. Y. Kwok, and J. A. Reizes. Numerical simulation of micro-fabricated zero mass-flux jet actuators. *Sensors and*

- Actuators, A: Physical*, 105(3):229–236, 2003. ISSN 09244247. doi: 10.1016/S0924-4247(03)00204-8.
- [63] Ari Glezer and Michael Amitay. Synthetic jets. *Annu. Rev. Fluid Mech*, 34:503–529, 2002.
- [64] Paweł Gil and Piotr Strzelczyk. Performance and efficiency of loudspeaker driven synthetic jet actuator. *Experimental Thermal and Fluid Science*, 76:163–174, 2016. ISSN 08941777. doi: 10.1016/j.expthermflusci.2016.03.020.
- [65] Luis Teia Gomes. *on the Modelling of Anisotropic Piezoelectric Diaphragms for the Development of High Subsonic Synthetic Jet Actuators*. PhD thesis, University of Manchester, 2009.
- [66] Luis Gomes and William Crowther. Towards a practical piezoceramic diaphragm based synthetic jet actuator for high subsonic applications - effect of chamber and orifice depth on actuator peak velocity. In *3rd AIAA Flow Control Conference*, Reno, NV, 2006. ISBN 978-1-62410-036-9. doi: 10.2514/6.2006-2859. URL <http://arc.aiaa.org/doi/10.2514/6.2006-2859>.
- [67] Tyler Van Buren, Edward Whalen, and Michael Amitay. Synthetic Jet Actuator Cavity Acoustics: Helmholtz Versus Quarter-Wave Resonance. *Journal of Vibration and Acoustics*, 137(5):054501, 2015. ISSN 0739-3717. doi: 10.1115/1.4030216. URL <http://vibrationacoustics.asmedigitalcollection.asme.org/article.aspx?doi=10.1115/1.4030216>.
- [68] Mark A. Feero, Philippe Lavoie, and Pierre E. Sullivan. Influence of cavity shape on synthetic jet performance. *Sensors and Actuators, A: Physical*, 223:1–10, 2015. ISSN 09244247. doi: 10.1016/j.sna.2014.12.004. URL <http://dx.doi.org/10.1016/j.sna.2014.12.004>.
- [69] Luigi de Luca, Michele Girfoglio, and Gennaro Coppola. Modeling and Experimental Validation of the Frequency Response of Synthetic Jet Actuators. *AIAA Journal*, 52(8):1733–1748, 2014. ISSN 0001-1452. doi: 10.2514/1.J052674. URL <http://arc.aiaa.org/doi/10.2514/1.J052674>.
- [70] Yuan Wei Lv, Jing Zhou Zhang, Yong Shan, and Xiao Ming Tan. Numerical investigation for effects of actuator parameters and excitation frequencies on synthetic jet fluidic characteristics. *Sensors and Actuators, A: Physical*, 219:100–111, 2014. ISSN 09244247. doi: 10.1016/j.sna.2014.08.009.
- [71] Ruben Rathnasingham and Kenneth Breuer. Characteristics of resonant actuators for flow control. *34th Aerospace Sciences Meeting and Exhibit*, 35(January), 1996. doi: doi:10.2514/6.1996-311. URL <http://dx.doi.org/10.2514/6.1996-311>.

- [72] R. D. Blevins. *Formulas for natural frequency and mode shape*. Van Nostrand Reinhold Co., New York, 6th ed. edition, 1979. ISBN 0442207107. doi: 10.1115/1.3153712.
- [73] Mark Jabbal. An Experimental Study of Synthetic Jets for Flow Separation Control. *System*, 2004.
- [74] Shan Zhong, Mark Jabbal, Hui Tang, Luis Garcillan, Fushui Guo, Norman Wood, and Clyde Warsop. Towards the design of synthetic-jet actuators for full-scale flight conditions : Part 1: The fluid mechanics of synthetic-jet actuators. *Flow, Turbulence and Combustion*, 78(3-4): 283–307, 2007. ISSN 13866184. doi: 10.1007/s10494-006-9064-0.
- [75] Quentin Gallas. *On the Modeling and Design of Zero-Net Mass Flux Actuators*. PhD thesis, University of Florida, 2005.
- [76] Ryan Holman, Yogen Utturkar, Rajat Mittal, Barton L. Smith, and Louis Cattafesta. Formation Criterion for Synthetic Jets. *AIAA Journal*, 43(10):2110–2116, 2005. ISSN 0001-1452. doi: 10.2514/1.12033. URL <http://arc.aiaa.org/doi/10.2514/1.12033>.
- [77] V. Timchenko, J. Reizes, E. Leonardi, and G. De Vahl Davis. A criterion for the formation of micro synthetic jets. *American Society of Mechanical Engineers, Fluids Engineering Division (Publication) FED*, 260:197–203, 2004. ISSN 08888116. doi: 10.1115/IMECE2004-61374.
- [78] Jue Zhou, Hui Tang, and Shan Zhong. Vortex roll-up criterion for synthetic jets. *AIAA Journal*, 47(5):1252–1262, 2009. ISSN 00011452. doi: 10.2514/1.40602.
- [79] Zdeněk Trávníček, Zuzana Broučková, and Jozef Kordík. Formation criterion for axisymmetric synthetic jets at high stokes numbers. *AIAA Journal*, 50(9):2012–2017, 2012. ISSN 00011452. doi: 10.2514/1.J051649.
- [80] Ivana M. Milanovic and K. B. Zaman. Synthetic Jets in Cross-Flow. *AIAA Journal*, 43(5):929–940, 2005. ISSN 0001-1452. doi: 10.2514/1.4714. URL <http://arc.aiaa.org/doi/10.2514/1.4714>.
- [81] Tyler Van Buren, Edward Whalen, and Michael Amitay. Achieving a High-Speed and Momentum Synthetic Jet Actuator. *Journal of Aerospace Engineering*, 29(2):04015040, 2016. ISSN 0893-1321. doi: 10.1061/(ASCE)AS.1943-5525.0000530. URL <http://ascelibrary.org/doi/10.1061/%28ASCE%29AS.1943-5525.0000530>.
- [82] Mark Jabbal and Jonne Jeyalingam. Towards the noise reduction of piezoelectrical-driven synthetic jet actuators. *Sensors and Actuators, A: Physical*, 266(October):273–284, 2017. ISSN 09244247. doi: 10.1016/j.sna.2017.09.036.
- [83] Jozef Kordík and Zdeněk Trávníček. Optimal diameter of nozzles of synthetic jet actuators based on electrodynamic transducers. *Experimental Thermal and Fluid Science*, 86:281–294, 2017. ISSN 08941777. doi: 10.1016/j.expthermflusci.2017.03.010.

- [84] Paweł Gil and Emil Smyk. Synthetic jet actuator efficiency based on the reaction force measurement. *Sensors and Actuators, A: Physical*, 295: 405–413, 2019. ISSN 09244247. doi: 10.1016/j.sna.2019.06.011. URL <https://doi.org/10.1016/j.sna.2019.06.011>.
- [85] A. Seifert. Closed-loop active flow control systems: Actuators. *Notes on Numerical Fluid Mechanics and Multidisciplinary Design*, 95:85–102, 2007. ISSN 16122909. doi: 10.1007/978-3-540-71439-2_6.
- [86] Mark Jabbal and Stephanos Kykkotis. Towards the Noise Reduction of Piezoelectrical-Driven Synthetic Jet Actuators. *32nd AIAA Applied Aerodynamics Conference*, 266(June):273–284, 2014. ISSN 09244247. doi: 10.2514/6.2014-2975. URL <http://linkinghub.elsevier.com/retrieve/pii/S0924424717301929%0Ahttp://arc.aiaa.org/doi/10.2514/6.2014-2975>.
- [87] Ri Li, Rajdeep Sharma, and Mehmet Arik. Energy conversion efficiency of synthetic jets. *ASME 2011 Pacific Rim Technical Conference and Exhibition on Packaging and Integration of Electronic and Photonic Systems, InterPACK 2011*, 1(January):115–122, 2011. doi: 10.1115/IPACK2011-52034.
- [88] Michele Girfoglio, Carlo Salvatore Greco, Matteo Chiatto, and Luigi De Luca. Modelling of efficiency of synthetic jet actuators. *Sensors and Actuators, A: Physical*, 233(L):512–521, 2015. ISSN 09244247. doi: 10.1016/j.sna.2015.07.030. URL <http://dx.doi.org/10.1016/j.sna.2015.07.030>.
- [89] Emil Smyk, Sylwester Wawrzyniak, and Kazimierz Peszyński. Synthetic jet actuator with two opposite diaphragms. *Mechanics and Mechanical Engineering*, 24(1):17–25, 2020. ISSN 14281511. doi: 10.2478/mme-2020-0004.
- [90] Matteo Chiatto, Francesco Capuano, Gennaro Coppola, and Luigi De Luca. LEM characterization of synthetic jet actuators driven by piezoelectric element: A review. *Sensors (Switzerland)*, 17(6), 2017. ISSN 14248220. doi: 10.3390/s17061216.
- [91] D C McCormick. Boundary Layer Separation Directed Synthetic Jets Control with Directed Synthetic Jets. In *38th Aerospace Sciences Meeting Exhibit*, number January, 2000. doi: 10.2514/6.2000-519.
- [92] Quentin Gallas, Guiqin Wang, Melih Papila, Mark Sheplak, and Louis Cattafesta. Optimization of synthetic jet actuators. In *41st Aerospace Sciences Meeting and Exhibit*, number January, pages 1–10, Reno, NV, 2003. ISBN 9781624100994. doi: 10.2514/6.2003-635.
- [93] Hui Tang and Shan Zhong. Lumped element modelling of synthetic jet actuators. *Aerospace Science and Technology*, 13(6):331–339, 2009. ISSN 12709638. doi: 10.1016/j.ast.2009.06.004. URL <http://dx.doi.org/10.1016/j.ast.2009.06.004>.

- [94] Tim Persoons. General reduced-order model to design and operate synthetic jet actuators. *AIAA Journal*, 50(4):916–927, 2012. ISSN 00011452. doi: 10.2514/1.J051381.
- [95] Zhong. S. Tang, H. Incompressible Flow Model of Synthetic Jet Actuators. *AIAA*, 44(6):908–912, 2006.
- [96] H. Tang and S. Zhong. A static compressible flow model of synthetic jet actuators. *Aeronautical Journal*, 111(1121):421–431, 2007. ISSN 00019240. doi: 10.1017/S0001924000004681.
- [97] L. D. Kral, J.F. Donovan, A.B. Cain, and A.W. Cary. Numerical Simulation of Synthetic Jet Actuators. *Aiaa 97-1824*, page 14, 1997.
- [98] Donald P. Rizzetta, Miguel R. Visbal, and Michael J. Stanek. Numerical Investigation of Synthetic-Jet Flowfields. *AIAA Journal*, 37(8):919–927, 1999. ISSN 0001-1452. doi: 10.2514/2.811. URL <http://arc.aiaa.org/doi/10.2514/2.811>.
- [99] S.G. Mallinson, J.A. Reizes, and G. Hong. An experimental and numerical study of synthetic jet flow. *Aeronautical Journal*, 105(1043), 2001. ISSN 00019240.
- [100] Razvan Rusovici and George A. Lesieutre. Design of a single-crystal piezoceramic-driven synthetic jet actuator. *Smart Structures and Materials 2004: Smart Structures and Integrated Systems*, 5390(814):276, 2004. ISSN 0277786X. doi: 10.1117/12.539576.
- [101] H. Tang and S. Zhong. 2D numerical study of circular synthetic jets in quiescent flows. *Aeronautical Journal*, 109(1092):89–97, 2005. ISSN 00019240. doi: 10.1017/S0001924000000592.
- [102] Manu Jain, Bhalchandra Puranik, and Amit Agrawal. A numerical investigation of effects of cavity and orifice parameters on the characteristics of a synthetic jet flow. *Sensors and Actuators, A: Physical*, 165(2):351–366, 2011. ISSN 09244247. doi: 10.1016/j.sna.2010.11.001. URL <http://dx.doi.org/10.1016/j.sna.2010.11.001>.
- [103] Sajad Alimohammadi, Eoin Fanning, Tim Persoons, and Darina B. Murray. Characterization of flow vectoring phenomenon in adjacent synthetic jets using CFD and PIV. *Computers and Fluids*, 140:232–246, 2016. ISSN 00457930. doi: 10.1016/j.compfluid.2016.09.022.
- [104] A. Qayoum and A. Malik. Influence of the Excitation Frequency and Orifice Geometry on the Fluid Flow and Heat Transfer Characteristics of Synthetic Jet Actuators. *Fluid Dynamics*, 54(4):575–589, 2019. ISSN 15738507. doi: 10.1134/S0015462819040086.
- [105] Poorna Mane, Karla Mossi, and Robert Bryant. Synthetic jets with piezoelectric diaphragms. *Smart Structures and Materials*, 5761(1):233, 2005. ISSN 0277786X. doi: 10.1117/12.599584. URL <http://proceedings.spiedigitallibrary.org/proceeding.aspx?doi=10.1117/12.599584>.

- [106] Robert Oshana. Overview of Digital Signal Processing Algorithms. *DSP Software Development Techniques for Embedded and Real-Time Systems*, pages 59–121, jan 2006. doi: 10.1016/B978-075067759-2/50006-5.
- [107] Obo Pro 2 Inc. Piezoelectric Ceramic Element, 2020. URL <http://www.pro2inc.com/files/13-1311-21823.php?Lang=en>.
- [108] American Piezo Company. Piezoelectric Disc Benders, 2020. URL <https://www.americanpiezo.com/standard-products/disc-benders.html>.
- [109] Inc. TRS Technologies. PMN-PT - Single Crystal Material Properties, 2021. URL <http://www.trstechnologies.com/Materials/High-Performance-PMN-PT-Piezoelectric-Single-Crystal>.
- [110] Hui Tang, Shan Zhong, Mark Jabbal, Luis Garcillan, Fushui Guo, Norman Wood, and Clyde Warsop. Towards the design of synthetic-jet actuators for full-scale flight conditions : Part 2: Low-dimensional performance prediction models and actuator design method. *Flow, Turbulence and Combustion*, 78(3-4):309–329, 2007. ISSN 13866184. doi: 10.1007/s10494-006-9061-3.
- [111] Polytec. Polytec Scanning Vibrometer Manual, 2004.
- [112] Dantec Company. MiniCTA and Multichannel CTA Systems: Compact CTA Systems for accurate flow investigations, 2013.
- [113] Michael Amitay, Anthony E. Washburn, Scott G. Anders, and David E. Parekh. Active Flow Control on the Stingray Uninhabited Air Vehicle: Transient Behaviour. *AIAA Journal*, 42(11):2205–2215, 2004. ISSN 0001-1452. doi: 10.2514/1.5697.
- [114] Michael Amitay and Ari Glezer. Aerodynamic Flow Control Using Synthetic Jet Actuators. *Control of Fluid Flow*, pages 45–73, 2006.
- [115] Mathworks. MATLAB Version 2020b, 2020. URL www.mathworks.com.
- [116] Meggitt Energy. How to wire a 8507C with a 136 Power Amplifier? A Connection and setting manual, 2019.
- [117] Girish K. Jankee and Bharathram Ganapathisubramani. Influence of internal orifice geometry on synthetic jet performance. *Experiments in Fluids*, 60(4):1–11, 2019. ISSN 07234864. doi: 10.1007/s00348-019-2697-2. URL <http://dx.doi.org/10.1007/s00348-019-2697-2>.
- [118] J. Chopra, Inderjit; Siroshi. *Smart Structures Theroy*. Cambridge University Press, 2014.
- [119] Kenji Uchino. Piezoelectric ultrasonic motors: Overview. *Smart Materials and Structures*, 7(3):273–285, 1998. ISSN 09641726. doi: 10.1088/0964-1726/7/3/002.

- [120] D. J. Laser and J. G. Santiago. A review of micropumps. *Journal of Micromechanics and Microengineering*, 14(6), 2004. ISSN 09601317. doi: 10.1088/0960-1317/14/6/R01.
- [121] Singiresu S. Rao. *Vibration of Continuous Systems*. John Wiley Sons, Inc, Hoboken, N.J., 2007. ISBN 0471771716. doi: 10.1002/9780470117866.
- [122] Andrzej B. Dobrucki and Piotr Pruchnicki. Theory of piezoelectric axisymmetric bimorph. *Sensors and Actuators, A: Physical*, 58(3):203–212, 1997. ISSN 09244247. doi: 10.1016/S0924-4247(97)01401-5.
- [123] Clinton Y.K. Chee, Liyong Tong, and Grant P. Steven. A review on the modelling of piezoelectric sensors and actuators incorporated in intelligent structures. *Journal of Intelligent Material Systems and Structures*, 9(1):3–19, 1998. ISSN 1045389X. doi: 10.1177/1045389X9800900101.
- [124] Samuel I En Lin. The theoretical and experimental studies of a circular multi-layered annular piezoelectric actuator. *Sensors and Actuators, A: Physical*, 165(2):280–287, 2011. ISSN 09244247. doi: 10.1016/j.sna.2010.01.018.
- [125] F.A. Pestel E.C.; Leckie. *Matrix Methods in Elastomechanics*. McGraw-Hill Book Company, Inc, New York, 1963.
- [126] Higham N. J. *Functions of Matrices: Theory and Computation*. Society for Industrial and Applied Mathematics, Philadelphia, 2008.
- [127] J. N. Reddy. *Theory and Analysis of Elastic Plates and Shells*. CRC Press, 2nd edition, 2007.
- [128] N. McLachnan. *Bessel Functionf for Engineers*. Oxford University Press, 1948.
- [129] Louis N. Cattafesta, Sanjay Garg, and Deepak Shukla. Development of piezoelectric actuators for active flow control. *AIAA Journal*, 39(8): 1562–1568, 2001. ISSN 00011452. doi: 10.2514/2.1481.
- [130] N. Coddington, E.A; Levinson. *Theory ofd Ordinary Differential Equations*. McGraw-Hill Book Company, Inc, New York, 1955.
- [131] S. Timoshenko S.; Woinowsky-Krieger. *Theory of Plates and Shells, 2nd Edition*. McGraw-Hill Book Company, Inc, New York, 1959. doi: 10.1016/0006-8993(74)90278-9.
- [132] A.A Popov. Free vibration of functionally graded beams and frameworks using the dynamic stiffness method. *Journal of Sound and Vibration*, 422 (466):34–47, 2018. URL doi:10.1016/j.jsv.2019.115007.
- [133] Frazer R.A.; Duncan W.J. *Elementary Matrices and Some Applications to Dynamics and Differential Equations*. Cambridge University Press, Cambridge, 1938.

- [134] Marlis Hochbruck and Alexander Ostermann. Exponential integrators. *Acta Numerica*, 19:209–286, 2010. ISSN 09624929. doi: 10.1017/S0962492910000048.
- [135] Kenji Uchino. Introduction to piezoelectric actuators: Research misconceptions and rectifications. *Japanese Journal of Applied Physics*, 58 (SG), 2019. ISSN 13474065. doi: 10.7567/1347-4065/ab1645.
- [136] Comsol Multiphysics v5.3a. Comsol Multiphysics Acoustics Module Users Guide, 2018. URL <https://doc.comsol.com/5.4/doc/com.comsol.help.aco/AcousticsModuleUsersGuide.pdf>.
- [137] A.N. Norris. The Isotropic Material Closest to a Given Anisotropic Material. *Mechanics of Materials and Structures*, 1(2), 2006.
- [138] Heckl M. Cremer L. *Structure-Borne Sound*. Springer-Verlag, Berlin, 1973. ISBN 8439717504.
- [139] A. W. Leissa. *Vibration of Plates*. NASA, Washington D.C., 1969. ISBN 9781420053968. doi: 10.1115/1.801993.ch7.
- [140] P P Rao, J L Gilarranz, J Ko, T Strganac, and O K Rediniotis. Flow separation control via synthetic jet actuation. *AIAA, Aerospace Sciences Meeting and Exhibit, 38 th, Reno, NV*, pages 1–21, 2000.
- [141] R.A. Calvert, J.R.; Farrar. *An Engineering Data Book*. Macmillan Education UK, London, 1999.
- [142] Victor Giurgiutiu. Piezoelectric Wafer Active Sensors. In *Structural Health Monitoring*, pages 239–307. Elsevier, jan 2008. doi: 10.1016/b978-012088760-6.50008-8.
- [143] George A. Papagiannopoulos and George D. Hatzigeorgiou. On the use of the half-power bandwidth method to estimate damping in building structures. *Soil Dynamics and Earthquake Engineering*, 31(7):1075–1079, 2011. ISSN 02677261. doi: 10.1016/j.soildyn.2011.02.007. URL <http://dx.doi.org/10.1016/j.soildyn.2011.02.007>.
- [144] Ivan Wang. An analysis of higher order effects in the half power method for calculating damping. *Journal of Applied Mechanics, Transactions ASME*, 78(1):0145011–0145013, 2011. ISSN 00218936. doi: 10.1115/1.4002208.
- [145] Baisheng Wu. A correction of the half-power bandwidth method for estimating damping. *Archive of Applied Mechanics*, 85(2):315–320, 2015. ISSN 14320681. doi: 10.1007/s00419-014-0908-0.
- [146] Gopi Krishnan and Kamran Mobseni. Axisymmetric synthetic jets: An experimental and theoretical examination. *AIAA Journal*, 47(10):2273–2283, 2009. ISSN 00011452. doi: 10.2514/1.42967.
- [147] Celerino Resendiz Rosas. Numerical simulation of flow separation control by oscillatory fluid injection. *Texas AM University, Doctoral*(May), 2003.

- [148] Matteo Chiatto, Andrea Palumbo, and Luigi de Luca. Design approach to predict synthetic jet formation and resonance amplifications. *Experimental Thermal and Fluid Science*, 107(May):79–87, 2019. ISSN 08941777. doi: 10.1016/j.expthermflusci.2019.05.013. URL <https://doi.org/10.1016/j.expthermflusci.2019.05.013>.
- [149] F. M. White. *Fluid mechanics (seventh ed.)*. McGraw-Hill Book Company, Inc, New York, 2009. ISBN 0070622329.
- [150] Jonne Jeyalingam and Mark Jabbal. Optimization of Synthetic Jet Actuator design for noise reduction and velocity enhancement. In *8th AIAA Flow Control Conference*, number June, 2016. ISBN 978-1-62410-432-9. doi: 10.2514/6.2016-4236. URL <http://arc.aiaa.org/doi/10.2514/6.2016-4236>.
- [151] Mark Jabbal and Jonne Jeyalingam. Towards the noise reduction of piezoelectrical-driven synthetic jet actuators. *Sensors and Actuators, A: Physical*, 266:273–284, 2017. ISSN 09244247. doi: 10.1016/j.sna.2017.09.036. URL <https://doi.org/10.1016/j.sna.2017.09.036>.
- [152] K. H. Lam, H. L.W. Chan, H. S. Luo, Q. R. Yin, and Z. W. Yin. Piezoelectrically actuated ejector using PMN-PT single crystal. *Sensors and Actuators, A: Physical*, 121(1):197–202, 2005. ISSN 09244247. doi: 10.1016/j.sna.2005.01.003.
- [153] Tianliang Yu, George A. Lesieutre, Steven F. Griffin, and Aaron Sassoon. Bimorph-driven synthetic jet actuators optimized for various piezoelectric materials using a low-order coupled electro-elastic-acoustic model. In *AIAA Scitech 2019 Forum*, number January, San Diego, California, 2019. doi: 10.2514/6.2019-1353.
- [154] Poorna Mane, Karla Mossi, Ali Rostami, Robert Bryant, and Nicolas Castro. Piezoelectric actuators as synthetic jets: Cavity dimension effects. *Journal of Intelligent Material Systems and Structures*, 18(11):1175–1190, 2007. ISSN 1045389X. doi: 10.1177/1045389X06075658.
- [155] Kenji Uchino. Private Communication, 2019.
- [156] Nicholas W. Rathay, Matthew J. Boucher, Michael Amitay, and Edward Whalen. Performance enhancement of a vertical stabilizer using synthetic jet actuators: Non-zero sideslip. In *6th AIAA Flow Control Conference 2012*, number January, pages 1–15, Nashville, Tennessee, 2012. ISBN 9781624101885. doi: 10.2514/6.2012-71.
- [157] Nicholas Rathay, Matthew Boucher, Michael Amitay, and Edward Whalen. Parametric study of synthetic-jet-based control for performance enhancement of a vertical tail. *AIAA Journal*, 52(11):2440–2454, 2014. ISSN 00011452. doi: 10.2514/1.J052887.